Direct measurement of the top-quark decay width with the ATLAS detector

Dissertation

zur Erlangung des mathematisch-naturwissenschaftlichen Doktorgrades
„Doctor rerum naturalium“
der Georg-August-Universität Göttingen

im Promotionsprogramm ProPhys
der Georg-August University School of Science (GAUSS)

vorgelegt von

Tomáš Dado

aus Bratislava

Bratislava, 2019

Comenius University Bratislava
Faculty of Mathematics, Physics and Informatics

Direct measurement of the top-quark decay width with the ATLAS detector

PhD Thesis

Mgr. Tomáš Dado

Study field: 1124 Nuclear And Subnuclear Physics
Study program: Nuclear And Subnuclear Physics

Supervisor: **prof. RNDr. Stanislav Tokár, DrSc.**

Department of Nuclear Physics and Biophysics

BRATISLAVA, 2019

Univerzita Komenského v Bratislave
Fakulta matematiky, fyziky a informatiky

ZADANIE ZÁVEREČNEJ PRÁCE

Meno a priezvisko študenta: Mgr. Tomáš Dado
Študijný program: jadrová a subjadrová fyzika (Jednoodborové štúdium, doktorandské III. st., denná forma)
Študijný odbor: jadrová a subjadrová fyzika
Typ záverečnej práce: dizertačná
Jazyk záverečnej práce: anglický
Sekundárny jazyk: slovenský

Názov: Direct measurement of the top-quark decay width with the ATLAS detector
Priame meranie rozpadovej šírrky top kvarku na experimente ATLAS

Anotácia: Meranie vlastností top kvarku je jedna zo základných projektov v ATLAS kolaborácií. Práca sa bude zaoberať priamym meraním rozpadovej šírky top kvarku. Práca použije dáta zozbierané v protón-protónových zrážkach detektorom ATLAS pri ťažiskovej energii 8 a 13 TeV.

Cieľ: Zmerať rozpadovú šírku top kvarku použijúc dáta z protón-protónových zrážok zozbieraných na detektore ATLAS.

Literatúra: 1. M. Beneke et al., Top Quark Physics, Proc. of the Workshop on Standard Model Physics at LHC, CERN 2000-004
2.The ATLAS collaboration, Expected Performance of the ATLAS Experiment, CERN-OPEN-2008-020, Geneva 2009
3. J.F. Donoghue, E.Golowich and B.R. Holstein, Dynamics of the Standard Model, Cambridge University Press, New York 1992

Poznámka:

Kľúčové slová: top kvark, rozpadová šírka top kvarku

Školiteľ: prof. RNDr. Stanislav Tokár, DrSc.
Konzultant: Mgr. Pavol Bartoš, PhD.
Katedra: FMFI.KJFB - Katedra jadrovej fyziky a biofyziky
Vedúci katedry: prof. RNDr. Stanislav Tokár, DrSc.

Dátum zadania: 25.02.2014

Dátum schválenia: 25.04.2014 prof. RNDr. Jozef Masarik, DrSc.
garant študijného programu

....
študent školiteľ

Comenius University in Bratislava
Faculty of Mathematics, Physics and Informatics

THESIS ASSIGNMENT

Name and Surname: Mgr. Tomáš Dado
Study programme: Nuclear and Subnuclear Physics (Single degree study, Ph.D. III. deg., full time form)
Field of Study: Nuclear And Subnuclear Physics
Type of Thesis: Dissertation thesis
Language of Thesis: English
Secondary language: Slovak

Title: Direct measurement of the top-quark decay width with the ATLAS detector

Annotation: Measurement of the top quark properties is one of the most important topics in the ATLAS collaboration. The thesis will deal with a direct measurement of the top-quark decay width. Data collected in proton-proton collisions by the ATLAS detector at a centre-of-mass energy of 8 and 13 TeV will be used.

Aim: Measure the top-quark decay width using data from proton-proton collisions recorded by the ATLAS detector.

Literature: 1. M. Beneke et al., Top Quark Physics, Proc. of the Workshop on Standard Model Physics at LHC, CERN 2000-004
2.The ATLAS collaboration, Expected Performance of the ATLAS Experiment, CERN-OPEN-2008-020, Geneva 2009
3. J.F. Donoghue, E.Golowich and B.R. Holstein, Dynamics of the Standard Model, Cambridge University Press, New York 1992

Comment:

Keywords: top quark, top-quark decay width

Tutor: prof. RNDr. Stanislav Tokár, DrSc.
Consultant: Mgr. Pavol Bartoš, PhD.
Department: FMFI.KJFB - Department of Nuclear Physics and Biophysics
Head of department: prof. RNDr. Stanislav Tokár, DrSc.

Assigned: 25.02.2014

Approved: 25.04.2014 prof. RNDr. Jozef Masarik, DrSc.
Guarantor of Study Programme

.... Student

.... Tutor

Betreuungsausschuss

Prof. Dr. Arnulf Quadt

Prof. Dr. Stan Lai

Prof. Dr. Steffen Schumann

Mitglieder der Prüfungskommission:

Vorsitzender: Prof. Dr. Jozef Masarik
Faculty of Mathematics, Physics and Informatics, Comenius University in Bratislava

Referent: Assoc. Prof. Dr. Jiří Dolejší
Institute of Particle and Nuclear Physics, Charles University, Prague

Referent: Dr. Ivan Králik
Institute of Experimental Physics, Slovak Academy of Sciences

Referent: Prof. Dr. Steffen Schumann
Institut für Theoretische Physik, Georg-August-Universität Göttingen

Mitglied: Prof. Dr. Zuzana Dubničková
Faculty of Mathematics, Physics and Informatics, Comenius University in Bratislava

Mitglied: Assoc. Prof. Dr. Pavol Valko
Faculty of Electrical Engineering and Information Technology, Slovak University of Technology

Mitglied: Prof. Dr. Stan Lai
II. Physikalisches Institut, Georg-August-Universität Göttingen

Betreuer: Prof. Dr. Stanislav Tokár
Faculty of Mathematics, Physics and Informatics, Comenius University in Bratislava

Betreuer: Prof. Dr. Arnulf Quadt
II. Physikalisches Institut, Georg-August-Universität Göttingen

Tag der mündlichen Prüfung: 12. Juni 2019

Referenz: II.Physik-UniGö-Diss-2019/05

Direct measurement of the top-quark decay width with the ATLAS detector

Abstract

The top quark is the heaviest known elementary particle. Due to its large mass, the top quark decays before it forms bound states. This makes the top quark a unique particle in the Standard Model. Precise measurements of its properties could be used as tests of the consistency of the Standard Model and potential deviations could point to physics Beyond the Standard Model. This thesis deals with the direct measurement of the top-quark decay width using data collected in proton-proton collisions at centre-of-mass energies of 8 and 13 TeV with the ATLAS detector at the Large Hadron Collider. The thesis focuses on the more recent measurement at 13 TeV while the most important highlights of the 8 TeV measurement are summarised. The decay width of the top quark is extracted from the data using a likelihood fit of distributions of variables sensitive to the top-quark decay width in $t\bar{t}$ pair production. The measurement is performed in a direct way, thus it is less model-dependent compared to indirect methods.

Priame meranie rozpadovej šírky top kvarku na experimente ATLAS

Abstrakt

Top kvark je najťažšia známa elementárna častica. Vďaka svojej veľkej hmotnosti sa top kvark rozpadá skôr ako vytvorí viazané stavy. Táto vlastnostť robí top kvark unikátnou časticou v Štandardnom Modeli. Presné merania vlastností top kvarku sa môžu využiť ako testy konzistentnosti Štandardného Modelu a prípadné odchýlky možu poukázať na fyziku za Štandardným Modelom. Táto práca sa venuje priamemu meraniu rozpadovej šírky top kvarku na dátach z protón-protónových zrážok pri ťažiskovej energii 8 a 13 TeV získaných detektorom ATLAS na urýchľovači LHC. Práca sa zameriava na analýzu dát pri energii 13 TeV, pričom sú však spomenuté aj najdôležitejšie výsledky z analýzy vykonanej na dátovej vzorke s ťažiskovou energiou 8 TeV. Rozpadová šírka top kvarku je získaná z dát pomocou fitu rozdelení premenných citlivých na rozpadovú šírku top kvarku v produkcií top kvarkových párov. Ide o tzv. priame meranie top kvarkovej šírky, ktoré je menej modelovo závislé ako nepriame merania.

Direkte Messung der Top-Quark-Zerfallsbreite mit dem ATLAS-Detektor

Zusammenfassung

Das Top-Quark ist das schwerste bekannte Elementarteilchen. Da es ob seiner großen Masse zerfällt bevor es gebundene Zustände eingehen kann, nimmt es im Standardmodell der Teilchenphysik eine besondere Rolle ein. Genaue Messungen von Eigenschaften des Top-Quarks erlauben einerseits Konsistenztests des Standardmodells, andererseits könnten Abweichungen von Vorhersagen aber auch auf Physik jenseits des Standardmodells hindeuten. Für diese Arbeit wurden Daten aus Proton-Proton-Kollisionen bei 8 und 13 TeV Schwerpunktsenergie, die mit dem ATLAS-Detektor am Large Hadron Collider aufgezeichnet wurden, ausgewertet und aus ihnen die Top-Quark-Zerfallsbreite bestimmt. Während der Fokus der Arbeit auf den neueren Ergebnissen bei 13 TeV liegt, werden zusätzlich die wichtigsten Punkte der 8 TeV-Messung zusammengefasst. Um die Top-Quark-Zerfallsbreite aus den Daten zu extrahieren, wurden Likelihood-Fits von Observablen in Top-Quark-Paarproduktion durchgeführt, die sensitiv auf die Zerfallsbreite sind. Hierbei handelt es sich um eine direkte Messung der Zerfallsbreite, die entsprechend weniger modellabhängig als indirekte Messungen ist.

Acknowledgements

I would like to use this place to thank everyone who was essential in the steps that were vital for the thesis.

I am especially grateful to both of my supervisors Stanislav Tokár and Arnulf Quadt for their valuable guidance throughout the analysis. Without this guidance my thesis would hardly see the light of day.

I would also like to thank my colleagues, who have also become my friends, in both institutions in Bratislava and Göttingen for the endless talks about the analysis and related problems. I must also thank my friends in Göttingen for their warm welcome I received when I first arrived to Germany. A special ”thank you” is reserved for Lucie Hamdi, who welcomed me in her home and helped me with many every-day-life situations.

I would like to thank Thomas Peiffer and particularly Lisa Shabalina for the technical discussions and help with the analysis. I am grateful to Philipp Stolte-Cord-to-Crax, who worked with me on the 8 TeV analysis and with whom I discussed many technical problems we faced.

I thank all people who read and corrected the thesis, especially Thomas Peiffer and Clara Nellist who had to correct many misused or missing articles.

Last, but not least, I would like to thank my family and friends for their supports during my PhD study.

Contents

CHAPTER 1

Introduction

”Measure what is measurable, and make measurable what is not so” – this simple statement, usually attributed to Galileo Galilei, is the quintessence of experimental physics, or more generally, experimental sciences. The process of systematically studying nature via experiments in Western civilisation could be traced back to the giants of ancient Greece, Socrates and Aristotle. Socrates showed us that only when we acknowledge our ignorance we can try to pursuit true knowledge, a fact that seems unquestionable nowadays which shows the true wisdom of Socrates. Using thorough experiments as a tool to observe nature was probably developed by Aristotle in his book *On the soul*, better known by its Latin translation *De Anima*. Science, and especially physics, has come a long way since the Aristotelian concepts of motion and cosmic order. It is no longer believed that there are only four basic elements: earth, air, fire and water as was believed in Aristotle's times. Moreover, we know that gravity cannot be explained by different ratios of the four basic components in objects that try to reach their original source. In Aristotelian physics this explains why heavy objects, like rocks, fall towards the centre of Aristotelian cosmos (Earth) and light objects that are composed of light elements like air and fire rise up, away from the centre. Although these theories seem rather odd from the current point of view, they were one of the driving forces of science – searching for a universal rule or theory that describes a vast number of phenomena. In particle physics, or *high energy physics*, we replaced the Aristotle's four elements with *elementary particles*[1] that play a similar role.

The birth of particle physics in the modern sense could be dated to 1897 when J. J. Thomson discovered an electron using cathode rays [1]. Experiments with a gold foil carried out by H. Geiger and E. Rutherford between 1908 and 1913 [2] led to the discovery of atom nuclei and a model of the atom was hypothesised. In 1930, W. Pauli proposed the chargeless neutrino as a new particle that could explain inconsistencies in the theory of β decays. After the discovery of muons [3] from cosmic rays in 1937 by C. D. Anderson, it became obvious that the theory of elementary particles needed significant improvements to account for all the observed particles. This became an even more important question during the 1950s when many new particles were observed. The process of searching for a theory of elementary particles resulted in the *Standard*

---

[1] The word ”elementary” originates from Latin ”elementum” meaning ”first principle, matter in the most basic form”. Origins could be traced to the *Canaanite* alphabet with its first three letters L M N, thus the word elementary could be considered as a short version of the phrase ”It is as easy as ABC”.

Model of elementary particles.

With the advance of technology, the experiments involving particles became more complex, reaching higher energies. First fixed-target experiments soon became insufficient and they have been replaced with collider experiments that can reach higher energies of the colliding particles, thus probing particles with higher masses. Currently, the *Large Hadron Collider* (LHC) is the most powerful particle accelerator, built to reach of energies up to 7 TeV per beam, thus reaching the centre-of-mass energy up to 14 TeV. In July 2012, the observation [4,5] of the last missing piece of the Standard Model, the Higgs Boson, was announced by two LHC experiments: ATLAS and CMS. Despite the discovery of the Higgs boson, the LHC programme is not finished, it continues searching for possible hints of Physics Beyond the Standard Model, as well as probing the parameters of the Standard Model and their self-consistency.

The top quark is the heaviest known elementary particle and it has the largest coupling to the Higgs boson, suggesting it could play an important role in the Standard Model. It was discovered [6,7] in 1995 by the CDF and D0 collaborations in proton-antiproton collisions at the Tevatron. The top quark is predicted to have large decay width, consequently it is predicted to have very short lifetime. This makes the top quark a unique particle amongst other elementary particles of the Standard Model.

This thesis presents direct measurements of the top-quark decay width conducted at centre-of-mass energies of 8 and 13 TeV using the data collected by the ATLAS detector. The thesis focuses on the 13 TeV measurement, that exploits both semileptonic and dileptonic decays of the $t\bar{t}$ pairs, and all steps of the analysis will be discussed in detail. The 8 TeV measurement, that exploits only semileptonic decays of the $t\bar{t}$ pair, will be briefly summarised, as the author of the thesis made significant contributions to this measurement, especially for the estimation of the systematic uncertainties. Both analyses rely on the template fit of simulated distributions for various input top-quark decay widths to the observed data. The two measurements will be compared and the significant differences will be emphasised.

The chapters of this thesis are ordered as follows: Chapter 2 briefly summarises the theoretical concepts of the theory behind the Standard Model. Chapter 3 describes important properties of the top quarks with a particular emphasis on its decay width. Chapter 4 focuses on the description of the LHC and the ATLAS detector. Physics objects exploited in the decay width measurement are summarised in Chapter 5. The simulated samples and the observed data are reported in Chapter 6. Chapter 7 focuses on the selection employed in the decay width measurement. Reconstruction techniques used to solve the ambiguity of the matching of the reconstructed objects to their final state counterparts from the $t\bar{t}$ decay are summarised in Chapter 8. Systematic uncertainties considered in the analysis are presented in Chapter 9. Chapter 10 is devoted to the analysis strategy used for both 8 TeV and 13 TeV measurements, this chapter also provides a very brief summary of the 8 TeV measurement and lessons learned from this measurement that are applied for the 13 TeV analysis. Results of both measurements are reported in Chapter 11. Finally, Chapter 12 concludes the thesis and provides an outlook for the future direct measurements of the top-quark decay width.

The thesis follows the “natural units” convention, where $\hbar = c = 1$, except Chapters 4 and 5, where mostly physical dimensions of the detector or mean life-time of the particles are described.

CHAPTER 2

Standard Model

The SM of elementary particles describes the current knowledge of elementary particles and their interactions. The SM relies on two concepts: gauge theories based on $SU(3) \otimes SU(2) \otimes U(1)$ symmetry, that describes combined strong and electroweak interactions, and the Spontaneous Symmetry Breaking mechanism. The gauge theories provide a well-defined procedure on how to add interaction terms to the Lagrangian describing free (non-interacting) particles by exploiting local (depending on four-position) transformations. The gauge theories relevant for the SM are discussed in Section 2.1. The Spontaneous Symmetry Breaking mechanism, that dynamically generates the masses of the elementary particles that is closely related to the gauge theories, is summarised in Section 2.2.3. The fundamental experimental and theoretical achievements that led to the SM, as well as important properties of the SM, are outlined in the following sections.

2.1. Gauge theories

One of the most fundamental breakthroughs in the process of building the SM was the recipe to generate interaction theories from theories without interaction in the Quantum Field Theory (QFT). The recipe is summarised below. Let us first look at the QFT Lagrangian for free spin one-half particles

$$\mathcal{L} = \bar{\Psi} \left(i\not{\partial} - m \right) \Psi, \tag{2.1}$$

where the slash notation $\not{\partial} \equiv \gamma^{\mu}\partial_{\mu}$, and similarly for any slashed operator, is used. γ^{μ} are four gamma matrices[1]. Ψ and $\bar{\Psi}$ are bi-spinors.

It is possible to introduce an interaction term to a Lagrangian describing free particles by exploiting the local gauge symmetry of the Lagrangian. The first observation for a field of a half-integer spin is that the free Lagrangian (2.1) is trivially invariant under global transformation

$$\Psi(x) \rightarrow e^{-i\alpha}\Psi(x), \tag{2.2}$$

---

[1] $\gamma^{\mu}\gamma^{\nu} + \gamma^{\nu}\gamma^{\mu} = 2\eta^{\mu\nu}$, where $\eta^{\mu\nu}$ is the metric tensor of Minkowski space.

for any fixed real value α. However, the free Lagrangian is not invariant under *local* (gauge) transformation

$$\Psi(x) \to e^{-i\alpha(x)}\Psi(x), \tag{2.3}$$

where $\alpha(x)$ is a real function of the four-position due to the presence of the derivative. We can force the Lagrangian to be invariant under local transformation, but we need to add additional terms to the Lagrangian[2]. The additional terms come from substituting

$$\partial_\mu \to D_\mu \equiv \partial_\mu + ieA_\mu, \tag{2.4}$$

where we introduced a new vector (spin one) field, that itself transforms as $A_\mu \to A_\mu + \partial_\mu \alpha(x)$. The e denotes an elementary electric charge. The new field interacts with the free $\Psi(x)$ field via $\bar{\Psi}\not{A}\Psi$ term. The field A_μ has no dynamic (free-propagating) component and thus a term for the electromagnetic tensor $F_{\mu\nu}F^{\mu\nu}$, $F_{\mu\nu} = \partial_\mu A_\nu - \partial_\nu A_\mu$, has to be added. It should be noted that the newly introduced field A_μ is massless and explicitly adding a mass term for this field in form of $m^2 A_\mu A^\mu$ breaks the gauge symmetry. This fact will become important when we will talk about the Higgs mechanism in the next chapter. The obtained Lagrangian is the Lagrangian of QED. The transformation of the $\Psi(x)$ field is called $U(1)$ gauge transformation as $e^{-ie\alpha(x)}$ is an element of the $U(1)$ group[3].

Using the $U(1)$ gauge transformation is not the only possible solution. For multi-component fields it is possible to apply a gauge transformation of non-Abelian[4] groups such as $SU(2)$ or $SU(3)$[5] as was shown by Yang and Mills [8]. They provided a recipe on how to make a free Lagrangian gauge invariant under non-Abelian transformations. The rules can be summarised as follows:

$$\begin{aligned} \Psi &\to U\Psi, \\ \partial_\mu &\to D_\mu \equiv \partial_\mu + igA_\mu^a T^a, \\ F_{\mu\nu}^a &= \partial_\mu A_\nu^a - \partial_\nu A_\mu^a - gf^{abc}A_\mu^b A_\nu^c, \end{aligned} \tag{2.5}$$

where we introduced a new *set* of fields A^a, U is an element of the symmetry group, T^a represents generators of the given group, g is a coupling constant and f^{abc} are the antisymmetric structure constants of the symmetry group.

There are significant differences compared to the Abelian $U(1)$ gauge. We have introduced multiple gauge fields and their number depends on the number of generators of the symmetry group. The structure constants f^{abc} are zero for the Abelian groups, however they are non-zero in the case of a non-Abelian group. The additional terms introduced in $F_{\mu\nu}^a F^{a\mu\nu}$ contain the

---

[2] Sometimes, it is argued that only the invariance with respect to local transformation makes sense, however there are symmetries in our world that are global and are not local, e.g. lepton number symmetry.

[3] $e^{ie\alpha(x)Q}$, Q is the charge operator - the generator of $U(1)$ group.

[4] Non-Abelian groups are groups, where the elements do not commute, e.g. $SU(2)$ matrices do not commute in general.

[5] $SU(n)$ denotes $n \times n$ complex unitary matrices that have determinant equal to 1. Correspondingly, Pauli matrices can be used as the generators of $SU(2)$ group with commutation relations $[\sigma_i, \sigma_j] = i\epsilon_{ijk}\sigma_k$, where ϵ_{ijk} is the fully antisymmetric Levi-Civita symbol. In the case of $SU(3)$, the generators can be described by Gell-Mann matrices $[T_i, T_j] = if_{ijk}T_k$, where $f_{123} = 1$, $f_{147} = f_{165} = f_{246} = f_{257} = f_{345} = f_{376} = 1/2$, $f_{458} = f_{678} = \sqrt{3}/2$ and zero for others.

third and fourth power of the gauge fields which translates to self interaction of the gauge fields, a phenomenon that is not present in QED.

The procedure outlined above does not only provide a highly convenient way how to generate interacting theories from a theory of non-interacting particles, most of the theories that are gauge invariant have very interesting properties. Some of the gauge invariant theories are *renormalisable* [9,10] which is a rare property[6]. Another important property of some of the gauge theories, e.g. $SU(2)$ and $SU(3)$ theories, is the behaviour of the running coupling constants. Contrary to what the name suggests, a coupling constant is not a constant but depends on the energy scale Q^2. The coupling constant depends on the specific choice of the *renormalisation scale* μ_R. For the strong interaction, which is an $SU(3)$ gauge theory, as we will see in Section 2.2, the strong coupling constant, α_s, obeys at the one-loop approximation [11]

$$\alpha_\mathrm{s}\left(Q^2,\mu_\mathrm{R}^2\right) = \frac{\alpha_\mathrm{s}\left(\mu_\mathrm{R}^2\right)}{1+\frac{\alpha_\mathrm{s}\left(\mu_\mathrm{R}^2\right)}{12\pi}\left(11n_\mathrm{C}-2n_\mathrm{f}\right)\ln\left(Q^2/\mu_\mathrm{R}^2\right)}, \tag{2.6}$$

where n_C is the number of colours and n_f is the number of the effectively involved quark flavours. It is obvious from Equation (2.6) that as long as $n_\mathrm{f} < \frac{11}{2}n_\mathrm{C}$ holds, the strong coupling constant goes to zero with Q^2 going to infinity.

$$\lim_{Q^2\to\infty} \alpha_\mathrm{s} = 0. \tag{2.7}$$

This behaviour is called *asymptotic freedom* [12] as the particles bound by the strong coupling constant become less and less bound and approach freedom with an increased energy Q^2. Equation (2.6) can be reorganised into

$$\alpha_\mathrm{s}\left(Q^2,\mu_\mathrm{R}^2\right) = \frac{12\pi}{\left(12n_\mathrm{C}-2n_\mathrm{f}\right)\ln\left(Q^2/\Lambda_\mathrm{QCD}^2\right)}, \tag{2.8}$$

with Λ_QCD being a parameter where the perturbation series no longer converges and is thus not valid. One might be tempted to claim that Equation (2.8) proves a *confinement*, an observation that any coloured particle, such as quarks and gluons cannot be observed directly and must form a compound particle, which is a phenomenon that agrees with experiments as no free quarks or gluons are observed and has been shown in lattice calculations [13]. However, one cannot claim this from the perturbation expansion as this argument relies on extrapolation of the perturbation series to a region where it is not longer valid. Nevertheless, it provides a hint to the phenomenon of confinement.

2.2. The Standard Model of elementary particles

Armed with the knowledge from previous section we can schematically write the Lagrangian of the SM, $\mathcal{L}_\mathrm{SM}$ [14,15]

$$\mathcal{L}_\mathrm{SM} = \mathcal{L}_\mathrm{fermion} + \mathcal{L}_\mathrm{gauge} + \mathcal{L}_\mathrm{Yukawa} + \mathcal{L}_\mathrm{Higgs} + \mathcal{L}_\mathrm{technical}. \tag{2.9}$$

---

[6] The Standard Model includes only theories that are renormalisable.

The first term, $\mathcal{L}_{\text{fermion}}$, describes fermions and their interactions with the corresponding gauge fields

$$\mathcal{L}_{\text{fermion}} = \bar{\Psi}'_L i\not{D}\Psi'_L + \bar{\Psi}_R i\not{D}\Psi_R, \tag{2.10}$$

where the symbols Ψ describe both quarks and leptons, where the exact form of the D_μ depends on the gauge group and will be further discussed in the following sections. The R and L describe left - $\Psi_L \equiv \frac{1}{2}(1-\gamma^5)\Psi$ and right - $\Psi_R \equiv \frac{1}{2}(1+\gamma^5)\Psi$ components of the fields. There are three families, or generations, of the fermions; particles in the second generation are heavier "cousins" of the fermions from the second generation and particles in third generation are even heavier[7]. For one generation the $\bar{\Psi}'_L$ and $\bar{\Psi}_R$ are four component objects

$$\Psi'_L = \begin{pmatrix} \begin{pmatrix} u_L \\ d'_L \end{pmatrix} \\ \begin{pmatrix} \nu^e_L \\ e_L \end{pmatrix} \end{pmatrix} \qquad \Psi'_R = \begin{pmatrix} u_R \\ d_R \\ \nu^e_R \\ e_R \end{pmatrix} \tag{2.11}$$

where u_L and d'_L describe left components of up and down-type bi-spinors for up and down-type quarks, respectively. Each quark bi-spinor contains three components and each represents one colour. ν^e_L refers to the left component of the electron-neutrino bi-spinor. e_L is the left component of the electron bi-spinor, and similarly for the right components. The main difference between left and right components is illustrated by the inner parentheses for the left-handed bi-spinors, these form $SU(2)$-doublets, while the right handed do not[8]. In the minimal version of the SM, neutrinos are massless and no right-handed component ν_R exists[9]. Equations (2.10) and (2.11) show only the first generation, the remaining two generations of the SM particles are included analogically.

The prime in Ψ' comes from the fact that the three families of down-type quarks d', s', b' enter the Lagrangian in a linear combination of d, s, b fields[10]. The mixing is described by Cabbibo-Kobayashi-Maskawa (CKM) matrix [17, 18]

$$\begin{pmatrix} d' \\ s' \\ b' \end{pmatrix} = \begin{pmatrix} V_{ud} & V_{us} & V_{ub} \\ V_{cd} & V_{cs} & V_{cb} \\ V_{td} & V_{ts} & V_{tb} \end{pmatrix} \begin{pmatrix} d \\ s \\ b \end{pmatrix}. \tag{2.12}$$

The interactions of these fields are hidden in the covariant derivative D_μ

$$D_\mu = \partial_\mu + ig_s G_\mu + igW_\mu + ig\tan\theta_{\text{W}} Y_w/2B_\mu, \tag{2.13}$$

corresponding to the $SU(3) \otimes SU(2) \otimes U(1)$ gauge symmetry, where g_s, g and $g\tan\theta_{\text{W}}$ are coupling constants. The gluon field, G_μ, represents the strong-force carriers, gluons. The field corresponds to the $SU(3)$ symmetry

---

[7] This is not necessarily true for neutrinos for which the mass hierarchy is not known yet [16].

[8] Their representation is trivial.

[9] Even if they existed they would not interact via the electroweak interaction nor the strong interaction. And being massless particles they would not even interact gravitationally, making them completely decoupled from other elementary particles.

[10] The fields marked with a prime d', s', b' are simple (non-mixed) in terms of electroweak interactions, while the non-prime fields d, s, b are simple in terms of masses.

$$G_\mu = G^a_\mu \frac{\lambda^a}{2}, \tag{2.14}$$

where λ^a refers to Gell-Mann matrices [19] and this component acts on "coloured" objects: quarks and gluons. The W_μ term comes from $SU(2)$ symmetry

$$W_\mu = W^a_\mu \frac{\tau^a}{2}, \tag{2.15}$$

where τ^a are Pauli matrices and their components act on the left $SU(2)$ doublets. $W^\pm$ bosons are linear combinations of these fields.

Finally, the B_μ term corresponds to a $U(1)$ symmetry with factor Y_w, called *weak hypercharge* [20, 21]

$$Y_w = 2\left(Q - T_3\right), \tag{2.16}$$

where Q is the electric charge of the particle and T_3 is the third component of the weak-isospin, the $SU(2)$ component of the gauge symmetry. A photon and a Z boson are linear combinations of B_μ and W_μ fields, the exact form of the fields will be provided later in this chapter.

Table 2.1 illustrates the electric charge Q, the third component of the weak isospin T_3, the hypercharge Y_w and a flag whether the field carries colour charge.

Field	**Q[e]**	$\mathbf{T_3}$	$\mathbf{Y_w}$	**Colour?**
u_L	+2/3	+1/2	+1/3	Yes
u_R	+2/3	0	+4/3	Yes
d_L	−1/3	−1/2	+1/3	Yes
d_R	−1/3	0	−2/3	Yes
ν_L	0	+1/2	−1	No
ν_R	0	0	0	No
e_L	−1	−1/2	−1	No
e_R	−1	0	−2	No
H	0	−1/2	+1	No

Table 2.1.: A summary of the first generation of leptons and the Higgs boson with their corresponding electric charges Q, the third component of the weak isospin T_3, the weak hypercharge Y_w and a flag whether the fields carry a colour charge. The second and the third generation of leptons follow this table analogically.

The second term, $\mathcal{L}_{\text{gauge}}$, describes the gauge fields with their self-interactions

$$B_{\mu\nu} = \partial_\mu B_\nu - \partial_\nu B_\mu \tag{2.17}$$

$$W^a_{\mu\nu} = \partial_\mu W^a_\nu - \partial_\nu W^a_\mu - g\epsilon^{abc} W^b_\mu W^c_\nu \tag{2.18}$$

$$G^a_{\mu\nu} = \partial_\mu G^a_\nu - \partial_\nu G^a_\mu - g \tan\theta_{\mathrm{W}} f^{abc} G^b_\mu G^c_\nu, \tag{2.19}$$

where $\epsilon^{abc}(f^{abc})$ are structure constants of the $SU(2)(SU(3))$ group.

The third term, $\mathcal{L}_{\text{Yukawa}}$, describes interactions of fermions with the Higgs field. This term is responsible for mass generation for fermions as will be discussed in Section 2.2.3.

The fourth term, $\mathcal{L}_{\text{Higgs}}$, describes the Higgs field and its self-interactions and together with the third term it is responsible for the Spontaneous Symmetry Breaking, a process responsible for creation of mass of the elementary particles as will be discussed in Section 2.2.3.

The fifth term, $\mathcal{L}_{\text{technical}}$, contains technical parts of the SM, including gauge fixing terms and also Faddeev-Popov Lagrangian for the ghost fields [22]. The description of this part goes beyond the scope of this thesis and will not be discussed further.

It is instructive to spend some words on the historical timeline that lead to the Lagrangian of the SM and the properties of the individual forces.

2.2.1. Strong interaction

Historically, there were two distinct approaches to the theory of the strong interaction. One approach focused on observed symmetries for hadrons, their masses and apparent conservation rules. This approach can be called *flavour symmetry* approach. On the other hand, *parton model* focused on a theory that could describe hadron interactions by using form-factors. Both approaches converged to Quantum Chromodynamics (QCD), the theory of strong interactions, that was described in the previous chapter.

Flavour symmetry is a type of symmetry that has been observed for masses of hadrons. A proton and a neutron have masses of 938.9 MeV and 939.6 MeV, respectively. It was hypothesised that the only difference in the masses is caused by an electromagnetic interaction, and in terms of the strong interaction, both particles are just two states of the *same particle* [23]

$$|N\rangle = a\,|p\rangle + b\,|n\rangle \to |N'\rangle = a'\,|p\rangle + b'\,|n\rangle \qquad \begin{pmatrix} a' \\ b' \end{pmatrix} = U \begin{pmatrix} a \\ b \end{pmatrix} \tag{2.20}$$

where $|N\rangle$ is a nucleon state, $|p\rangle$ and $|n\rangle$ are proton and neutron states, respectively. U is an element of the $SU(2)$ group and thus this symmetry was called *isospin* symmetry (iso = "like") because, mathematically, it is identical to the spin group.

After a discovery of π mesons [24] with very similar masses of the charged and the neutral pions, it has been hypothesised that the isospin symmetry does not only apply to nucleons, but to strongly interacting particles in general. With the discovery of the new particles in 1950s, they could be grouped into multiplets - sets of particles with similar masses, where each multiplet could be described by the isospin value, I, and the baryon number, B, where each particle inside the given multiplet had a unique third component of the isospin.

Gell-Mann and Nèeman proposed [25] that there is even higher symmetry that includes $SU(2)$ isospin symmetry naturally as a subgroup. A natural choice for the symmetry is the $SU(3)$. Due to the dimensionality of 8 of the adjoint representation of $SU(3)$, the theory is referred to as *eightfold way*[11]. The $SU(3)$ group has two non-equivalent irreducible representations labelled 3 and $\bar{3}$ and other irreducible representations can be constructed as their direct multiplication, e.g.

$$3 \otimes 3 = 6 \oplus \bar{3} \qquad 3 \otimes \bar{3} = 8 \oplus 1 \qquad 3 \otimes 3 \otimes 3 = 10 \oplus 8 \oplus 8 \oplus 1. \tag{2.21}$$

The representations have the same meaning as in the case of $SU(2)$ symmetry, they lead to multiplets of particles with similar masses while also including the original $SU(2)$ symmetries.

---

[11] This is a reference to "Noble eightfold path" in Buddhism.

This was, indeed, observed and octets (8-multiples) and decuplets (10-multiples) were found. One problem at the time was the apparent existence of 9-multiplet, this was interpreted as a decuplet with one particle that had not yet been discovered. Based on the group theory of combined representations, the properties of the particle, isospin, spin and masses have been predicted. The particle was called Ω baryon and was discovered two years after its prediction [26].

At the time, the $SU(3)$ flavour symmetry was considered only a mathematical formalism and no physics meaning was associated with it. Gell-Mann and Zweig hypothesised [27, 28] that the irreducible 3-dimensional representations correspond to the elementary particles, quarks[12]. The doublets are created by *up* and *down* quarks, the iso-singlet from the $SU(3)$ was called *strange* quark. The automatic consequence of this hypothesis is that the quarks must have fractional electric charges (and baryon numbers). The problem with the whole hypothesis is that the quarks had never been observed at the time.

It should be noted that the $SU(3)$ flavour symmetry *is not* the symmetry that enters the Lagrangian of QCD, $SU(3)$ flavour symmetry is now considered an accidental symmetry that comes from the fact that up, down and strange quarks have similar masses and it is only an approximate symmetry. The QCD $SU(3)$ symmetry is an exact gauge symmetry which describes colour states - each colour represents a unique quantum state. However, the works of Gell-Mann, Zweig and Nèeman brought the group $SU(3)$ to attention and laid the basic mathematical formalism needed for future development. Moreover, the quark hypothesis, the fractional charges of quarks and how they combine to form hadrons was fundamental in the development of the QCD.

Parton model is an approach to strong interactions that was based on few key experimental observations. Due to, at that time, the unknown nature of the hadronic interactions, the cross-sections were parametrised with so called *form-factors*, similarly to non-relativistic form-factors from the quantum mechanics

$$\frac{d\sigma}{d\Omega} = \left(\frac{d\sigma}{d\Omega}\right)_{\mathrm{QED}} \left|F(q^2)\right| , \tag{2.22}$$

with the form-factor F that depends on the transferred momentum q. It was observed that for Deep Inelastic Scattering (DIS)[13] two phenomena occur. Inelastic scatterings seem to resemble elastic scatterings on a free particle [29]. Furthermore, two relativistic form-factors that are needed to describe lepton-hadron interactions and are in general functions of two independent variables were observed to be a function of *one* variable [30]. Both of these properties suggested that hadrons consists of point-like particles, called *partons*. The DIS of hadrons can be interpreted as an elastic scattering of the partons inside the hadrons where each parton carries a fractional momentum xp, where x is the fraction of the original hadron momentum p. The structure of a parton can be described by a probability distribution function $\rho(x)$, called *a structure function*, that describes the probability of a scattering on a parton with momentum xp.

A natural combination of the parton model and the previously mentioned flavour symmetry leads to identification of quarks as partons. For this to happen, the quarks need to be asymptotically free for DIS - this is where the non-Abelian gauge theories come in place. Each type of (anti-)quark has its own structure constant for each hadron. These distributions are called *parton distribution functions* (PDF) and can be experimentally measured. However, the PDFs are not

---

[12] The word *quark* comes from James Joyce's book Finnegan Wake from a phrase "Three quarks for Muster Mark".

[13] Scattering with large $|q^2|$.

fixed and depend on the q^2 according to Dokshitzer-Gribov-Lipatov-Altarelli-Parisi (DGLAP) equations [31–33]. Several collaborations extracted the PDFs from various measurements, e.g. CTEQ [34], NNPDF [35], MSTW [36] and others. The quark-parton model could not explain the structure of the protons completely. From the quark model the proton should consist of two up and one down quark, which would require $\bar{u}(x) = \bar{d}(x) = s(x) = \bar{s}(x) = 0$, which is not true. Furthermore,

$$\int_0^1 dx\, x \left[u(x) + \bar{u}(x) + d(x) + \bar{d}(x) + s(x) + \bar{s}(x)\right] < 1, \tag{2.23}$$

which suggests that there are other partons that contribute to the proton momentum. This leads to intermediate particles, gluons.

2.2.2. Electroweak interaction

In 1930s, Fermi proposed [37] that the interaction Lagrangian for weak processes can be written as

$$\mathcal{L}_{\text{int}} = G\bar{p}\gamma^{\mu}n\bar{e}\gamma_{\mu}\nu + \text{h.c.}, \tag{2.24}$$

where $\bar{p}$ and n represent fields for an anti-proton or a neutron, respectively. More generally, Equation 2.24 has the form

$$\mathcal{L}_{\text{int}} = GJ^{\dagger}_{\mu}J'^{\mu}, \tag{2.25}$$

with a constant G, and the weak charged currents J^{μ} to be determined. The theory is called *four-fermion contact* theory as the interactive Lagrangian contains two charged currents, each containing two bi-spinors for fermions. The exact form of the charged current J_{μ} was a mystery and it became even more difficult with a proposal that the parity may not be conserved[14] in weak interactions [38]. The suggestion was later confirmed by an experiment [39], which lead to a proposal that maybe the parity is *maximally violated*. Maximum violation of parity is achieved by a *vector minus axial vector* ($V-A$) structure of the charged current [40]. The $V-A$ structure for the J^{μ} reads

$$J^{\mu} = \bar{e}\gamma^{\mu}\left(1-\gamma^5\right)\nu_e, \tag{2.26}$$

using the fact that the term $(1-\gamma^5)$ is a projector and thus can be replaced with $(1-\gamma^5)^2$, then splitting it into two projectors and applying one projector to the $\bar{e}$ term and the other one to ν_e, the current J^{μ} yields

$$J^{\mu} = \bar{e}_L\gamma^{\mu}\nu_{e,L}. \tag{2.27}$$

The $V-A$ theory was very successful, but it lacks one crucial property, it is not renormalisable. As mentioned in Section 2.1, gauge theories are good candidates for a renormalisable theory,

---

[14] This means that the Lagrangian may be a pseudoscalar.

thus the obvious question was if the $V-A$ theory can be modified to become a gauge theory. The Lagrangian for the leptonic part of the $V-A$ theory can be rewritten as

$$\mathcal{L}_{\text{int}} = \frac{g}{2}\left(\bar{e}_L \not{W}^+ \nu_L + \bar{\nu}_L \not{W}^- e_L\right), \tag{2.28}$$

where we introduced two new fields W^+ and W^-. Note that the lepton fields enter only with their left chiral components. But the W fields have not been observed experimentally and the $V-A$ four fermion theory gave a good description for many processes. How can the new fields be simply added to the theory without contradicting the observations? The idea is that the contact theory is just an approximation of a "real" theory that includes the W fields as illustrated in Figure 2.1. This could be true if the masses of the new W boson particles were very large so that their propagators effectively became constants

$$\frac{1}{p^2 - m^2} \rightarrow \frac{1}{m^2} \equiv \text{const.} \tag{2.29}$$

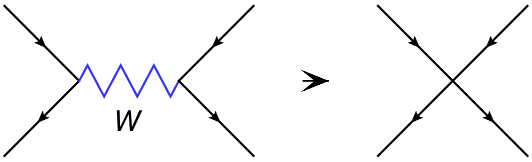

Figure 2.1.: An illustration of the transition from the theory with an intermediate boson to the four-fermion contact theory.

Introducing new fields $W^{\pm} = \frac{1}{\sqrt{2}}\left(W^1 \pm iW^2\right)$ and a lepton field L

$$L = \begin{pmatrix} \nu_L \\ e_L \end{pmatrix}, \tag{2.30}$$

Lagrangian (2.28) can be rewritten using Pauli matrices σ as

$$\mathcal{L}_{\text{int}} = \frac{g}{2}\bar{L}(\sigma_1 \not{W}^1 + \sigma_2 \not{W}^2)L. \tag{2.31}$$

Lagrangian (2.31) almost has the $SU(2)$ gauge symmetry but it lacks the third generator of the $SU(2)$ group, the third Pauli matrix. The third generator can be added together with a new third W field and, naively, the $U(1)$ gauge symmetry of the QED can be inserted to yield a covariant derivative

$$D_\mu = \partial_\mu + igW^a_\mu \sigma^a + ig'\left(-\frac{1}{2}B_\mu\right), \tag{2.32}$$

where the unity (2×2) matrix has been omitted from the ∂_μ and B_μ terms, the factor $-1/2$ is just a convention. The corresponding Lagrangian transforms to

$$\mathcal{L} = \bar{L} i \not{D} L. \tag{2.33}$$

This would correspond to B_μ describing photons, analogously to the QED. However, this is not true because either the B field would interact with neutral leptons (neutrinos) or the covariant derivative would be different for each component, breaking the gauge symmetry. But the combination of W_3 and B fields

$$A_\mu \equiv gW^3_\mu + g'B_\mu \qquad Z_\mu \equiv gW^3_\mu - g'B_\mu, \tag{2.34}$$

has the desired property that the A field interacts only with the charged fields. Thus the B field does not correspond to the photon field as in the QED, but rather to a different $U(1)$ group, the hypercharge $U(1)$. The only problem that needs to be solved is that the linear combination is not orthogonal and thus the quadratic terms from the full Lagrangian $W^3_{\mu\nu}W^{3\mu\nu}$ would lead to term $\partial_\mu A_\nu \partial^\mu Z^\nu$ which does not have a clear interpretation. The solution [41] is to define A and Z as an orthogonal combination, using the weak mixing angle, θ_W

$$A_\mu = B_\mu \cos\theta_\mathrm{W} + W^3_\mu \sin\theta_W, \tag{2.35}$$
$$Z_\mu = B_\mu \sin\theta_\mathrm{W} - W^3_\mu \cos\theta_W, \tag{2.36}$$

which leads to a formula for coupling constants

$$e = g\sin\theta_\mathrm{W} = g'\cos\theta_\mathrm{W}. \tag{2.37}$$

The right components of the fields do not enter the weak interaction, but they appear in the mass terms and also in the purely electromagnetic interactions. This can be solved easily by requiring right fields to obey a trivial representation of $SU(2)$ but a non-trivial representation of $U(1)$.

2.2.3. Spontaneous Symmetry Breaking

The last problem that needed to be solved is obvious from Sections 2.1 and 2.2.2 where two opposing requirements on the W and Z bosons were imposed: requiring exactly zero mass due to the gauge symmetry and requiring very large mass to comply with the four-fermion contact theory. Indeed, the W [42, 43] and Z [44, 45] bosons were observed with large masses. In Slovak language we have a saying that we need to “find a solution so that the wolf is fed and the goat is kept alive” which refers to the similar problem that apparently has no solution. The solution has been found and it lies in the dynamic creation of the particle masses, called the Brout-Englert-Higgs (BEH) mechanism [46–49].

The main idea behind the BEH mechanism is to include an $SU(2)$ doublet, Higgs field, equivalent to adding four real scalar fields, with an additional self interaction. The following terms are added to the Lagrangian

$$\mathcal{L}_\mathrm{Higgs} = \left(D_\mu\Phi\right)^\dagger \left(D^\mu\Phi\right) - V(\Phi), \tag{2.38}$$

where

$$V(\Phi) = -\mu^2\Phi^\dagger\Phi + \lambda\left(\Phi^\dagger\Phi\right)^2, \qquad \mu^2 > 0, \tag{2.39}$$

with a constant λ.

The potential $V(\Phi)$ has a "wrong" mass term μ^2 and thus does not have minimum in the $\Phi(x) = 0$. Assigning a vacuum expectation-value (VEV), v, to one component of the four scalar fields the symmetry of the electroweak is *broken*. The electromagnetic component of the electroweak symmetry remains invariant, reducing $SU(2)_\mathrm{L} \otimes U(1)_\mathrm{Y}$ to $U(1)_\mathrm{EM}$. Expanding the covariant derivative in Equation (2.38) yields mass terms for the gauge bosons (for the W and Z bosons). The masses of the W, M_W, and Z, M_Z, bosons depend on the coupling constants and the VEV of the Higgs field.

$$M_W = \frac{gv}{2}, \tag{2.40}$$

$$M_Z = \frac{gv}{2\cos\theta_\mathrm{W}}. \tag{2.41}$$

Three real components of the Higgs field can be removed by fixing the gauge symmetry and the one remaining field is the *Higgs boson*. The mass of the Higgs boson, M_H, and the VEV are connected via parameters of the potential, μ and λ

$$M_H = \sqrt{\frac{\lambda}{2}}v, \tag{2.42}$$

$$v = \sqrt{\frac{\mu^2}{\lambda}}. \tag{2.43}$$

To have the model be consistent, masses of the fermions are also generated via the BEH mechanism. New terms are added to the Lagrangian that includes the *Yukawa* couplings[15] of the fermions to the Higgs field. These terms lead to fermion interaction with the Higgs boson. Once the Higgs fields obtains the v the mass term for fermions with a mass m_f, $m_f = \frac{y_f}{\sqrt{2}}v$ is generated. The y_f represents the Yukawa coupling constant for the given fermion. This shows that more massive particles have stronger coupling to a Higgs boson.

More than forty years after its prediction, a particle consistent with the Higgs boson was discovered [4, 5], thus completing the SM framework.

2.2.4. Beyond the Standard Model

Although the SM has been successful in the prediction of various phenomena, as can be illustrated by Figure 2.2, which shows the predictions and the measured values of the cross-sections of various SM processes that span over several orders of magnitude, some phenomena are observed that cannot be explained by the SM.

Astrophysical observations show non-baryonic matter that does not interact electromagnetically, *dark matter*, which cannot be explained by particles from the SM [50]. Furthermore, baryogenesis in the early Universe requires baryon number violation [51] which also cannot be explained by the SM[16]. Additionally, evidence [52, 53] for the *dark energy*, an unknown form of energy that accelerates the expansion of the Universe, cannot be explained within the SM.

Several frameworks of physics Beyond the Standard Model (BSM) attempt to describe the new phenomena by extending the SM. These frameworks include, e.g. SuperSymmetry (SUSY) [54–

---

[15] $\mathcal{L} = \bar{\Psi}\Phi\Psi$.

[16] SM allows baryonic asymmetry, however the values predicted by the SM are orders of magnitude different from what is observed in the Universe.

57] – a theory that includes symmetry between fermions and bosons; models with flavour-changing neutral currents (FCNC), that are forbidden in the SM at tree level and are heavily suppressed by the GIM mechanism [58], and others. These models provide predictions for a vast number of properties and can be excluded or constrained by a precise measurement of some of the properties of the SM.

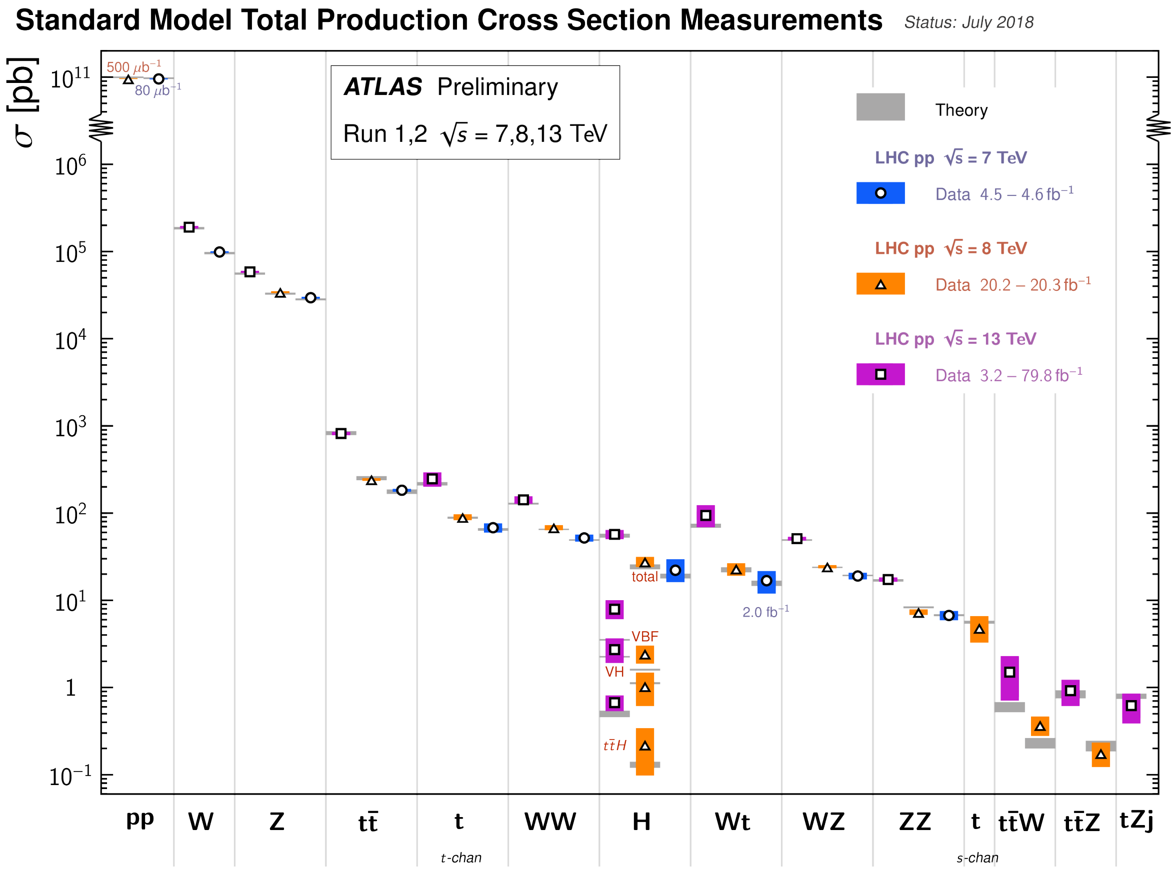

Figure 2.2.: Summary of various SM total and fiducial cross-sections corrected for leptonic branching fractions, compared to the corresponding theoretical expectations [59]. The experimental results are measured by the ATLAS Collaboration.

CHAPTER 3

The top quark and its decay width

The observation of CP-violation in neutral K-mesons [60] could not be explained within the framework of the SM that included, at that time, only two generations of quarks and leptons. The proposed solution was that there are in fact three generations of fermions, with the third generation yet to be observed. Including the third generations of quarks extends the quark mixing matrix from a 2×2 matrix, parametrised with a single parameter, to a 3×3 matrix, parametrised by four parameters. This additional freedom allows for complex coefficients that could result in CP violating terms [17]. This idea became more interesting after the discovery of a third generation lepton, the τ lepton [61]. After the discovery of the third generation quark [62], the *bottom*[1] quark, it was natural to assume the existence of its weak isospin partner, the *top quark*. The top quark was finally discovered in 1995 by the CDF [7] and DØ [6] Collaborations at the Tevatron at Fermilab.

With its mass around 173 GeV [63], the top quark is the heaviest known elementary particle of the SM. Because of this large mass, the top-Higgs Yukawa coupling is $y_t \sim 1$ which suggests that the top quark plays an important role in the spontaneous symmetry breaking mechanism. The precise measurement of the top-quark decay width, Γ_t, or its mean lifetime, τ_t – these two quantities are trivially connected via $\tau_t = 1/\Gamma_t$ – is the topic of this thesis, but the order of magnitude expectation for the top-quark mean lifetime yields $\tau_t \approx 10^{-25}$ s [63]. This is important since the average time needed for the top quark to hadronise is of the order of 10^{-24} s [64] and thus the top quark decays before it forms bound states. This makes the top quark unique among other quarks, as it provides an opportunity to study a pseudo-bare quark. Furthermore, because of its short mean-lifetime, the top quark transfers all its properties to its decay products, thus properties like the spin correlations of the top quarks are not smeared by hadronisation and consequently can be directly studied on the decay products distributions.

3.1. Top quark production and decay

In general, there are two classes of processes where the top quark is produced at the hadron colliders: top-quark pair production, where top (t) and anti-top ($\bar{t}$) are produced in pairs, and

---

[1] Sometimes *beauty* is used.

single top production via electroweak interaction[2].

The cross-section, σ, of each process can be calculated using the *factorisation theorem* [65], which states that the total cross-section can be factorised into a non-perturbative part, described by PDFs, and a perturbative part

$$\sigma_{pp\to t\bar{t}X}(s, m_t^2) = \sum_{i,j=q,\bar{q},g} \int_{4m_t^2}^{s} d\hat{s}\, \hat{L}_{ij}\left(\hat{s}, s, \mu_f\right) \hat{\sigma}_{ij\to t\bar{t}}\left(\hat{s}, m_t^2, \mu_f^2, \mu_r^2\right), \tag{3.1}$$

where s, is the square of the pp centre-of-mass energy, $\hat{\sigma}_{ij\to t\bar{t}}$ is the partonic cross-section, μ_f is a *factorisation scale*, which is a scale that separates the non-perturbative and the perturbative part, the renormalisation scale μ_r has been introduced in Section 2.1. The *partonic density* $\hat{L}_{ij}\left(\hat{s}, s, \mu_f\right)$ reads

$$\hat{L}_{ij}\left(\hat{s}, s, \mu_f\right) = \frac{1}{s} \int_{\hat{s}}^{s} \frac{ds'}{s'} f_{i/p}\left(\mu_f^2, \frac{s'}{s}\right) f_{j/p}\left(\mu_f^2, \frac{\hat{s}}{s'}\right), \tag{3.2}$$

where $f_{i/p}$ represents the initial state prescription via PDF of a parton i in a proton p, and similarly for $f_{j/p}$. The square of the partonic centre-of mass energy is denoted as $\hat{s}$. It is common to set the renormalisation scale and factorisation scale to be equal to the top mass, $\mu_f = \mu_r = m_t$.

3.1.1. Top quark pair-production

Top quarks are predominantly produced in pairs via the strong interaction, however, also electroweak processes contribute to the pair production cross-section, but the contribution is below the theoretical uncertainty on the pair cross-section originating from the PDF uncertainty [66] and can thus be neglected.

At leading order (LO), quark-antiquark annihilation and gluon-fusion processes produce $t\bar{t}$ pairs as is illustrated in Figures 3.1 and 3.2.

The relative contribution from the annihilation process and the fusion processes depends on the colliding objects. In proton-antiproton ($p\bar{p}$) collisions, both quark and antiquark can be valence quarks and thus the contribution from the quark-antiquark annihilation can dominate, as in the case of the Tevatron collider. However, in proton-proton (pp) colliders, like the LHC, antiquarks can only come from the quark sea, and thus the gluon fusion dominates the production. Additionally, the relative contribution also depends on the centre-of-mass energy of the colliding objects, with the gluon density increasing with the increasing collision energy, and thus dominating the production, irrespective of the collision type (pp versus $p\bar{p}$). Furthermore, the $t\bar{t}$ cross-section increases with the increased centre-of-mass energy, $\sqrt{s}$, because a smaller fraction of the (anti)proton energy, x, is needed to reach the $t\bar{t}$ production threshold.

Theoretical calculations of $t\bar{t}$ cross-section [67–71] at next-to-next-to-leading order (NNLO) with next-to-next-to-leading resummation of logarithmic soft gluon terms (NNLL) are computed using the `top++2.0` program [72]. The latest calculations take advantage of MSTW2008 68 % CL NNLO PDF set [36] with the mass of the top quark set to $m_t = 172.5$ GeV, predictions for the Tevatron at $\sqrt{s} = 1.98$ TeV use $m_t = 173.3$ GeV. The uncertainties on the predictions originate from variations of renormalisation and factorisation scales as well as an uncertainty from the

---

[2] Also combinations of these processes, such as four-top and three-top production are possible within the SM, but the cross-section of these processes is negligible.

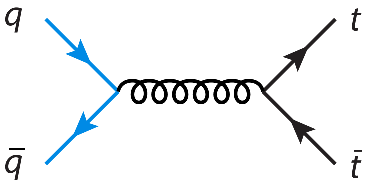

Figure 3.1.: LO Feynman diagrams for the top quark pair-production via quark-antiquark annihilation.

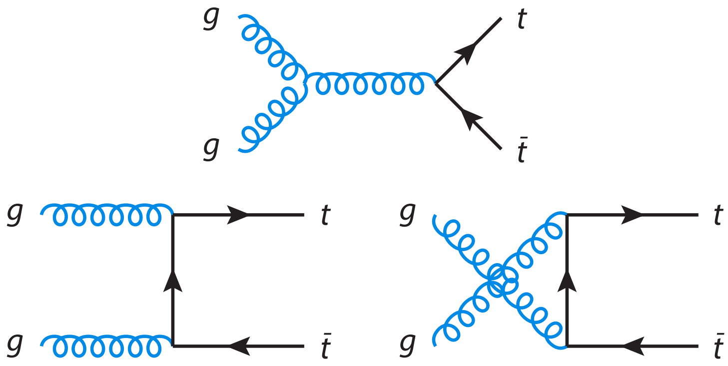

Figure 3.2.: LO Feynman diagrams for the top quark pair-production via gluon fusion.

PDF. Table 3.1 summarises theoretical predictions of $t\bar{t}$ cross-sections for various centre-of-mass energies, $\sqrt{s}$ and different colliders.

The theoretical predictions for $t\bar{t}$ cross-section have been checked by experiments—all observed values agree within their uncertainties with the predictions, as is summarised in Figure 3.3.

Accelerator	$\sqrt{s}$ [TeV]	$\sigma_{t\bar{t}}$ [pb]
Tevatron	1.98	$7.16^{+0.20}_{-0.23}$
LHC	7	$172^{+6.4}_{-7.5}$
LHC	8	253^{+15}_{-16}
LHC	13	832^{+40}_{-46}

Table 3.1.: Theoretical predictions [71] for $t\bar{t}$ cross-section for the Tevatron ($\bar{p}p$) and LHC (pp) colliders for various centre-of-mass energies. The uncertainties include variations of renormalisation and factorisation scales as well as uncertainty from PDF variations.

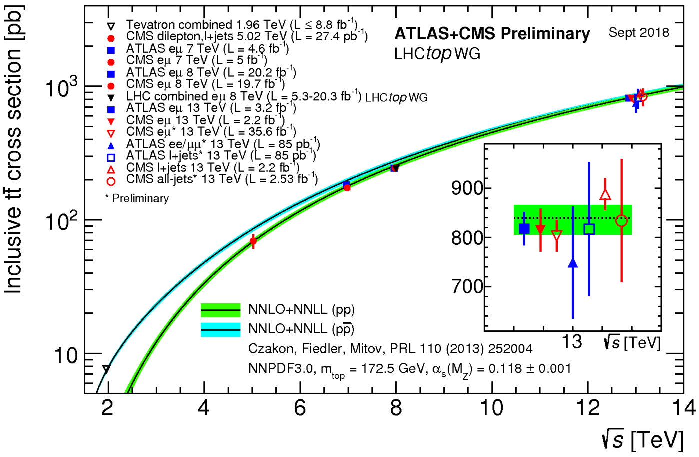

Figure 3.3.: Summary of LHC and Tevatron results [73–80] for the top-quark pair production cross-section measurements as a function of the centre-of-mass energy compared to the theoretical prediction [71]. Both theory and experimental results assume $m_t = 172.5$ GeV. The figure is taken from [81].

3.1.2. Single top quark production

Single top quarks are produced via weak interactions. There are three distinct single top channels at LO: s-channel, t-channel and Wt-channel as illustrated in Figure 3.4. Theoretical calculations [82–84] at approximate NNLO precision for all three channels and various $\sqrt{s}$ are summarised in Table 3.2. The calculations for s and t-channels have been prepared using the `Hathor v2.1` program [85, 86].

The ATLAS and CMS collaborations have measured [87–103] the single top production cross-section for all three single top processes at $\sqrt{s}$ = 7, 8 TeVand some at 13 TeV. The results are summarised in Figure 3.5. The measured values for the single top quark productions cross-section agree with the theoretical predictions within the uncertainties.

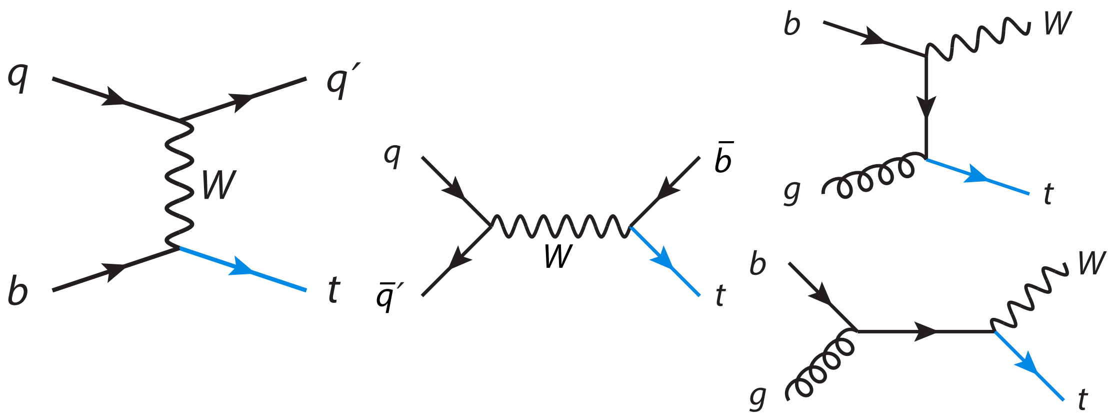

(a) The s-channel. (b) The t-channel. (c) The Wt-channel.

Figure 3.4.: LO Feynman diagrams for single top quark production in s-channel 3.4a, t-channel 3.4b and Wt-channel 3.4c.

		s-channel		t-channel		Wt-channel	
Accelerator	$\sqrt{s}$ [TeV]	σ_t [pb]	$\sigma_{\bar{t}}$ [pb]	σ_t [pb]	$\sigma_{\bar{t}}$ [pb]	σ_t [pb]	$\sigma_{\bar{t}}$ [pb]
Tevatron	1.98	0.52		1.04		-	
LHC	7	3.17	1.42	41.7	22.5	7.8	
LHC	8	3.43	1.90	54.87	29.74	11.18	
LHC	13	6.35	3.97	136.02	80.95	71.7	

Table 3.2.: Theoretical predictions [82–84] for single top quarks production cross-section for Tevatron ($\bar{p}p$) and LHC (pp) colliders for various centre-of-mass energies. For the Tevatron, the cross-sections are identical for top and anti-top quarks, which is also true for Wt channel in the case of the LHC collider.

3.1.3. Top quark decays

Due to an extremely short mean life-time, top quarks can be experimentally observed only via their decay products. The top quark decays via the weak interaction to a W boson and a down-type quark, $t \to W^+q$ ($\bar{t} \to W^-\bar{q}$). The flavour of the produced quarks are governed by CKM matrix elements, $|V_{tq}|$. In the SM assuming three generations of elementary particles, the $|V_{tq}|$ element is equal to $|V_{tb}| = 0.99915 \pm 0.00005$ [63], assuming unitarity of the CKM matrix. This allows, in the SM, to consider only decays of the top quark into the W boson and a b quark. The global measured W boson decay width reads $\Gamma_W = 2.085 \pm 0.042$ GeV [63] which only allows the W boson to be studied via its decay products. The W boson decays in 67.4 % into hadrons [63], and in the remaining cases it decays into a charged lepton and a corresponding neutrino. The decay channels of the $t\bar{t}$ pair can thus be characterised by the subsequent decays of the W boson from individual top (anti-)quark decays into three channels:

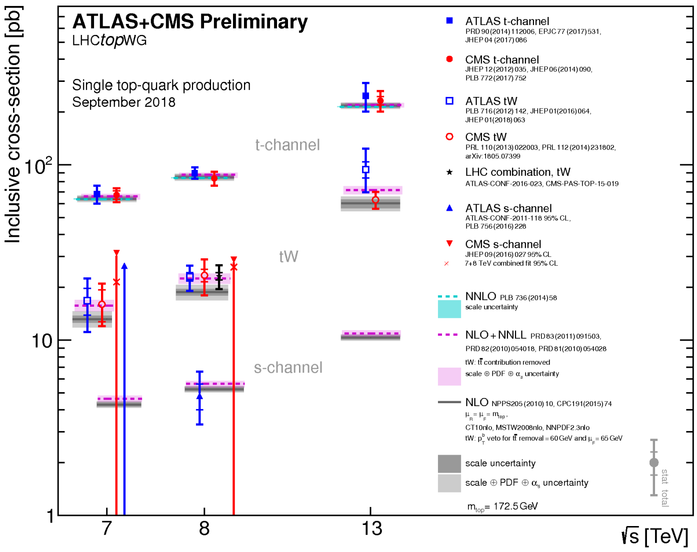

Figure 3.5.: Summary of the LHC results [87–103] for the single top quark production cross-section measurements as a function of the centre-of-mass energy compared to the theoretical prediction [82–84]. The figure is taken from [104].

All-hadronic channel[3] where both W bosons, originating from $t\bar{t}$, decay hadronically into quarks, $t\bar{t} \to W^+bW^-\bar{b} \to b\bar{b}\bar{q}'q''\bar{q}'''$. This decay channel benefits from the largest branching ratio, due to the high branching ratio of $W \to$ hadrons. However, it suffers from a large multijet background that is also very difficult to model, which results in a worse signal-to-background ratio compared to other channels. Furthermore, experimental resolutions of jets are broader compared to charged leptons and thus variables like reconstructed invariant masses suffer from poor resolution and large systematic uncertainties. Additionally, matching reconstructed jets to the partons from the $t\bar{t}$ decay poses a difficult challenge due to the combinatorial nature of the problem.

Dilepton channel where both W bosons decay leptonically into a charged lepton and a corresponding neutrino. This channel has the lowest branching ratio from all $t\bar{t}$ decay channels but has the highest signal-to-background ratio. Due to the presence of only two jets, the measurement has reduced uncertainties originating from reconstruction of jet kinematics. One disadvantage of the dilepton channel is the final state that contains two neutrinos which results in an under-constrained system for the reconstruction of $t\bar{t}$ kinematics.

Lepton+jets (ℓ+jets) channel[4] where one W boson decays hadronically into two quarks and the other W boson decays leptonically into a charged lepton and a corresponding neutrino. This channel has been called a *golden channel* due to the larger signal-to-background ratio compared to the all-hadronic channel and higher branching ratio compared to the dilepton channel. This is becoming less and less relevant with more data collected. However, the ℓ+jets channel still has one advantage over the other $t\bar{t}$ decay channels. Due to the presence of only one neutrino, the kinematics of the $t\bar{t}$ system can be reconstructed more precisely with respect to the dilepton channel.

The $t\bar{t}$ decay rates are illustrated in Figure 3.6. In the case of the W boson decaying into

---

[3] Sometimes called *full-hadronic* or *all-jets* channel.

[4] Sometimes called *single-lepton* channel.

a (anti-)tau lepton, the τ lepton cannot be measured directly due to its short mean life-time of $\tau_\tau = 2.9 \times 10^{-13}$ s [63]. The tau lepton decays hadronically into a tau neutrino and one or more hadrons in 62.97 % of the decays [63]. In the remaining decays, the tau decays into two neutrinos and either an electron or a muon. Usually in an experiment, only electrons and muons are considered in the decay, but these may also come from leptonic decays of the tau leptons, if they pass the required selection criteria.

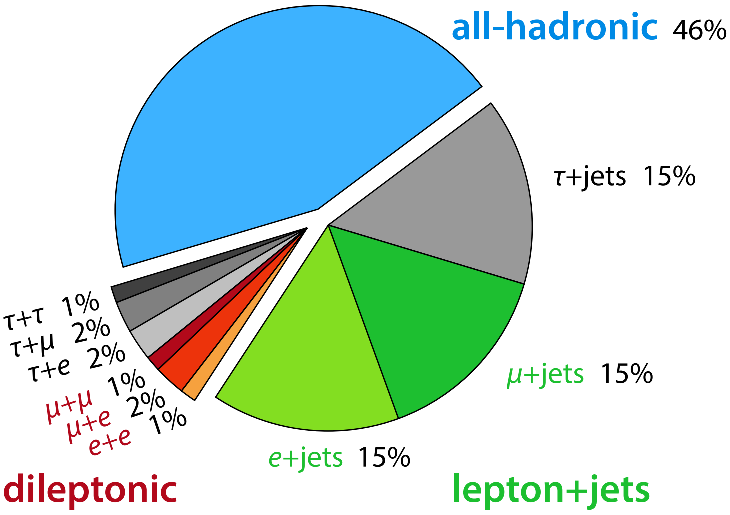

Figure 3.6.: A pie chart representing individual $t\bar{t}$ pair decay rates.

3.2. Top-quark mass

The top-quark mass is an extremely important parameter as it is a free parameter of the SM and cannot be calculated from first principles. Moreover, precise measurements of the top-quark mass, m_t provide an important check for the consistency of the electroweak parameters in the SM [105, 106] and its precise value plays an important role for the question of the electroweak vacuum stability. Furthermore, it has serious consequences for the early stages of our Universe evolution (inflation stage) [107]. The top-quark mass has been measured directly by experiments at the Tevatron and the LHC at various energies and in different $t\bar{t}$ and single top decay channels [108–121]. The world combination of the top-quark mass measurements from March 2014 yields $m_t^{\text{world}} = 173.34 \pm 0.76$ GeV [108]. The combination of ATLAS measurements from September 2017 gives $m_t^{\text{ATLAS}} = 172.51 \pm 0.50$ GeV [114].

An important topic in the top-quark mass measurements is a question what exactly is experimentally measured. Direct measurements of the top quark reconstruct invariant mass from its decay products and compare various predictions to the observed data. Usually, these measurements rely on predictions based on the top-quark pole mass which has an intrinsic theoretical uncertainty of the order of Λ_{QCD} [122–124]. Furthermore, experimentally, it is not possible to reconstruct the b-quarks from the top quark decay due to hadronisation. Several attempts [125,126] have been made to measure the top-quark pole-mass, measured via the cross-section dependence on the top-quark pole-mass. Another approach is to use purely leptonic distributions to circumvent the problem of hadronisation to achieve a theoretically clean measurement of the top-quark mass [127]. The most precise pole-mass measurement reads $m_t^{\text{pole}} = 173.2 \pm 1.6$ GeV [127].

3.3. Top-quark decay width

3.3.1. Exponential decay

In classical physics, the decay of unstable particles is governed by a differential equation

$$\frac{d}{dt}N(t) = -\Gamma N(t), \tag{3.3}$$

where $N(t)$ is the number of unstable particles at a given time t and Γ is a constant. Equation (3.3) reflects the assumption that the decay of a particle does not depend on the time the particle has lived. The solution for Equation (3.3) is

$$N(t) = N_0 e^{-\Gamma t}, \tag{3.4}$$

where N_0 is a constant describing the number of unstable particles at initial time t_0. The decay width is related to the mean-lifetime via

$$\Gamma = \frac{1}{\tau}, \tag{3.5}$$

or, more explicitly

$$\Gamma = \frac{\hbar}{\tau}, \tag{3.6}$$

with reduced Planck constant, $\hbar = h/2\pi = 6.582119514(40) \times 10^{-16}$ eV [63].

How does the exponential decay in classical mechanics reflect to quantum mechanics and QFT? In quantum mechanics, a given state is described by $|\Psi(t)\rangle = \int a_E e^{-iEt} |\varphi_E\rangle \, dE$, with $H|\varphi_E\rangle = E|\varphi_E\rangle$. To achieve an exponential decay, one has to set

$$|\langle\Psi_0|\Psi_t\rangle|^2 = \left|\int p(E)e^{-iEt}dE\right|^2 \overset{!}{=} e^{-\Gamma|t|}, \tag{3.7}$$

where $|\Psi_0\rangle$ is the initial state and $p(E) = |a_E|^2$. The solution for $p(E)$ is

$$p(E) = \frac{1}{2\pi}\frac{1}{iE - iE_0 + \Gamma/2} - \frac{1}{2\pi}\frac{1}{iE - iE_0 - \Gamma/2} = \frac{1}{2\pi}\frac{\Gamma}{(E-E_0)^2 + \Gamma^2/4}, \tag{3.8}$$

which is called the *Breit-Wigner* distribution[5] since such a distribution was observed for cross-sections of slow neutron capture [128]. The calculation is based on the assumption that there is an exponential decay present. But why does the exponential decay appear, or in other words, where does the Breit-Wigner distribution come from? Surprisingly, the answer can be found easily in a QFT approach.

A bare propagator in QFT is described by

---

[5] Sometimes *Lorentz* or *Cauchy* distribution is used.

$$\mathcal{P}(p) = \frac{i\xi}{p^2 - m^2}, \tag{3.9}$$

where ξ depends on the particle's spin,

$$\xi = \begin{cases} 1 & \text{for spin 0 particle,} \\ \not{p} + m & \text{for spin 1/2 particle,} \\ \eta^{\mu\nu} & \text{for spin 1 particle.} \end{cases} \tag{3.10}$$

The dressed propagator reads

$$\mathcal{P}(p) = \frac{i\xi}{p^2 - m^2 - \Sigma(p^2)}, \tag{3.11}$$

where $\Sigma(p^2)$ is a self-energy of the particle. If the self-energy has an imaginary component, the resulting square of matrix element $|M_{fi}|^2$ follows the Breit-Wigner distribution

$$\begin{aligned} M_{fi} &\sim \frac{1}{p^2 - m^2 + im\Gamma}, \\ |M_{fi}|^2 &\sim \frac{1}{\left(p^2 - m^2\right)^2 + m^2\Gamma^2}. \end{aligned} \tag{3.12}$$

Thus the particle mass, m, is related to the real pole of the $|M_{fi}|^2$ element and the decay width, Γ, is related to the imaginary part of the pole of the $|M_{fi}|^2$ matrix element, which allows for clear experimental procedure how to measure both mass and the decay width. Equation (3.12) is called the *relativistic Breit-Wigner* distribution.

3.3.2. Theoretical prediction

The total top-quark decay width is usually calculated only from the $t \to Wb$ process, which is a very good approximation in the SM. At LO and assuming the mass of the b quark to be $m_b = 0$, the decay width of $t \to Wb$, $\Gamma(t \to Wb)$, yields

$$\Gamma(t \to Wb) = \frac{G_\mathrm{F}}{8\pi\sqrt{2}} m_t^3 \left(1 - \frac{m_W^2}{m_t^2}\right)^2 \left(1 + 2\frac{m_W^2}{m_t^2}\right), \tag{3.13}$$

where G_F is the Fermi constant, $G_\mathrm{F} = 1.1663787(6)10^{-5}$ GeV^{-2} [63] and $m_t(m_W)$ is the top-quark (W boson) mass. Equation (3.13) shows that in the SM the decay width of the top quark depends on third power of the top-quark mass. Plugging back V_{tb}, Equation (3.13) can be rewritten [129]

$$\Gamma(t \to Wb) = \frac{G_\mathrm{F}}{8\pi\sqrt{2}} m_t^3 |V_{tb}|^2 \left(1 - 3\left(\frac{m_W}{m_t}\right)^4 + 2\left(\frac{m_W}{m_t}\right)^6\right). \tag{3.14}$$

Higher order corrections to the LO results are known. The QCD corrections are parametrised as

$$\Gamma(t \to Wb) = \Gamma_0 \left(A^{(0)} + \frac{\alpha_s}{\pi} C_{\mathrm{F}} A^{(1)} + \left(\frac{\alpha_s}{\pi}\right)^2 A^{(2)} + \dots \right), \tag{3.15}$$

where $\Gamma_0 A^{(0)}$ is the LO value from Equation (3.14) with $\Gamma_0 = \frac{G_{\mathrm{F}}}{8\pi\sqrt{2}} m_t^3 |V_{tb}|^2$, α_s is the strong coupling constant, C_{F} is a flavour factor set to 4/3 and $A^{(0)}(A^{(1)})$ represents first (second) order QCD corrections. The first order correction, $A^{(1)}$, is known in a closed form [129]

$$\begin{aligned} A^{(1)} = {} & \frac{5}{4} - \frac{\pi^2}{3} + \frac{3}{2}\frac{m_W^2}{m_t^2} \\ & + \frac{m_W^4}{m_t^4}\left(-6 + \pi^2 - \frac{3}{2}\ln\frac{m_t^2}{m_W^2}\right) \\ & + \frac{m_W^6}{m_t^6}\left(\frac{46}{9} - \frac{2}{3}\pi^2 + \frac{2}{3}\ln\frac{m_t^2}{m_W^2}\right) + \mathcal{O}\left(\frac{m_W^8}{m_t^8}\right). \end{aligned} \tag{3.16}$$

The second order correction, $A^{(2)}$ is further split into components

$$A^{(2)} = C_{\mathrm{F}}^2 A_{\mathrm{A}}^{(2)} + C_{\mathrm{A}} C_{\mathrm{F}} A_{\mathrm{NA}}^{(2)} + C_{\mathrm{F}} T n_\ell A_\ell^{(2)} C_{\mathrm{F}} T A_{\mathrm{F}}^{(2)}, \tag{3.17}$$

where colour factors are set to $C_{\mathrm{F}} = 4/3$, $C_{\mathrm{A}} = 3$ and $T = 1/2$. n_ℓ represents the number of flavours, set to 5 to account for all non-top flavours in the SM. $A_{\mathrm{A}}^{(2)}$ is the Abelian contribution and $A_{\mathrm{NA}}^{(2)}$ represents non-Abelian contribution. Corrections from massless (massive) fermions in loops contribute to $A_\ell^{(2)}(A_{\mathrm{F}}^{(2)})$. Decomposing the $A_{\mathrm{X}}^{(2)}$, X = A, NA, ℓ, F terms from Equation (3.17) into a similar structure as in Equation (3.16) reads

$$A_{\mathrm{X}}^{(2)} = A_{\mathrm{X}}^{(2)}|_{m_W=0} + \frac{m_W^2}{m_t^2} A_{\mathrm{X}}^{(2)}|_{m_W^2} + \frac{m_W^4}{m_t^4} A_{\mathrm{X}}^{(2)}|_{m_W^4} + \dots . \tag{3.18}$$

The contribution from $A_X^{(2)}|_{m_W=0}$ is known in a closed form and yields approximately 2.859 [130]. The other $A^{(2)}$ terms are known only numerically by calculating the self-energy with an expansion around $q^2/m_t^2 = 0$. Example Feynman diagrams for the top-quark self-energy are displayed in Figure 3.7. Taking into account all $A^{(2)}$ terms from Equation (3.18), the second order QCD correction reads [131]

$$A^{(2)} = -16.7(8) + 5.4(4)\frac{m_W^2}{m_t^2} + \frac{m_W^4}{m_t^4}\left(11.4(5.0) - 7.3(1)\ln\frac{m_t^2}{m_W^2}\right). \tag{3.19}$$

The most precise theoretical calculation of the top-quark decay width includes NLO electroweak corrections and effects of the finite b-quark mass and the finite W boson mass on top of the NLO and NNLO QCD corrections [132]. The calculation is presented in the form of corrections to the LO decay width value, $\Gamma_t^{(0)}$, from Equation (3.14)

$$\Gamma_t = \Gamma_t^{(0)} \left(1 + \delta_{\mathrm{QCD}}^{(1)} + \delta_{\mathrm{QCD}}^{(2)} + \delta_{\mathrm{EW}} + \delta_f^b + \delta_f^W\right), \tag{3.20}$$

where $\delta^{(1)}_{\text{QCD}}(\delta^{(2)}_{\text{QCD}})$ represents NLO(NNLO) QCD corrections[6] and δ_{EW} represents NLO electroweak corrections. Contributions from the finite b-quark mass are included in δ^{b}_{f} and contributions from the finite W boson width enter δ^{W}_{f}. The effect from each individual correction on the top-quark decay width for different input top-quark masses is summarised in Table 3.3. The dominant contribution comes from NLO QCD corrections, as expected. It is interesting to note that the effects of finite W boson width and NLO electroweak corrections almost cancel out. The resulting prediction for the top-quark decay width is $\Gamma_t \approx 1.322$ GeV for a top-quark mass $m_t = 172.5$ GeV.

The theoretical uncertainty accounts for relative uncertainty on the decay width prediction of about 0.8 % [132] and it originates from a variation of the renormalisation scale. Including experimental uncertainties on parameters that enter into the formulae increases the uncertainty to about 6 %, where the dominant source of uncertainty comes from the uncertainty of the $|V_{tb}|$ matrix element, where a conservative value from direct measurements, not assuming unitarity of the CKM matrix, $|V_{tb}| = 1.021 \pm 0.032$ [63] is used.

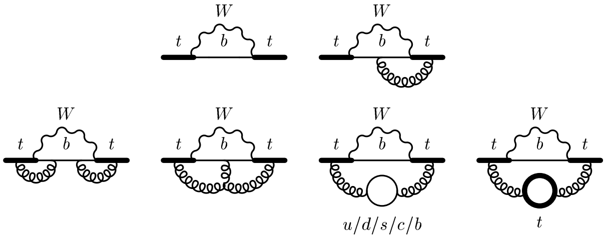

Figure 3.7.: Example Feynman diagrams used to calculate the top-quark self-energy.

m_t [GeV]	$\Gamma^{(0)}_t$ [GeV]	$\delta^{(1)}_{\text{QCD}}$ [%]	$\delta^{(2)}_{\text{QCD}}$ [%]	δ_{EW} [%]	δ^{b}_{f} [%]	δ^{W}_{f} [%]	Γ_t [GeV]
172.5	1.4806	-8.58	-2.09	1.68	-0.26	-1.49	1.3216
173.5	1.5109	-8.58	-2.09	1.69	-0.26	-1.49	1.3488
174.5	1.5415	-8.58	-2.09	1.69	-0.25	-1.48	1.3764

Table 3.3.: The SM prediction for the top-quark decay width, Γ_t, for various top-quark masses, m_t. The corrections [132] to LO prediction, $\Gamma^{(0)}_t$, include NLO(NNLO) QCD corrections, $\delta^{(1)}_{\text{QCD}}(\delta^{(2)}_{\text{QCD}})$, NLO electroweak corrections, δ_{EW}, finite mass of the b-quark, δ^{b}_{f} and, finally finite width of the W boson, δ^{W}_{f}. All corrections are given in percentages.

3.3.3. Possible BSM modifications

Several BSM scenarios predict different values for the top-quark decay width compared to the SM, even for the same underlying top-quark mass. Various sources lead to deviations from the SM expectation value. These sources include:

- Loop corrections, that enter into higher order calculations of the width, due to the presence of new particles.

---

[6] Terms $\delta^{(1)}_{\text{QCD}}$ and $\delta^{(2)}_{\text{QCD}}$ are related to terms $A^{(1)}$ and $A^{(2)}$ from Equation (3.15). The relation between these two can be easily derived by comparing Equations (3.15) and (3.20).

- New decay channels for the top quarks, due to new particles.
- Modification of some of the underlying fundamental parameters, e.g. the $|V_{tb}|$ CKM matrix element.
- Combination of the above effects.

Measuring the top-quark decay width could potentially point to some of the BSM models or could impose limits on some of the BSM parameters. Some of the models affecting the top-quark decay width are discussed.

SUSY and Two-Higgs-Doublet models

As was briefly mentioned in Section 2.2.4, SUSY is a famous extension of the SM which adds *super-partners* for all SM particles that differ by half a unit of spin, thus adding boson partners to SM fermions and adding fermion partners to SM bosons. In the Minimal Sypersymmetric Standard Model (MSSM) version of SUSY, two $SU(2)$ Higgs doublets,

$$\begin{pmatrix} \tilde{H}_1^+ \\ \tilde{H}_1^0 \end{pmatrix} \text{ and } \begin{pmatrix} \tilde{H}_2^+ \\ \tilde{H}_2^0 \end{pmatrix}, \tag{3.21}$$

exist. The two $SU(2)$ Higgs doublets contain eight physical degrees of freedom, three are required to give mass to SM massive bosons $W^{\pm}, Z$ via electroweak symmetry breaking. The remaining five degrees of freedom correspond to five new Higgs-like particles: two neutral scalars h^0 and H^0, one neutral pseudoscalar A^0 and two charged Higgs bosons $H^{\pm}$. The effect on the top-quark decay width in MSSM is two-fold: via loop corrections and via new decay channels of the top quark. The SUSY particles enter one-loop corrections and thus modify the calculation of Γ_t. The magnitude of these corrections depends on the value of $\tan\beta$, the ratio of the vacuum expectation values for the two neutral Higgs fields

$$\langle 0| \tilde{H}_{1,2}^0 |0\rangle = \frac{1}{\sqrt{2}} v_{1,2}. \tag{3.22}$$

The corrections to the width are dominated by SUSY electroweak corrections, and can reach up to 10 % [133, 134]. Figure 3.8 shows the combined electroweak and strong SUSY corrections for Γ_t for typical SUSY parameters.

If the hypothetical charged Higgs boson has a mass below the mass of the top quark, a new decay channel for the top quark would open via $t \to H^+ b$. The partial decay width of this process, $\Gamma(t \to H^+ b)$, depends on the SUSY parameters, especially $\tan\beta$. The partial decay width of $t \to H^+ b$ is illustrated in Figure 3.9 alongside with the radiative correction to this decay. For values of $\tan\beta \approx 5$ the partial width becomes minimal and approximately reproduces the SM expectation. However, for small or large $\tan\beta$ values, a significant deviation from the SM is expected.

Furthermore, new particles allow for other decay channels of the top quark in SUSY models. Such a process could be a decay of the top quark into a b and a chargino or into a stop quark and a neutralino which could modify the Γ_t by about 20 % [134]. However, the current limits exclude the stop-quark mass below the top-quark mass [135–138]. Moreover, possible three (or more) body decays of the top quark could modify the top-quark decay width, although only by a few percent [139].

Although the discussion about charged Higgs bosons was provided in the context of SUSY, the existence of such particles is not unique to SUSY. Several scenarios include *two-Higgs-doublet*

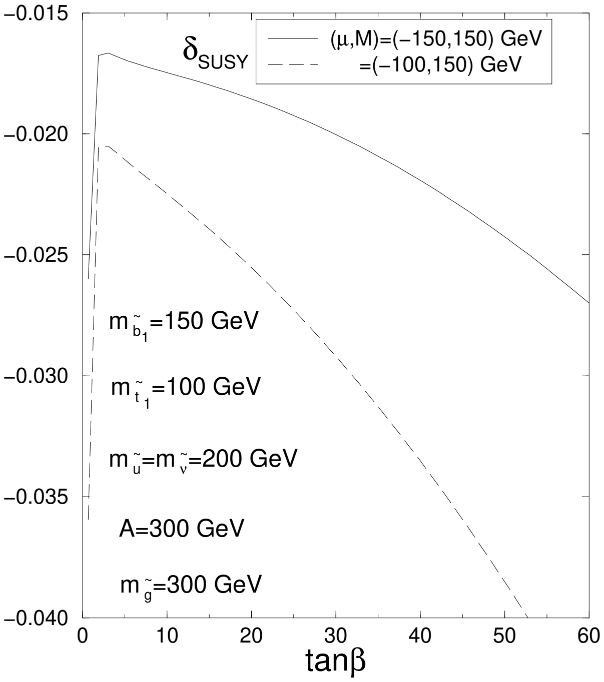

Figure 3.8.: Combined electroweak and strong SUSY corrections to $\Gamma(t \to W^+ b)$ for various SUSY parameters and fixed top mass $m_t = 175$ GeV. The figure is taken from [134].

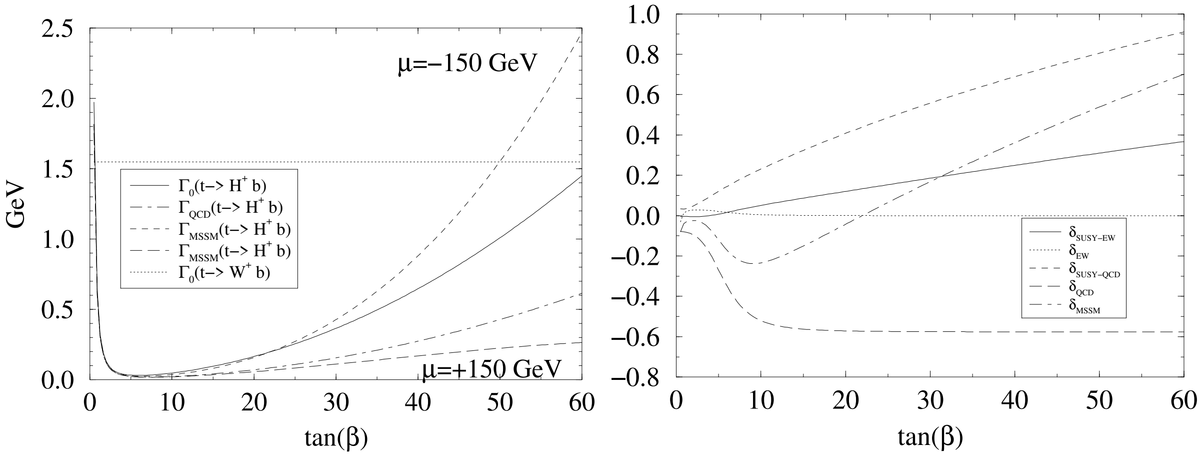

(a) (b)

Figure 3.9.: **(a)** The partial decay width $\Gamma(t \to H^+ b)$ compared to the SM total decay width as a function of $\tan\beta$. The results are shown for various SUSY parameter values with the charged Higgs mass $m_{H^\pm} = 120$ GeV. **(b)** Relative correction from SUSY and SM to $t \to H^+ b$ decay. The figures are taken from [134].

models (2HDM), for example models with axions [140] or models that explain baryogenesis [141–143]. The decay of the top quark is modified when the charged Higgs boson has a mass below the top mass and thus the decay is kinematically allowed. The magnitude of the modification depends on the individual models and their parameters. A discussion of the 2HDM scenarios goes beyond the scope of this thesis.

Flavour-changing neutral-currents

Flavour-changing neutral-currents (FCNCs) are forbidden in the SM at tree-level and are heavily suppressed by the GIM mechanism [58] otherwise. Possible top quark decays via Z boson, photon, Higgs boson or gluon would modify the top-quark decay width [144]. Some BSM models predict branching ratios for FCNC processes of the order of $10^{-4} - 10^{-5}$ which is several orders of magnitude higher than the SM prediction [145].

Models that modify the $\mathbf{V_{tb}}$ matrix element

The value of $|V_{tb}|$ is measured with very high precision, however, it is common to assume unitarity of the CKM matrix. If this assumption is dropped, significant deviations of $|V_{tb}|$ are possible, even while keeping

$$R = \frac{|V_{tb}|^2}{|V_{td}|^2 + |V_{ts}^2| + |V_{tb}^2|}, \tag{3.23}$$

invariant. This is possible by transforming $V_{ti} \rightarrow V_{ti}^{(0)} \cos\theta$ with any real θ. The minimal way in which to implement such rescaling is to introduce an iso-singlet vector-like quark with electric charge $q = +2/3$ [146]. If this hypothetical quark had a mass around the electroweak symmetry breaking scale, it would naturally mix with the SM top quark and the CKM matrix would need to be extended. This model allows for $|V_{tb}|$ to be smaller than 1 and thus modifying the prediction for the top quark decay width. This model would also lead to FCNC processes with much higher branching ratios with respect to the SM.

Other models that would modify $|V_{tb}|$ are models that introduce a fourth generation of quarks [147–149]. This would transform the standard 3 × 3 CKM matrix into a 4 × 4 matrix. The model does not allow FCNC at tree level, unlike the previous model with vector-like quark.

The BSM scenarios mentioned provide a simplified list of models that predict a different decay width of the top quark in comparison with the SM. The list of the models is, by no means, final and more complex alternative models can also affect Γ_t. Searches for the new models or constraining the existing ones are among the most important tasks of the LHC programme.

3.4. Previous measurements of the top-quark decay width

The top-quark decay width has been measured by experiments at the Tevatron and LHC. Generally, the width can be measured with two different approaches: *direct* and *indirect* measurements. A measurement is called direct when the top-quark decay width is extracted straight from the observed data and not via a different variable. On the other hand, indirect measurements refer to analyses where the width is extracted via another property that depends on Γ_t and the value for the width is only calculated based on the assumed dependence. Direct measurements are less model dependent as they do not rely on relations between Γ_t and the variable that is measured from the data in the case of indirect measurements. Recent measurements of the top-quark decay width are briefly summarised in this section.

3.4.1. Indirect measurements

The first indirect measurement of the top-quark decay width was conducted by the DØ Collaboration [150] which was later improved [151]. Recently, the CMS Collaboration has exploited the same technique [152]. The CMS measurement looked at $t\bar{t}$ events in the dilepton channel in proton-proton collisions at centre-of-mass energy of $\sqrt{s} = 8$ TeV with an integrated luminosity of 19.7 fb^{-1}. The measured quantity has been the top-quark branching fraction $\mathcal{R} = \mathcal{B}(t \to Wb)/\mathcal{B}(t \to Wq)$, where q denotes the sum of all down-type quarks. The fraction $\mathcal{R}$ has been extracted from a fit to observed b-tagged jet distributions with a parametric model that corrects for the fractions of jets in an event that do not originate from a single top quark decay. Using the results of the single top quark production cross-section in t-channel from [92], assuming $\sum_q \mathcal{B}(t \to Wq) = 1$ and the partial decay width of the top quark $\Gamma(t \to Wb) = 1.329$ GeV, the total decay width of the top quark can be determined from

$$\Gamma_t = \frac{\sigma_{t\text{-channel}}}{\sigma^{\text{theor.}}_{t\text{-channel}}} \frac{\Gamma(t \to Wb)}{\mathcal{B}(t \to Wb)}, \tag{3.24}$$

with a known theoretical single top t-channel production cross-section [83]. The resulting top quark decay width has been estimated as $\Gamma_t = 1.36 \pm 0.02(\text{stat.})^{+0.14}_{-0.11}(\text{syst.})$ GeV.

3.4.2. Direct measurements

The first direct measurement of the top-quark decay width was conducted by the CDF Collaboration [153] with a partial dataset which has been superseded by a measurement with the full Run II dataset [154] at $\sqrt{s} = 1.96$ TeV corresponding to an integrated luminosity of 8.7 fb^{-1}. The measurement used $t\bar{t}$ events in the lepton+jets channel. Several Monte Carlo (MC) signal samples were generated corresponding to a top-quark decay widths from 0.1 to 30 GeVwith a fixed mass $m_t = 172.5$ GeV. Moreover, to constrain jet energy scale (JES) systematic uncertainties, another set of samples with independently varied JES were generated. The energies of jets from data were corrected by a factor of $1 + \Delta_{\text{JES}}$, $\Delta_{JES} \in (-3\sigma, +3\sigma)$, reflecting the JES uncertainty. Invariant masses of the hadronically decaying top quark and hadronically decaying W boson were reconstructed from the data that passed the selection criteria. The reconstructed top mass is sensitive to Γ_t and the reconstructed mass of the W boson is sensitive to Δ_{JES} as illustrated in Figure 3.10. A template likelihood fit of both distributions was utilised to extract the width of the top quark and Δ_{JES} simultaneously. The resulting Γ_t reads

$$1.10 < \Gamma_t < 4.05 \text{ GeV}, \tag{3.25}$$

at 68 % confidence level (CL) for a fixed top-quark mass of $m_t = 172.5$ GeV.

The CMS Collaboration measured the top-quark decay width in a partial LHC Run II dataset at $\sqrt{s} = 13$ TeV corresponding to an integrated luminosity of 12.9 fb^{-1} [155]. The measurement exploits $t\bar{t}$ events, in this case, in the dilepton channel. Furthermore, single top Wt events are also considered as a signal. The observable sensitive to Γ_t used in the measurement is the invariant mass of the charged lepton (electron or muon) and the b-jet, $m_{\ell b}$. The pairing of the charged lepton and the b-jet is ambiguous, so all possible permutations are considered in the measurement. Templates corresponding to alternative Γ_t values are created by reweighting the parton level top mass distributions based on the theoretical Breit-Wigner distribution. The templates of $m_{\ell b}$ are compared to the observed data exploiting a profile likelihood technique.

Likelihood ratios of alternative top-quark width hypotheses and the null hypothesis, the SM prediction of $\Gamma_t = 1.32$ GeV, are tested as shown in Figure 3.11. The result yields

$$0.6 < \Gamma_t < 2.5 \text{ GeV}, \tag{3.26}$$

at 95 % CL for a top-quark mass $m_t = 172.5$ GeV.

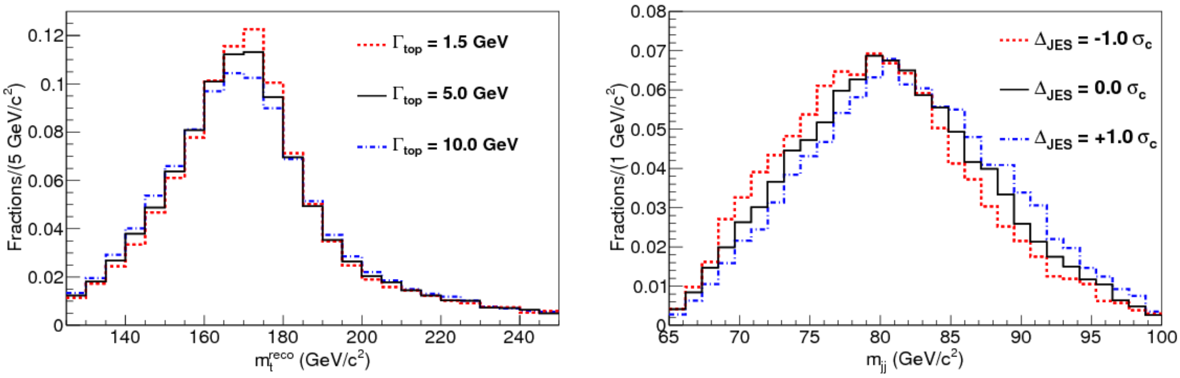

(a)

(b)

Figure 3.10.: **(a)** Reconstructed mass of the hadronically decaying top quark for three Γ_t templates corresponding to $\Gamma_t = 1.5, 5.0$ and 10.0 GeV. Δ_{JES} is set to 0 for all underlying widths. **(b)** Reconstructed mass of the hadronically decaying W boson for three Δ_{JES} values of $-1.0\ \sigma, 0$ and $+1.0\ \sigma$. The decay width is set to $\Gamma_t = 1.5$ GeV [154].

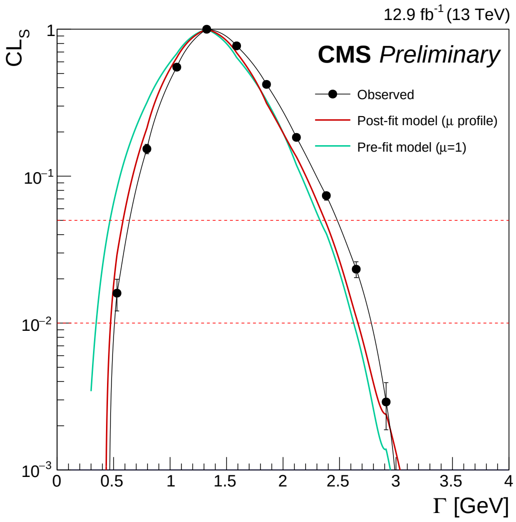

Figure 3.11.: Evolution of the CL_s as a function of the top-quark decay width. Limits of 95 % and 99 % CL limits are are shown as intersections of the curve with the line at CL_s = 0.05(0.01). Both pre-fit and post-fit results are shown [155].

CHAPTER 4

The LHC and the ATLAS experiment

After the closure of the Tevatron accelerator in 2011, the *Large Hadron Collider* [156] is the only accelerator capable of producing top quarks. The LHC is located at CERN (European Organization for Nuclear Research) near Geneva, Switzerland. It lies around 100 metres below surface in a 27 km long circular tunnel. The LHC was designed to accelerate protons and heavy ions with a centre-of-mass energy of 14 TeV in proton-proton collisions. The LHC schedule has been divided into phases, during which the LHC operated at different collision energy and configuration.

4.1. The LHC acceleration complex

The LHC is the most powerful particle accelerator till today. Operation of the LHC at these extreme energies requires the usage of superconductive magnets to bend and squeeze the beams of the circulating protons or heavy ions. Approximately 1200 dipole niobium-titanium magnets are used for keeping the protons on the circular orbit and additional 392 quadrupole, 688 sextupole and 168 octupole magnets are required to properly focus the beam. The magnets operate at 1.9 K temperature and produce a magnetic field of up to 8.3 T. The protons circulate in the LHC in bunches of around 1.3×10^{11} protons, and maximum of 2808 bunches are present in one beam at a time. The bunch spacing is 25 ns in the laboratory frame.

Before entering the LHC, protons pass a system of smaller accelerators. The overview of CERN's accelerator complex is shown in Figure 4.1. Protons are obtained by stripping electrons from Hydrogen atoms and then inserted into the first linear accelerator LINAC2, which accelerates them to 50 MeV. Then the protons are sent to the Proton Synchrotron Booster (PSB) where they are accelerated to 1.4 GeV. Protons are then transferred to the Proton Synchrotron (PS) with the maximal acquired energy of 26 GeV. The last accelerator before the LHC is the Super Proton Synchrotron (SPS) with a circumference of 7 km. Protons entering the LHC are accelerated up to 450 GeV per proton, half of them is sent in one direction and the other half in the opposite direction. Once inside the LHC, the protons are further accelerated using high-frequency electric fields up to the maximum energy of 7 TeV per proton[1].

---

[1] Only up to 6.5 TeV in Run 2.

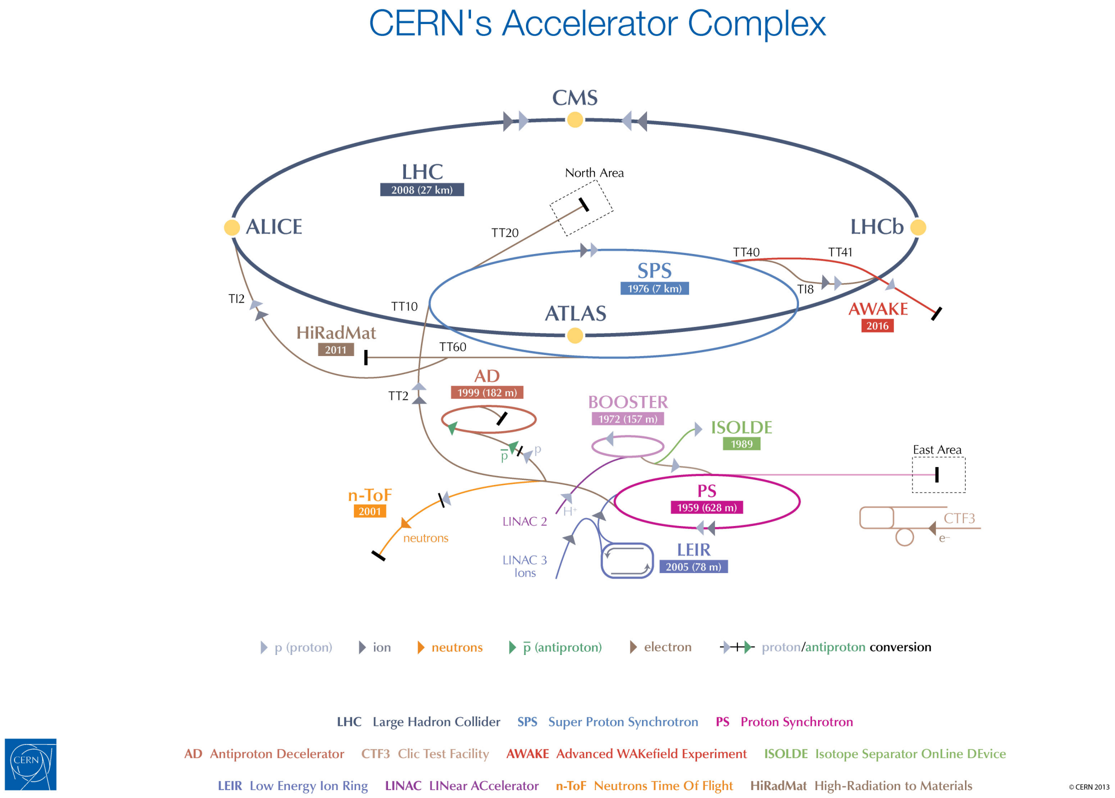

Figure 4.1.: The diagram of CERN's accelerating complex. © CERN.

The first LHC single beams were measured on 10th of September 2008. Unfortunately, after first successes, a major breakdown occurred and the LHC operation was suspended for more than a year. The LHC resumed its program on 20th of November 2009, when the first circulating beam after the breakdown was recorded. Shortly after, on 30th of November 2009, the LHC achieved the energy of 1.18 TeV per beam and has become the particle accelerator with the highest energy ever achieved, beating the previous record holder Tevatron. In 2011, the LHC operated at a centre-of-mass energy of 7 TeV with both ATLAS and CMS detectors recording about 5 fb^{-1} of data. On 5th of April 2012 the operation was restarted and the first collision with stable beams occurred with a centre-of-mass energy of $\sqrt{s} = 8$ TeV. Experiments recorded data from proton-proton collisions until the end of 2012, when the planned long shutdown started ending the Run 1 of the LHC programme. Both CMS and ATLAS detectors recorded around 20 fb^{-1} of proton-proton collision data at a centre-of-mass energy of 8 TeV. The LHC regained its stable beam conditions on June 3rd 2015, which marks the start of Run 2 data taking, with an unprecedented energy of 6.5 TeV per beam, resulting in a centre-of-mass energy of 13 TeV. The proton-proton collisions at $\sqrt{s} = 13$ TeV have been collected during 2016, 2017 and 2018 resulting in a combined total integrated luminosity of around 140 fb^{-1}. Figure 4.2 displays the cumulated luminosity delivered to the ATLAS detector during stable beams of pp collisions between years 2011 and 2018.

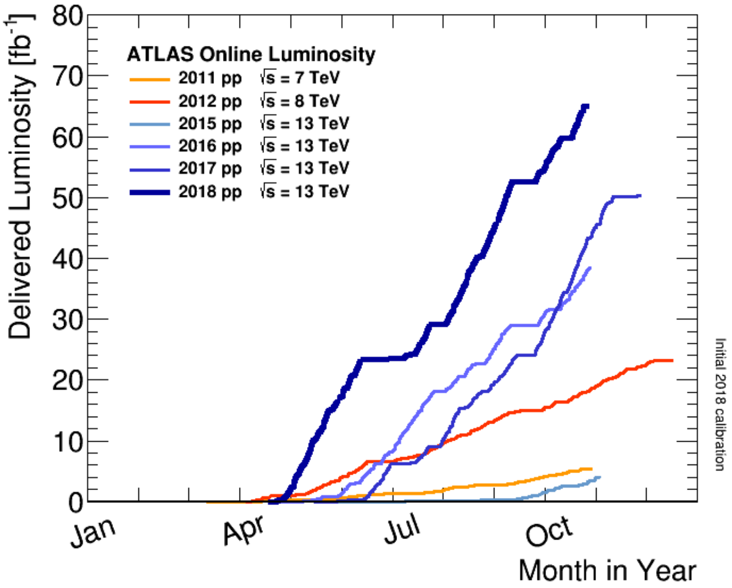

Figure 4.2.: Evolution of cumulated luminosity of recorded pp collisions by the ATLAS detector between years 2011 and 2018. The figure is taken from [157].

The proton beams in the LHC cross at four interaction points and at each of these points a particle detector is located. ATLAS (A Toroidal LHC ApparatuS) [158] and CMS (Compact Muon Solenoid) [159] are the two largest, general purpose detectors with the aim to precisely measure some of the SM properties, search for potential new particles and, ultimately, search for BSM physics. LHCb (LHC beauty) [160] is a forward detector that focuses mainly on physics of B-hadrons to study CP-violating processes in the early stages of the universe. ALICE (A Large Ion Collider Experiment) [161] studies heavy ion collisions with the emphasis on the quark-gluon plasma and the hadronisation processes. Several smaller experiments are located alongside the four main experiments: MoEDAL (Monopole & Exotics Detector at the LHC) [162] searching for magnetic monopoles, TOTEM (TOTal cross-section, Elastic scattering and diffraction dissociation Measurement) [163] measures the total cross-section of proton-proton interactions and the internal structure of the proton and LHCf (LHC forward) [164] that studies forward regions to imitate cosmic rays under laboratory conditions.

4.2. The ATLAS detector

The ATLAS detector is a general purpose detector that covers almost the full 4π solid angle around the interaction point. The detector was built to sustain collisions at 40 MHz at an instantaneous luminosity $\mathcal{L} = 10^{34}$ cm^{-2}s^{-1}. With length of 44 m, diameter of 25 m and weight of approximately 7000 tons, the ATLAS detector is one of the largest scientific experiments ever built. A longitudinal view of the ATLAS detector is shown in Figure 4.3. ATLAS is composed of system of sub-detectors with specific purposes: the *Inner Detector* responsible for tracking of particles and vertex identification, *calorimeters* which are crucial for energy measurements of photons, electrons and jets and *muon systems* needed to precisely reconstruct muon momenta. The individual sub-detectors are summarised in the following chapters.

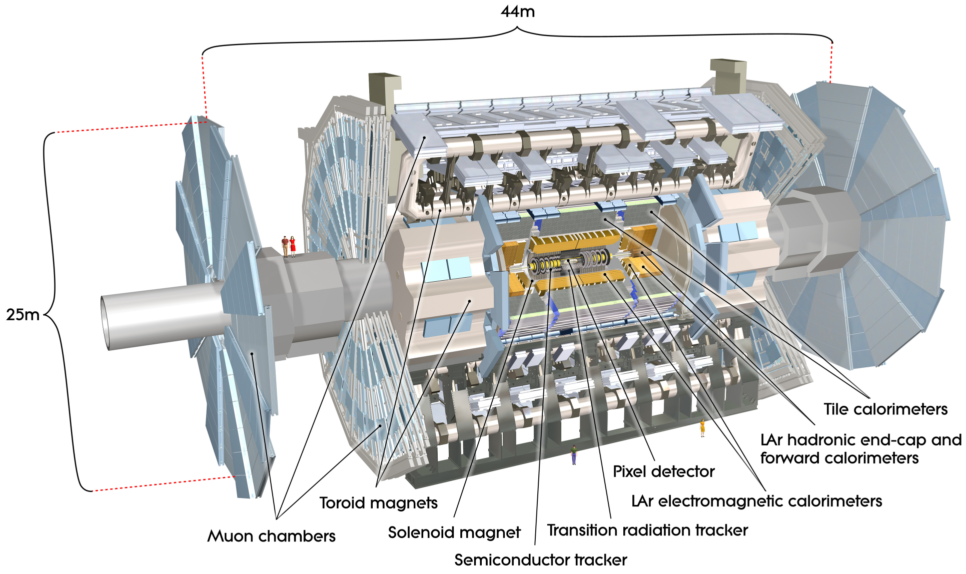

Figure 4.3.: The longitudinal view of the ATLAS detector and its sub-detectors. © CERN.

4.2.1. ATLAS coordinate system

The ATLAS coordinate system will be briefly explained as the convention is used throughout the thesis. ATLAS uses a right-handed coordinate system where the z-axis is defined by the beam direction. The z-axis is perpendicular to the x-y plane and the x-axis points from the interaction point inside ATLAS to the centre of the LHC acceleration ring. The y-axis point upwards. Usually, instead of a Cartesian coordinate system, a spherical system is used with azimuthal angle ϕ defined in the x-y plane. The polar angle θ is measured from the beam axis. The rapidity, y

$$y \equiv \frac{1}{2} \ln \left(\frac{E - p_{\mathrm{L}}}{E + p_{\mathrm{L}}} \right), \tag{4.1}$$

where p_{L} is the longitudinal momentum, is often used instead of the polar angle θ as the rapidity difference $y_1 - y_2$ is invariant under Lorentz boosts alongside the beam axis. In case of massless particles, the pseudorapidity, η

$$\eta \equiv -\ln \tan \frac{\theta}{2}, \tag{4.2}$$

is equivalent to the rapidity, and is a good approximation for massive particles as long as $p \gg m$. It is common to use the angular difference, ΔR, between two objects, defined as

$$\Delta R \equiv \sqrt{\Delta\phi^2 + \Delta\eta^2}, \tag{4.3}$$

where $\Delta\phi \equiv \phi_1 - \phi_2$, and similarly for $\Delta\eta$.

4.2.2. The Inner Detector

The Inner Detector (ID) is the sub-detector closest to the interaction point. The purposes of the inner detector are tracks pattern recognition, momentum and vertex measurements and electron identification. The whole ID is placed in a 2T magnetic field forcing charged particles to bend. By measuring the tracks of the particles, it enables to estimate the electric charge and momenta of the particles.

The ID is required to fulfil several important requirements: due to the large particle density close to the interaction point, the tracking measurements needs to be done with very high granularity to separate the individual tracks and interaction vertices. Furthermore, the ID suffers highest doses of radiation out of all ATLAS subdetectors and thus it needs to be constructed with a high radiation hardness. Additionally, the ID must modify the particle's trajectory as little as possible. To achieve this, the material needs to be minimal to have low radiation lengths, ξ_0 [2]. The ID combines several types of detectors, two semiconductor detectors: *Pixel Detector*, *Semiconductor Tracker* (SCT) and a straw tube detector *Transition Radiation Tracker* (TRT) that exploit the fact that charged particles ionise material they pass through and leave charges that can be measured. The layout of the ID is shown in Figure 4.4. Many of the ATLAS detector components are split into a central, barrel part and a forward part with end-caps.

The **Pixel Detector** is a semiconductor (silicon) pixel detector located in the innermost part of the ID, located only $R \geq 4.55$ cm from the interaction point. The nominal pixel size is $50 \times 400\ \mu\mathrm{m}^2$ as dictated by the readout pitch of the front-end electronics. The pixel detector contains more than 80 million readout channels. The spatial resolution of the pixel detector is $10 \times 115\ \mu\mathrm{m}^2$ in the $R/\phi \times z$. For Run 2 of the LHC, the pixel detector has been upgraded with an additional silicon layer. The new detector layer is called *Insertable B-Layer* (IBL) [165] and it is the innermost part of the ID, closest to the interaction point.

The **Semiconductor Tracker** surrounds the pixel detector. The SCT is a microstrip detector with similar purpose and technology as the pixel detector. The main difference is that SCT uses

---

[2] Radiation length, ξ_0, is defined as a distance on which an electron reduces its energy to e^{-1} due to bremsstrahlung.

strips instead of pixels. There are over 6 million SCT readout channels. Each strip measures 80 μm $\times 6 - 12$ cm, covering a larger area than the pixel detector. The spatial resolution of the SCT is 16 μm in R/ϕ and 580 μm in z.

The **Transition Radiation Tracker** is located in the outermost part of the ID. It is a combination of proportional drift tubes and a transition-radiation detector. There are almost 370 000 straw tubes in the ID. The straw is 144 cm long (37 cm for the end caps), with a diameter of 4 mm. Each straw contains a 30 μm diameter gold-plated W-Re wire that collects ionised electrons emitted when a charged particle passes through a straw tube. The straws are filled with a gas mixture of 70 % Xe, 27 % CO_2 and 3 % O_2. The electron collection time is 48 ns and the drift-time accuracy is 130 μm. Charged particles passing through environments with different refraction indices emit transition-radiation photons [166,167]. These photons are absorbed in the mixture of gases. The amplitude of the signal depends linearly (for ultra-relativistic particles) on the Lorentz factor γ. This factor is typically very large for lightest particles like electrons and positrons making it possible to use the signal from the TRT to identify these particles from other light particles like pions.

The tracking system covers regions with $|\eta| < 2.5$ (straw tubes cover only $|\eta| < 2$) with a momentum resolution

$$\sigma_{p_{\mathrm{T}}}/p_{\mathrm{T}} = 0.04\ \% \times p_{\mathrm{T}} \oplus 2\ \%, \tag{4.4}$$

where p_{T} is in GeV.

4.2.3. Calorimeters

Calorimeters cover a large pseudorapidity range of $|\eta| < 4.9$. The Electromagnetic (EM) calorimeter encapsulates η regions of the ID. The EM calorimeter has a fine granularity for

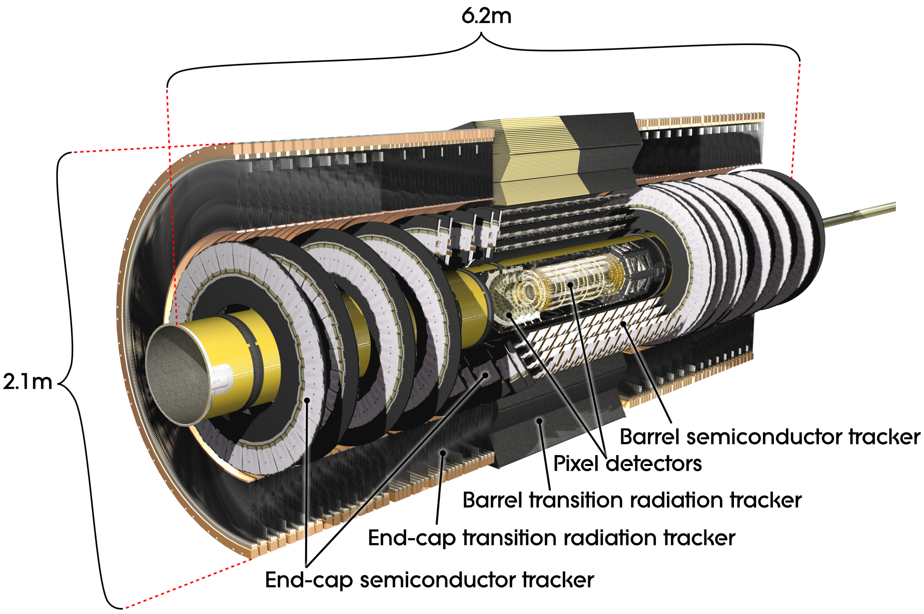

Figure 4.4.: The layout of the ATLAS inner detector. © CERN.

high precision measurements of the energy of electrons and photons. The EM calorimeter is covered by the hadronic calorimeter that has coarser granularity and is used for jet energy reconstruction and missing transverse momentum measurements. The layout of the ATLAS calorimeters is shown in Figure 4.5. The showers created by the incident particles must be fully contained within the calorimeters and thus they contain large amounts of material, leading to high ξ_0 to stop the particles with energies of up to units of TeV.

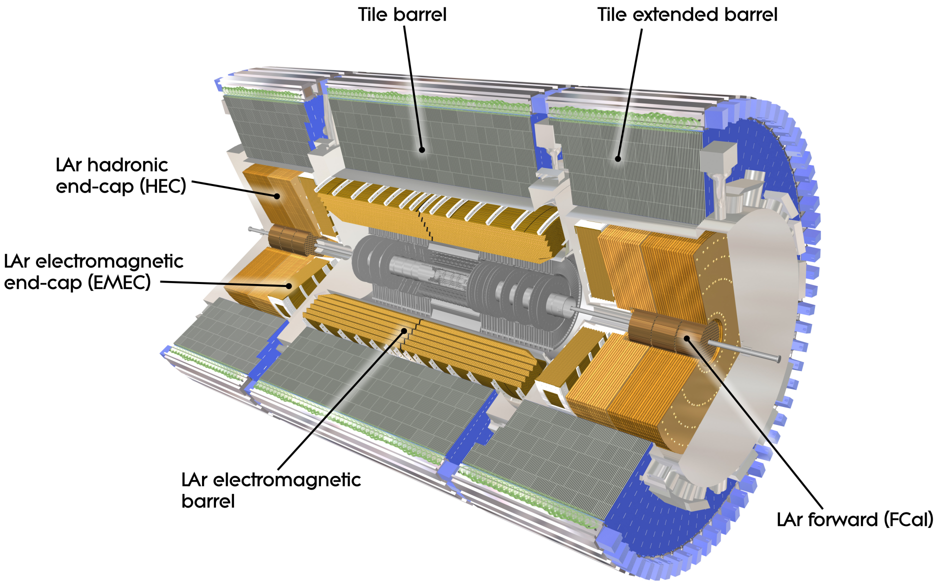

Figure 4.5.: The layout of the ATLAS calorimeters. © CERN.

The **Liquid Argon calorimeter** (LAr calorimeter) is an electromagnetic calorimeter which uses liquid argon as active material and lead plates as an absorber. An electromagnetic shower, initiated by incident particles, ionises liquid argon atoms. Then the collected electrons produce a signal. The LAr calorimeter is divided into three parts: a barrel part ($|\eta| < 1.475$) which is an electromagnetic calorimeter only, two end-cap components ($1.375 < |\eta| < 3.2$) which consist of both electromagnetic and hadronic calorimeters and the last part is the LAr forward calorimeter (FCal) which serves both as electromagnetic and hadronic calorimeter. The barrel part consists of two identical half-barrels, separated by a small gap (4 mm) at $z = 0$. The LAr consists of three layers with total number of 101760 readout channels in the barrel and 62208 channels in the end-cap. The granularity of the electromagnetic calorimeter depends on the layer and the barrel vs. end-cap region. The granularity in the first layer of barrel is $\Delta\eta \times \Delta\phi = 0.025/8 \times 0.1$ for $|\eta| < 1.4$. The energy resolution of the whole LAr reads

$$\frac{\sigma}{E} = \frac{0.1}{\sqrt{E}} \oplus 0.01 \oplus \frac{0.3}{E}, \tag{4.5}$$

with energy E in GeV.

The **Tile calorimeter** is placed directly outside the EM calorimeter. It is divided into two parts, the barrel ($|\eta| < 1$) and two extended barrels ($0.8 < |\eta| < 1.7$). It is a sampling calorimeter using steel as an absorber and scintillating tiles as an active material. The Tile calorimeter has

5760 readout channels in the long barrel and 4092 channels in the extended barrel. The achieved granularity in the Tile calorimeter is 0.1×0.1 in $\Delta\eta \times \Delta\phi$. The energy resolution of pions reads

$$\frac{\sigma}{E} = \frac{0.5}{\sqrt{E}} \oplus 0.03, \tag{4.6}$$

with energy E in GeV.

The **hadronic end-cap calorimeter** (HEC) is located directly behind the end-cap EM calorimeter. It consists of two wheels ranging from $1.5 < |\eta| < 3.2$. The wheels are made of copper plates interleaved with liquid argon gaps, which is an active medium of the calorimeter.

The **FCal** is integrated into the end-cap cryogenics. It is made of 3 layers, the first layer is made of copper, optimised for electromagnetic measurements. The other two layers are made of tungsten, optimised for hadronic interactions. Liquid argon is used as an active medium.

4.2.4. Muon spectrometer

The muon spectrometer is a system of detectors based on the magnetic deflection of muon tracks. Muons and neutrinos are the only SM particles that are not absorbed in calorimeters, although muons leave some portion of their energy in the calorimeters, which is used to improve the muon momenta resolution. The detectors measure momenta of charged particles in a region $|\eta| < 2.7$. The other purpose is to trigger on those particles in $|\eta| < 0.4$. In the barrel region tracks are measured in chambers arranged in three cylindrical layers around the beam axis. The layout of the ATLAS muon spectrometer is shown in Figure 4.6. The muon momentum resolution is 2–3 % in most of the kinematic region, except for very high momenta, where the resolution is 10 % for $p_{\mathrm{T}} = 1$ TeV. The muon spectrometer consists of several parts: the *cathode strip chambers* (CSC), the *monitored drift tubes* (MDT), the *resistive plate chambers* (RPC) and the *thin gap chambers* (TGC).

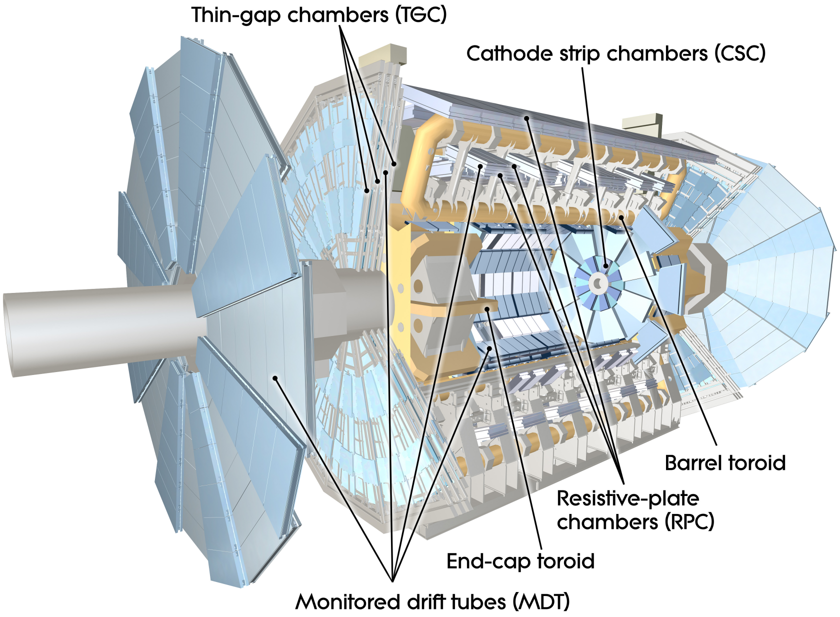

Figure 4.6.: The layout of the ATLAS muon system. © CERN.

MDTs together with **CSC** are used for precise measurements of muons momenta. The MDTs cover a range $|\eta| < 2$ and they are replaced by CSC in the region $2 < |\eta| < 2.7$. The chambers consist of three to eight drift tubes, the direction of the tubes is along ϕ. The average resolution per tube is 80 μm.

CSCs are multiwire proportional chambers with cathode planes segmented into strips in orthogonal directions. This enables CSCs to measure both coordinates of charged particles. The resolution of chambers is 40 μm in the bending plane and 5 mm in the transverse plane.

RPCs and **TGCs** are used for fast trigger decisions. The RPCs are gas detectors that detect gas ionisation induced by passing of charged particles. TGCs are multiwire proportional chambers, similar to RPCs. They have lower precision than CSCs and MDTs but they are extremely fast, they deliver track information in tens of nanoseconds after the passage of particles. The RPCs cover the barrel region ($|\eta| < 1.05$) and the TGCs cover the end-cap region ($1.05 < |\eta| < 2.4$). Both detectors provide signals in a spread of 15–25 ns allowing to tag the beam-crossing.

4.2.5. Magnets

The magnet system forms a crucial part of the detector systems, it is required for both particle momentum and charge measurement. It is divided into three parts: inner solenoid, barrel toroid, and end-cap toroids.

The superconducting **inner solenoid** is located around the inner detector. It creates a mostly homogeneous 2T magnetic field. The Inner solenoid is very thin to absorb as little particle energy as possible, it is only 0.66 radiation length thick. The inner and outer diameters of the solenoid are 2.46 m and 2.56 m and its axial length is 5.8 m. The solenoid is made of NbTi conductor to achieve a high magnetic field.

The **Barrel toroid** is assembled around the calorimeters and both end-caps. It consists of eight coils encased in stainless-steel vacuum vessels. The size of the barrel toroid is: 25.3 m in length, with inner and outer diameters of 9.4 m and 20.1 m. The barrel toroid generates a magnetic field of 4 T that is exploited by the MS as it allows to measure the momenta of muons as their tracks bend in the magnetic field.

The **End-cap toroids** work similarly to the barrel toroid. The magnetic field generated by the end-cap toroids is optimised for the end-cap muon spectrometer. Each end-cap toroid consists of eight flat, square coil units. The coils are assembled in an insulation vacuum vessel that is 5 m wide and 11 m in diameter.

4.2.6. Triggers

The Trigger system plays an important role in the *Trigger and Data Acquisition* (TDAQ) system. The expected event rate at ATLAS is approximately 1 GHz, which corresponds to more than 1 PB (peta byte) of data per second. Current technology is not able to process such huge amounts of data, that is why a trigger system is required. In Run 1, the trigger system consisted of three parts: *Level 1* (L1), *Level 2* (L2) and *event filter*. In Run 2, to cope with the higher luminosities delivered by the LHC, the trigger system was upgraded [168] and only two parts of the trigger have been used during the Run 2, the L2 and event filter triggers have been combined to a single *High Level Trigger* (HLT).

The L1 trigger identifies high p_T electrons, muons, photons and jets by combining information from RPC, TGC and calorimeters. The L1 is extremely fast with a latency around 2.5 μs. It reduces the data rate to around 100 kHz. In each event, the L1 also identifies one or more Regions-of-Interest (coordinates in η and ϕ) and passes the information to the HLT.

The HLT trigger is a software trigger that uses information from the L1 trigger. The HLT uses all the detector information within the Region-of-Interest. The HLT reduces the trigger rate to approximately 1 kHz with a latency around 200 ms.

4.2.7. Luminosity measurement and forward detectors

To predict the expected number of events in data, a precise measurement of the collected dataset luminosity is needed. Knowing the LHC parameters average visible inelastic interactions per bunch crossing, $\langle\mu\rangle$, the number of the LHC bunches, n_b, the revolution frequency of the bunches, f, production cross-section of inelastic interactions, $\sigma_{\text{inel.}}$ and the efficiency to measure them, ϵ, the luminosity, $\mathcal{L}$, can be calculated [169] as

$$\mathcal{L} = \frac{\langle\mu\rangle n_b f}{\epsilon\sigma_{\text{inel.}}}. \tag{4.7}$$

ATLAS uses three subdetectors to measure the online luminosity. **LUCID** (LUminosity measurement using a Cherenkov Integrating Detector) [170], as the name suggests, is a Cherenkov detector located at 17 m from the interaction point on both sides of the ATLAS detector. It consists of 16 aluminium tubes that are filled with C_4F_{10} gas. The **Zero Degree Calorimeters** (ZDC) [171] are located 140 m from the ATLAS interaction point at both sides of the detector. They measure neutral particles (neutrons and photons) in the forward regions that are produced in meson decays. The most forward subdetector of ATLAS, located at ±240 m from the interaction point, is the **ALFA** (Absolute Luminosity For ATLAS) [172] detector that measures elastic proton-proton scattering at very low angles.

Additionally, *van der Meer* scans [173] are used to measure the horizontal, Σ_x and vertical, Σ_y, profiles [174] of the LHC beams. Using the profiles, Equation 4.7 can be modified to

$$\mathcal{L} = \frac{n_b f n_1 n_2}{2\pi\Sigma_x\Sigma_y}, \tag{4.8}$$

to calculate the luminosity without the knowledge of the total inelastic cross-section.

The **ATLAS Forward Proton** (AFP) [175] detector identifies events in which one or two protons emerge intact from the proton-proton collisions at the LHC. This allows to study the soft and hard diffractive events at low luminosities. The AFP is placed 210 m from the ATLAS interaction point.

CHAPTER 5

Objects definition

Many particles are created at the LHC collisions, however not all of them need to be reconstructed in the detector as most of the created particles decay almost immediately and do not reach the detector. Only 14 particles have a lifetime $\tau c > 500\ \mu$m and can thus be detected. Out of these 14 particles, 6 are very rare and only 8 particles appear frequently [63], these are: $e^{\pm}$, $\mu^{\pm}$, γ, $\pi^{\pm}$, $K^{\pm}$, $p^{\pm}$, K^0_L and n. These particles differ by the type of their interactions, masses and electric charges. The ATLAS detector, described in Chapter 4.2, was build to identify and measure the properties of these long lived particles. Figure 5.1 illustrates different particles and their reconstruction inside the ATLAS detector.

Physics objects can appear in various stages. Particles originating from the hard process or scattering are referred to as as *parton level* or *truth level* objects. Contrary to what the name suggests, these also include leptons and photons, not only partons. The coloured objects from parton level shower emit additional particles via QCD and QED radiation and hadronise to form bound, colour singlet, objects. This stage is called *particle level*. When these particles pass through the detector they interact with the detector material and leave a characteristic signature, this is called *detector level* or *reconstruction level*. The detector level is the only stage of physics objects accessible by an experiment, both parton and particle level objects are accessible only via simulation.

The signature of $t\bar{t}$ events in the lepton+jets and the dilepton channel requires reconstruction of following physics objects: an electron or a muon[1], jets - which are collimated showers of hadrons created by an incident quark or a gluon - and missing transverse momentum due to the undetected neutrino. Tau leptons cannot be reconstructed directly as they decay before they reach the detector, however tau lepton events can contribute to the measurement of the top-quark decay, even though the analysis is not designed to select events with tau leptons. Furthermore, identification of a jet originating from a b-quark is important to identify top-quark events. The individual objects will be discussed in the following chapters. The detector reconstruction uses ATLAS software called *Athena* [176].

---

[1] No distinction between particles and antiparticles will be made from this point, unless explicitly mentioned.

5.1. Electrons

Being a charged particle interacting electroweakly, the electron should leave a track inside the ID and should be stopped inside the ECal. Identification and reconstruction of electrons uses information from both the ECal and the ID. When an electron leaves an energy deposition[2] $E_{\mathrm{T}} > 2.5$ GeV in the ECal, clusters of cells in $\eta \times \phi$ are matched to the tracks from the ID with $p_{\mathrm{T}} > 0.5$ GeV. The cluster reconstructions is done in cells of 3×7 in the barrel region and in cells of 5×5 in the end-cap ECal [177]. Electrons are further required to satisfy the impact parameter selection: $|d_0|/\sigma(d_0) < 5$ and $|z_0 \sin\theta| < 0.5$ mm[3]. The electron kinematics are reconstructed by taking the measured energy from the calorimeters and the three-momentum direction from the ID. Due to the limitations of the ID, only electron candidates with $|\eta_{\mathrm{cluster}}| < 2.47$ are considered, excluding the crack region between the barrel and the end-cap detector, $1.37 < |\eta_{\mathrm{cluster}}| < 1.52$. Electrons in the analysis are required to have $p_{\mathrm{T}} > 25$ GeV.

The algorithm that was used in Run 1 to identify prompt electrons from non-electron objects, such as jets and photons, reconstructed as electrons used a cut-based[4] method with quantities related to the electron cluster, calorimeter shower shapes, information from the TRT, track properties and track-cluster matching variables. In Run 2, similar variables have been used, however the cut-based algorithm has been replaced by a likelihood based algorithm. It is a multivariate technique that evaluates several input variables simultaneously. Likelihoods for the signal (prompt electron) and background (mis-reconstructed objects, non-prompt electrons) are combined into a single discriminant, $d_{\mathcal{L}}$ [178]

---

[2] $E_{\mathrm{T}} = E_{\mathrm{cluster}} / \cosh \eta_{\mathrm{track}}$.

[3] d_0 is the signed distance to the z-axis and $|z_0|$ is the z-coordinate of the track at the point of closest approach to the global z-axis.

[4] Simple selection criteria are applied to basic properties.

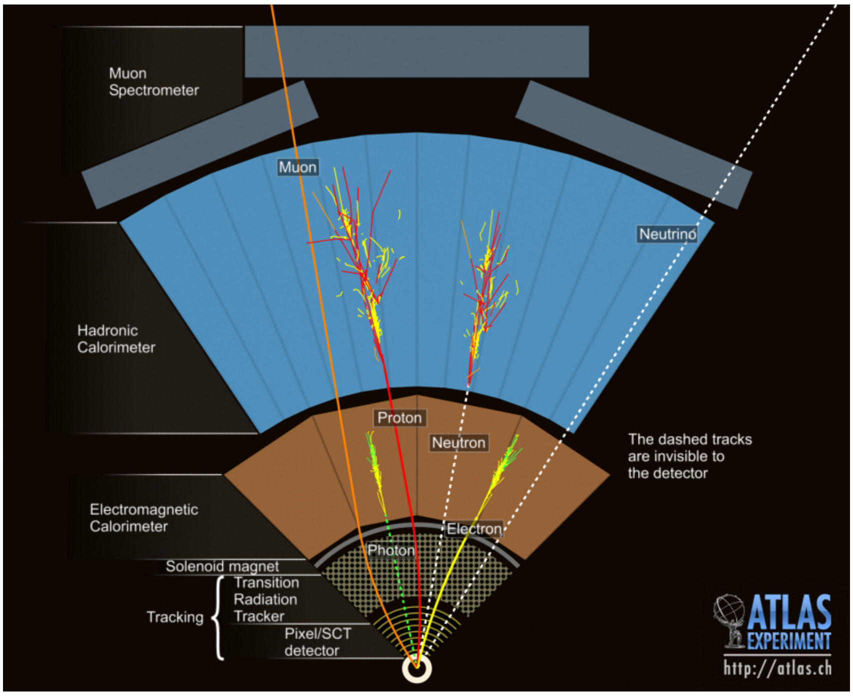

Figure 5.1.: An example of reconstruction of particles inside the ATLAS detector. © CERN.

$$d_{\mathcal{L}} = \frac{\mathcal{L}_{\mathrm{S}}}{\mathcal{L}_{\mathrm{S}} + \mathcal{L}_{\mathrm{B}}}, \qquad \mathcal{L}_{\mathrm{S(B)}}(\vec{x}) = \prod_{i=1}^{n} P_{S(B),i}(x_i), \tag{5.1}$$

where $\vec{x}$ is the vector of the discriminating variables and $P_{S(B),i}(x_i)$ is the value of the signal probability density function of the i^{th} variable evaluated at x_i. Three identification working points are provided: *loose*, *medium* and *tight*. Each working point uses the same input variables for the likelihood discriminant, but the selection on the discriminant variable is different for each working point. All electrons selected by *tight* are also selected by *medium*, and all electrons selected by *medium* are selected by *loose*. The analysis measuring the top-quark decay width uses electrons with *tight* identification working point, events with *medium* working point are used to estimate the contribution of non-prompt or mis-reconstructed electrons passing the event selection as will be summarised in Section 6.3.

To separate prompt electrons from electrons originating from semileptonic decays of heavy hadrons (non-prompt electrons) an additional requirement on the electron isolation is imposed. A *gradient* isolation is required for the electrons considered in the analysis. The *gradient* isolation working point imposes a 90 % efficient and η-dependent selection on the sum of the transverse momentum which is deposited within a cone of $\Delta R = 0.2$ around the calorimeter cells associated to the electron candidate, $E_{\mathrm{T}}^{\mathrm{cone20}}$. A correction from leakage of the electron cluster on the $E_{\mathrm{T}}^{\mathrm{cone20}}$ is also applied. Another η-dependent requirement with a 90 % efficiency is imposed on the sum of track transverse momenta around the electron candidate in a cone of $\Delta R = 0.3$, $p_{\mathrm{T}}^{\mathrm{cone30}}$. The combined calorimeter and track isolation leads to an electron reconstruction efficiency of 90 % at electron $p_{\mathrm{T}} = 25$ GeV and 99 % efficiency at electron $p_{\mathrm{T}} = 80$ GeV [178]. No isolation requirements are imposed on electrons used for the estimation of the non-prompt background.

The reconstruction, identification and trigger efficiencies in a simulated sample and in data can differ. To correct for the discrepancies, *scale factors* are derived and applied to the simulated events. The efficiencies in data and in MC are measured in $Z \to e^+e^-$ and in $J/\psi \to e^+e^-$ events [178] using the *tag-and-probe* method[5]. The scale factors are expressed as ratios of efficiencies in data vs MC as illustrated in Figure 5.2. Furthermore, the electron energy scale and resolution is measured in $Z \to e^+e^-$ events and is checked in $J/\psi \to e^+e^-$ and in events with radiative Z decay [179]. The energy scale calibration varies between 0.03 % to 0.2 % in most parts of the detector acceptance.

5.2. Muons

Muons are minimum ionizing particles and, consequently, they are not stopped in the calorimeters but they reach the ATLAS Muon Spectrometer (MS). Hence, muon reconstruction relies on information from both ID and the MS. Muon tracks are reconstructed independently in the ID and the MS and are then refitted globally. Muons are reconstructed using *outside-in* pattern where muons are first reconstructed in MS and then extrapolated and matched to an ID track [180].

Muon identification is performed by a cut-based selection of muon candidates. Muon candidates from in-flight decays have significantly different track quality properties. This is exploited in the muon identification process. Several variables offer good discrimination between prompt

---

[5] In the tag-and-probe method one object (in this case one electron) is required to have tight selection criteria and is used to identify given events - *tag*. The other object is selected with looser criteria and is used to study the given object - *probe*.

muons and muon background, including: the absolute value of the difference between the ratio of the charge and momentum of the muons measured in the ID and MS divided by the sum in quadrature of the corresponding uncertainties (q/p), the absolute value of the difference between the transverse momentum measurements in the ID and MS divided by the p_{T} of the combined track (ρ') and the normalised χ^2 of the combined track fit. Four identification working points are provided: *medium*, *loose*, *tight* and *high-*p_{T}. The analysis uses the *medium* muon identification working point that is characterised by requiring at least 3 hits in at least two MDT layers except for the region in $|\eta| < 0.1$ region, where tracks with at least one MDT layer are allowed. Furthermore, the q/p significance is required to be smaller than 7 [180]. Additionally, only muons passing $|d_0|/\sigma(d_0) < 3$, $|z_0 \sin\theta| < 0.5$ mm and $p_{\mathrm{T}} > 25$ GeV are considered in the analysis.

To suppress muons originating from semileptonic decays of heavy hadrons, muons used in the analysis are required to pass additional isolation criteria. Several isolation working points are provided, utilizing track and calorimeter-based isolation variables. The *gradient* isolation working point is used in the analysis, which has the same definition as for electrons in Section 5.1. The *gradient* isolation, in case of muons, reaches an efficiency above 95(99) % for muon $p_{\mathrm{T}} =$ 25(60) GeV [180]. No isolation requirement is imposed on muons used in the estimation of the non-prompt muon background.

Similarly as in the case of electrons, the reconstruction and identification efficiencies of muons may differ between the simulated samples and the observed data. The tag-and-probe technique is used in $Z \to \mu^+\mu^-$ and $J/\psi \to \mu^+\mu^-$ events is used to measure the efficiencies in data. Discrepancies, measured as ratios of efficiencies, are corrected by applying muon scale factors to the simulated samples. Figure 5.3 displays reconstruction efficiencies of *medium* muons as a function of p_{T} in both data and in MC. Moreover, muon momentum scale and resolution are measured in $Z \to \mu^+\mu^-$ and $J/\psi \to \mu^+\mu^-$ events and a set of corrections to the simulated

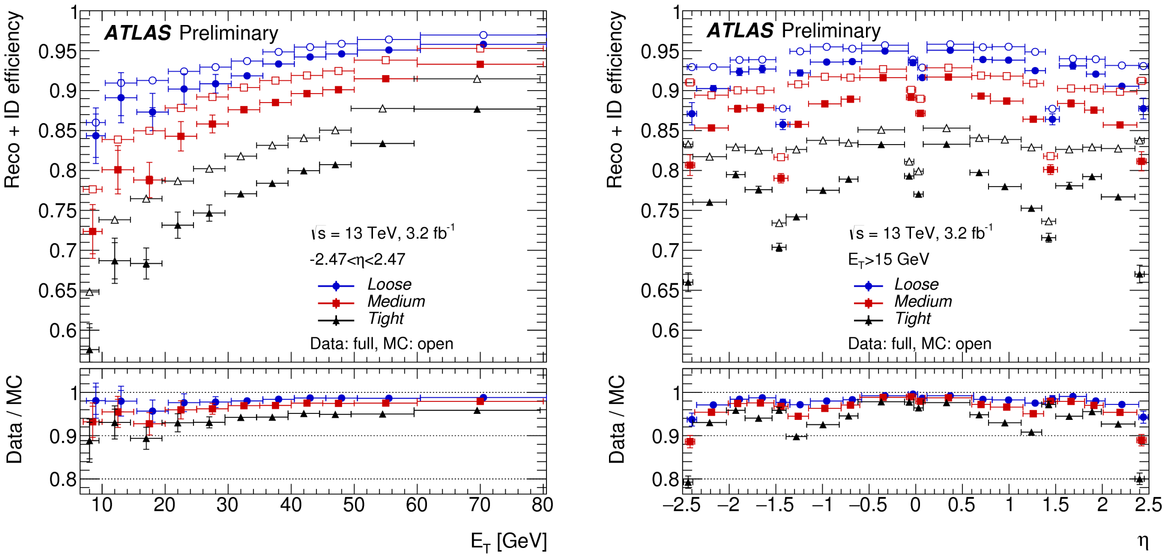

(a) (b)

Figure 5.2.: Reconstruction and identification efficiencies of electrons as a function of electron E_{T} (**a**) and electron η (**b**). Efficiencies for data and simulated samples are compared. The figure is taken from [178].

samples is applied to match the scale and resolution observed in data. Correction factors are derived by comparing maximum-likelihood fits of invariant masses of the Z boson and J/ψ in data and in the MC simulated samples [180].

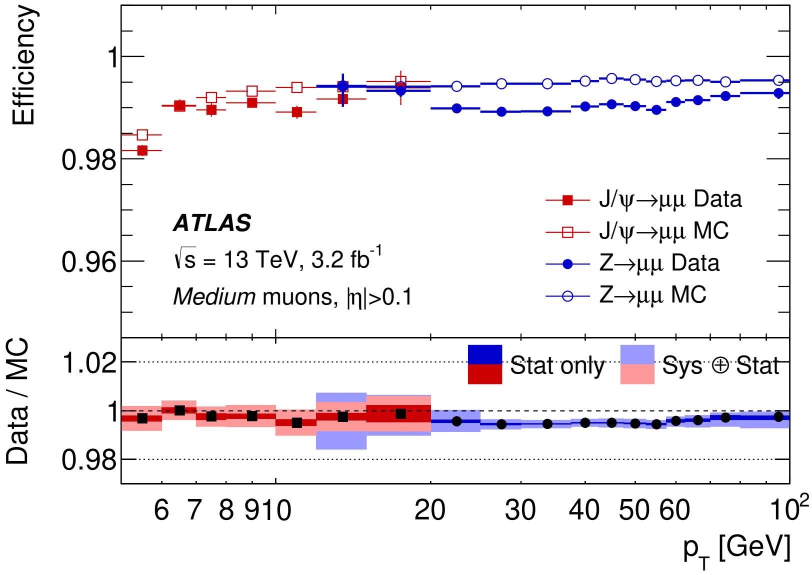

Figure 5.3.: Reconstruction efficiencies of *medium* muons as a function of muon p_{T} obtained from $Z \rightarrow \mu^+\mu^-$ and $J/\psi \rightarrow \mu^+\mu^-$ events. Efficiencies for both data and simulated samples are shown. The figure is taken from [180].

5.3. Jets

Quarks and gluons are particles carrying non-zero colour charge, consequently, they cannot be observed as free particles, they form colourless hadrons. These hadrons form highly collimated *jets*. Particles in a jet leave tracks in the ID if they are charged and leave energy deposits inside calorimeters even for uncharged particles. The energy deposited in the calorimeters is induced only from electromagnetic processes, in the case of the hadronic calorimeter, this is caused by ionisation processes from the hadronic showers and by excitations of molecules in the scintillators.

Energy depositions in topological clusters [177] are reconstructed using the *anti-k_t* algorithm [181, 182] with radius parameter $R = 0.4$, implemented via the *FastJet* computer program [183]. The *anti-k_t* algorithm combines energy clusters from calorimeters based on a distance parameter d_{ij} between clusters i and j

$$d_{ij} = \min\left(p_{\mathrm{T},i}^{2p}, p_{\mathrm{T},j}^{2p}\right)\frac{\Delta R_{ij}^2}{R^2}, \tag{5.2}$$

where the exponent[6] p is set to -1. The *anti-k_t* algorithm has two interesting properties that make it desirable at hadron colliders. Firstly, it prefers clusterings of hard particles instead of

---

[6] Two other algorithms are commonly used that are similar to the *anti-k_t* algorithm [184]. One with $p = 1$, called k_t algorithm, and with $p = 0$, called *Cambridge-Aachen* algorithm [185].

the soft ones which results in jets being almost circular around the hardest clusters. This allows for easier jet calibration as only one parameter, radius R, is enough to describe the shape of the corresponding reconstructed jets. Secondly, the *anti-k_t* algorithm is infrared and collinear safe (IRC safe) [186] which means that the algorithm is invariant with respect to an emission of a soft (infrared) or collinear particle. Jets in the analysis are required to have $p_{\mathrm{T}} > 25$ GeV and $|\eta| < 2.5$.

Since the energy in the calorimeters originates only from electromagnetic interactions and the whole jet energy must be deduced only from the electromagnetic component, a series of calibrations are applied to reconstructed jets to match the energy of corresponding particle-truth jets. Six sequential calibrations are applied [187] which will be briefly described. Starting from the electromagnetic scale, a correction to the jet origin is applied that recalculates the jet four-momentum to point to the hard-scatter primary vertex rather than the centre of the detector, while keeping the jet energy constant. The correction is calculated using simulated MC events. Next, corrections for multiple interactions from one bunch crossing (*in-time pile-up*) and from previous and following bunch crossings (*out-of-time pile-up*) are applied. These corrections are applied in two steps, first per-event area-based p_{T} density subtraction is applied and then a residual correction from MC simulation is used. Figure 5.4 shows the average energy response of jets after origin and pile-up corrections as a function of η. Next step is to apply an absolute jet energy scale and η calibration that corrects for the reconstructed jet four-momentum taking into account the η biases using MC simulated samples. Following the Global Sequential Calibration (GSC) using information from calorimeters, muon spectrometer and ID is applied to correct residual dependencies of the jet energy scale (JES) on the longitudinal and transverse features of the jets. Quark and gluon jets have different particle composition, quark-initiated jets tend to include hadrons with higher fraction of the jet p_{T} that traverse further in the calorimeters, while gluon-initiated jets typically contain more particles with smaller p_{T}, leading to a lower calorimeter response and a wider transverse profile. Five different variables are used to correct the JES through GSC procedure.

Finally, a set of *in-situ* calibrations is applied that takes into account differences between the simulated MC and the observed data [187]. The differences are corrected by balancing the p_{T} of a jet against other well-measured objects. The η-intercalibration corrects response of forward jets ($0.8 < |\eta| < 4.5$) to the well-measured central jets in dijet events and three other calibrations correct the average p_{T} response of the central jets. Events with a Z boson or a photon, with the Z boson decaying to a pair of electrons or muons is used to measure the response of the recoiling jets in regions up to 950 GeV. The multijet balance analysis utilises events with multiple jets to calibrate central ($|\eta| < 1.2$), high-p_{T} jets ($300 < p_{\mathrm{T}} < 2000$ GeV) recoiling against a collection of lower-p_{T} jets that are already well-calibrated from the previous calibration steps.

At the LHC, especially during Run 2, the proton collisions come with large pile-up, both in-time and out-of-time. The pile-up can contribute to the reconstructed jet energies and is typically subtracted as mentioned in Section 5.3. However, the pile-up activity can also mimic jets, especially low-p_{T} jets. During Run 2, the ATLAS Collaboration uses a multivariate technique to suppress the contribution of pile-up activity misidentified as jets from the hard scattering. The discriminant, *jet-vertex-tagger* (JVT) [188], is constructed from a two dimensional likelihood using two variables: $R_{p_{\mathrm{T}}}$ and corrJVF. $R_{p_{\mathrm{T}}}$ is defined as the scalar sum of p_{T} of tracks that are associated with a jet, $\sum_k p_{\mathrm{T}}^{\mathrm{trk}_k}(PV_0)$, divided by the fully calibrated jet p_{T} (includes pile-up subtraction)

$$R_{p_{\mathrm{T}}} = \frac{\sum_k p_{\mathrm{T}}^{\mathrm{trk}_k}\,(PV_0)}{p_{\mathrm{T}}^{\mathrm{jet}}}. \tag{5.3}$$

The second variable, corrJVF is a variable similar to Jet Vertex Fraction (JVF), a discriminant that was used for Run 1 measurements [189], but corrected for the number of reconstructed primary vertices, N_{Vtx}

$$\mathrm{corrJVF} = \frac{\sum_k p_{\mathrm{T}}^{\mathrm{trk}_k}\,(PV_0)}{\sum_l p_{\mathrm{T}}^{\mathrm{trk}_l}\,(PV_0) + \frac{\sum_{n\geq 1}\sum_l p_{\mathrm{T}}^{\mathrm{trk}_l}(PV_n)}{(k.n_{\mathrm{trk}}^{\mathrm{PU}})}}, \tag{5.4}$$

where $n_{\mathrm{trk}}^{\mathrm{PU}}$ corresponds to the total number of pile-up tracks, the constant k is chosen to be $k = 0.01$. Figure 5.5 illustrates the JVT discriminant for the pile-up and for hard-scatter jets with $20 < p_{\mathrm{T}} < 30$ GeV.

Events with $Z \to \mu^+\mu^-$+jets are used to validate the JVT discriminant in the observed data exploiting the tag-and-probe technique [188]. The well-measured Z boson is used to study the recoiling jets. The pileup contribution is estimated from a pile-up enriched control region, assuming $|\Delta\theta(Z,\mathrm{jet})|$ is flat for pile-up jets. Observed discrepancies in efficiencies between data and simulated MC samples are corrected by applying scale factors to the MC. The analysis jets are required to pass JVT > 0.59 for jets with $p_{\mathrm{T}} < 60$ GeV.

5.4. Missing transverse momentum

Neutrinos do not interact with the detector material and thus they cannot be reconstructed directly. However, due to momentum conservation they can be detected indirectly. In a proton-proton collision, the interacting particles of hard scattering are quarks and gluons and their

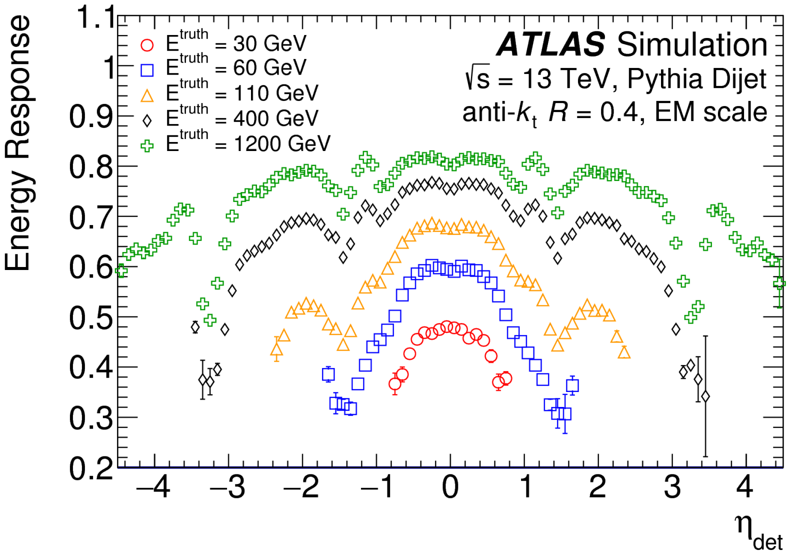

Figure 5.4.: The average jet energy response as a function of detector η for jets of various truth energy after the origin and pile-up corrections. The figure is taken from [187].

momenta depend on the corresponding parton densities and are intrinsically random. However, the parton transverse momentum can be considered to be exactly zero, consequently, also the transverse momenta of the products of the collision must add up to zero. Thus, non-zero measured transverse momentum hints to an undetected particle, such as neutrinoss. This quantity is called *missing transverse momentum* and its magnitude is missing transverse energy, $E_{\mathrm{T}}^{\mathrm{miss}}$.

The $E_{\mathrm{T}}^{\mathrm{miss}}$ is calculated based on the measured calibrated objects. The x and y components of the $E_{\mathrm{T}}^{\mathrm{miss}}$ read

$$E_{x(y)}^{\mathrm{miss}} = E_{x(y)}^{\mathrm{miss},e} + E_{x(y)}^{\mathrm{miss},\gamma} + E_{x(y)}^{\mathrm{miss},\tau} + E_{x(y)}^{\mathrm{miss,jets}} + E_{x(y)}^{\mathrm{miss},\mu} + E_{x(y)}^{\mathrm{miss,soft}}, \tag{5.5}$$

where each term corresponds to a negative vectorial sum of transverse momenta of both tracks and energy deposits. Energy deposits and tracks are matched to physics objects: electrons, photons, tau leptons (visible part), jets and muons. $E_{x(y)}^{\mathrm{miss,soft}}$ represents signals not related to any physics objects. The $E_{\mathrm{T}}^{\mathrm{miss}}$ is then defined [190] as

$$E_{\mathrm{T}}^{\mathrm{miss}} = \sqrt{\left(E_x^{\mathrm{miss}}\right)^2 + \left(E_y^{\mathrm{miss}}\right)^2} \qquad \text{and} \qquad \phi^{\mathrm{miss}} = \arctan\frac{E_x^{\mathrm{miss}}}{E_y^{\mathrm{miss}}}. \tag{5.6}$$

The $E_{x(y)}^{\mathrm{miss,soft}}$ is exclusively reconstructed from tracks from the ID. Otherwise, more inclusive definitions of $E_{x(y)}^{\mathrm{miss,soft}}$ exist that use the information from energy clusters, however these definitions are not used in the analysis. The terms associated from the physics objects need to pass object selection criteria: Medium electrons with $p_{\mathrm{T}} > 10$ GeV and $|\eta| < 1.37$ or $1.52 < |\eta| < 2.47$. Photons with $p_{\mathrm{T}} > 25$ GeV and $|\eta| < 1.37$ or $1.52 < |\eta| < 2.47$ are used. Hadronically decaying

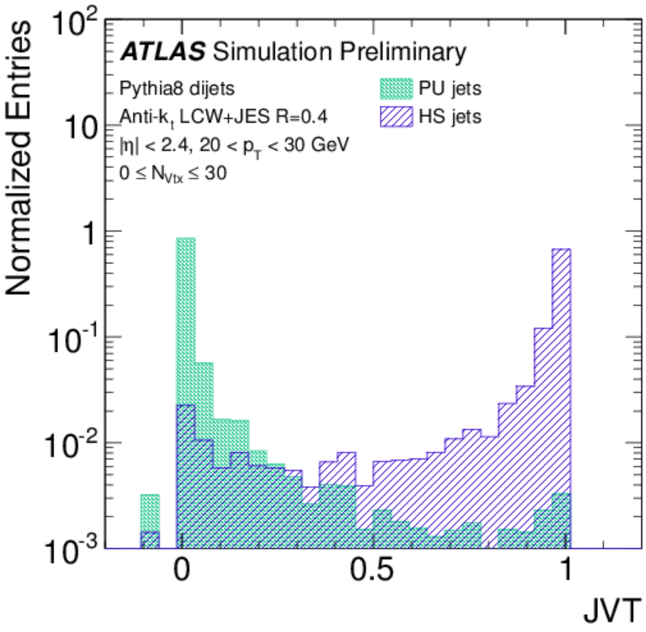

Figure 5.5.: The distribution of JVT for pile-up (PU) jets and hard-scatter (HS) jets with $20 < p_{\mathrm{T}} < 30$ GeV. The figure is taken from [188].

τ leptons with $p_{\mathrm{T}} > 20$ GeV and $|\eta| < 1.37$ or $1.52 < |\eta| < 2.47$ are considered. Medium muons with $p_{\mathrm{T}} > 10$ GeV in $|\eta| < 2.5$ contribute to the $E_{\mathrm{T}}^{\mathrm{miss}}$ terms. Jets are reconstructed using the anti-k_t algorithm with radius $R = 0.4$ including electromagnetic+JES and pile-up corrections. The $E_{x(y)}^{\mathrm{miss,soft}}$ term is constructed from tracks that have $p_{\mathrm{T}} > 400$ MeV and $|\eta| < 2.5$ and additional fit quality criteria. Vertices are constructed from at least two tracks passing selections on the transverse (longitudinal) impact parameter $|d_0| < 1.5$ mm ($|z_0 \sin\theta| < 1.5$ mm) relative to the vertex candidate [190].

The $E_{\mathrm{T}}^{\mathrm{miss}}$ scale and resolution is calibrated using events with $Z \to \mu^+\mu^-$, where no genuine $E_{\mathrm{T}}^{\mathrm{miss}}$ is present, thus the channel can be used to check the quality of the missing transverse momentum measurement. Events with $W \to e\nu$ or $W \to \mu\nu$ provide a well-defined topology with neutrinos produced in the hard-scatter process. Events with $t\bar{t}$ are used to evaluate the $E_{\mathrm{T}}^{\mathrm{miss}}$ performance in events with large jet multiplicity.

5.5. Identification of *b*-jets

The identification of jets originating from b quarks is crucial for analyses including a top quark as it decays into a W boson and a b quark in almost 100 % of cases in the SM. This allows to discriminate events with the top quark from background events. The identification of b-jets, and their discrimination from light quark- and gluon-jets is often called *b-tagging* and it will be briefly described.

Algorithms designed to discriminate b-jets from other jets exploit the fact that jets originated from a b quark contain B hadrons that have a relatively large mean lifetime of up to $\tau_B = 1.5$ ps [63] which makes them travel a macroscopic distances of up to a few millimetres. Thus, the decay of B hadrons can be associated with a secondary vertex. Furthermore, around 20 % of B hadrons contain an electron or a muon in their decay products [63] and due to the large B hadron mass, compared to the masses of the electron or the muon, the charged leptons tend to have large transverse momentum with respect to the b-quark direction (jet axis). Both of these properties are widely used for b-tagging.

This analysis takes advantage of the ATLAS *MV2c10* b-tagging algorithm [191], which is a multivariate algorithm, that exploits the Boosted Decision Tree (BDT) technique. The input variables for the BDT include: a likelihood-based combination of the transverse and longitudinal impact parameter significances, implemented in the *IP3D* algorithm that is based on a likelihood ratio where the impact parameters of the track are compared to simulated b- and light-flavour-hypothesis; identification of secondary (and tertiary) vertex algorithms, *SV0* and *SV1*; and the reconstruction of the B-hadron decay chain using the Kalman Filter technique [192] to identify the topology of the decay chain, implemented in the *JetFitter* algorithm. Additionally, jet p_{T} and η are included in the *MV2c10* algorithm. A similar algorithm has been used in Run 1, called *MV1* [193]. However, the *MV2c10* algorithm is specially trained to suppress c-jets being mis-tagged as b-jets[7] and includes the improved tracking information available in Run 2, as mentioned in Section 4.2.2. All the input variables are combined into a single discriminant variable, the *MV2c10* output. Figure 5.6 illustrates the *MV2c10* BDT discriminant output for b-jets, c-jets and light-flavour-jets. In this analysis, a *60 % working point* for b-tagging is used, this corresponds to around 60 % of true b-jets passing the selection, while the rejection rate (one over fraction of mistakenly tagged jets) is 22 for c-jets and approximately 1204 for light-flavour-jets. However, these efficiencies are a function of a jet p_{T}. The *60 % working point* selection requires jets to pass the *MV2c10* BDT discriminant > 0.94 to be considered b-tagged.

---

[7] The *c10* in the *MV2c10* stands for a 10 % c-jet contamination used in the BDT training.

Scale factors are applied to simulated events to compensate for the observed discrepancies in the tagging efficiencies between the simulated MC events and the observed data. The b-jet efficiency measurement has been carried out in dilepton $t\bar{t}$ events [191] using both tag-and-probe and likelihood methods. The $t\bar{t}$ events provide a good source of genuine b-jets, for the tag-and-probe technique one b-jet is required to be b-tagged (tag) and other jets are studied (probe). The likelihood method has been performed in dilepton channels: $e\mu$ and combined $ee/\mu\mu$ that are further split into events with exactly two jets and events with three or more jets. The likelihood method exploits per-event jet tagging correlations. Both methods are used to measure b-tagging efficiencies in the simulated MC events and the observed data and to derive the corresponding scale factors. The b-tagging efficiency of genuine c-jets is measured exploiting the tag-and-probe technique in semileptonic $t\bar{t}$ events [194]. This measurement takes advantage of the fact that the W boson has a c-quark in its decay products in 33.3 % of all W decays [63], this provides a good source of genuine c-jets in the selected events. Finally, the b-tagging efficiency of light-flavour-jets (mistagging) is measured in multijet events [195]. The measurement relies on the fact that, to a large extent, light-flavour-jets are mistagged as b-jets mainly because of the finite resolution of the reconstructed inner detector track trajectories and impact parameters.

5.6. Object overlap removal

Multiple physics objects can be reconstructed from one true object. To avoid double counting of reconstructed objects an *overlap removal* procedure is applied to solve the ambiguities. Following steps are applied in order:

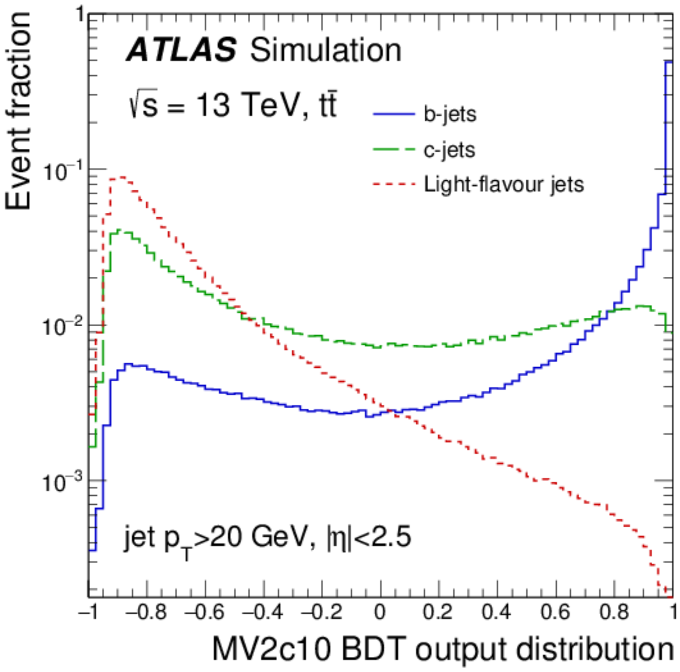

Figure 5.6.: The *MV2c10* BDT discriminant distribution for b-jets, c-jets and light-flavour-jets with $p_{\mathrm{T}} > 20$ GeV and $|\eta| < 2.5$. The distribution includes jets from simulated $t\bar{t}$ events. The figure is taken from [191].

1. An electron candidate track overlapping with another electron is removed.
2. A muon identified using calorimeter information that shares a track with an electron is removed.
3. Electron candidates which share a track with muon candidates are removed.
4. If ΔR between a jet and an electron candidate is smaller than 0.2, the jet is dropped. In case of multiple jets fulfilling this criteria are found, only the jet closest (in ΔR) is dropped.
5. Any electron subsequently found within ΔR of 0.4 of a jet is removed.
6. A jet with less than three tracks associated is removed when found within $\Delta R < 0.2$ of a muon.
7. A jet with less than three associated tracks which has a muon inner-detector track matched to it, is removed.
8. If the distance between a jet and a muon candidate is $\Delta R < 0.4$, the muon is removed.

CHAPTER 6

Signal and background modelling

Often in high energy physics, measurements can be carried out only with the help of simulations of signal and background processes. Many analyses rely on a comparison of simulated events and the experimentally observed data. Monte Carlo simulations are frequently used to estimate predictions of various physics models, including the SM. The MC simulations include: PDFs, the hard scattering process, parton shower and hadronisation including decays of unstable particles, and simulation of the ATLAS detector response and event reconstruction. However, the full simulation of nucleon-nucleon interaction is very computationally expensive and for some of the estimates of the modelling uncertainties, the fast simulation AtlFast-II [196, 197] - which utilises parametrisations of the hadronic showers in the electromagnetic and hadronic calorimeters to speed up the simulation is used. The following chapters describe the simulated signal and background MC samples used in the analysis. Section 6.3 provides a description of the data-driven method used to estimate the contribution of events that come from misreconstructed electrons or muons, or events with non-prompt electrons or muons identified as prompt leptons.

To account for additional pp interactions from the same or close-by bunch crossings, a set of minimum-bias interactions generated with Pythia 8 [198–200] and the *MSTW2008LO* PDF set [36] is superimposed to the hard scattering events. Furthermore, the MC simulated events are reweighted to match the pile-up levels observed in the data. Additionally, scale factors introduced in Chapter 5 are applied to all simulated events. All MC samples are processed with the same reconstruction software as the data samples. The MC samples are split into three production campaigns, *mc16a*, *mc16d* and *mc16e*, with the mc16a campaign simulated with pile-up conditions representing those of LHC during data taking in 2015 and 2016[1], while the mc16d campaign corresponds to 2017 data taking period and mc16e campaign corresponds to 2018 data taking conditions. The pile-up conditions could be corrected even from a single campaign, however, due to the differences in the pile-up profile between individual years, these corrections would be large thus effectively increasing the MC statistical uncertainty of the simulated samples. The events in the campaigns are produced from a statistically independent set and thus can be combined to yield the total prediction corresponding to 2015, 2016, 2017 and 2018 data taking.

---

[1] Pile-up conditions in 2015 and 2016 are not identical, the mc16a samples are split into events corresponding to 2015 and 2016 data taking. The ratio of events in each year is equal to the ratio of collected luminosities between 2015 and 2016.

6.1. Signal Monte Carlo samples

The nominal signal $t\bar{t}$ MC sample is generated using Powheg-Box-v2 [201–203] which is based on NLO QCD matrix element calculations. The heavy flavour decays are modelled using the *EvtGen* program [204]. The matrix element (ME) generator is interfaced with Pythia 8, version 8.230, that simulates parton shower (PS), hadronisation, fragmentation and the underlying event. The ME calculation uses the *NNPDF3.0NLO* PDF set [205] with a top-quark mass of 172.5 GeV. The h_{damp} parameter that controls the cross-section of the emission of the first gluon is set to 1.5 times the top-quark mass. The *A14* [206] tune together with the *NNPDF2.3LO* PDF set [205] is applied for Pythia 8 showering. The events are normalised to the NNLO cross-section including the resummation of soft gluon emissions at NNLL accuracy [67–71] using the Top++2.0 [72] program. The resulting cross-section for the $t\bar{t}$ process at $\sqrt{s} = 13$ TeV is $\sigma_{t\bar{t}} = 831.76$ pb with a corresponding theoretical uncertainty from missing higher order corrections of around 3 %.

To estimate the impact of the chosen modelling technique in the nominal sample, different $t\bar{t}$ samples have been compared. Powheg-Box-v2 with h_{damp} equal to 1.5 times the top-quark mass $m_t = 172.5$ GeV and with *NNPDF3.0NLO* PDF set interfaced with *Herwig 7* [207, 208] with *MMHT2014* tune [209] is used to compare the effect of different parton shower models. To estimate the effect of different matching to the parton shower, the nominal sample is compared to the aMC@NLO [210] ME generator interfaced with Pythia 8 with *A14* tune and *NNPDF2.3LO* PDF set. The Powheg-Box-v2 generator with h_{damp} parameter equal to 3 times the top-quark mass is used for the estimation of the initial state radiation (ISR) modelling uncertainty. A detailed description of the modelling uncertainties is presented in Section 9.2.

All $t\bar{t}$ MC samples used in the analysis are simulated with NLO precision (and normalised to the NNLO+NNLL cross-section) in the production but only with LO+LL precision in the decay vertex. Furthermore, an approximation of the finite width and interference effects are assumed in the modelling. This approximation could have an impact on the measurement of the top-quark decay width as some of the effects are ignored. This impact will be further discussed in Chapter 10. Dedicated MC sample with full NLO precision in the decay with full non-resonant and interference effects, referred to as $b\bar{b}4\ell$, exists for the dilepton channel [211], however it is not available for the lepton+jets channel. The $b\bar{b}4\ell$ generator, based on the Powheg-Box-Res [212] framework generates the $pp \rightarrow \ell^+\nu_\ell\ell'^-\bar{\nu}_{\ell'}b\bar{b}$ process. The generator is interfaced with Pythia 8 using the resonance aware Powheg method [212]. This sample includes full NLO accuracy in the $t\bar{t}$ production and decay, consistent NLO+PS treatment of the top-quark resonances, quantum corrections to top-quark propagators and off-shell decay chains of the top quark, exact spin correlation at NLO and interference between NLO radiation from top-quark production and decay. It also includes a unified treatment of $t\bar{t}$ and Wt single top processes with NLO interferences and an improved modelling of b quark kinematics, as b-quark mass effects are taken into account. Although the $b\bar{b}4\ell$ samples exist on truth level, no sample is available with the ATLAS detector simulation. Thus the $b\bar{b}4\ell$ sample can only be used at truth level studies and cannot replace the nominal samples that are processed with the ATLAS detector simulation.

For the lepton+jets channel analysis, the signal samples contain $t\bar{t}$ decays with at least one charged lepton, so called *non-allhad* channel. Dedicated samples with exactly two leptons from the hard-scattering in the final states are available and are used for the dilepton selection to increase the number of effective events in the MC.

6.2. Background Monte Carlo samples

6.2.1. Single top quark

Single top quark processes are split into s-channel, t-channel and Wt-channel contributions, each process having two dedicated samples where top and anti-top quarks are generated, respectively. All three processes are generated using the Powheg-Box-v2 ME generators interfaced with the Pythia 8 using the *A14* tune. Similarly to the $t\bar{t}$ samples, the heavy flavour decays are modelled using the *EvtGen* program [204]. The PDF set used is *NNPDF2.3LO*. An overlap between $t\bar{t}$ and single top quark Wt final state is removed using the diagram removal technique [213]. The samples are normalised to the approximate NNLO precision [82, 83].

6.2.2. V+jets

Events with Z or W bosons in association with additional jets are simulated with the Sherpa 2.2.1 generator [214], the simulation includes both the simulation of the hard scattering and the hadronisation. The NNPDF3.0 PDF set is used with the dedicated tune provided by the Sherpa authors. The samples are normalised to the NNLO cross-section [215, 216].

6.2.3. Diboson

Diboson ($WW/WZ/ZZ$) samples are generated using Sherpa 2.2.2 with the dedicated tune from the Sherpa authors. The PDF set is *NNPDF3.0NNLO*. The samples are normalised to the NLO QCD theoretical cross-sections [217].

6.2.4. Associated production of $t\bar{t}$ and a vector boson

The associated production of $t\bar{t}$ with a Z or a W boson ($t\bar{t}V$) is simulated using the MadGraph5_aMC@NLO generator interfaced to Pythia 8. The PDF set is *NNPDF3.0NLO* for the ME. The *A14* tune is applied to parton shower generator with *NNPDF2.3LO* PDF set. The events are normalised to a NLO QCD+EW cross-section calculation [218].

6.2.5. Associated production of $t\bar{t}$ and the Higgs boson

The events with associated production of $t\bar{t}$ and a Higgs boson ($t\bar{t}H$) are generated using MadGraph5_aMC@NLO with the *NNPDF3.0* PDF set. The events are showered with Pythia 8 with the *A14* tune. The mass of the Higgs boson is set to $m_H = 125$ GeV.

Table 6.1 summarises basis MC generator setting for the SM processes simulated in the analysis.

6.3. Multijet background and non-prompt leptons

Events where jets or photons are reconstructed as electrons can pass the analysis selection. These *fake* electrons can occur in multijet events and thus this background is sometimes called *multijet background*. Estimation of the fake leptons is difficult as the probability of a singular jet or photon faking an electron is very small but the cross-section of multijet background is very high and thus a very large number of simulated events would be required. Furthermore, electrons and muons that originate from semileptonic decays of hadrons can pass the charged lepton identification and isolation criteria for prompt leptons. Simulation of these contributions

Sample	Generator	ME PDF	Shower	Normalisation	Cross section [pb]
$t\bar{t}$	POWHEG +`EvtGen`	NNPDF3.0	PYTHIA 8	NNLO+NNLL	831.76
Single top (Wt)	POWHEG +`EvtGen`	NNPDF3.0	PYTHIA 8	(app.)NLO	71.7
Single top (t)	POWHEG +`EvtGen`	NNPDF3.0	PYTHIA 8	(app.)NLO	70.43
Single top (s)	POWHEG +`EvtGen`	NNPDF3.0	PYTHIA 8	(app.)NLO	3.35
W+jets	SHERPA 2.2.1	NNPDF3.0		NNLO	20080.0
Z+jets	SHERPA 2.2.1	NNPDF3.0		NNLO	2107.0
Diboson	SHERPA 2.2.2	NNPDF3.0		NLO	176.0
$t\bar{t}Z$	MADGRAPH5_aMC@NLO	NNPDF3.0	PYTHIA 8	NLO	0.88
$t\bar{t}W$	MADGRAPH5_aMC@NLO	NNPDF3.0	PYTHIA 8	NLO	0.60
$t\bar{t}H$	MADGRAPH5_aMC@NLO	NNPDF3.0	PYTHIA 8	NLO	0.51

Table 6.1.: A summary of basic MC generator settings used to simulate various SM processes.

is difficult, and thus if the contribution of these processes is expected to be large the background has to be estimated using a data-driven technique.

The *Matrix Method* [219] is used to estimate the contribution of the multijet background in the lepton+jets channel. Two separate selections on charged leptons are applied: *tight* and *loose* selection, leading to two different datasets for both electrons and muons. The difference between the selection is defined by applying *gradient* isolation criteria for *tight* leptons, while for *loose* leptons, no requirement on the isolation is imposed, see Sections 5.1 and 5.2. The total number of events passing the *loose* (N^{loose}) and *tight* (N^{tight}) selection reads

$$\begin{aligned} N^{\text{loose}} &= N^{\text{loose}}_{\text{real}} + N^{\text{loose}}_{\text{fake}}\,, \\ N^{\text{tight}} &= N^{\text{tight}}_{\text{real}} + N^{\text{tight}}_{\text{fake}}\,, \end{aligned} \tag{6.1}$$

where $N^{\text{loose(tight)}}_{\text{real}}$ denotes the total number of events passing the *loose*(*tight*) criteria that consist of real prompt leptons, and similarly for $N^{\text{loose(tight)}}_{\text{fake}}$. Since every event passing the *tight* selection must also pass the *loose* selection, selection efficiencies for real and fake leptons can be defined as

$$\begin{aligned} \epsilon_{\text{real}} &= \frac{N^{\text{tight}}_{\text{real}}}{N^{\text{loose}}_{\text{real}}}\,, \\ \epsilon_{\text{fake}} &= \frac{N^{\text{tight}}_{\text{fake}}}{N^{\text{loose}}_{\text{fake}}}\,. \end{aligned} \tag{6.2}$$

Thus the interesting value, the number of fake leptons passing the tight selection, can be calculated combining Equation (6.1) and (6.2)

$$N^{\text{tight}}_{\text{fake}} = \frac{\epsilon_{\text{fake}}}{\epsilon_{\text{real}} - \epsilon_{\text{fake}}} \left(\epsilon_{\text{real}} N^{\text{loose}} - N^{\text{tight}} \right)\,. \tag{6.3}$$

Technically, the estimation is implemented by applying per-event weights, w, to the data events passing the *loose* selection

$$w = \frac{\epsilon_{\text{fake}}}{\epsilon_{\text{real}} - \epsilon_{\text{fake}}} \left(\epsilon_{\text{real}} - f \right)\,, \tag{6.4}$$

where f is equal to 1 if the (*loose*) lepton passes the *tight* criteria and 0 otherwise.

The real lepton efficiencies are estimated in measurements described in Section 5.1 for electrons, and in Section 5.2 for muons. The fake lepton efficiencies are measured in fake enriched regions of exactly one lepton and at least one jet. To further increase the probability of the lepton to be a fake lepton, the selected events are required to have $E_{\mathrm{T}}^{\mathrm{miss}} < 20$ GeV and low transverse mass of the W boson, $m_{\mathrm{T}}^{W} < 60$ GeV, where

$$m_{\mathrm{T}}^{W} \equiv \sqrt{E_{\mathrm{T}}^{\mathrm{miss}} p_{\mathrm{T}} \left(1 - \cos\left(\Delta\phi\right)\right)}, \tag{6.5}$$

to decrease the chance that a neutrino is present in the event. The real and fake efficiencies are parametrised as a function of differential distributions of various parameters. This analysis utilises the following parametrisation of the efficiencies: the distribution of the leading (highest in p_{T}) jet p_{T} and the distribution of ΔR between the lepton and the closest reconstructed jet are used for muons while for electrons distributions of lepton p_{T} and $\Delta\phi$ between the lepton and the missing transverse momentum are exploited.

The multijet background in the dilepton channel is not estimated via the *Matrix Method* as the contribution in this channel is expected to be small and conservative uncertainties on the estimation are applied as will be discussed in Section 9.3. The processes with the highest contribution to non-prompt lepton in the dilepton channel are W+jets, $t\bar{t}$ single lepton channel and single top processes with only one genuine charged lepton in the final state. In the dilepton channel, the multijet background contribution is estimated from the MC simulation by splitting events into two categories: events with real prompt leptons and events with fake or non-prompt leptons using the MC truth information. All the SM processes where the real lepton contribution is expected are processed in this way, furthermore, processes where no real lepton can pass the selection but other kinematic properties are similar, are also considered.

CHAPTER 7

Event selection

The measurement of the top-quark decay width uses data recorded by the ATLAS detector at a centre-of-mass energy of 13 TeV in proton-proton collisions in years 2015, 2016, 2017 and 2018. Section 7.1 describes the used dataset and the corresponding data taking conditions. In the following, the signature of the $t\bar{t}$ decay in events with at least one electron or one muon selection of $t\bar{t}$ events is split into two orthogonal channels: lepton+jets and dilepton channels. Section 7.2 summarises basic selection criteria that are identical for both the lepton+jets and the dilepton channels, optimised to select events that are rich in $t\bar{t}$ events and to suppress non-$t\bar{t}$ events. Individual selections in the lepton+jets and the dilepton channels are presented in Section 7.3 and Section 7.4, respectively.

7.1. Dataset

The dataset is split into four separate subsets, each corresponding to a different year of data taking. Each subset consists of a number of individual runs, representing time periods of stable beams of the LHC. Each run contains many luminosity blocks (LBs), where each LB corresponds to one minute of data taking. Not all events recorded by the ATLAS detector are used in the analysis, only events passing certain quality criteria are selected. Data quality criteria require all detector subsystems to be in the fully operational status. The "good" LBs are stored in a *good run list* (GRL) that is available for each year separately.

The LHC conditions that affect the instantaneous luminosity and the pile-up values varied between and within each year of the data collection period are illustrated in Figure 7.1 and Figure 7.2. The pile-up conditions change significantly between years 2015, where the average number of interactions, $\langle\mu\rangle$, peaked at around 13.4, and 2017 $\langle\mu\rangle$ was 37.8 with some runs reaching up to $\langle\mu\rangle = 80$. The total luminosity corresponding to the GRL in each year is summarised in Table 7.1. The luminosity is measured with techniques described in Section 4.2.7.

7.2. Preselection

Events passing either of the two considered channels, lepton+jets or dilepton channel, need to pass the basic selection criteria summarised in this chapter. Firstly, events need to fire one of

Year	Integrated luminosity in GRL
2015	3.2 fb^{-1}
2016	33 fb^{-1}
2017	44 fb^{-1}
2018	60 fb^{-1}
Combined	140 fb^{-1}

Table 7.1.: Total integrated luminosity for each year of data taking. The values correspond to LBs listed in the GRL. The combined luminosity from years 2015, 2016, 2017 and 2018 is shown.

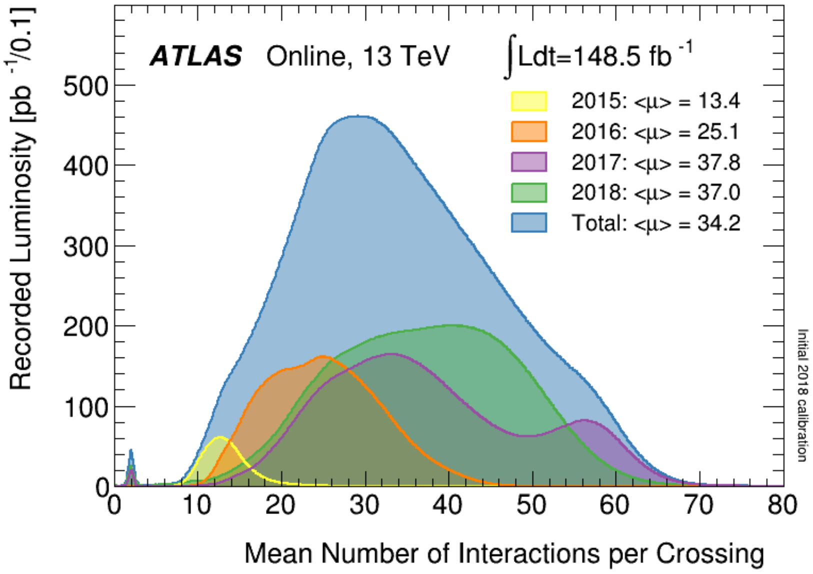

Figure 7.1.: Distribution of the mean number of interactions per bunch-crossing between years 2015, 2016, 2017, and 2018 in pp data collisions at $\sqrt{s} = 13$ TeV. The figure is taken from [157].

the single-lepton triggers for electrons or muons. For electrons (muons) three (two) different trigger chains are used with different lepton p_{T} requirements. For 2015 data taking the electron trigger chains are: *HLT_e24_lhmedium_L1EM20VH*, *HLT_e60_lhmedium* and *HLT_e120_lhloose*. Their thresholds correspond to 24 GeV, 60 GeV and 120 GeV, respectively. Muon trigger chains are: *HLT_mu20_iloose_L1MU15* and *HLT_mu50* with 20 GeV and 50 GeV thresholds. The lower p_{T} triggers require tighter isolation criteria to reduce the high rate of events while the higher p_{T} triggers impose only looser isolation. In order to operate in > 99 % trigger efficiency region, both electrons and muons are required to have $p_{\mathrm{T}} > 25$ GeV for the 2015 data taking period. Due to increased instantaneous luminosity and pile-up, trigger chains for 2016, 2017 and 2018 data taking have been updated with increased thresholds. The electron trigger chains for 2016, 2017 and 2018 are *HLT_e26_lhtight_nod0_ivarloose*, *HLT_e60_lhmedium_nod0* and *HLT_e140_lhloose_nod0*. The muon trigger chains for 2016, 2017 and 2018 are *HLT_mu26_ivarmedium* and *HLT_mu50*. The increased thresholds of trigger chains require that electrons and muons in 2016, 2017 and 2018 data taking periods are required to have $p_{\mathrm{T}} > 27$ GeV. Furthermore, in the offline selection, the selected lepton (in case of dilepton events one of the selected leptons) needs to match the lepton that fired the trigger for the event to be selected. The same trigger requirements are also imposed on the simulated MC events. Both the simulated events and the observed data events are processed using the ROOT [220] framework based on C++ code.

Additionally, events are required to have at least one primary vertex reconstructed with at least two tracks with $p_{\mathrm{T}} > 400$ MeV matched to this vertex. All objects need to pass the object definition criteria summarised in Chapter 5. Events containing fake jets from non-collision background or cosmic events or events containing fake signal in the calorimeter are removed using techniques described in Section 5.3. The overlap removal procedure outlined in Section 5.6 is employed and if at least one of the jets fails these cleaning criteria the whole event is rejected.

7.3. Lepton+jets selection

Following the signature of the $t\bar{t}$ signal in the lepton+jets decay channel, the events are expected to have four jets out of which two originate from b-quark, one electron or muon, and one neutrino. Consequently, the selected events are required to have exactly one reconstructed electron or muon

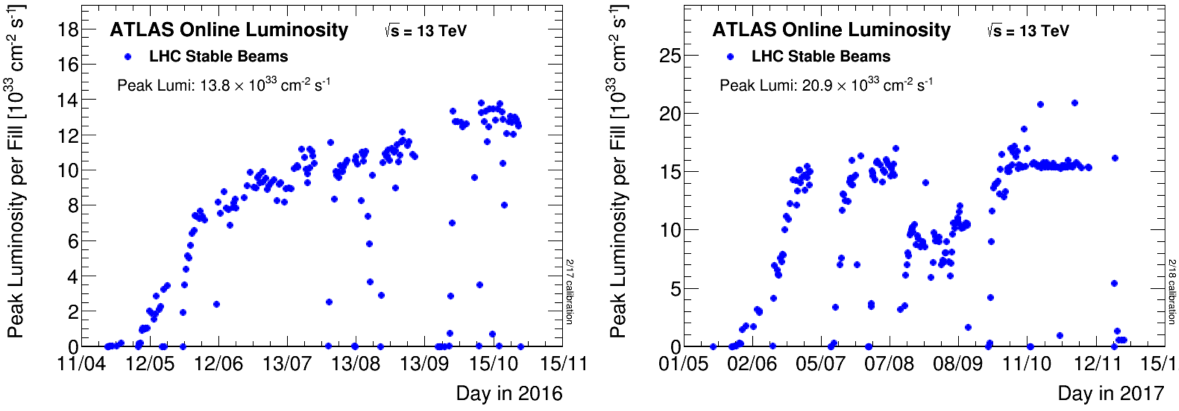

(a)

(b)

Figure 7.2.: The maximum luminosity per beam crossing during $\sqrt{s} = 13$ TeV pp collisions for each fill in 2016 **(a)** and in 2017 **(b)**. The figure is taken from [157].

with $p_{\mathrm{T}} > 25$ GeV for 2015 data taking and $p_{\mathrm{T}} > 27$ GeV for 2016, 2017 and 2018 data taking. Furthermore, events are required to have at least four reconstructed jets with $p_{\mathrm{T}} > 25$ GeV, with at least two of the reconstructed jets being b-tagged with 60 % efficiency working point of the MV2c10 tagger, introduced in Section 5.5. The high-purity and low-efficiency b-tagging working point has been chosen to significantly suppress non-$t\bar{t}$ background, especially the W+jets background. Additionally, requirements on $E_{\mathrm{T}}^{\mathrm{miss}}$ and m_{T}^{W} are imposed. Events are required to have $E_{\mathrm{T}}^{\mathrm{miss}} > 30$ GeV and $m_{\mathrm{T}}^{W} > 30$ GeV for the electron+jets channel and $E_{\mathrm{T}}^{\mathrm{miss}} + m_{\mathrm{T}}^{W} > 60$ GeV for the muon+jets channel. These cuts are chosen to suppress the multijet background, including non-prompt leptons and fake leptons (misidentified leptons).

Moreover, a selection on the reconstruction BDT output, that will be discussed in Section 8.1, is applied requiring the events to have a BDT score > 0.7. This requirement further reduces non-$t\bar{t}$ backgrounds and improves the total precision of the measurement.

After the event selection, the events are split into two orthogonal regions according to the charged lepton flavour: into electron+jets and muon+jets events. Table 7.2 shows expected event yields without additional requirement on the BDT discriminant as well as selection with the BDT score > 0.7 in the lepton+jets channel. This table demonstrates that in the analysis region the dominant background originates from single top quark production. Other significant backgrounds are due to the multijet background processes and associated production of W or Z bosons and jets. Smaller backgrounds are diboson production ($ZZ/ZW/WW$), associated production of $t\bar{t}$ with a vector boson (Z or W) and associated production of $t\bar{t}$ with a Higgs boson. The table illustrates that requiring the BDT output score to be larger than 0.7 significantly reduces non-$t\bar{t}$ contributions. All signal and background yields in Table 7.2 are obtained from the samples described in Chapter 6.

Control histograms that include signal and all considered background contributions illustrate the comparison between the prediction and the observed data in Figures 7.3–7.6. The events are split by the lepton flavours into electron+jets and muon+jets events. The events are required to have the BDT score > 0.7. It can be seen that good agreement between the prediction and the observed data is given.

One of the motivations for the selection on the BDT discriminant is visible in Figure 7.7 which clearly demonstrates that the backgrounds populate mostly bins with low BDT score, further motivations for this selection will be discussed in Section 8.1. The control histograms for events without the requirement of the BDT score are presented in Appendix A.

7.4. Dilepton selection

Events in the dilepton channel are required to have exactly two leptons (electrons or muons) of opposite electric charge with $p_{\mathrm{T}} > 25$ GeV and $p_{\mathrm{T}} > 27$ GeV for the 2015 and 2016–2018 data taking periods, respectively. These selections create three sub channels in the dilepton final state: ee (exactly 2 electrons with sufficient p_{T}), $\mu\mu$ (exactly 2 muons with sufficient p_{T}) and $e\mu$ (exactly 1 electron and 1 muon with sufficient p_{T}). Events are also required to have at least two jets with $p_{\mathrm{T}} > 25$ GeV, at least two of which have to be b-tagged by the MV2c10 tagger at 60 % efficiency working point. This selection is used in order to suppress non-$t\bar{t}$ backgrounds. A window of the lepton invariant mass, $m_{\ell\ell}$, at 80 GeV $< m_{\ell\ell} <$ 100 GeV is excluded in the ee and $\mu\mu$ channels to suppress the Z+jets background which resonates at the Z boson mass of around 91 GeV. Furthermore, a requirement of $E_{\mathrm{T}}^{\mathrm{miss}} > 60$ GeV is used in ee and $\mu\mu$ channels to account for the two neutrinos produced in the dilepton decay of $t\bar{t}$ and to suppress Z+jets contribution. The Z boson mass window and the $E_{\mathrm{T}}^{\mathrm{miss}}$ requirements are not imposed on the

Event Yields - No additional BDT selection

	Electron+jets	Muon+jets
$t\bar{t}$	950000±50000	1100000±50000
Single top	43000±6000	49000±7000
W+jets	19000±9000	25000±12000
Z+jets	5900±2800	5600±2700
Diboson	1200±600	1500±700
$t\bar{t}V$	3270±330	3600±400
$t\bar{t}H$	1980±200	2150±220
Multijet	32000±16000	17000±9000
Total prediction	1060000±50000	1200000±50000
Data	1062486	1233103

Event Yields - BDT score $>$ 0.7

	Electron+jets	Muon+jets
$t\bar{t}$	336000±17000	396000±20000
Single top	6200±900	7400±1100
W+jets	1000±500	1300±600
Z+jets	520±250	370±180
Diboson	90±40	100±50
$t\bar{t}V$	740±70	830±80
$t\bar{t}H$	460±50	500±50
Multijet	5000±2500	4000±2000
Total prediction	350000±17000	411000±20000
Data	347934	411162

Table 7.2.: Event yields obtained after the event selection in the electron (left column) and muon (right column) decay channels. Event yields before the additional requirement on the BDT output score are presented in the upper table, event yields after additional selection of the BDT score, BDT $>$ 0.7 are shown in the table on the bottom. Uncertainties on the signal and background yields originate from the uncertainty on normalisation of signal and backgrounds. Observed data yields agree with the prediction.

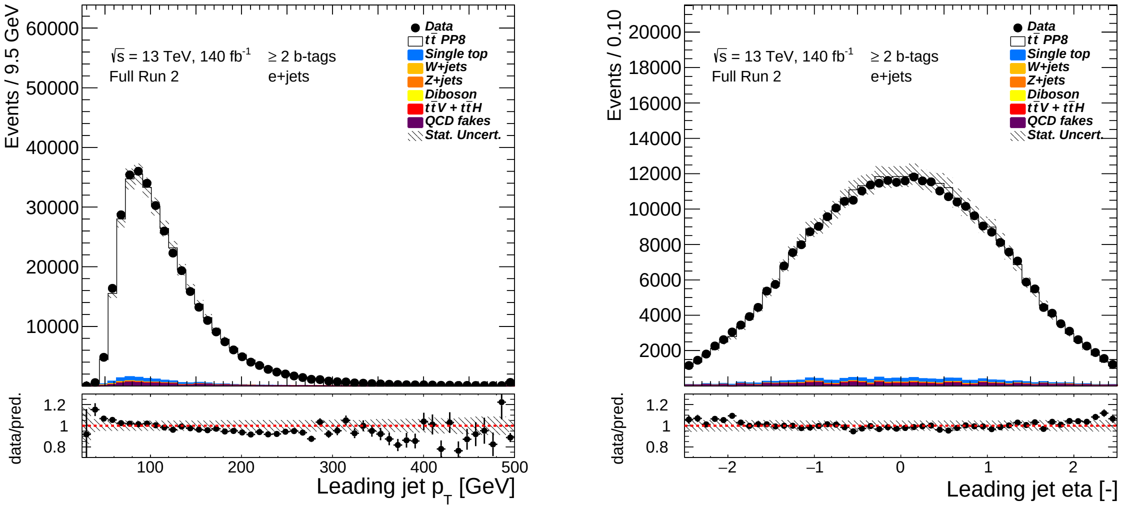

(a) Leading (highest p_{T}) jet p_{T}.

(b) Leading (highest p_{T}) jet η.

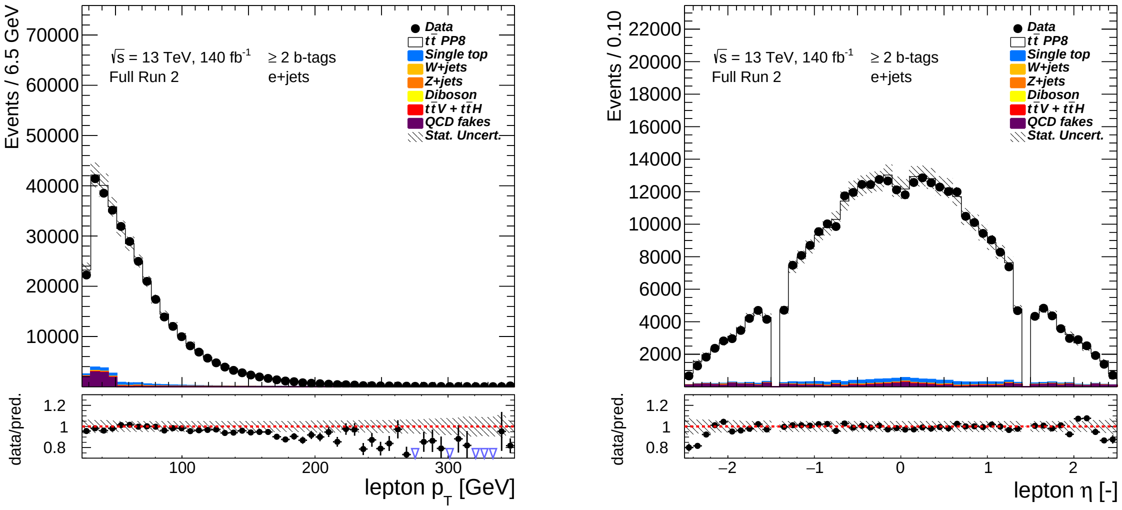

(c) Electron p_{T}.

(d) Electron η.

Figure 7.3.: Data/MC comparison for basic kinematic properties in the electron+jets decay channel. Selection on the BDT output score > 0.7 is applied. The hashed bands show the uncertainty originating from finite statistics in the MC samples as well as normalisation uncertainty on each signal/background source. The first and last bin contain underflow and overflow events, respectively. Symbol [−] denotes dimensionless quantities.

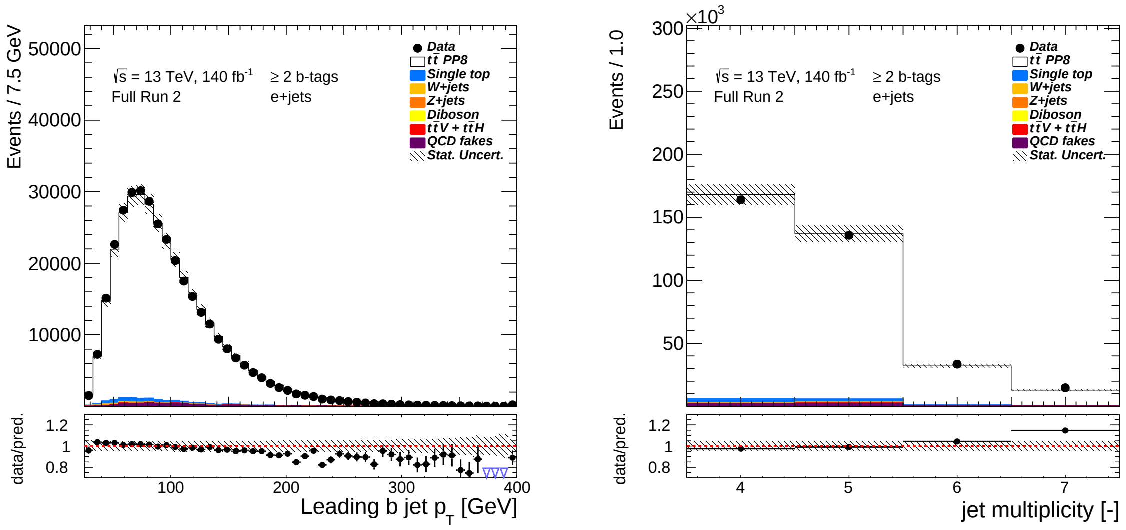

(a) Leading b-tagged jet p_{T}.

(b) Number of jets.

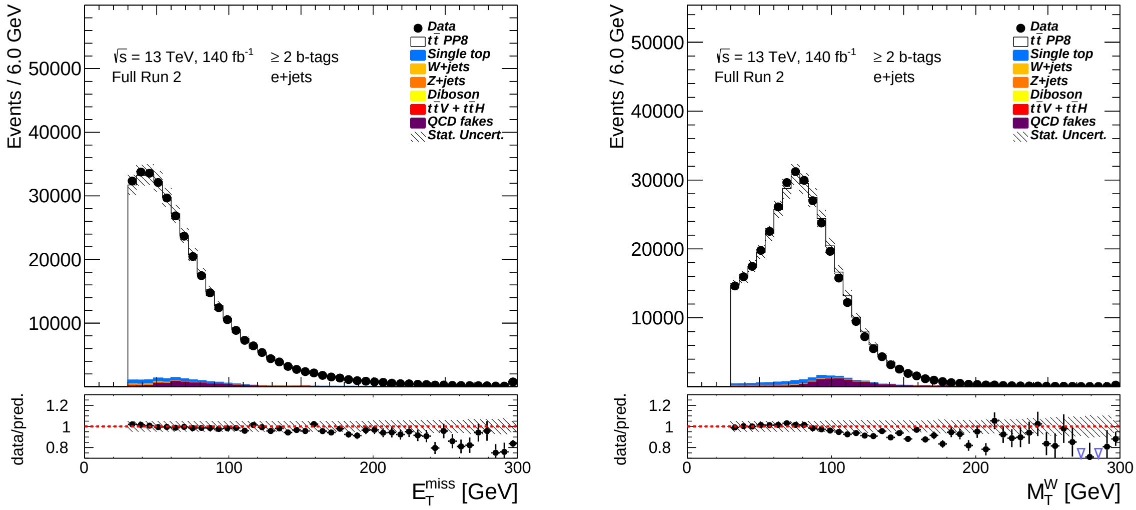

(c) Missing transverse momentum.

(d) Transverse mass of the W boson.

Figure 7.4.: Data/MC comparison for basic kinematic properties in the electron+jets decay channel. Selection on the BDT output score > 0.7 is applied. The hashed bands show the uncertainty originating from finite statistics in the MC samples as well as normalisation uncertainty on each signal/background source. The first and last bin contain underflow and overflow events, respectively.

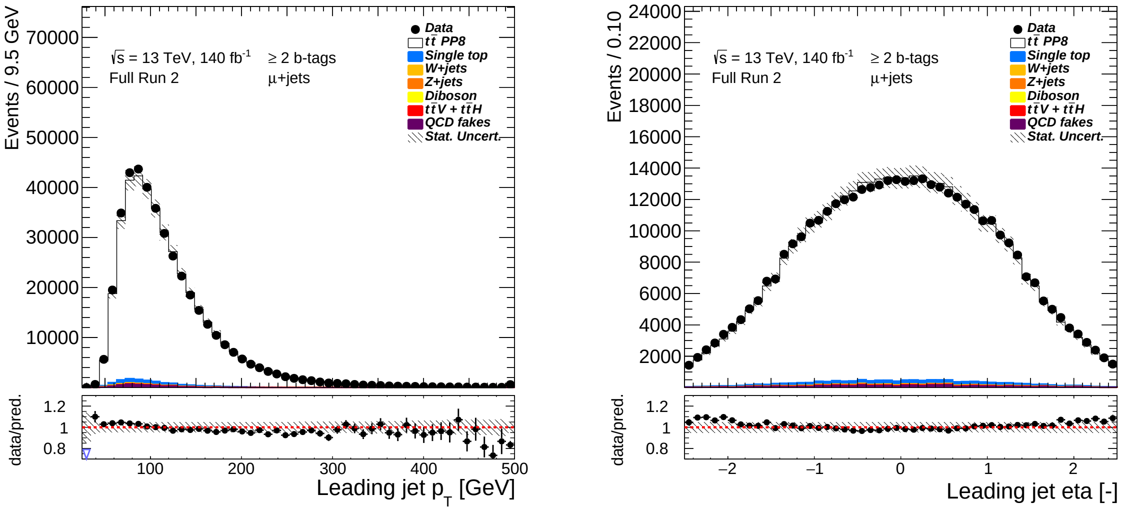

(a) Leading (highest p_{T}) jet p_{T}.

(b) Leading (highest p_{T}) jet η.

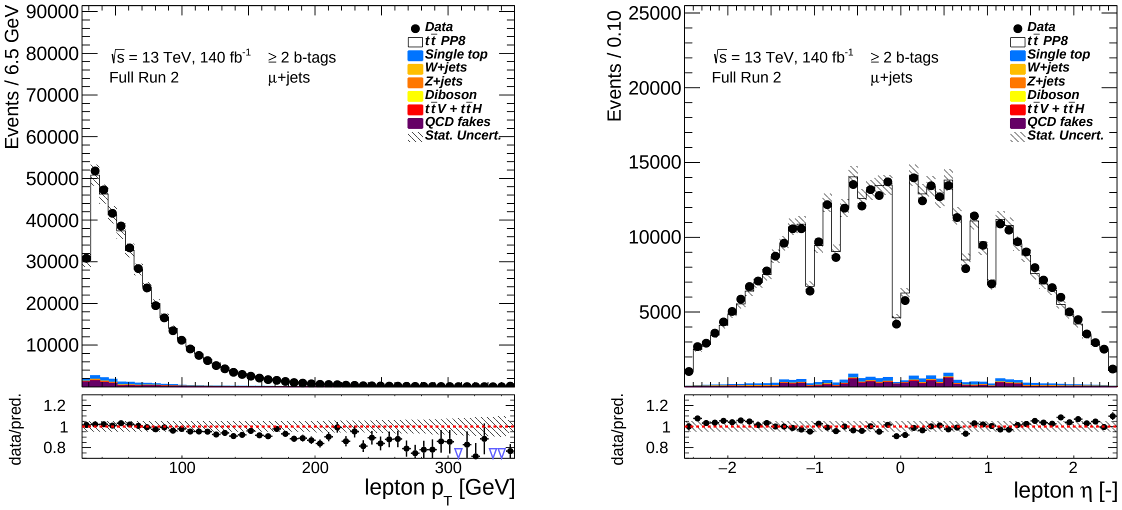

(c) Muon p_{T}.

(d) Muon η.

Figure 7.5.: Data/MC comparison for basic kinematic properties in the muon+jets decay channel. Selection on the BDT output score > 0.7 is applied. The hashed bands show the uncertainty originating from finite statistics in the MC samples as well as normalisation uncertainty on each signal/background source. The first and last bin contain underflow and overflow events, respectively.

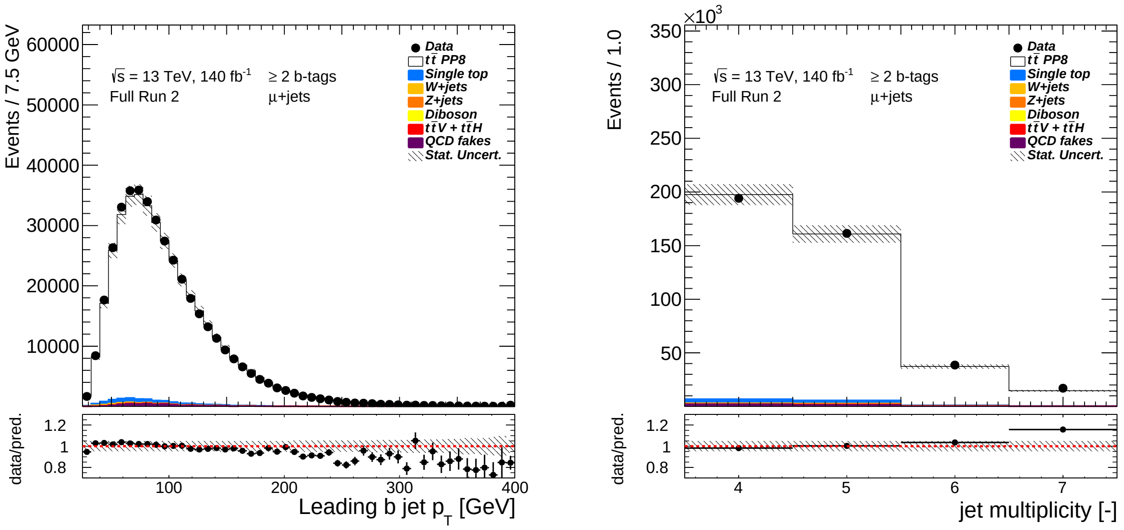

(a) Leading b-tagged jet p_{T}.

(b) Number of jets.

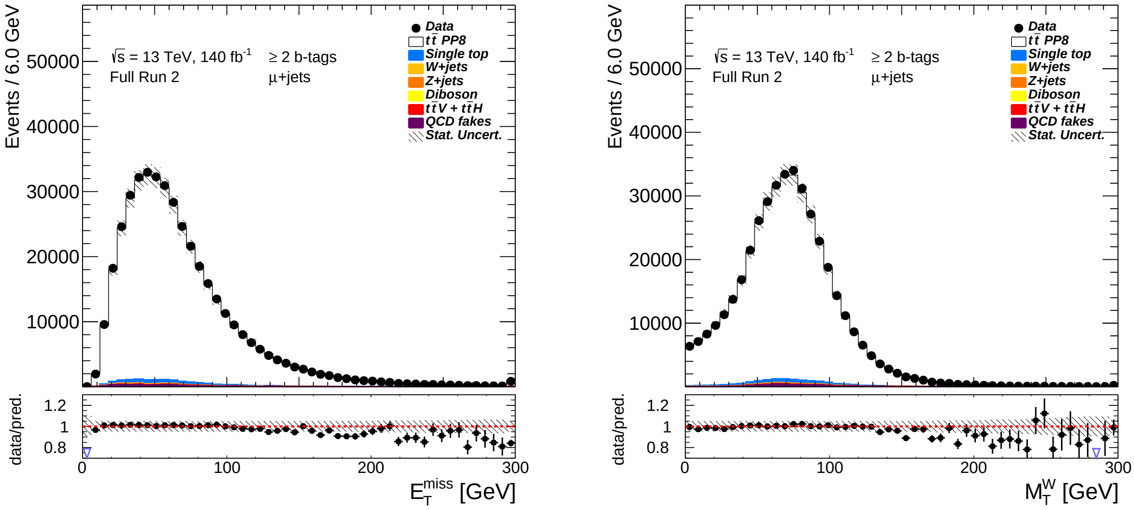

(c) Missing transverse momentum.

(d) Transverse mass of the W boson.

Figure 7.6.: Data/MC comparison for basic kinematic properties in the muon+jets decay channel. Selection on the BDT output score > 0.7 is applied. The hashed bands show the uncertainty originating from finite statistics in the MC samples as well as normalisation uncertainty on each signal/background source. The first and last bin contain underflow and overflow events, respectively.

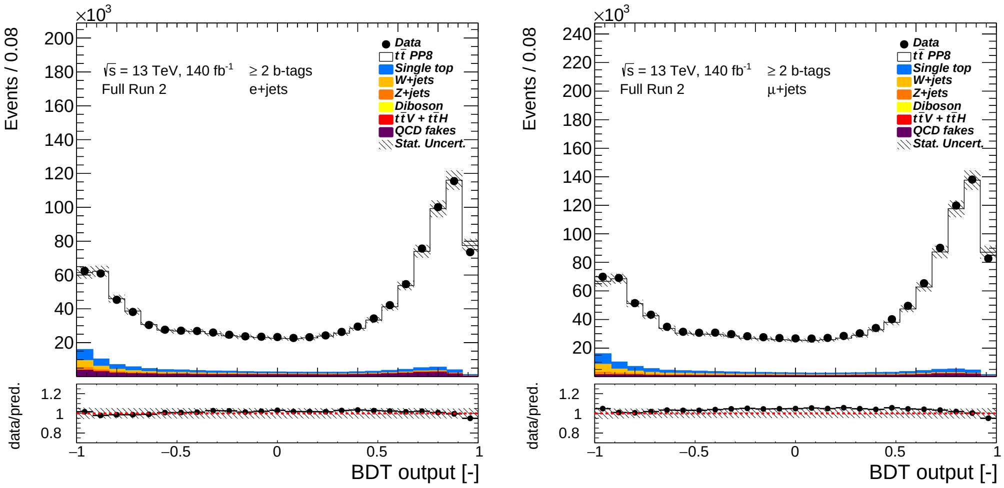

Figure 7.7.: Data/MC comparison of the reconstruction BDT discriminant in lepton+jets decay channel. Non-$t\bar{t}$ events populate mostly low region of the BDT discriminant. Applying a cut on the BDT score will increase the purity of the $t\bar{t}$ signal. The hashed bands show the uncertainty originating from finite statistics in the MC samples as well as normalisation uncertainty on each signal/background source.

$e\mu$ channel because in the SM, the Z boson decays into leptons of the same flavour[1]. All three channels are also required to have $m_{\ell\ell} > 15$ GeV to reduce events where leptons originate from meson decays or photon conversions.

The expected number of events, as well as observed data, obtained after applying the dilepton selection are shown in Table 7.3. Yields for the $t\bar{t}$ MC events and all the considered backgrounds are further divided into three subchannels according to lepton flavours: ee, $\mu\mu$ and $e\mu$ channels. It can be seen from the table that the purity of the $t\bar{t}$ selection is very high, the backgrounds constitute only a small portion of the passed events.

Control histograms in Figures 7.8 and 7.9 show the agreement of the observed data and the MC prediction for the $e\mu$ channel. It can be seen that the data agree well with the MC prediction within the uncertainties. Additional control histograms for ee and $\mu\mu$ channels are summarised in Appendix A.

---

[1] One electron and one muon can originate from the Z boson decay when the Z boson decays into a pair of tau leptons and they subsequently decay into one electron and one muon. However, this is heavily suppressed by low branching fraction of both tau leptons decaying leptonically.

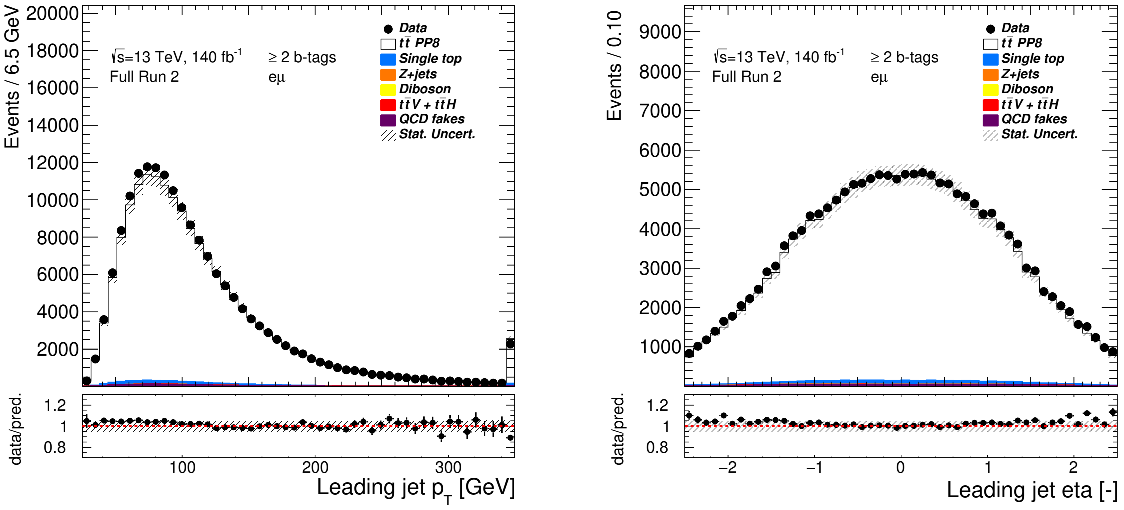

(a) Leading (highest p_{T}) jet p_{T}.

(b) Leading (highest p_{T}) jet η.

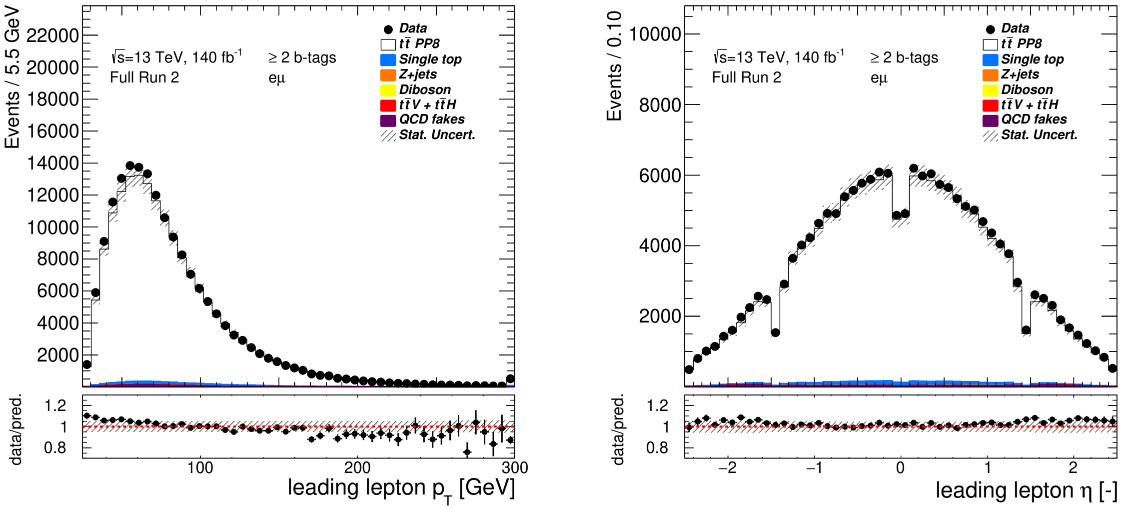

(c) Leading lepton p_{T}.

(d) Leading lepton η.

Figure 7.8.: Data/MC comparison for basic kinematic properties in the dilepton decay channel with electron-muon events. MC statistical uncertainty together with the normalisation uncertainty is shown by the hashed fields. The first and the last bins correspond to the underflow and the overflow events respectively.

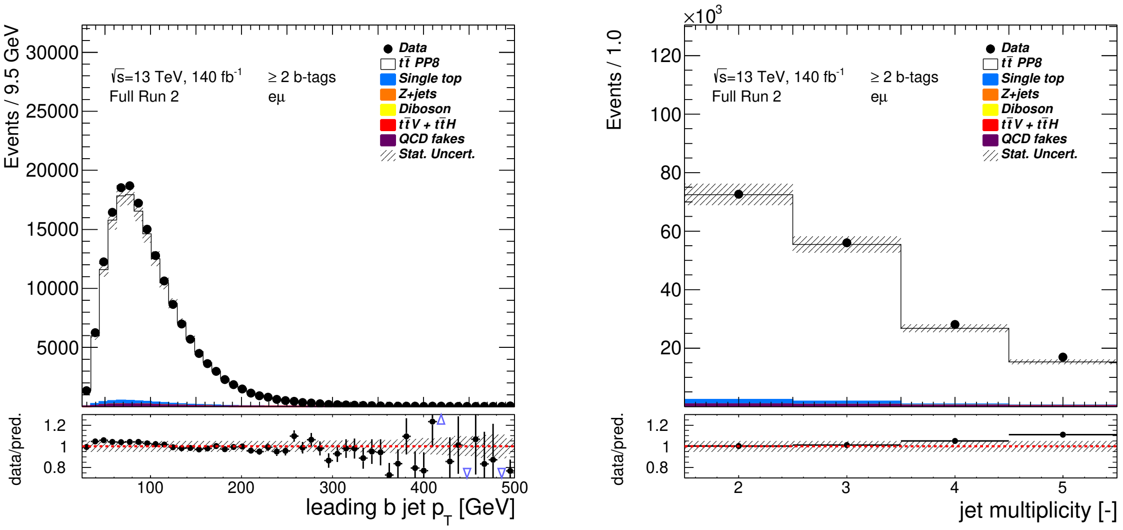

(a) Leading b-tagged jet p_{T}.

(b) Number of jets.

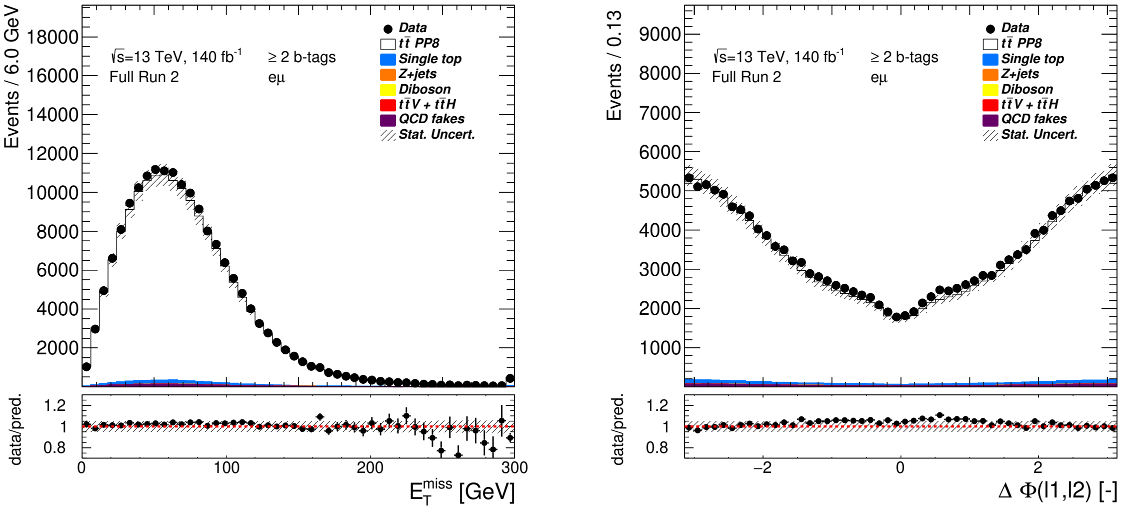

(c) Missing transverse momentum.

(d) $\Delta\phi$ between the electron and the muon.

Figure 7.9.: Data/MC comparison for basic kinematic properties in the dilepton decay channel with electron-muon events. MC statistical uncertainty together with the normalisation uncertainty is shown by the hashed fields. The first and the last bins correspond to the underflow and the overflow events respectively.

	Event Yields		
	ee	$\mu\mu$	$e\mu$
$t\bar{t}$	35000±1800	42700±2100	164000±8000
Single top	780± 120	960± 140	3400± 500
Z+jets	140± 70	190± 90	48± 23
Diboson	$< 1\pm < 1$	6± 3	$< 1\pm < 1$
$t\bar{t}V$	56± 6	66± 7	204± 20
$t\bar{t}H$	$< 1\pm < 1$	$< 1\pm < 1$	$3\pm < 1$
Multijet	800± 400	24± 12	1900± 900
Total prediction	36800±1800	43900±2100	170000±8000
Data	37659	45294	173687

Table 7.3.: Event yields obtained after the event selection in the ee, $\mu\mu$ and $e\mu$ decay channels. Uncertainties on the signal and background yields originate from the uncertainty on normalisation of signal and backgrounds. The measured number of events is compatible with the prediction to within the uncertainty.

CHAPTER 8

Event reconstruction

As top quarks decay before hadronisation, their four-momenta can only be reconstructed from their decay products: quarks and the (charged) lepton(s). Hence, the identification of jets corresponding to the partons from the $t\bar{t}$ decay is a crucial step of the direct top-quark decay width measurement as it allows to construct observables that are sensitive to the decay width. However, no prior information can be utilised to unambiguously identify the jet-to-parton assignment, thus some reconstruction algorithm has to be used. The $t\bar{t}$ reconstruction poses different problems in the lepton+jets and in the dilepton decay channels. In the lepton+jets channel, the difficulty of the reconstruction arises from the number of possible jet-to-parton assignments, referred to as a combinatorial background. On the other hand, in the dilepton channel, the combinatorial background is significantly reduced due to the smaller average number of jets in events compared to the lepton+jets case. However, presence of two prompt neutrinos means the system of equations that can be used to calculate the neutrino four-momenta using the W masses is under-constrained. The $t\bar{t}$ reconstruction used in this analysis is described in Section 8.1, while the reconstruction technique used in the dilepton channel is described in Section 8.2.

8.1. Lepton+jets reconstruction

Due to the large combinatorial background, the lepton+jets reconstruction technique chosen in the analysis makes use of a multivariate BDT technique implemented in the ROOT package TMVA [221]. In a decision tree, ordered decision nodes are used to identify the event as a signal or a background event. Each node decides if the event is signal-like or background-like based on a single variable. Multiple decision nodes form a decision tree. Training is a process to identify the optimal order of the decision nodes as well as the optimal selection threshold in each node. During the training process, a selection is applied to the variable with the highest separation in the first node and then repeating the process for each subsample creating two new nodes during each step. This process is terminated when a certain node reaches maximum separation power, the minimum number of events is used or the maximum number of subsequent decisions (5) is made. Boosting of the decision trees means that signal events that end in the background category are assigned a larger weight than events correctly categorised and a new training with adjusted weights is performed. To combine the information from multiple trees, a likelihood discriminant is built from all trees based on how often the signal event is correctly flagged as signal event in the decision trees.

Different kinematic variables obtained from the reconstructed objects four-momenta as well as additional variables utilising the b-tagging information are provided to the BDT algorithm to identify the correct jet-to-parton assignment. Permutations of jet-to-parton assignment are evaluated by the BDT and the permutation with the highest BDT discriminant value is considered to be the correct permutation and is used further in the analysis. Since the number of possible permutations increases as $\sim n!$ for n jets in the event, only permutations with four, and possibly five jets, are evaluated in the BDT. If more than five jets are present in an event, only two jets with the highest b-tagging value and then three jets ordered by their p_{T} are considered in the permutations. This results in $4!/2 = 12$ permutations for four-jet events[1] and $5!/2 = 60$ permutations for events with five or more jets where no b-tagging information is used to reduce the number of permutations.

8.1.1. BDT input variables

A list of the variables for the BDT used for the reconstruction in the lepton+jets channel is shown in Table 8.1. The variables are ordered by their separation power, defined as

$$\text{Separation} = \frac{1}{2}\frac{\sum_i (s_i - b_i)^2}{\sum_i (s_i + b_i)}, \tag{8.1}$$

where s_i represents the number of signal events in bin i, and b_i represents the number of background events in bin i. Separation illustrates the power to discriminate signal from backgrounds for given distributions for signal and background normalised to the same expected number of events. One of the input variables is KLFitter $\ln \mathcal{L}$ which is the logarithm of the likelihood provided by the KLFitter reconstruction algorithm [222].

The KLFitter is a likelihood-based event reconstruction tool that utilises the *Bayesian Analysis Toolkit* (BAT) [223]. The KLFitter has been used in many measurements, e.g. see Refs. [224–226], as a reconstruction technique to identify the correct jet-to-parton pairing. The KLFitter lepton+jets likelihood has the following form

$$\begin{aligned}\mathcal{L} = {} & \mathrm{BW}(m_{q_1q_2q_3}|m_t,\Gamma_t)\cdot \mathrm{BW}(m_{q_1q_2}|m_W,\Gamma_W)\cdot \mathrm{BW}(m_{q_4\ell\nu}|m_t,\Gamma_t)\cdot \mathrm{BW}(m_{\ell\nu}|m_W,\Gamma_W)\cdot \\ & \cdot \prod_{i=1}^{4} W_{\mathrm{jet}}(E_i^{\mathrm{meas}}|E_i)\cdot W_\ell(E_\ell^{\mathrm{meas}}|E_\ell)\cdot W_{\mathrm{miss}}(E_x^{\mathrm{miss}}|p_x^\nu)\cdot W_{\mathrm{miss}}(E_y^{\mathrm{miss}}|p_y^\nu)\,,\end{aligned} \tag{8.2}$$

where $W_x(E_x^{\mathrm{meas}}|E_x)$ are transfer functions that map the distribution of the "true" parton energies E_x to the reconstructed energies of the corresponding objects x, E_x^{meas}, this allows energies of the objects to float within the detector resolution. More details about transfer functions can be found in Appendix B. The indices q_1-q_4 refer to the four quarks from the $t\bar{t}$ decay in the lepton+jets channel. The $\mathrm{BW}(m_{ij(k)}|m_P,\Gamma_P)$ terms represent Breit-Wigner functions with $m_P(\Gamma_P)$ denoting the mass (decay width) of the decaying particle. The x and y components of the neutrino (ν) momentum, p_x^ν and p_y^ν together with parton energies are free parameters of the likelihood maximisation. The z component of the neutrino momentum is a free parameter of the fit with the initial starting point set to the constraint from the W boson mass, $m_W^2 = (p_\nu + p_\ell)^2$.

---

[1] Permutations where only two jets from the W boson decay are swapped, are removed from the consideration.

The mass of the W boson is fixed in the likelihood to a value of $m_W = 80.4$ GeV, its decay width is fixed to $\Gamma_W = 2.1$ GeV. The mass of the top quarks is free floating in the fit, but is kept equal between the two top quarks, assuming equal mass constraint. The top quark-decay width is fixed to the LO SM prediction corresponding to the fitted top-quark mass.

The pure kinematic reconstruction of the KLFitter can be extended using the b-tagging information to improve the overall KLFitter reconstruction. The resulting separation variable is called *Event Probability*, p_i, and for a given permutation i it reads

$$p_i \equiv \frac{\mathcal{L}_i \prod_j \Delta p_{i,j}}{\sum_k \mathcal{L}_k \prod_j \Delta p_{k,j}}, \tag{8.3}$$

where $\mathcal{L}_i$ is the likelihood value for permutation i as defined in Equation (8.2). $\Delta p_{k,j}$ refers to additional weights from the b-tagging information. It is calculated from b-tagging efficiency, ϵ and the rejection factor, r, for each jet. For b-jets it reads

$$\Delta p_{k,j} = \begin{cases} \epsilon & b\text{-jet was } b\text{-tagged,} \\ (1-\epsilon) & b\text{-jet was not } b\text{-tagged,} \end{cases} \tag{8.4}$$

and for light-flavour jets

$$\Delta p_{k,j} = \begin{cases} 1/r & \text{light-flavour-jet was } b\text{-tagged,} \\ (1-1/r) & \text{light-flavour-jet was not } b\text{-tagged.} \end{cases} \tag{8.5}$$

The values of ϵ and r depend on the jet p_T and jet η as described in Section 5.5.

In order to reconstruct the mass of the semileptonically decaying top quark, which is one of the input variables for the BDT, the four-momentum of the neutrino has to be reconstructed. The only experimentally accessible properties of the neutrino are the magnitude of the neutrino three-momentum in the transverse direction, represented by $E_\mathrm{T}^\mathrm{miss}$ and its ϕ angle. Assuming zero mass of the neutrino this still leaves one parameter of the neutrino four-momentum to be determined. The missing parameter is calculated using the W mass constraint, $m_W^2 = (p_\nu + p_\ell)^2$. This leads to a quadratic equation for the z component of the neutrino three-momentum. If the solutions are real, the solution which leads to a reconstructed mass of the semileptonically top quark closer to 172.5 GeV is considered to be the correct one. If the quadratic equation for p_z^ν has only imaginary solutions, x and y components of the neutrino three-momentum are varied until a real solution for p_z^ν is found.

Data to prediction comparison, separation power and correlation between the BDT input variables are summarised in Appendix C.

8.1.2. BDT training

For the training purpose, in each simulated $t\bar{t}$ event the considered permutations of jet-to-parton assignments (permutations of four or five jets, if available) are split into two categories: “signal” and “background”. Permutations where each quark from the $t\bar{t}$ decay has exactly one jet within $\Delta R = 0.3$ fall into the signal category as these permutations have all four jets from the $t\bar{t}$ decay correctly assigned to their corresponding partons. All the other permutations fall into the background category as at least one of the quarks from the $t\bar{t}$ decay does not have a

Variable	**Definition**	**Separation**
m_t^{had}	Reconstructed mass of the hadronically decaying top quark	26.5 %
b-tag light jet 1	Represents if the first light jet from the W boson decay is b-tagged	18.9 %
KLFitter $\ln \mathcal{L}$	Logarithm of the likelihood from the KLFitter algorithm	17.9 %
b-tag blep	Represents if the assumed b-jet from the top quark that decays semileptonically is b-tagged	16.8 %
b-tag bhad	Represents if the assumed b-jet from the top quark that decays hadronically is b-tagged	16.0 %
m_W	Reconstructed mass of the hadronically decaying W boson	15.5 %
m_t^{lep}	Reconstructed mass of the semileptonically decaying top quark	13.2 %
$\Delta R(j_b, \ell)$	ΔR between lepton and assumed b-jet from the semileptonically decaying top quark	6.9 %
$\Delta R(j_{l1}, j_{l2})$	ΔR between two light jets from the hadronically decaying W boson	3.7 %
$p_{\text{T}}^{\ell b}$	p_{T} of the lepton and assumed b-jet from the semileptonically decaying top quark	1.5 %
N jets	Number of jets in an event	1.2 %
η_t	Absolute value of η of the reconstructed hadronically decaying top quark	0.7 %
$\Delta R(j_b^{\text{had}}, j_b^{\text{lep}})$	ΔR between two b-jets from the $t\bar{t}$ decay	0.6 %

Table 8.1.: Input variables used for the BDT in the lepton+jets channel. Variables are ordered by their separation power (third column). The N jets variable has no separation power on itself but the correlations with the other variables bring additional information, the non-zero separation in the table comes from the definition of signal and background in the training process.

properly assigned reconstructed jet. For some events no considered permutation has all four jets from the $t\bar{t}$ decay assigned correctly, consequently, all permutations are flagged as background for the event. The BDT is trained to discriminate signal permutations from the background permutations. Due to the combinatorial nature of the permutations, the number of permutations flagged as background is more than one order of magnitude higher than the number of signal permutations. However, a significant number of background permutations has properties that make them very easy to distinguish from the signal permutations, e.g. these permutations have reconstructed masses far from the expected masses of decaying particles. Thus, in order to optimise the performance of the BDT, not every permutation from the background category is considered in the training process. Background permutations are split into four orthogonal categories based on the number of correct jet-to-parton assignments (based on the ΔR criterion) into permutations with exactly 0, 1, 2 or 3 jets correctly assigned to their corresponding partons.

From each background category, only the permutation with the highest KLFitter Event Probability is used further in the training process[2]. Taking only the permutation with the highest KLFitter Event Probability for the background category, selects permutations with similar kinematics and b-tagging information as the signal permutation, thus making the separation between signal and background more difficult, in order to improve the overall performance of the training process. Due to limited computational resources, the BDT is trained only on events corresponding to 2015 and 2016 LHC conditions (mc16a campaign) but is applied to all events. Reconstruction efficiencies for events corresponding to 2017 and 2018 LHC conditions (mc16d

---

[2] The KLFitter Event Probability is not identical to the KLFitter likelihood value which is used as one of the input variables for the BDT. The KLFitter Event Probability takes into account b-tagging information while the KLFitter likelihood takes into account purely kinematic properties and no b-tagging information

and mc16e campaign) are within 1 % with respect to the training conditions for all objects and thus no training on mc16d samples is needed.

Electron+jets and muon+jets events are trained together in the training algorithms. 500 decision trees are trained with 20 grid points in each variable used to find the optimal selection for. During the training, the *loss-function*, $L(F, y)$ that describes the deviation from the model response, $F(x)$, and the true value, y, is minimised. The exact form of the loss-function reads

$$L(F, y) = \ln\left(1 + e^{-2F(x)y}\right), \tag{8.6}$$

which corresponds to *GradientBoost* setting in the TMVA [221]. The learning rate, set via the *Shrinkage* parameter, that controls how fast the individual variable selections are changed, is set to 0.3. *BaggingFraction* that controls the *bagging*, a resampling technique where a classifier is repeatedly trained on the resampled training events such that it represents the average of the individual classifiers, is set to 0.6 [221]. Both *Shrinkage* and *BaggingFraction* parameters are employed to minimise *overtraining* of the BDT. A multivariate (MVA) technique is overtrained when the classifier can misidentify some of the statistical fluctuations, due to the finite number of events for signal and background, in the samples as the features that discriminate signal and background. These fluctuations can then be propagated to the final MVA discriminant and thus reduce the performance of the MVA discriminating power. Several different training settings have been tested, e.g. increasing the number of decision trees, increasing number of the grid points, however, no significant improvement of the BDT performance has been observed while the processing time increased significantly.

To verify that the BDT is not overtrained, all available events are randomly split into two halves with one half being used for the training process (train sample) and the other half being used in the evaluation of the BDT (test sample). The *Receiver-operation-characteristic* (ROC) curve that shows background rejection (1 minus background efficiency) as a function of the signal efficiency for the training sample and for the testing sample is presented in Figure 8.1. The *Area Under Curve* (AUC) that represents the BDT performance shows that no overtraining of the BDT is observed as the curves for the training and the testing samples match. The final BDT discriminant is presented in Figure 8.2. The AUC value or the BDT separation cannot be directly translated to the reconstruction efficiency of the $t\bar{t}$ system because the training process does not reflect all combinatorial background present in real data. Furthermore, the classification into signal and background for the reconstruction BDT does not follow standard binary discrimination where one event can be either a signal or a background event. The reconstruction BDT needs to identify one correct permutation out of 12(60) for events with 4(5) jets considered in the permutations.

8.1.3. Performance and comparison

The BDT discriminant is calculated for each considered permutation (permutation of 4 or 5 jets) and the permutation with the highest BDT score is considered to be the correct one. The reconstruction efficiency of the BDT, which is defined as ratio of events with correctly assigned jets to their corresponding partons and the number of events that pass the event selection, is estimated in $t\bar{t}$ events using the MC truth information. In each event, all four partons from the $t\bar{t}$ decay are compared to the assigned reconstructed jet from the BDT algorithm. If the angular distance of the parton and the assigned jet, ΔR is smaller than 0.3, the jet-to-parton assignment is considered to be correct. The matching between partons and jets is unique, one

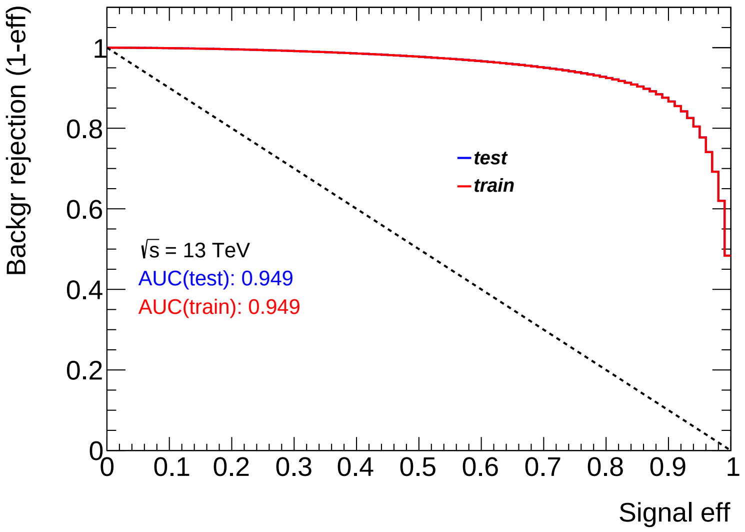

Figure 8.1.: The ROC curve for the reconstruction BDT. Electron+jets and muon+jets events are plotted together. AUC represents the area under curve. The dashed line represents no separation, corresponding to AUC = 0.5. ROC curves for the testing sample (in blue) and for the training sample (in red) are superimposed. The curves for the training and the testing samples match, confirming that no over-training is observed.

reconstructed jet can be assigned only to one parton. Signal $t\bar{t}$ events are split into different categories of events:

1. Events where all four partons from the $t\bar{t}$ decay are assigned correctly.
2. Events where three partons from the hadronically decaying top quark are assigned correctly but the b-quark from the semileptonically decaying top quark is not matched to the corresponding jet.
3. Events where the two partons from the hadronically decaying W boson are assigned correctly, but neither of the b-quarks is matched to their corresponding jets.
4. Events where only the b-quark from the semileptonically decaying top quark is assigned correctly.
5. Events where none of the partons from the $t\bar{t}$ decay is assigned to their corresponding jets.

The BDT reconstruction efficiency is visualised in Figure 8.3 where the BDT score for the best considered permutation is shown. Signal $t\bar{t}$ events are split following the above criteria. The figure illustrates that the higher the BDT discriminant value is, the higher the ratio of correctly assigned jets is. It can also be seen that in events with BDT score < 0 almost no events are reconstructed properly and thus requiring a minimum BDT discriminant value can be used to increase the purity of the reconstruction.

It is natural to compare the reconstruction performance of the BDT with the performance of KLFitter reconstruction as a standalone tool. Only the permutation with the highest BDT score

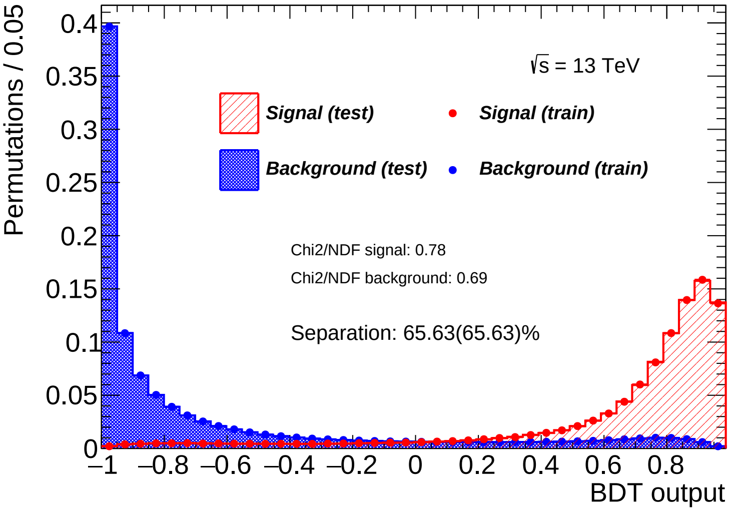

Figure 8.2.: The BDT output discriminant. Electron+jets and muon+jets events are plotted together. The distributions are normalised to unity. BDT discriminants in the signal events (in red) and the background events (in blue) are superimposed. The discriminant is plotted for the testing sample (shaded area) and for the training samples (full dots). The χ^2 divided by number of degrees of freedom (NDF) shows good agreement between the training and the testing samples for both signal and background permutations. Separation power of the BDT discriminant is displayed.

is considered for the BDT reconstruction while the permutation with the highest KLFitter Event Probability is considered in the case of KLFitter reconstruction. Table 8.2 shows a comparison of the reconstruction efficiencies of BDT and KLFitter for the same events and the same considered permutations. The table also shows the percentage of events passing the selection where jets are *present*, meaning that for the given parton there is a unique reconstructed jet within $\Delta R < 0.3$ that passed the selection criteria (but may not be considered in the jet permutations). The ratio of the correctly reconstructed events and the number of *present* events represents the performance of the algorithm with respect to the theoretically ideal reconstruction algorithm. The table shows that the reconstruction when using BDT with KLFitter $\ln \mathcal{L}$, as one of the input variables yields better efficiencies compared to the pure KLFitter reconstruction. The difference between the two algorithms is even more visible in Table 8.3 which shows events with an additional cut on BDT score > 0.7. It can be concluded that the BDT reconstruction yields better $t\bar{t}$ reconstruction and selects events with higher purity than pure KLFitter algorithm and is thus the chosen reconstruction algorithm for this analysis.

Figures 8.4–8.7 illustrate data and prediction agreement for variables that require the BDT reconstruction. Some of the predicted distributions do not agree perfectly with the observed data, especially in top quark η and p_{T} distribution. To take the discrepancy into account, a special systematic uncertainty that compares the nominal distribution with the distribution obtained from reweighting of top quark p_{T} on the truth level is considered in the analysis as will be discussed in Section 9.2. Additional control plots where no selection on the BDT score is applied are summarised in Appendix A.2.

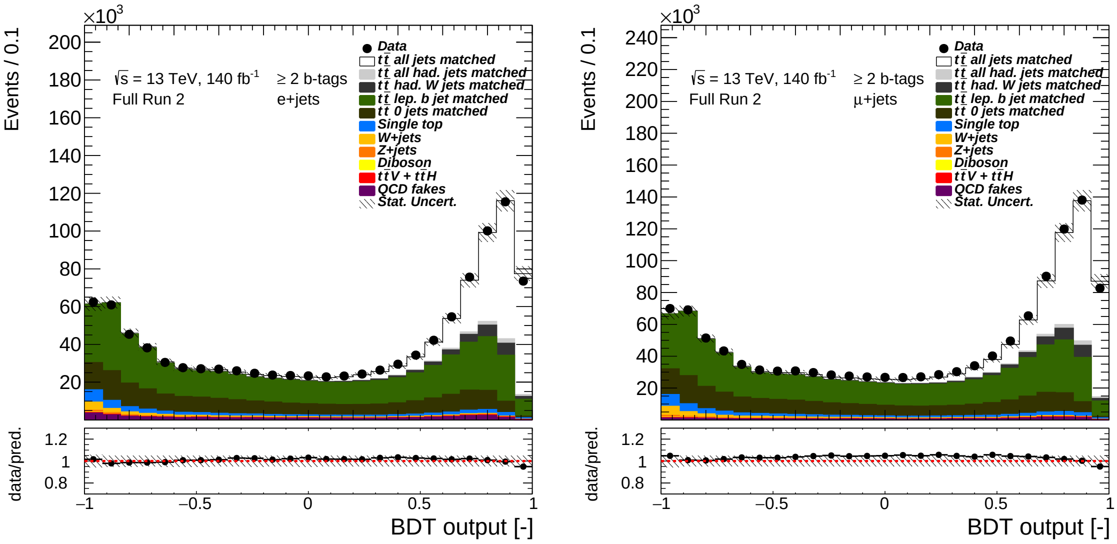

Figure 8.3.: Data/MC agreement of the BDT discriminant for electron+jets (left) and muon+jets (right) events. Signal $t\bar{t}$ events are split into reconstruction categories based on the reconstruction performance of the BDT. Only the permutation with the highest BDT score is shown. The hashed bands show the uncertainty originating from finite number of events in the MC modelling as well as normalisation uncertainty on each signal/background source. The first and last bin contain underflow and overflow events, respectively.

Reco eff. [%]	Lep. b	Had. b	First light jet	Second light jet	Had. W	Had. top	All
Present	96	96	74	74	53	51	49
KLF correct vs. total	57	58	63	58	39	30	28
KLF correct vs. present	59	60	85	79	74	59	57
BDT correct vs. total	75	74	68	58	41	36	35
BDT correct vs. present	79	77	91	79	77	71	71

Table 8.2.: Reconstruction efficiencies of BDT and KLFitter with respect to all events passing basic selection criteria (third and fifth row) and with respect to the events where partons have the corresponding jet *present* (fourth and sixth row). The second row represents the ratio of events with present jets and the total number of events passing the basic selection. The columns represent from left to right: the pairing efficiency for b-jets from semileptonically decaying top quark, the pairing efficiency for b-jets from hadronically decaying top quark, the pairing efficiency for the first non-b-jet from the hadronically decaying W boson, the pairing efficiency for the second non-b-jet from the hadronically decaying W boson, pairing efficiency for both non-b-jets from the hadronically decaying W boson (logical AND), pairing efficiency for all three jets from the hadronically decaying top quark (logical AND) and finally, the pairing efficiency for all four jets from the $t\bar{t}$ decay (logical AND). Highlighted columns (in grey) mark reconstruction efficiencies of objects that are important for the direct measurement of the top-quark decay width. One event can fall into multiple categories. Statistical uncertainties on the efficiencies are below 1 % and are thus negligible.

Reco eff. [%]	Lep. b	Had. b	First light jet	Second light jet	Had. W	Had. top	All
Present	97	97	90	89	81	79	76
BDT correct vs. total	86	85	88	80	73	66	64
BDT correct vs. present	89	87	99	90	91	84	84

Table 8.3.: Reconstruction efficiencies of BDT and KLFitter with respect to all events passing basic selection criteria as well as additional requirement BDT score $>$ 0.7 for the best permutation (third row) and with respect to the events where partons have the corresponding jet *present* (fourth row). The second row represents the ratio of events with present jets and the total number of events passing the basic selection. The columns represent from left to right: the pairing efficiency for b-jets from semileptonically decaying top quark, the pairing efficiency for b-jets from hadronically decaying top quark, the pairing efficiency for the first non-b-jet from the hadronically decaying W boson, the pairing efficiency for the second non-b-jet from the hadronically decaying W boson, pairing efficiency for both non-b-jets from the hadronically decaying W boson (logical AND), pairing efficiency for all three jets from the hadronically decaying top quark (logical AND) and finally, the pairing efficiency for all four jets from the $t\bar{t}$ decay (logical AND). Highlighted columns (in grey) mark reconstruction efficiencies of objects that are important for the direct measurement of the top-quark decay width. One event can fall into multiple categories. Statistical uncertainties on the efficiencies are below 1 % and are thus negligible.

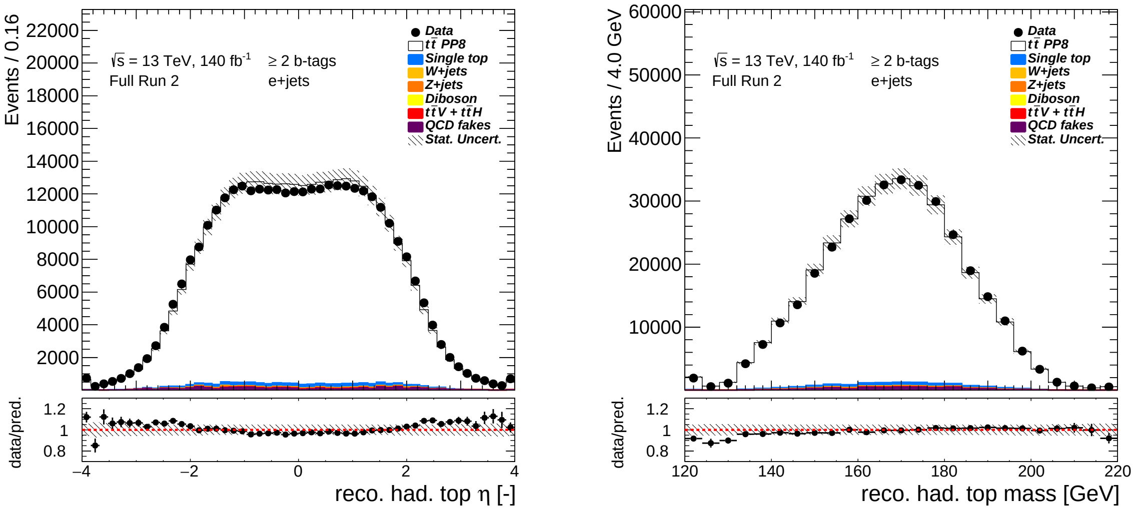

(a) Reconstructed hadronic top-quark η.

(b) Reconstructed hadronic top-quark mass.

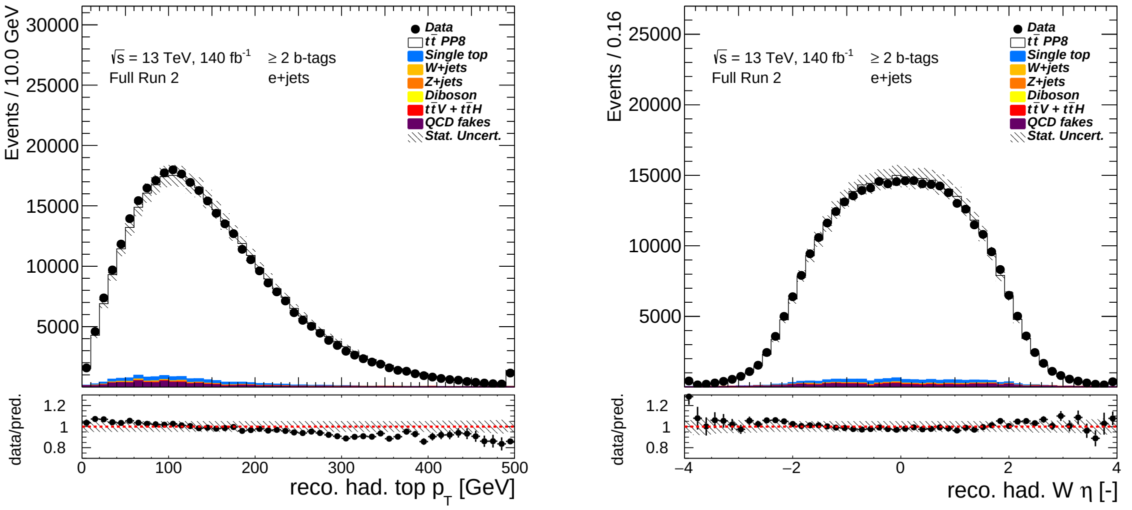

(c) Reconstructed hadronic top-quark p_{T}.

(d) Reconstructed hadronic W boson η.

Figure 8.4.: Control plots for the reconstructed hadronically decaying top quark (top) and hadronically decaying W boson (bottom) in the analysis for electron+jets events. Additional selection on BDT score > 0.7 is applied. Shaded areas show MC statistical uncertainty and normalisation uncertainty. The first and last bin contain underflow and overflow events, respectively.

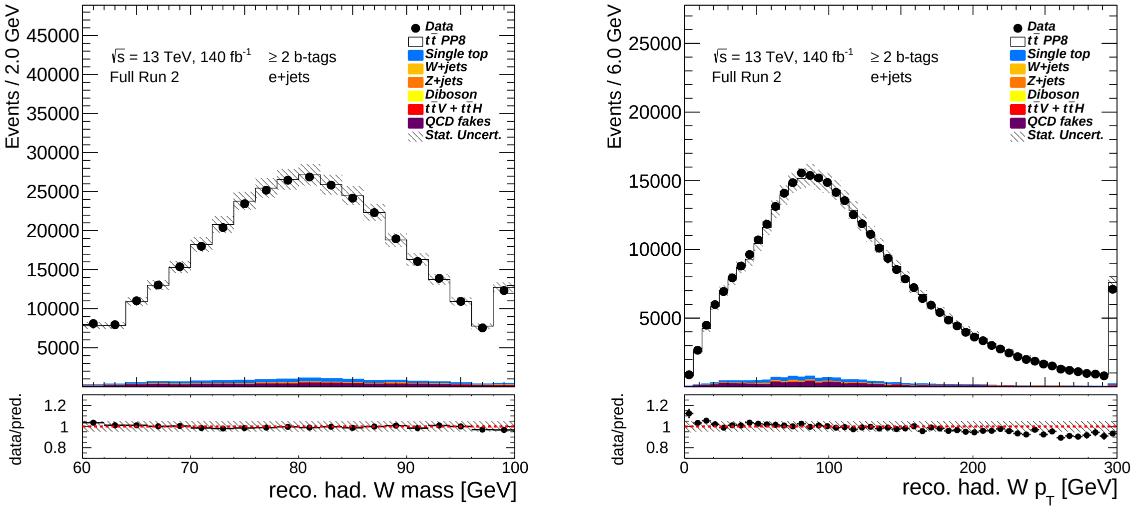

(a) Reconstructed hadronic W boson mass.

(b) Reconstructed hadronic W boson p_{T}.

Figure 8.5.: Control plots for the reconstructed hadronically decaying top quark (top) and hadronically decaying W boson (bottom) in the analysis for electron+jets events. Additional selection on BDT score > 0.7 is applied. Shaded areas show MC statistical uncertainty and normalisation uncertainty. The first and last bin contain underflow and overflow events, respectively.

8.2. Dilepton reconstruction

The reconstruction of the top-quark four momentum is difficult due to the presence of two neutrinos which leave the system of equations, that exploit the W mass constrain to identify the neutrino four momenta, unconstrained. Reconstruction techniques exist that address this problem, e.g. the neutrino weighting technique [227] that is based on integrating neutrino rapidities for a chosen top-quark mass hypothesis. In this technique, the comparison of the vector sum of neutrino momentum solutions at each chosen point of phase space and the observed $E_{\mathrm{T}}^{\mathrm{miss}}$ is exploited to assign a weight that describes the level of agreement. However, no attempt to reconstruct neutrinos is made in the measurement of the top-quark decay width, as $E_{\mathrm{T}}^{\mathrm{miss}}$ resolution is low and suffers from large systematic uncertainties. The invariant mass of the charged lepton (electron or muon) and the corresponding b-jet from the same top quark decay, $m_{\ell b}$, is used as an observable sensitive to the top-quark decay width in the dilepton channel.

Thus the problem of event reconstruction significantly simplifies since only the correct identification of the charged lepton with the corresponding b-jet is required. Two different approaches for the reconstruction in the dilepton channel have been tested. The first approach (referred to as minimum ΔR) uses the angular separation to match jets to their corresponding leptons. Events having two or more b-tagged jets are reconstructed by calculating ΔR between all possible combinations of leptons and b-tagged jets and consequently assigning the first lepton (ordered in p_{T}) to the closest b-tagged jet in ΔR and the second lepton to the closest non-assigned b-tagged jet. Figure 8.8 shows the distribution of the ΔR between charged leptons and their assigned jets for $t\bar{t}$ and background events, where $t\bar{t}$ events are further subdivided into events where none, one and two b-jets were correctly matched. A b-jet is considered correctly matched if its ΔR distance from the corresponding truth b-quark from the $t\bar{t}$ decay is not greater than $\Delta R = 0.3$.

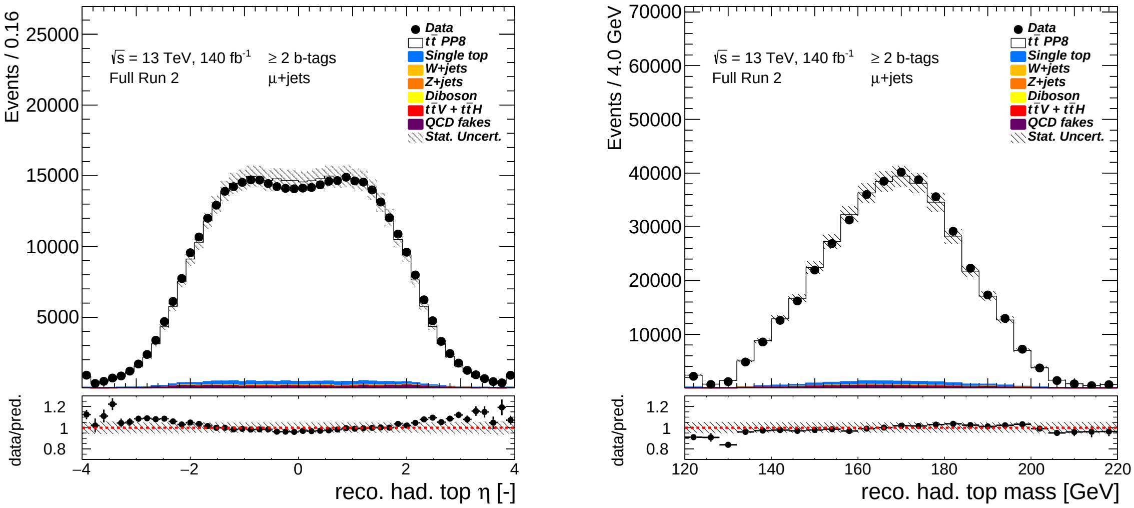

(a) Reconstructed hadronic top-quark η. (b) Reconstructed hadronic top-quark mass.

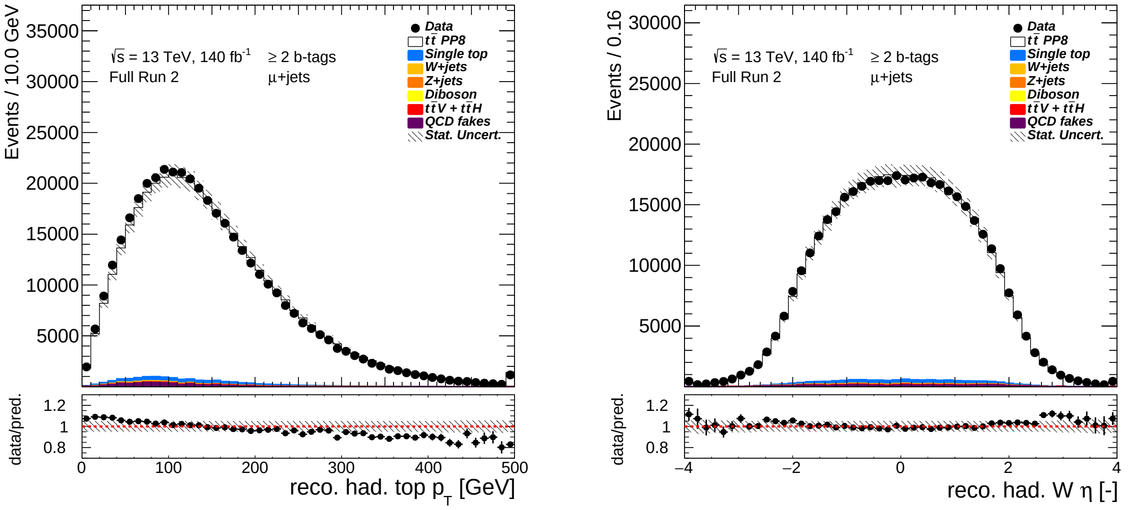

(c) Reconstructed hadronic top-quark p_{T}. (d) Reconstructed hadronic W boson η.

Figure 8.6.: Control plots for the reconstructed hadronically decaying top quark (top) and hadronically decaying W boson (bottom) in the analysis for muon+jets events. Additional selection on BDT score > 0.7 is applied. Shaded areas show MC statistical uncertainty and normalisation uncertainty. The first and last bin contain underflow and overflow events, respectively.

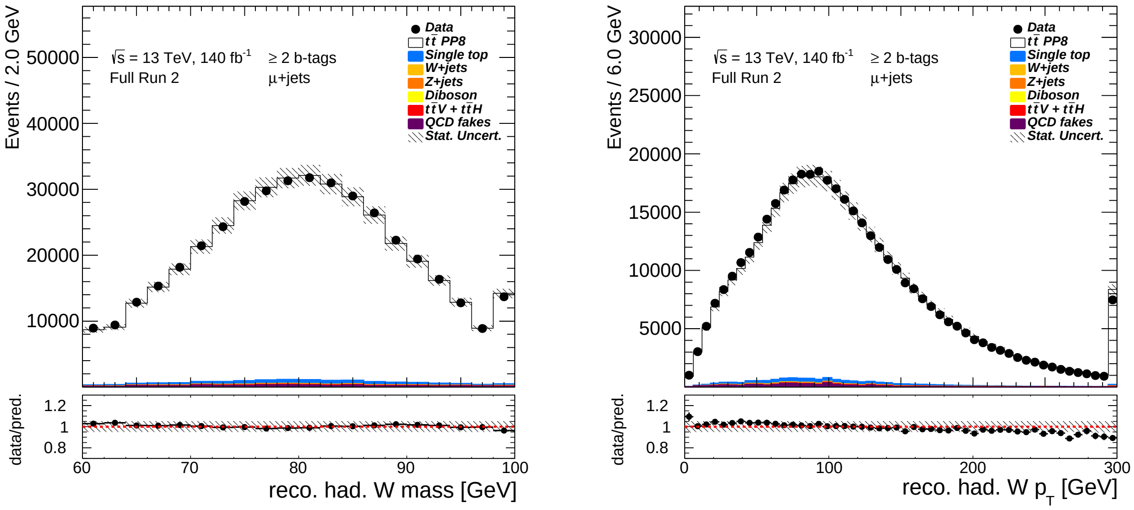

(a) Reconstructed hadronic W boson mass.

(b) Reconstructed hadronic W boson p_{T}.

Figure 8.7.: Control plots for the reconstructed hadronically decaying top quark (top) and hadronically decaying W boson (bottom) in the analysis for muon+jets events. Additional selection on BDT score > 0.7 is applied. Shaded areas show MC statistical uncertainty and normalisation uncertainty. The first and last bin contain underflow and overflow events, respectively.

The second approach (referred to as *minimum* $m_{\ell b}$) performs the pairing by searching for such a combination of the two charged leptons and two jets which minimises the difference in the combined invariant mass of the two ℓb systems. The $m_{\ell b}$ distribution has an upper limit originating from the mass of the top quark. As a consequence, incorrectly matched lepton-to-jet pairs are more likely to have larger invariant mass. This reconstruction technique has been used in the top-quark mass measurement [114].

Although the minimum $m_{\ell b}$ algorithm was found to be a little more efficient than the ΔR pairing, as shown in Table 8.4, it is not used in the analysis since the usage of the same variable for both the reconstruction and the template fit might bias the top-quark decay width measurement and the reconstruction efficiency is similar between the two methods.

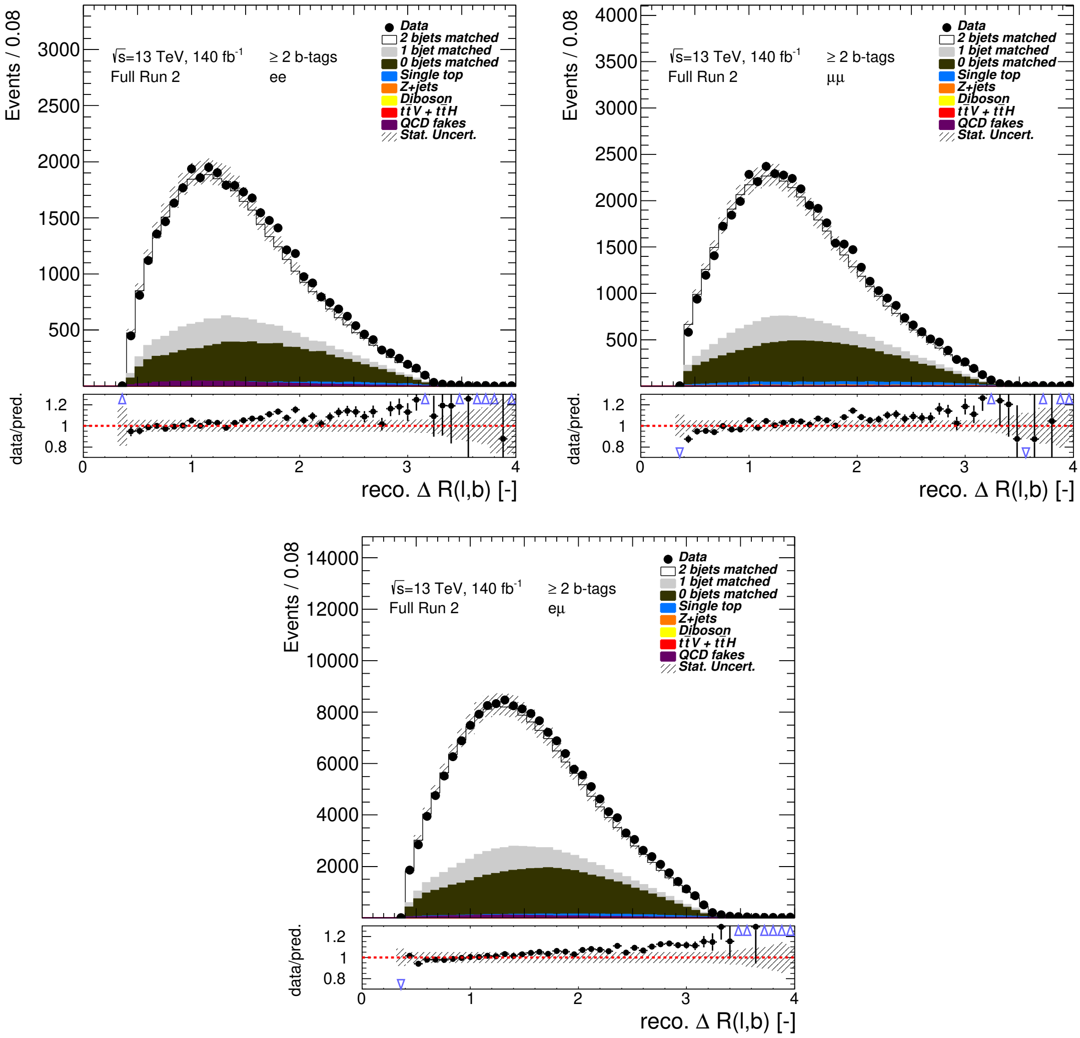

Figure 8.8.: Reconstructed ΔR between the charged leptons and their assigned b-tagged jets. $t\bar{t}$ events are split into three categories based on the number of correctly matched b-tagged jets. Events having exactly two correctly matched b-tagged jets are shown in white colour while grey and green colour represent events with one and none correctly matched b-tagged jets, respectively. Hashed areas represent the statistical uncertainty. Above results were obtained using the minimum ΔR pairing.

Reconstruction method [%]	b from t	b from $\bar{t}$	both b
Minimum ΔR	69	69	63
Minimum $m_{\ell b}$	69	69	66

Table 8.4.: Efficiencies of charged lepton and corresponding b-jet pairing in percentages. The minimum ΔR and the minimum $m_{\ell b}$ reconstruction algorithms are compared in the $e\mu$ channel. The highlighted column (in grey) marks the pairing efficiency that is important for the top-quark decay width measurement. One event can fall into multiple categories. Statistical uncertainties on the efficiencies are below 1 % and are thus negligible. The high efficiency for reconstruction of both b-jets (last column) with respect to the individual b-jet reconstruction efficiencies reflects a high correlation of the reconstruction between the individual b-jets.

CHAPTER 9

Systematic uncertainties

Systematic uncertainties affecting the measurement of the top-quark decay width enter the fit directly via nuisance parameters (NPs) as will be described in Section 10.3. Each source of the systematic uncertainty modifies the nominal distribution by modifying its shape, normalisation or both at the same time. To evaluate the systematics uncertainties on the signal width templates, an assumption is made that each systematic variation has the same absolute effect on all templates. Thus the uncertainty on each width template is calculated from the nominal distribution, corresponding to the SM prediction for the top-quark decay width $\Gamma_t = 1.32$ GeV, and then propagated bin-wise to all the templates.

The systematic uncertainties originating from the uncertainty of the modelling of the experiment are summarised in Section 9.1. The uncertainties originating from the imperfect knowledge of the modelling of the processes together with the uncertainties of the normalisation of the individual background components are described in Section 9.2. The uncertainties related to the finite number of simulated events are summarised in Section 9.3. The systematic distributions are *smoothed* and *pruned*, as described in details in Section 9.4, to improve the numerical stability of the fit.

9.1. Experimental uncertainties

The experimental systematic uncertainties include uncertainties on the modelling of the physics objects: charged leptons, jets, $E_{\mathrm{T}}^{\mathrm{miss}}$, flavour-tagging as well as an uncertainty on the integrated luminosity.

9.1.1. Charged leptons

Two categories of uncertainties are associated with the electrons and muons: the first category includes uncertainties originating from trigger and reconstruction efficiencies and the lepton identification, the second category includes uncertainties arising from lepton momentum resolution and scales. Trigger, reconstruction and identification efficiencies differ between the simulated events and the observed data, scale factors are applied to the simulated events as described in Section 5.1 (electrons) and Section 5.2 (muons). The scale factors are varied within their uncertainties, estimated from the tag-and-probe method using events with Z and W bosons and J/ψ [178, 180], to derive the variations on the observables used in the fit.

The precision of the lepton momentum scale and resolution may differ between the simulated events and the observed data. The simulation is checked with reconstructed distributions of $Z \to \ell^+\ell^-$ and $J/\psi \to \ell^+\ell^-$ masses using methods similar to Refs. [179, 180]. In the case of electrons, also events with $W \to e\nu$ are used. Observed discrepancies between the data and the simulation are corrected by applying recommended corrections tools. For muons, corrections to momentum scale and resolution are applied only to the simulation, while for electrons corrections are applied to both data and simulated events. Uncertainties on momentum scale and resolution of muons originating from the inner detector and the muon spectrometer are considered and varied separately.

9.1.2. Jet energy scale

The JES and its uncertainty are estimated both from the test-beam data, the collision data and the simulation using techniques described in Section 5.3. Data taken at $\sqrt{s} = 13$ TeV are used to calibrate the residual uncertainty on the JES [187]. Events with a vector boson and additional jets are used to calibrate jets in the central region. Dijet events are exploited to calibrate forward jets against the jets in the central region of the detector. Multi-jet events are used to calibrate high p_{T} jets. The measurements are then combined and decorrelated into a set of 29 eigen vectors that depend on jet p_{T} and jet η. The 29 NPs are split into various categories: 16 NPs arise from the in-situ calibration uncertainty, 4 NPs originate from the uncertainty on the pile-up components, 5 NPs comprise the uncertainty of the η intercalibration, 2 NPs arise from the uncertainty on flavour composition of the jets and the uncertainty on the response to different jet flavours, 1 NP originates from the uncertainty of the *punch-through*[1] modelling and, finally, 1 NP describes the uncertainty of the high-p_{T} jets.

The *flavour composition* and *flavour response* JES uncertainties are closely related to the fraction of the gluon-initiated jets and quark-initiated jets. As a result of gluons being colour octet particles, while quarks are colour triplets, the gluon-initiated jets have different properties than the quark-initiated jets. The gluon-initiated jets contain, on average, more constituents, consequently, the gluon-initiated jets leave more tracks in the ID compared to the quark-initiated jets [228]. Furthermore, the gluon-initiated jets tend to have a broader radiation pattern than the quark-initiated jets [229].

In the default configuration of the jet reconstruction software, the most conservative estimate of the fractions of gluon-initiated jets and quark-initiated jets fraction is set to 0.5 ± 0.5 which leads to an overestimation of the flavour composition JES uncertainty, which arises from the uncertainty on the quark and gluon jet fraction. Furthermore, the flavour response JES uncertainty that originates from the uncertainty on the JES response to the gluon-initiated jets, is affected by the conservative choice of the quark-gluon jet fraction. A more realistic estimation of the JES flavour uncertainties is provided by measuring the quark-gluon jet fraction in the $t\bar{t}$ signal events that pass the analysis selection using MC truth information. Each jet is matched with a corresponding parton if it lies within $\Delta R < 0.3$. Based on the parton truth information, the matched jets are identified as quark or gluon-initiated jets. To estimate the uncertainty of the quark-gluon jet fraction, the same procedure is repeated on the systematic variation used to estimate the uncertainty on the modelling of the $t\bar{t}$ signal, summarised in Section 9.2, and the uncertainties are summed in quadrature. The outlined procedure results in the fraction of quark

---

[1] An event where a jet constituent passes the whole calorimeter, and does not leave all of its energy in the calorimeters.

and gluon initiated jet, and its uncertainty in various jet η and p_{T} bins. The fractions and their uncertainties are then propagated to the software that estimates the flavour composition and flavour response JES uncertainties that are used further in the analysis. Figure 9.1 illustrates the quark-gluon jet fraction and their uncertainties in different jet η and p_{T} bins.

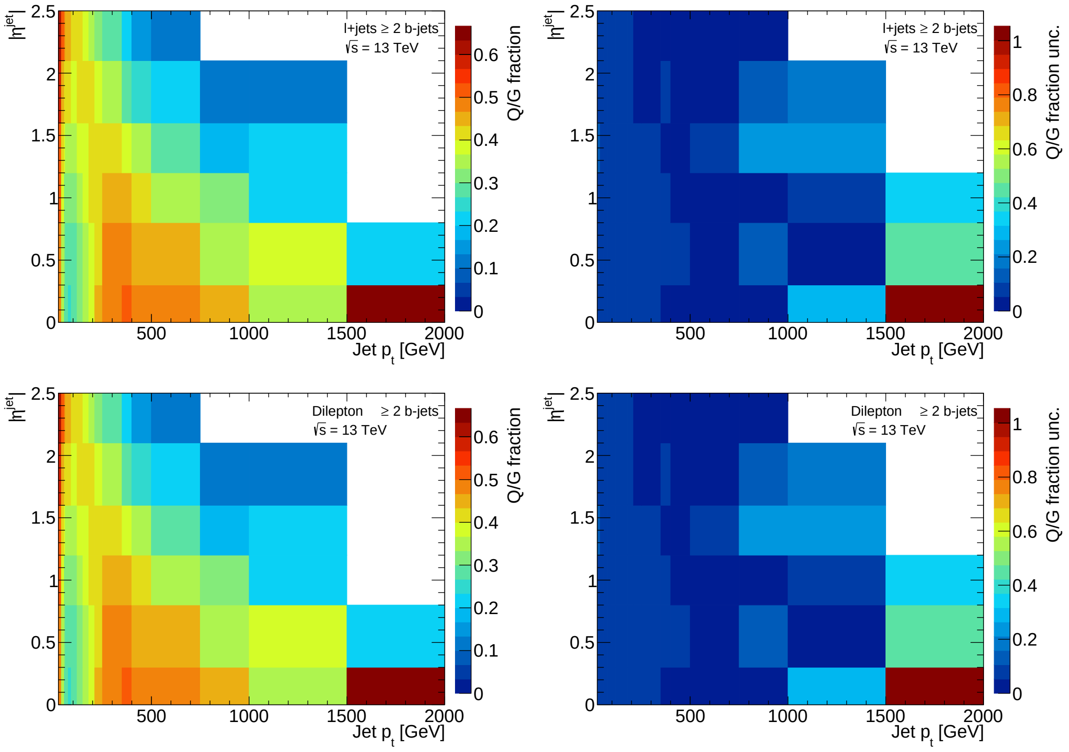

Figure 9.1.: Relative fractions of quark and gluon initiated jets (left) and their corresponding uncertainties (right) in events that pass the lepton+jets (top) and the dilepton (bottom) selection. The fractions are split into jet p_{T} and η bins.

9.1.3. Jet energy resolution

The JER is measured in the data using events with $Z \to \ell^+\ell^-$ or a photon, and an additional jet using in-situ techniques similar to Ref. [230]. The JER is measured in various jet p_{T} and jet η bins. Additionally, the JER is measured in simulated dijet events using the particle truth information. In simulation, the reconstructed jets are matched to the particle truth jets if they are within $\Delta R < 0.3$. The reconstructed energy of the matched jets is compared to the energy of the particle jets from the truth record and filled into a histogram. The histograms are fitted with a Gaussian function around the peak of the distribution. The width of the fitted Gaussian distribution, σ, is the JER in the simulation. The JER in the simulation is measured in different jet η and p_{T} bins. For each η bin, the JER values for different jet p_{T} bins are fitted with a calorimeter response function to interpolate the measured JER to all p_{T} values. The JER in simulated events is smeared to match the JER measured in the data. The JER uncertainty originates from the uncertainty on the measured JER in the data and is estimated by applying the uncertainty on the MC smearing factors.

The JER MC smearing factors, a factor that additionally smears the JER obtained from a simulation to match the data, are different for samples with the GEANT 4 detector simulation and the fast detector simulation. The differences depend on the jet p_{T} and $|\eta|$. Since some of the $t\bar{t}$ signal modelling uncertainties require processing samples with the fast simulation of the detector, smearing factors for the fast simulation are important for the analysis of the top-quark decay width to estimate the $t\bar{t}$ modelling uncertainties correctly. During the analysis, the derivation of the JER smearing factors for the fast simulation has been done as illustrated in Figure 9.2.

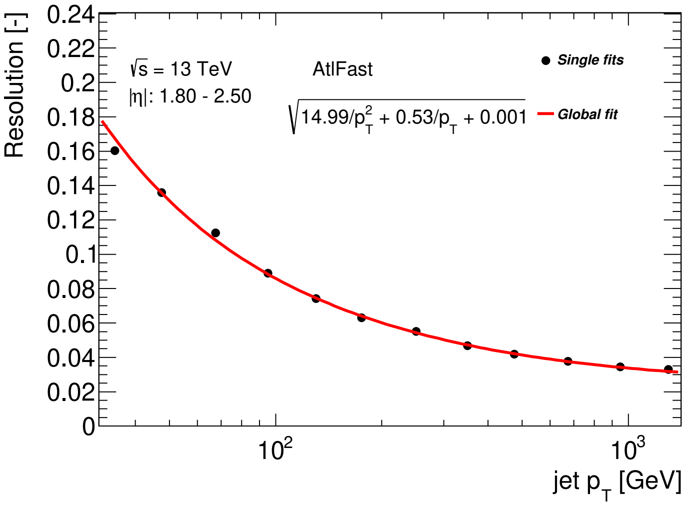

Figure 9.2.: Measured JER in the simulated dijet events for jets with $1.8 < |\eta| < 2.5$ with the fast detector simulation. The points represent the measured JER values for a given jet p_{T} bin. The individual points are fitted with the calorimeter response function. Each term in the formula represents different sources of the energy resolution contribution: the first term represents statistical fluctuations (noise), the second term represents sampling fluctuations from alternating material and the last term represents a non-homogeneity contribution.

9.1.4. Jet vertex fraction

The efficiency of jets passing the JVT selection differs between the simulated events and the observed data. To correct for these discrepancies, the simulated events are modified with scale factors obtained from tag-and-probe measurements with $Z \to \mu^+\mu^-$ and additional jets [188]. The JVT scale factors are varied within their uncertainties that originate from a 20 % uncertainty on the estimation of the residual contamination from pile-up jets after pile-up suppression. The scale factor variation also includes a systematic uncertainty assessed by using different generators for the MC simulation of the Z+jets events.

9.1.5. $E_{\mathrm{T}}^{\mathrm{miss}}$ scale and resolution

$E_{\mathrm{T}}^{\mathrm{miss}}$ is calculated from several terms corresponding to different types of reconstructed objects as is discussed in Section 5.4. The uncertainty on each object is evaluated and then propagated to the uncertainty on $E_{\mathrm{T}}^{\mathrm{miss}}$. Two methods are used to estimate the uncertainty on the soft term that enters the $E_{\mathrm{T}}^{\mathrm{miss}}$ calculation in events with $Z \rightarrow \mu^{+}\mu^{-}$ exploiting the transverse momentum balance of the muons, using techniques similar to Ref. [231]. Different uncertainty sources are combined into a total uncertainty on scale and resolution of $E_{\mathrm{T}}^{\mathrm{miss}}$.

9.1.6. Flavour tagging

Flavour-dependent scale factors are applied to simulated events to correct for the discrepancy of flavour-tagging efficiency between data and simulation, as discussed in Section 5.5. The uncertainty of the flavour-tagging is estimated by varying the flavour-tagging scale factors within their intrinsic uncertainties obtained from the efficiency measurements. The decorrelated source of the systematic uncertainties result in 9 NPs for the b-tagging efficiencies, 4 NPs for c-mis-tag rate and 6 NPs for light-flavour-mis-tag rate. The uncertainties depend on the jet p_{T}, and in the case of the light-flavour-mis-tag rate, also on the jet η.

9.1.7. Pile-up reweighting

To account for the additional pp collisions (pile-up) a set of minimum-bias events is superimposed onto the hard scattering events. The simulated events are reweighted [232] to match the pile-up profile of the LHC data. The weights are varied within their uncertainties to estimate the systematic uncertainty.

9.1.8. Luminosity

An uncertainty of 1.7 % is assigned to the luminosity measurement of the combined dataset collected in years 2015, 2016, 2017 and 2018 using techniques similar to Ref. [169]. This uncertainty is applied to all MC simulated processes to evaluate the effect on the measurement of the top-quark decay width.

9.2. Signal and background modelling uncertainties

9.2.1. Background normalisation

The normalisation of the $t\bar{t}$ signal is a free parameter of the fit. The uncertainty on normalisation of the considered backgrounds enters the consideration of the systematic uncertainties via NPs. To reduce the fit complexity, only the dominant backgrounds, summarised in Chapter 7, enter the fit individually, these correspond to: single top and multijet backgrounds. The other considered backgrounds are combined to a single contribution in the fit. Table 9.1 summarises the normalisation of the background components entering the fit.

9.2.2. Multijet background modelling

A special uncertainty, apart from the normalisation uncertainty, on the multijet background modelling is considered in the analysis. The analysis differs between the lepton+jets and the dilepton channel.

To allow the variation in the shapes of the predicted multijet distributions, an alternative parametrisation (see Section 6.3) for the estimation of the background is used to generate new multijet distributions. The differences between the distributions are symmetrised and considered as an uncertainty on the modelling of the multijet background.

Component	**Channel**	
	Lepton+jets	Dilepton
Single-top	15 %	15 %
Multijet	50 %	50 %
Other (combined) backgrounds	50 %	50 %

Table 9.1.: Uncertainties corresponding to a 1 σ variation for different background sources that enter the likelihood fit. Uncertainties in percentage are shown for the lepton+jets channel (left) and the dilepton channel (right). The last row represents a combined contribution from smaller backgrounds considered in the analysis, a conservative 50 % uncertainty is used for this category. Normalisation of the multijet background is fully decorrelated in the combination of the two channels. The normalisation of the $t\bar{t}$ signal is left free floating in the fit.

In the dilepton channel, a selection identical to the selection described in Section 7.4 is applied to the data with the only modification that the charged leptons are required to have the opposite electric charge. This selects events with high contamination of mis-reconstructed or non-prompt leptons as in the SM the processes that result in same-sign charged leptons have very small cross-section. The resulting distributions are then normalised to the same expected number of observed events as the nominal distributions. The difference between the distributions is symmetrised and considered as the uncertainty on the multijet background modelling in the dilepton channel.

9.2.3. $t\bar{t}$ matrix element to parton shower modelling

The uncertainty originating from the choice of the $t\bar{t}$ nominal MC generator, ME to parton shower modelling uncertainty, is evaluated by comparing the nominal MC sample, POWHEG interfaced with PYTHIA, and an alternative generator aMC@NLO interfaced with PYTHIA. Both samples are generated with the fast simulation of the detector. The symmetrised difference between the distributions of the nominal generator and the alternative generator is the modelling uncertainty. The difference is modified to have only shape effect (normalisation component is dropped) to minimise potential constraints originating from the difference in the normalisation component. This procedure does not underestimate the uncertainty on the $t\bar{t}$ modelling, as the normalisation of the $t\bar{t}$ is a free floating parameter of the fit.

9.2.4. $t\bar{t}$ parton shower, hadronisation and fragmentation modelling

A parton shower is the process of QCD radiation after the hard-scatter event. The partons originating from the ISR and FSR then scatter, decreasing their momentum scale. At some point, the momentum scale reaches the non-perturbative region where the hadronisation starts. The two commonly used models of hadronisation are the *string model* and the *cluster model*.

The string fragmentation model [233] simulates the concept of the hadronisation with colour lines (strings) between quark and antiquark pairs. Each string has a certain tension associated with it. The string tension evolves in time until the $q\bar{q}$ breaks into $q\bar{q} \to q\bar{q}' + q'\bar{q}$.

The cluster model [234] uses colour singlet clusters that are built around partons after the parton shower. The model is based on the idea that gluons are mainly emitted between partons that form clusters (that are connected). The remaining gluons form $q\bar{q}$ pairs. Observable hadrons originate from the decay of the clusters.

Uncertainty	h_{damp}**[GeV]**	μ_{r}	μ_{f}	**Shower Scale**
Higher radiation	517.5	0.5	0.5	`Var3cUp`
Lower radiation	258.75	2.0	2.0	`Var3cDown`

Table 9.2.: A summary of the two POWHEG interfaced with PYTHIA 8 settings used to estimate the ISR uncertainty.

The uncertainty originating from the choice of the parton shower, hadronisation and fragmentation generator is estimated by comparing the nominal MC generator, POWHEG interfaced with PYTHIA, with POWHEG interfaced with HERWIG. This corresponds to a comparison of two hadronisation models as PYTHIA employs the string fragmentation model and HERWIG employs the cluster model. Additionally, the samples have different *underlying event* (UE)[2] modelling thus comparing the two generators also includes uncertaintie originating from the choice of the UE model. For both samples, the h_{damp} parameter is set to 1.5 time the nominal value for the top-quark mass, 258.75 GeV. The symmetrised difference of the distributions enter the likelihood fit as a NP that only has a shape component (the normalisation component is dropped).

9.2.5. $t\bar{t}$ initial state radiation modelling

The uncertainty arising from the initial state radiation modelling is estimated by comparing two alternative MC setups of POWHEG interfaced with PYTHIA. The samples differ in the choice of factorisation scale, renormalisation scale, h_{damp} and hadronisation tunes. Two variations, one increasing and one decreasing the amount of initial state radiation, are compared with the nominal sample. The variation that increase radiation utilises a dedicated MC sample with $h_{\mathrm{damp}} = 517.5$ GeV (three times the nominal top-quark mass) with the choice $\mu_f = \mu_r = 0.5$ of the nominal dynamic scale. Additionally, the hadronisation tune *Var3cUp*, a variation of the α_s coupling in the ISR of the parton shower [235], is used. The variation that decreases radiation, on the other hand, uses the same h_{damp} as the nominal sample, $h_{\mathrm{damp}} = 258.75$ GeV with $\mu_f = \mu_r = 2.0$ of the nominal scale. The hadronisation tune is *Var3cDown*.

Both ISR variations are compared to the nominal distribution. The variation that leads to higher total expected uncertainty on Γ_t is symmetrised and considered in the analysis. Table 9.2 summarises the setting and samples used for the ISR uncertainty estimation. Events are simulated with the fast detector simulation and are compared to the nominal distribution with fast simulation.

In the 8 TeV measurement, the ISR[3] radiation uncertainty was a limiting uncertainty for many considered observables, frequently resulting in few GeV uncertainties on Γ_t, depending on the observables tested. The uncertainty for the 8 TeV followed a similar procedure as the 13 TeV analysis, but the considered hadronisation variations were different. The 8 TeV variations were only extrapolated from non-LHC data [236], although the variations in the parton shower were combined with the scale variations in the ME and compared to the 7 TeV LHC data [237]. This resulted in a conservative radiation modelling uncertainty. For the 13 TeV, the LHC $\sqrt{s} = 7$ TeV data are used, which leads to a more realistic radiation uncertainty.

---

[2] Underlying event is a particle production process not associated with the hardest parton-parton process.

[3] In the 8 TeV measurement the radiation uncertainty combined both ISR and FSR uncertainty.

9.2.6. $t\bar{t}$ final state radiation modelling

The strong coupling constant, α_s, in the final state radiation of PYTHIA 8 is varied by setting the renormalisation scale to half of the nominal value, $\alpha_s^{\mathrm{up}} = \alpha_s^{\mathrm{nominal}}(0.5\mu)$. The variation is then symmetrised and the shape effect (normalisation dropped) is considered in the measurement as the FSR uncertainty.

9.2.7. $t\bar{t}$ PDF uncertainty

The uncertainty originating from the uncertainty of the PDF parameters is estimated following the *PDF4LHC* recommendations [238]. These recommendations combine various PDF sets with their uncertainties. The considered PDF sets are *CT14* [239], *MMHT2014* [209] and *NNPDF3.0* [205]. A set of 30 uncorrelated NPs is symmetrised and considered in the analysis. These cover the intrinsic uncertainties of each of the PDF sets as well as the differences between the datasets. The nominal $t\bar{t}$ sample is generated with the *NNPDF3.0* set, as described in Section 6.1, which validates the chosen approach of the *PDF4LHC* recommendations.

9.2.8. $t\bar{t}$ NNLO QCD reweighting

The $t\bar{t}$ signal samples are generated with NLO corrections in the production and are then normalised to the theoretical NNLO cross-section with soft-gluon resummations as summarised in Section 6.1. To include the uncertainty from the difference between NLO and NNLO QCD prediction, the nominal $t\bar{t}$ distributions are reweighted to match the top-quark p_{T} distribution at NNLO [68–71] using the MC truth information. The reweighted distributions are then compared to the nominal distribution. The difference between the distributions is symmetrised and considered as an uncertainty in the analysis.

9.2.9. Single-top Wt overlap modelling

In the nominal setting, the *diagram removal* (DR) technique [213] is used to remove the overlap between the $t\bar{t}$ signal and the Wt process in the final states. An alternative removal technique, *diagram subtraction* (DS) [213], is employed to estimate the uncertainty originating from the choice of the removal technique. The distributions obtained from the DS scheme are compared to the distributions obtained from the DR scheme for the Wt single top channel. The symmetrised difference is the single top Wt modelling uncertainty.

9.3. Other uncertainties

The last set of considered uncertainties that do not originate in the detector uncertainties nor in the uncertainties of the modelling, but they originate from limited computation resources. The limited resources imply finite number of generated events in the MC simulation, consequently, the expected number of events in each bin of the generated distribution has a corresponding statistical uncertainty. The MC statistical uncertainty is considered differently for the signal $t\bar{t}$ sample and the background samples.

9.3.1. MC statistical uncertainty on the width templates

The MC statistical uncertainty in the MC affects the width templates. Since the width templates are generated by reweighting the nominal prediction, as discussed in Section 10.4, the

MC statistical uncertainty is correlated between the individual width templates. To estimate the effect of the finite number of events in the MC $t\bar{t}$ sample, for each bin of the considered distributions a unique NP enters the likelihood, corresponding to a subsidiary measurement obeying the Poisson statistics, thus having a Gamma function prior in the likelihood. For the individual regions considered in the fit, these NPs are uncorrelated. To take into account the statistical correlations between the individual width templates, for a given bin the NP representing the MC statistical uncertainty is fully correlated between the templates.

9.3.2. MC statistical uncertainty on the backgrounds

Similarly to the previous section, the MC statistical uncertainty also affects the bins in the considered background distributions. Ideally, each individual sample contributing to the background processes would have a set of NPs for each bin of the distributions. This is, however, not practical as this would result in large number of NPs making the minimisation procedure impossible. Generally, a compromise solution between adding NPs for each individual sample and ignoring the source of the uncertainty is to provide one NP for each bin from the combined background instead of the individual samples. This approach leads to one NP for each bin of the combined single top and the *other* backgrounds in the lepton+jets channel, and includes single top, multijet and the *other* background in the dilepton channel. These NPs correspond to a Poisson subsidiary measurement, resulting in Gamma function priors. Only bins that have a relative MC statistical uncertainty larger than 3 % in each bin are considered in the model.

9.4. Smoothing and pruning

9.4.1. Smoothing

The distributions obtained from the variations of the systematic uncertainties are generated from a finite set of events and this can result in statistical fluctuations of the variations with respect to the nominal distributions. If the fluctuations are present in some bins of the distributions used in the fit, the fluctuations could result in the constraint of the NP in some bins. However, since only one NP describes one source of the systematic uncertainty, the constraint would apply to all bins of the observable chosen for the fit. This unwanted constraint could lead to an underestimation of the impact of the source of the uncertainty on the measurement of the top-quark width. To prevent the constraints originating only from the statistical fluctuations of the distribution, the smoothing procedure is applied.

The smoothing procedure starts from evaluating the smoothing threshold, δM, calculated from the nominal histogram, N, and the systematic variation, S, in each bin

$$\delta M = \begin{cases} \sqrt{\delta S^2 + \delta N^2} & \text{for independent variations,} \\ \max\left(\delta S, \delta N\right) & \text{for correlated variations,} \end{cases} \tag{9.1}$$

where δS denotes the statistical uncertainty of the systematic variation originating from the finite number of simulated events, and similarly for the nominal histogram, δN. The smoothing threshold definition in Equation 9.1 allows to smooth variations that come from the same statistical population and also for variations created from statistically independent population. To reduce the statistical fluctuations of the systematic variations, for each pair of the neighbouring bins, $i-1$ and i, a difference $x_{i-1,i}$ is calculated as

$$x_{i-1,i} = \left| \frac{S_i - N_i}{N_i} - \frac{S_{i-1} - N_{i-1}}{N_{i-1}} \right|, \tag{9.2}$$

and the relative statistical uncertainty on the difference

$$\delta x_{i-1,i} = \sqrt{\frac{\delta M_i^2}{N_i^2} + \frac{\delta M_{i-1}^2}{N_{i-1}^2}}. \tag{9.3}$$

If at least one bin satisfies $x_{i-1,i} < \delta x_{i-1,i}$, the smoothing algorithm looks for neighbouring bins $b-1$ and b with the highest ratio

$$\frac{\delta x_{b-1,b}}{x_{b-1,b}}, \tag{9.4}$$

then these bins are merged. The process continues until there is no bin in the distribution that satisfies $x_{i-1,i} < \delta x_{i-1,i}$. The last step of the smoothing procedure applies a smoothing algorithm known as *353QH twice* [240] on the distribution corresponding to a relative systematic variation, $(S-N)/N$, to create smooth transitions between the merged bins.

9.4.2. Pruning

Each source of systematic uncertainties enters the likelihood calculation and adds complexity to the multidimensional problem of the likelihood maximisation. However, not all sources of the systematic uncertainties are significant. The pruning technique is applied to remove the impact of the insignificant systematic uncertainties that would otherwise result in many local minima of the multidimensional likelihood, making the process of minimisation depend on the initial starting point of the minimisation and generally unstable.

The effect of each systematic variation is split into two orthogonal components affecting only the normalisation and affecting only the shape. If the effect of the normalisation of the systematic variation for a given process is smaller than 0.1 %, the effect of the normalisation is dropped for the distribution of the given process. If the shape effect, defined as the maximum difference between the systematic variation and the nominal distribution from all bins of the distribution, is smaller than 0.01 %, then only the normalisation component of the uncertainty is considered. If both shape effect and normalisation effect are dropped from the distribution, the systematic uncertainty is removed for that distribution. If the systematic variation is removed from all processes for all distributions considered in the fit, the systematic uncertainty is dropped from the consideration.

Table 9.3 summarises systematic uncertainties and the number of NPs considered in the analysis before and after the removal of the non-significant systematic uncertainties.

Systematic Uncertainty	Components Lepton+jets	 Dilepton	 Initial
Luminosity	1	1	1
Physics Objects			
Electron	5	5	7
Muon	4	11	15
Jet energy scale	22	14	28
Jet energy resolution	8	8	8
Jet vertex fraction	1	1	1
Pile-up profile	1	1	1
$E_{\mathrm{T}}^{\mathrm{miss}}$ scale and resolution	3	3	3
b-tagging efficiency	7	8	9
c-tagging efficiency	4	4	4
Light-jet-tagging efficiency	4	4	6
Efficiency extrapolation	1	2	2
Background Model			
Single top normalisation	1	1	1
Multijet normalisation	1	1	1
Other processes normalisation	1	1	1
$t\bar{t}$ and Wt overlap modelling	1	1	1
Multijet shape	1	0	1
Signal Model			
$t\bar{t}$ ISR modelling	2	2	2
$t\bar{t}$ FSR modelling	1	1	1
$t\bar{t}$ ME generator	1	1	1
$t\bar{t}$ Shower & hadronisation	1	1	1
$t\bar{t}$ PDF	21	30	30
$t\bar{t}$ Template MC stat.	25	25	-
$t\bar{t}$ NNLO reweighting	1	1	1

Table 9.3.: A summary of the number of systematic uncertainties considered in the analysis with their corresponding number of NPs that enter the fit. Systematic uncertainties are listed separately for lepton+jets events (left) and dilepton events (right). The first two columns show systematic uncertainties that are considered significant. The last column shows the initial number of considered systematic uncertainties.

CHAPTER 10

Analysis strategy

This chapter describes the preparation of the width templates and the fit strategy. Section 10.1 summarises the creation of the width templates as well as the validation of the procedure. The template creation strategy is used for both the 8 TeV and the 13 TeV measurement. Section 10.2 is dedicated to the fitting strategy used in the 8 TeV measurement. The main differences in the experimental setup between the analyses conducted at 8 and 13 TeV are summarised. Important analysis steps, challenges and lessons learned from the 8 TeV measurement are described. The remaining sections in this chapter are dedicated to the 13 TeV measurement.

10.1. Templates

Distributions of variables sensitive to the top-quark decay width corresponding to different underlying Γ_t, width templates, are fitted to the observed data to extract the decay width. The exact strategies of the fit differ between the 8 TeV analysis, summarised in Section 10.2, and 13 TeV analysis, summarised in Section 10.3. Despite the differences in the fitting strategy, the procedure of template creation is similar in both analyses, as described in Section 10.1.1.

10.1.1. Template creation

Ideally, dedicated MC samples would be generated corresponding to various top-quark decay width values that could be used in a template fit. However, this would require an immense amount of computing resources, thus this approach is not pursued in the analysis. Due to the absence of the dedicated MC samples, the width templates are generated from the nominal $t\bar{t}$ sample, with $m_t = 172.5$ GeV and $\Gamma_t = 1.32$ GeV by reweighting utilising the parton truth information[1]. The reweighting uses a theoretical Breit-Wigner distribution, $\mathrm{BW}(x)$, which describes the parton-level top-quark mass distribution

---

[1] For the 8 TeV measurement, the decay width of the top quark was set to 1.33 GeV for a top-quark mass of 172.5 GeV.

$$\mathrm{BW}(x) = \frac{2\sqrt{2} m_t \Gamma_t \sqrt{m_t^2 (m_t^2 + \Gamma_t^2)}}{\pi \sqrt{m_t^2 + \sqrt{m_t^2 (m_t^2 + \Gamma_t^2)}} \cdot ((x^2 - m_t^2)^2 + m_t^2 \Gamma_t^2)}, \tag{10.1}$$

where m_t is set to 172.5 GeV. The masses x represent the truth top-quark masses from the MC truth record for top-quarks after FSR but before the decay of the particles. The values x vary on an event-by-event basis. To generate a distribution that corresponds to the given top-quark decay width Γ_t^{new}, a per-event-weight equal to the ratio of the BW functions is assigned where the nominator corresponds to the Breit-Wigner function with $\Gamma_t = \Gamma_t^{\mathrm{new}}$ and the top-quark mass equal to the truth top mass of the semileptonically decaying top quark for distributions created from semileptonically decaying top quarks in the case of lepton+jets events. In the dilepton channel, two per-event weights are assigned, one for the top quark and one for the anti-top quark. The $m_{\ell b}$ observable with a positively charged lepton is assigned the weight calculated for the top quark and analogously for the $m_{\ell b}$ observable with a negatively charged lepton. The denominator represents the Breit-Wigner function with the top-quark decay width $\Gamma_t = 1.32$ GeV and the top-quark mass $m_t = 172.5$ GeV corresponding to the nominal MC $t\bar{t}$ sample. Using the reweighting procedure, distributions for any top-quark decay width value can be generated. In the 8 TeV analysis, the width templates are generated in steps of 0.1 GeV in the range $0.1 < \Gamma_t < 5.0$ GeV with additional templates for $\Gamma_t = 0.01, 6, 7, 8$ GeV to account for very small and very large decay widths. The 13 TeV measurement uses templates corresponding to decay widths of $\Gamma_t = 0.2, 0.4, 0.7, 1.0, 1.4, 1.8, 2.2, 2.6, 3.0, 3.5, 4.0$ GeV in both considered $t\bar{t}$ decay channels. The differences between the steps in the templates arise from the difference in the fitting strategy. Figure 10.1 illustrates the distribution of the weights used to generate various top-quark decay widths from the nominal distribution.

10.1.2. Template validation

To validate the reweighting procedure described in the previous section, two dedicated Powheg interfaced with Pythia 8 MC samples have been generated for non-all hadronic[2] $t\bar{t}$ decay channels. The special samples have been generated with the identical settings as in the case of the nominal $t\bar{t}$ MC sample, apart from the value of the top-quark decay width. The alternative samples have $\Gamma_t = 0.7$ and 3.0 GeV while keeping the same top-quark mass as the nominal sample, $m_t = 172.5$ GeV. Since generating samples with alternative top-quark decay width, while keeping the same top-quark mass, violates the SM, the total expected number of events differs between the reweighted and the generated distributions. Figure 10.2 shows the distributions with the expected number of events normalised, focusing only on the shape differences between the distributions. The shapes of the reweighted and the generated distribution agree within the statistical uncertainty as illustrated by the χ^2 test values. To account for the differences in the normalisation, the width templates are normalised to the same number of expected events as predicted by the nominal $t\bar{t}$ MC sample, corresponding to the SM prediction for the width, $\Gamma_t = 1.32$ GeV and the normalisation of the $t\bar{t}$ signal is left free floating in the fit.

To take into account detector simulation effects, the top-quark mass distribution obtained using the reweighing procedure and the generated distribution are compared at the reconstruction level, as illustrated in Figure 10.3. No significant deviations in the shape are observed, thus the reweighting procedure is considered valid.

---

[2] Lepton+jets and dilepton decay channels.

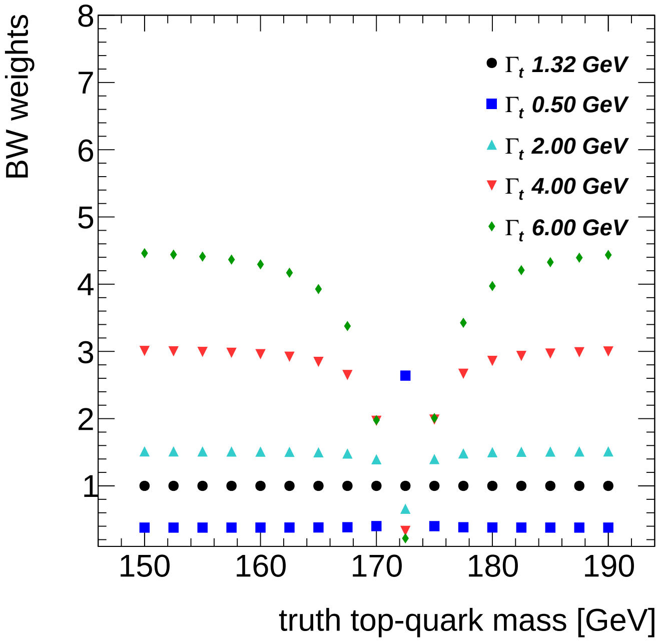

Figure 10.1.: Distribution of weights used in the reweighting process for the generation of distributions for various top-quark decay widths as a function of the truth top-quark mass.

A similar validation procedure has been used also for the 8 TeV measurement. The conclusions of the reweighting procedure validation are identical to the conclusions for the 13 TeV measurement outlined above.

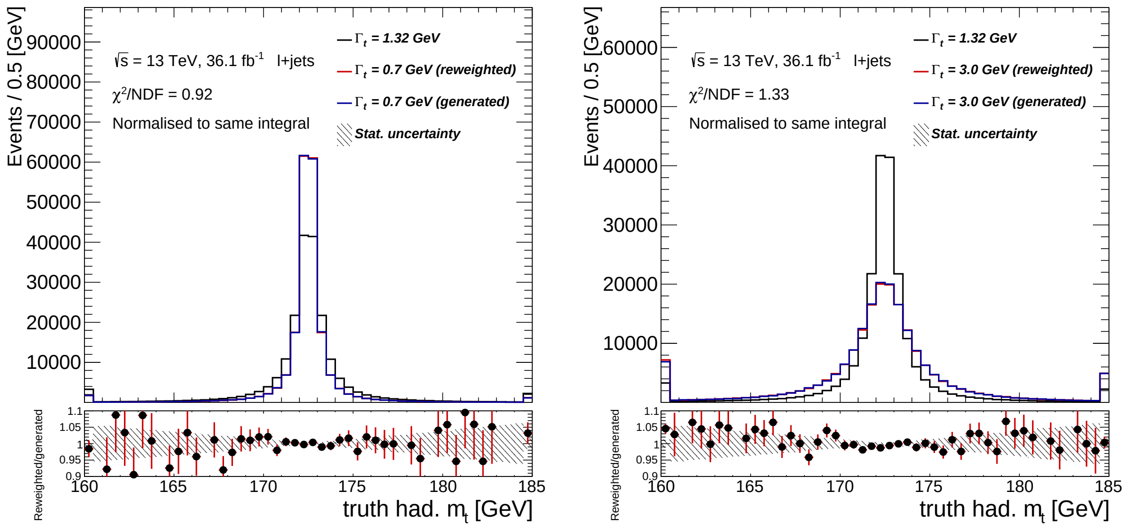

Figure 10.2.: Comparison of the truth top-quark mass distributions for the reweighting procedure and the dedicated MC samples with the top-quark decay widths set to $\Gamma_t = 0.7$ GeV (left) and $\Gamma_t = 3.0$ GeV (right). The distributions are normalised to the same expected number of events. The χ^2 value divided by the number of degrees of freedom (NDF) is shown to represent the level of agreement between the samples. The bottom panel shows the ratio between the generated and reweighted distributions. The shaded areas represent the MC statistical uncertainty. The electron+jets and the muon+jets events are combined.

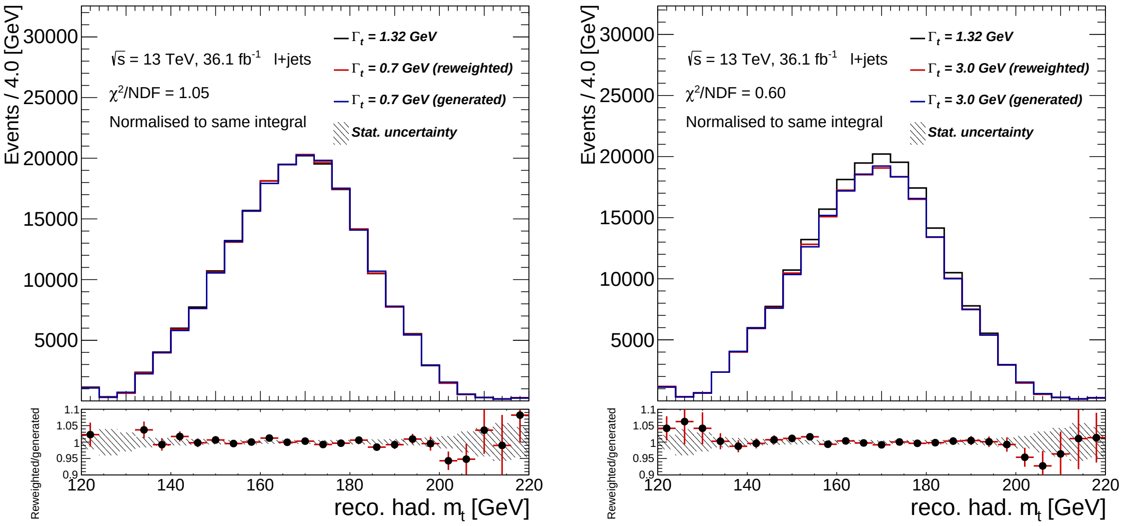

Figure 10.3.: Comparison of the reconstructed top-quark mass distributions for the reweighting procedure and the dedicated MC samples with the top-quark decay widths set to $\Gamma_t = 0.7$ GeV (left) and $\Gamma_t = 3.0$ GeV (right). Events are required to have the BDT score > 0.7. The distributions are normalised to the same expected number of events. The χ^2 value divided by the number of degrees of freedom (NDF) is shown to represent the level of agreement between the samples. The bottom panel shows the ratio between the generated and reweighted distributions. The shaded areas represent the MC statistical uncertainty. The electron+jets and the muon+jets events are combined.

10.2. 8 TeV fit strategy

This section describes the basic strategy used for the 8 TeV direct measurement of the top quark decay width, corresponding to an integrated luminosity of 20.2 fb^{-1}. Similarities and differences between the measurements at 8 and 13 TeV are emphasised. Section 10.2.1 summarises differences originating from the centre-of-mass energies and the related effects on kinematics and cross-sections as well as differences in the detector setup. Section 10.2.2 describes the 8 TeV $t\bar{t}$ reconstruction algorithm. Section 10.2.3 illustrates the 8 TeV fitting strategy. Observables considered in the 8 TeV measurement are summarised in Section 10.2.4. Section 10.2.5 summarises lessons learned from the 8 TeV measurement, focusing on the choice of the $t\bar{t}$ reconstruction, choice of observables and the fit procedure. A detailed description of the 8 TeV analysis can be found in the thesis of Philipp Stolte-Cord-to-Crax [241] and the corresponding internal note [242].

10.2.1. Differences related to the detector setup and the centre-of-mass energy

Many changes in the detector setup happened between 2012 (8 TeV data taking) and the beginning of Run 2 with $\sqrt{s} = 13$ TeV (year 2015). Some of the differences between the detector properties are summarised in Chapters 4 and 5. The most important differences affecting the measurement of the top-quark decay width originate from the addition of the IBL, as described in Section 4.2.2, which improves vertex resolution, resulting in a better performance of the b-tagging algorithm. This improvement allows better identification of events containing top quarks. Furthermore, the total luminosity ($\mathcal{L} = 20.2$ fb^{-1}), available for physics analysis, collected by the ATLAS experiment at $\sqrt{s} = 8$ TeV is approximately seven times smaller than the full Run 2 dataset, corresponding to about $\mathcal{L} = 140$ fb^{-1}. Additionally, the pile-up contamination was significantly lower for 2012 data taking conditions, thus the object calibrations applied different pile-up suppression techniques.

Besides the changes in the detector and the LHC conditions, kinematics and cross-sections depend on the centre-of-mass energy. As summarised in Section 3.1, the predicted $t\bar{t}$ cross-section at $\sqrt{s} = 13$ TeV is about 3.5 times larger compared to the cross-section at $\sqrt{s} = 8$ TeV. Combined with the difference in the integrated luminosity, around 25 times more $t\bar{t}$ pairs are expected in the full Run 2 dataset with respect to the 8 TeV dataset. Moreover, the cross-section of the production of the W boson with additional jets, one of the dominant backgrounds for the $t\bar{t}$ lepton+jets channel, increases by a factor smaller than 3.5, naturally resulting in smaller background contamination for the 13 TeV analysis. Additionally, the increased centre-of-mass energy results in an increased average energy of the produced top-quarks and, as a consequence, in higher energy of the ISR and FSR gluons, represented by more reconstructed jets passing the selection criteria, as well as more collimated top-quark decay products.

Due to the relatively larger contribution of the W+jets background in the 8 TeV measurement, the background has been split based on the flavour composition of the jets into events with a W boson and light jets (W+light), events with a W boson and c-jets ($W+c$) and events with at least two b or c-jets ($W+bb/cc$). The normalisation of each W+jets component is measured by in-situ techniques in the measurement of the $t\bar{t}$ charge asymmetry [243].

10.2.2. $t\bar{t}$ reconstruction

In the 8 TeV measurement, an event selection in the lepton+jets channel similar to the selection outlined in Section 7.3 has been employed with one significant difference that at least one b-tagged jet has been required using b-tagging algorithm operating at 70 % efficiency. However, events with exactly one b-tagged jet have larger non-$t\bar{t}$ background contamination compared to events with two b-tagged jets, their usage in the 8 TeV analysis was necessary to reduce the statistical uncertainty of the measurement.

The reconstruction of the kinematics of the top quarks poses similar challenges in the 8 TeV measurement as summarised in Section 8.1. In the 8 TeV measurement, the reconstruction is performed by using solely the KLFitter algorithm [222] to identify the correct jet-to-parton assignments. The top-quark mass has been fixed to the value of $m_t = 172.5$ GeV and correspondingly, the top-quark width has been fixed to $\Gamma_t = 1.33$ GeV, in agreement with the NLO SM prediction. Up to five jets are selected and passed to the KLFitter algorithm.

Several configurations of the KLFitter algorithm have been tested to find the optimal setting for the measurement of the decay width. The setting where only the first four jets ordered in jet p_{T} are considered in KLFitter has been compared with the setting where up to five jets, ordered in jet p_{T} are considered[3]. The matching efficiency for the jets originating from the $t\bar{t}$ decay has been found to be higher in the setting where up to five jets are passed to the KLFitter algorithm. However, this setting has not been used in the measurement as it has led to large systematic uncertainties originating from the modelling uncertainty of the ISR and FSR for $t\bar{t}$ events in POWHEG interfaced with PYTHIA 6, the nominal $t\bar{t}$ sample used for the 8 TeV measurement. Furthermore, the fixed value for Γ_t in the KLFitter likelihood, has been changed to a value of $\Gamma_t = 0.6$ GeV and $\Gamma_t = 2.0$ GeV, while keeping the top-quark mass fixed to $m_t = 172.5$ GeV. The effect on the considered distributions has been evaluated and has been found to be negligible, as $O(1)$ events change their value for the considered observables. To further improve the reconstruction performance of KLFitter, the best permutation from KLFitter has been required to have the logarithm of the likelihood, $\ln L > -50$. This value has been optimised to lead to the best expected total uncertainty on the measurement.

10.2.3. Fitting procedure

To maximise the shape information, the events passing the selection are split into eight mutually orthogonal regions based on the lepton flavour, electron+jets and muon+jets channel; based on the number of b-tagged jets, exactly one b-tagged jet and more than one b-tagged jet; and finally based on the jet $|\eta|$, into regions where all four jets identified to be from the $t\bar{t}$ decay have $|\eta| < 1$ and the events where at least one jet has $|\eta| > 1$. The split into the lepton flavour channels and number of b-tags is motivated by the different background compositions in the different regions as well as different sensitivity to the systematic uncertainties originating from the uncertainty on the flavour-tagging and charged lepton related uncertainties (efficiency of identification, triggering, energy and momentum scale and resolution). The motivation for the split into the jet $|\eta|$ regions is twofold: granularity of the ATLAS calorimeters differs between the central and forward regions, as described in Section 4.2.3, where the central region has better jet energy resolution than the forward region, resulting in smaller JES and JER uncertainty, the dominant detector uncertainties for the width measurement. The second motivation comes from the pile-up distribution, where forward regions of the detector are more affected by the pile-up, resulting in worse jet energy reconstruction. Thus the events where all jets have $|\eta| < 1$ have better jet energy reconstruction which translates to a higher sensitivity to the decay width. Although the events with at least one jet with $|\eta| > 1$ have worse jet energy reconstruction, these are included in the fit to decrease the statistical uncertainty and to better constrain the normalisation of the considered backgrounds.

---

[3] Two jets with the highest b-tagging score and then up to three jets with the highest p_{T} are considered.

A binned likelihood fit is set up to extract Γ_t exploiting the signal templates created by the reweighting procedure described in Section 10.1.1 for the signal $t\bar{t}$ contribution. The distributions for the background processes are fixed in the fit. The normalisation of the $t\bar{t}$ is left free floating in the fit, while the normalisation of backgrounds is allowed to fluctuate within Gaussian constraints, summarised in Table 10.1. The multijet background normalisation uncertainty is decorrelated between the eight regions. The total expected number of events, n_{total}, is equal to the sum of the expected number of events from signal and each background

$$\begin{aligned} n_{\text{total}} = n_{t\bar{t}} + n_{\text{singletop}} + n_{W+bb/cc} + n_{W+c} + n_{W+\text{light}} \\ + n_{Z+\text{jets}} + n_{\text{diboson}} + n_{\text{multijet}}. \end{aligned} \tag{10.2}$$

Similarly, the expected total number of entries, $n_{\text{total},i}$, in a bin i yields

$$n_{\text{total},i} = n_{t\bar{t},i} + \sum_{j=1}^{B} n_{\text{bkg},j,i}, \tag{10.3}$$

where B represents the total number of considered background processes, and j represents the individual backgrounds. The likelihood for an observable $\mathcal{O}$ reads

$$\mathfrak{L}\left(\mathcal{O}|\Gamma_t\right) = \prod_{i=1}^{N_{\text{bins}}} \text{Poisson}\left(\mathcal{O}|n_{\text{data},i}, n_{\text{total},i}, \Gamma_t\right) \cdot \prod_{j=1}^{B} \frac{1}{\sqrt{2\pi}\sigma_{\text{bkg},j}} \exp\left(-\frac{\left(n_{\text{bkg},j} - \hat{n}_{\text{bkg},j}\right)^2}{2\sigma^2_{\text{bkg},j}}\right), \tag{10.4}$$

where N_{bins} represents the number of bins in the templates, $n_{\text{bkg},j}$ is the expected number of events from a background source, obtained by summing over all bins i of $n_{\text{bkg},i,j}$. $n_{\text{data},i}$ denotes the number of data events in bin i. The Gaussian term of Equation (10.4) implements the Gaussian constraints for the background normalisation with the expected number of background events $\hat{n}_{\text{bkg},j}$ for a background j with an uncertainty represented by $\sigma_{\text{bkg},j}$.

The fit is repeated 55 times, each time the signal distribution is replaced with the distribution corresponding to a different underlying top-quark decay width. The combined likelihood, given in Equation (10.4), multiplied by the Gaussian constraints, of all considered templates in all regions is maximised during each fit. The obtained negative logarithm of likelihood values for each width are fitted with a quadratic function. The minimum of the fitted function represents the measured Γ_t. The statistical uncertainty of the measurement is obtained from the width of the likelihood curve at $-2\Delta\ln\mathfrak{L} = 1$ around the minimum. The implementation of the likelihood building and the minimisation of the negative logarithm of the likelihood utilises the *RooFit* [244] tool.

The estimation of the effect of the systematic uncertainties relies on *ensemble tests*. Signal and background templates are normalised to the expected number of events in data and so-called *pseudo-data* distributions are generated using the following procedure. Since the predicted number of events in each bin of the considered distributions follows Poisson statistics, a new distributions can be generated by taking a Poisson random number with the mean value corresponding to the expected number of events in the bin. Thus the new distribution follows statistical fluctuations of the expected data yields. To take into account the Gaussian constraints, Gaussian fluctuations are imposed on the normalisation of the individual background contributions with

Fit parameter	$\sigma_{\mathrm{bkg},j}$
$n_{t\bar{t}}$	-
$n_{\mathrm{singletop}}$	0.17
$n_{W+bb/cc}$	0.07
n_{W+c}	0.25
$n_{W+\mathrm{light}}$	0.05
$n_{Z+\mathrm{jets}}$	0.48
n_{diboson}	0.48
n_{multijet}	0.30

Table 10.1.: Signal and background parameters that enter the binned likelihood fit and the relative normalisation uncertainties $\sigma_{\mathrm{bkg},j}$.

the mean value corresponding to the nominal value of the normalisation and the width of the Gaussian corresponding to one standard deviation of the uncertainty on the normalisation. The original (non-smeared) signal templates combined with the background templates are fitted to the smeared distributions. The value of Γ_t is extracted by taking the minimum of the quadratic fit to the likelihood points. This process is repeated 1000 times and the fitted values for each fit are stored in a histogram. The mean value of these *pseudo-experiments* is used to cross-check the procedure, as this value should correspond to the input top-quark decay width used to build the distributions at the start of the smearing procedure. Furthermore, the standard deviation of the fitted values represents the expected statistical uncertainty of the measurement.

The estimation of the systematic uncertainties follows a similar procedure as outlined above, however, for each considered systematic uncertainty the nominal distributions are replaced by the systematically varied distributions. The varied distributions are then fitted with the combined nominal signal and background templates. The deviation of the mean of the fitted values from the input width ($\Gamma_t = 1.33$ GeV in case of 8 TeV) is the systematic uncertainty originating from the varied systematic distribution. The systematic uncertainties are considered uncorrelated, thus their effects are summed in quadratures. The total expected uncertainty is estimated by summing the total systematic uncertainty and the expected statistical uncertainty in quadratures.

10.2.4. Observables tested

Several observables have been tested for the 8 TeV measurement. Observables that have one or more of the following properties have been considered: large sensitivity to Γ_t, small sensitivity to m_t or small sensitivity to the dominant systematic uncertainties. Table 10.2 summarises observables that have been tested for the 8 TeV measurement. The reconstructed mass of the hadronically decaying top quark is a natural choice as it directly translated to the decay width, however it is very sensitive to the top-quark mass and jet-related systematic uncertainties. The $m_{\ell b}$ observable is closely related to the top-quark mass and the top-quark decay width but has lower sensitivity to the jet related systematic uncertainties. Furthermore, the $m_{\ell b}$ observable originates from a semileptonically decaying top quark, thus it can be combined with observables arising from the hadronically decaying top quark. The observables $R_{3/2}$ and $D_{3/2}$ are designed to be sensitive to the decay width while having smaller systematic uncertainties related to jets, as these uncertainties partially cancel out in the ratio ($R_{3/2}$) or in the difference ($D_{3/2}$) of the reconstructed masses. Angular distributions, SdR and $\Delta R_{\mathrm{min}}(j_b, j_l)$, have smaller sensitivity to the top-quark decay width (they are "missing" the energy component) but have also small jet related uncertainties.

The expected statistical, systematic and total uncertainties estimated with the methods described in Section 10.2.3 for the considered observables are summarised in Table 10.3. It can be seen that the variables directly related to the top-quark mass have the highest sensitivity to the width, demonstrated by the smallest expected statistical uncertainties. However, most of these variables have large systematic uncertainties. The dominant systematic uncertainties originate from JES, JER and the modelling uncertainties. On the other hand, observables with smaller sensitivity (larger expected statistical uncertainty) have smaller expected systematic uncertainties. The $m_{\ell b}$ variable provides a good compromise for the sensitivity to the width and insensitivity to the systematic uncertainties. Table 10.4 shows the expected uncertainties for combinations of $m_{\ell b}$ and other considered observables in a simultaneous fit. A significant improvement in the expected uncertainties is observed when $m_{\ell b}$ is combined with other variables. The smallest uncertainty of $^{+0.86}_{-0.76}$ GeV is expected for the combination of $m_{\ell b}$ and $\Delta R_{\mathrm{min}}(j_b, j_l)$, thus these variables are used in the simultaneous fit to the data. Contributions of the individual sources of systematic uncertainties are summarised in Appendix D. Figure 10.4 illustrates the nominal $t\bar{t}$ distribution for $m_{\ell b}$ and $\Delta R_{\mathrm{min}}(j_b, j_l)$ for the underlying values of $\Gamma_t = 0.7, 1.33$ and 3.0 GeV.

Observable	**Description**
m_t^{had}	Reconstructed mass of the hadronically decaying top quark.
$m_{\ell b}$	Invariant mass of the b-jet and the associated charged lepton from the semileptonically decaying top quark.
$R_{3/2}$	Ratio of the reconstructed mass of the hadronically decaying top quark (3-jet mass) and the reconstructed mass of the hadronically decaying W boson (2-jet mass).
$D_{3/2}$	Difference between the reconstructed mass of the hadronically decaying top quark (3-jet mass) and the reconstructed mass of the hadronically decaying W boson (2-jet mass).
SdR	Sum of the ΔR of the jets from the hadronically decaying top quark.
$\Delta R_{\mathrm{min}}(j_b, j_l)$	ΔR between the b jet and the light-flavour jet that is closest to the b-jet from the hadronically decaying top quark.

Table 10.2.: Observables considered for the fit in the 8 TeV measurement.

10.2.5. Lessons learnt from the 8 TeV measurement

Many lessons have been learnt during the $\sqrt{s} = 8$ TeV measurement. One of the most important observations is that the $m_{\ell b}$ variable is a very powerful observable for the direct measurement of Γ_t due to its large sensitivity to the decay width and small sensitivity to dominant systematic uncertainties. Considering the fact that the $m_{\ell b}$ observable is reconstructed from the semileptonically decaying top quark, it is natural to include the dilepton channel in the 13 TeV measurement. To reduce the effect of the missing NLO terms in the decay vertex of the top quark, which has turned out to be non-negligible and difficult to estimate its uncertainty, only events with $m_{\ell b} < 150$ GeV are considered. Furthermore, two key points to improve the analysis are identified: better reconstruction of the kinematics of the top quarks in the lepton+jets chan-

	Uncertainty [GeV]		
Observable	**Stat. uncert.**	**Syst. uncert.**	**Total uncert.**
m_t^{had}	$+0.29$ -0.29	$+4.31$ -3.26	$+4.32$ -3.27
$m_{\ell b}$	$+0.31$ -0.31	$+1.01$ -0.89	$+1.06$ -0.95
$R_{3/2}$	$+0.36$ -0.36	$+3.26$ -3.26	$+3.28$ -3.28
$D_{3/2}$	$+0.23$ -0.23	$+2.11$ -1.85	$+2.12$ -1.96
SdR	$+0.60$ -0.60	$+1.91$ -1.90	$+2.00$ -2.00
$\Delta R_{\mathrm{min}}(j_b, j_l)$	$+0.65$ -0.65	$+1.42$ -1.43	$+1.56$ -1.57

Table 10.3.: Expected statistical, systematic and total uncertainties on the top-quark decay width for the considered observables in the 8 TeV measurement. For the total uncertainties, the statistical and systematic component are summed in quadratures.

	Uncertainties [GeV] for $m_{\ell b}$ +		
Observable	**Stat. uncert.**	**Syst. uncert.**	**Total uncert.**
$+m_t^{\mathrm{had}}$	$+0.26$ -0.26	$+3.12$ -2.23	$+3.13$ -2.25
$+R_{3/2}$	$+0.28$ -0.28	$+1.36$ -1.33	$+1.39$ -1.36
$+D_{3/2}$	$+0.22$ -0.22	$+1.79$ -1.54	$+1.81$ -1.54
+SdR	$+0.30$ -0.30	$+0.87$ -0.78	$+0.92$ -0.84
$+\Delta R_{\mathrm{min}}(j_b, j_l)$	$+0.28$ -0.28	$+0.64$ -0.61	$+0.70$ -0.68

Table 10.4.: Expected statistical, systematic and total uncertainties on the top-quark decay width for the considered observables in combination with the $m_{\ell b}$, in the 8 TeV measurement. For the total uncertainties, the statistical and systematic component are summed in quadratures.

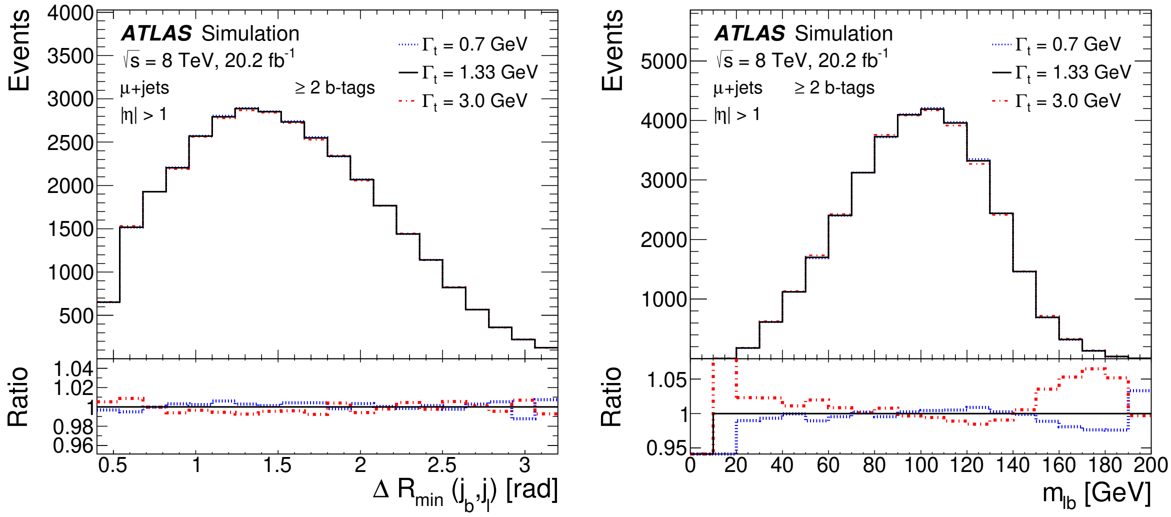

Figure 10.4.: Templates for the $\Delta R_{\min}(j_b, j_l)$ (left) and $m_{\ell b}$ (right) distributions for $\Gamma_t = 0.7, 1.33$ and 3.0 GeV in the muon+jets channel for events with at least two b-tagged jets in the region with at least one jet with $|\eta| > 1$, at $\sqrt{s} = 8$ TeV [245]. The lower panel shows the ratio of templates with the varied Γ_t to the nominal template generated with $\Gamma_t = 1.33$ GeV. The mass of the top quark is set to $m_t = 172.5$ GeV.

nel and a more powerful statistical analysis. An improved reconstruction allows for selection of a more pure correctly reconstructed $t\bar{t}$ sample which is beneficial for the measurements as was demonstrated by the KLFitter likelihood selection studies at 8 TeV. Thus, the 13 TeV measurement further improves the $t\bar{t}$ reconstruction by the dedicated BDT algorithm, as discussed in Section 8.1.

Several problems have been observed with the ensemble test procedure employed in the 8 TeV measurement. The procedure cannot identify over-conservative estimates for the systematic uncertainties, such as the 8 TeV estimation of the ISR/FSR uncertainty, as discussed in Section 9.2. Moreover, the fitting technique exploited in the 8 TeV measurement does not provide enough freedom to the fit to compensate for the discrepancies observed between the data and the prediction, as it allows only the normalisation of the individual signal and background components to float. To address all the challenges outlined above, the 13 TeV measurement exploits a profile likelihood technique that includes the systematic variations as nuisance parameters directly in the fit, as is described in detail in Section 10.3.

In the 8 TeV measurement, the effect of systematic uncertainties are minimised by the choice of observables with low sensitivity to the systematic uncertainties. The logic of the approach to the fit is flipped for the 13 TeV measurement, as observables insensitive to Γ_t, but with large sensitivity to the dominant systematic uncertainties, enter the fit alongside the variables that are sensitive to the decay width. This allows the data to constrain some of the systematic uncertainties, minimising their effect on the measurement of the top-quark decay width. Additionally, the profile likelihood method builds correlations of the systematic uncertainties, unlike the ensemble tests technique where the uncertainties are assumed to be uncorrelated, which allows the uncertainties on the measurement to be further decreased.

10.3. Profile likelihood template fit for 13 TeV measurement

The profile likelihood technique is a method to include the effects of systematic uncertainties directly in the fit to the data and provides a coherent statistical interpretation. Section 10.3.1 describes the profile likelihood fits and the development of this technique for the fits with templates for Γ_t are summarised in Section 10.3.3. Since finding the maximum of the likelihood, which is equivalent to finding the minimum of the negative logarithm of the likelihood, plays a crucial role in the determination of the correlations between the sources of the systematic uncertainties, the minimisation technique is briefly summarised in Section 10.3.2.

10.3.1. Likelihood definition

Let us first start from the definition of the profile likelihood for "standard" measurements where the parameter of interest (POI) is the observed cross-section of a rare process. The *signal strength*, μ, defined such that $\mu = 0$ corresponds to the background-only hypothesis, and $\mu = 1$ corresponds to the signal+background hypothesis, replaces the cross-section of the process, and is the POI in the "standard" measurements. The probability of observing n events when $\mu S + B$ events are expected, where S and B denote the number of signal and background events, respectively, is described [246] by

$$\mathcal{P}\left(x_1 \dots x_n|\mu\right) = \text{Poisson}\left(n|\mu S + B\right)\left[\prod_{e=1}^{n} \frac{\mu S f_{\text{S}}(x_e) + B f_{\text{B}}(x_e)}{\mu S + B}\right], \tag{10.5}$$

where the discriminating variable for event e has a value x_e, so the full dataset is denoted as $x_1 \dots x_n$. The terms $f_{\text{S}}(x)$ and $f_{\text{B}}(x)$ describe probability density functions for signal and background, respectively. When the data is fixed, $\mathcal{P}\left(x_1 \dots x_n|\mu\right)$ from Equation (10.5) is a function of μ. Using $\text{Poisson}(n|\nu) = \nu^n e^{-\nu}/n!$ the *extended likelihood* formula for the negative logarithm of the likelihood reads

$$\begin{aligned} -\ln \mathcal{L}(\mu) &= -n \ln\left(\mu S + B\right) + \left(\mu S + B\right) + \ln n! - \sum_{e=1}^{n} \ln\left[\frac{\mu S f_{\text{S}(x_e)} + B f_{\text{B}}(x_e)}{\mu S + B}\right] \\ &= \left(\mu S + B\right) + \ln n! - \sum_{e=1}^{n} \ln\left[\mu S f_{\text{S}}(x_e) + B f_{\text{B}}(x_e)\right]. \end{aligned} \tag{10.6}$$

Since in realistic measurements, where the measured distribution does not follow a known mathematical expression and only a finite number of events is available, binned distributions are used. The fractions f_{S} and f_{B} can be replaced with

$$f_{\text{S}}(x_e) = \frac{\nu_b^{\text{sig}}}{S\Delta_b} \qquad \text{and} \qquad f_{\text{B}}(x_e) = \frac{\nu_b^{\text{bkg}}}{B\Delta_b}, \tag{10.7}$$

where b is the index of the bin containing x_e and Δ_b is the width of the same bin. Normalisation of the $f(x)$ to unity implies

$$S = \sum_b \nu_b^{\text{sig}} \qquad \text{and} \qquad B = \sum_b \nu_b^{\text{bkg}}. \tag{10.8}$$

The probability model can be expressed in terms of a product of Poisson probabilities in each bin as

$$\begin{aligned}\mathcal{P}(n|\mu) &= \text{Poisson}\left(n|\mu S + B\right)\left[\prod_{b\in\text{bins}} \frac{\mu\nu_b^{\text{sig}} + \nu_b^{\text{bkg}}}{\mu S + B}\right] \\ &= \mathcal{N}_{\text{comb}} \prod_{b\in\text{bins}} \text{Poisson}\left(n_b|\mu\nu_b^{\text{sig}} + \nu_b^{\text{bkg}}\right). \end{aligned} \tag{10.9}$$

where n represents the data histogram. The combinatorial factor $\mathcal{N}_{\text{comb}}$ is constant and can thus be dropped.

The above mentioned approach allows for a clear statistical interpretation, but it needs to be modified to include systematic uncertainties of the measurement. Various sources of systematic uncertainties are considered that affect the measurement of the top-quark decay width, as is discussed in Chapter 9. For each source of the systematic uncertainty a varied distribution is produced that can be compared to the nominal distribution. Each source of systematic uncertainty is described by a single NP with an uncertainty that is measured in a dedicated *auxiliary* measurement. The likelihood with the NPs reads

$$\mathfrak{L}(n, \theta^{\mathbf{0}}|\mu, \theta) = \prod_{b\in\text{bins}} \text{Poisson}\left(n_b|\nu_b\right) \times \prod_{j\in\text{syst}+\gamma} f\left(a_j|\alpha_j\right), \tag{10.10}$$

where n_b describes the number of data events in a bin b. The term $f\left(a_j|\alpha_j\right)$ denotes the penalty from the auxiliary measurement a_j that constraints NP α_j for the source of systematic uncertainty j, including uncertainties that are fully decorrelated between the individual bins, γ. The expected number of events in bin b for a process[4] p, $\nu_{b,p}$ depends on the product of unconstrained normalisation factors for a process p, ϕ_p, on the normalisation component of the uncertainty, $\eta_p(\alpha)$, on the shape component of the uncertainty, $\sigma_{b,p}$, and on the bin-by-bin uncertainty, γ_b, and it reads

$$\nu_{b,p}(\theta_p, \alpha, \gamma_b) = \gamma_b\theta_p(\alpha)\eta_p(\alpha)\sigma_{b,p}(\alpha). \tag{10.11}$$

The total expected number of events in a bin b, ν_b is obtained by summing the expected number of events in bin b over all processes, $\nu_b = \sum_p \nu_{b,p}$. The constraint terms, $f\left(a_j|\alpha_j\right)$, depend on the type of the auxiliary measurements. Usually in an experiment, the systematic variations are provided in the form of the nominal value and $\pm 1\ \sigma$ variations represented by the related distributions. The uncertainty of the auxiliary measurements are assumed to be Gaussian thus the corresponding constraint terms are Gaussian[5]. An interpolation has to be employed to get a continuous parametrisation for the normalisation and shape effects of each NP. Each systematic variation is split into a pure normalisation effect (no shape) and a pure shape effect (no normalisation). The shape effect in a bin b for a process p is interpolated using piece-wise linear interpolation

---

[4] Process means a distribution (histogram) representing one or more physics processes.

[5] At this point a frequentist and Bayesian statistical approaches are used at the same time. The POI does not have a prior probability and it follows the frequentist approach, however the NPs do have a prior probability distribution.

$$\sigma_{b,p}(\alpha) = \sigma^0_{b,p} + I_{b,p,\mathrm{lin}}, \qquad \text{where} \qquad I_{b,p,\mathrm{lin}}(b,p,\alpha,I^0_{b,p},I^+_{b,p},I^-_{b,p}) = \begin{cases} \alpha(I^+_{b,p} - I^0_{b,p}) & \alpha \geq 0 \\ \alpha(I^0_{b,p} - I^-_{b,p}) & \alpha < 0 \end{cases}, \tag{10.12}$$

where the $I^+_{b,p}$, $I^-_{b,p}$ and $I^0_{b,p}$ terms represent the expected yields for the systematic up variation, down variation and the nominal prediction for a process p in a bin b, respectively. This allows for non-symmetric up and down systematic variations, however, the interpolation results in a kink around the nominal expected yield where the first derivative has a discontinuity. The non-differentiable property of the interpolation can cause problems during the minimisation process, and thus all systematic variations are symmetrised by taking the average up minus down variation.

The normalisation component of the systematic source for a process p is interpolated using an exponential interpolation

$$\eta_p(\alpha) = I_{\mathrm{exp}}, \qquad \text{where} \qquad I_{\mathrm{exp}}(p,\alpha,I^0_p,I^+_p,I^-_p) = \begin{cases} \left(I^+_p/I^0_p\right)^{\alpha} & \alpha \geq 0 \\ \left(I^-_p/I^0_p\right)^{-\alpha} & \alpha < 0 \end{cases}. \tag{10.13}$$

The exponential interpolation with a Gaussian constraint is equivalent to a log-normal distribution. For small response, $\alpha \ll 1$, the exponential interpolation behaves like a piece-wise linear interpolation. The main benefit of the exponential interpolation is that it prevents negative normalisation contributions.

The treatment of the MC statistical uncertainty, originating from the finite number of simulated events, follows the procedure outlined by Barlow and Beeston [247]. In an individual bin, b, the contribution to the statistical model from the finite MC sample yields

$$\mathrm{Poisson}\left(n_b|\nu_b(\alpha) + \gamma_b\nu^{\mathrm{MC}}_b(\alpha)\right)\mathrm{Poisson}\left(m_b|\gamma_b\tau_b\right), \tag{10.14}$$

where n_b is the number of events observed in the bin, $\nu_b(\alpha)$ is the number of events expected in the bin where MC statistical uncertainties do no need to be included, ν^{MC}_b is the number of events estimated using MC samples where the statistical uncertainty needs to be taken into account. The factor γ_b is the nuisance parameter[6], with a Poisson constraint term. It should be noted that this does not follow the Barlow-Beeston procedure completely, as only one NP per bin enters the fit for the total MC expectation, instead of each MC sample, which is a good compromise between including the MC statistical uncertainty and having hundreds of NPs in the fit. The actual implementation of the MC statistical uncertainties in the measurement is slightly modified, as explained in Section 9.3. The likelihood model building utilises the *HistFactory* software package [246].

10.3.2. Minimisation of the negative logarithm of the likelihood

The most probable value for the POI corresponds to the position of the maximum of the likelihood which is equivalent to finding the minimum of the negative logarithm of the likelihood. The measurement at 13 TeV utilises distributions with $O(10)$ bins and $O(100)$ sources of systematic

---

[6] Symbol γ is used because in the Bayesian approach with a flat prior distribution, the posterior distribution follows the Gamma distribution.

uncertainties, thus finding the minimum of the negative logarithm of the likelihood poses an extremely complex, multi-dimensional minimisation problem.

The minimisation algorithm exploits the *MINUIT* [248] framework with the *MIGRAD* minimisation technique. The *MIGRAD* technique implements the *Davidon–Fletcher–Powell* approach [249–251] to the minimisation that can be summarised in the following steps.

1. Start from given values of parameters, $\mathbf{x}$.
2. Calculate the gradient (first derivatives) G in the given point, assume the Hessian matrix (matrix of second derivatives) is unity.
3. Perform a linear search, along the direction of the gradient: find α which minimises $F(\mathbf{x} - \alpha V \times G)$, where F is the negative logarithm of the likelihood function. V is a covariance matrix of the parameters of the fit which is equal to the inverse of the Hessian matrix.
4. Correct the covariance matrix V using formulae from [251].
5. Repeat until the estimated distance to minimum (EDM)[7], $\mathrm{EDM} = G^{\mathrm{T}} V G$ is sufficiently small ($\mathrm{EDM} < 0.001$).

The *MIGRAD* technique prevents the minimisation from being stuck in a local minimum, as the procedure outlined above allows to "climb hills" (local maxima) around the local minima. Additionally, the correlation matrix of the NPs, that can be trivially obtained from the covariance matrix, is available almost as a by-product of the minimisation procedure. The diagonal elements of the correlation matrix are used to derive the posterior (post-fit) uncertainties of the NPs and the POI. The correlation matrix is a symmetric matrix, thus the posterior uncertainties are also symmetric. However, it provides a good description of the region around the minimum only if the region is represented well by a quadratic function of the parameters. To obtain a more accurate estimation of the uncertainty of the POI, the *MINOS* [248] technique, which takes into account correlations of the parameters and does not rely on the quadratic shape of the logarithm of the likelihood function, is used which may lead to non-symmetric uncertainties on the POI, the top-quark decay width.

10.3.3. Adaptation to templates

The likelihood definition described in Section 10.3.1 is a powerful tool for measurements of cross-sections, more precisely, signal strength. However, it does not provide an optimal tool for the fitting of multiple different distributions representing a continuous parameter, a procedure that is crucial in the measurement of the top-quark decay width. The main problem arises from the fact that the standard profile likelihood implementation allows only 1 σ variations for the histograms, which is insufficient for the width measurement as more than three templates are used in the measurement. The approach chosen for the analysis transforms the problem of fitting of multiple distributions corresponding to the variable parameter into a well known problem of normalisation fitting. Symbolically, this can be expressed by the transformation

$$\mu S_b(\theta) \rightarrow S_b(\mu, \theta). \tag{10.15}$$

---

[7] EDM represents vertical distance to minimum in the case of a quadratic function.

To achieve this transformation, an interpolation between the width templates is employed. The normalisation of width templates, T_i, is additionally weighted with w_i that depends on Γ_t representing template i and it can be expressed as

$$T(\Gamma_t) = \sum_{i=1}^{N} w_i(\Gamma_t) T_i, \tag{10.16}$$

given N generated templates, T_i, for Γ_t. The simplest expression for the weight w_i uses a piece-wise linear interpolation

$$w_i(\Gamma_t) = \begin{cases} 0 & \text{if} \quad \Gamma_t < \Gamma_{t,i-1}, \\ 1 - \frac{\Gamma_{t,i}-\Gamma_t}{\Gamma_{t,i}-\Gamma_{t,i-1}} & \text{if} \quad \Gamma_{t,i-1} < \Gamma_t < \Gamma_{t,i}, \\ 1 - \frac{\Gamma_t-\Gamma_{t,i}}{\Gamma_{t,i+1}-\Gamma_{t,i}} & \text{if} \quad \Gamma_{t,i} < \Gamma_t < \Gamma_{t,i+1}, \\ 0 & \text{if} \quad \Gamma_t > \Gamma_{t,i+1}. \end{cases}$$

Figure 10.5 illustrates the weights for the piece-wise linear interpolation for the values of Γ_t templates chosen for the 13 TeV measurement. The chosen interpolation allows for a clear interpretation where for each value of the Γ_t, only two templates contribute. The fit minimisation procedure optimises the normalisation of individual templates and the resulting normalisation is translated to the POI value using the piece-wise interpolation. To better illustrate the procedure, let us assume that the "true" decay width has value a of $\Gamma_t^{\text{true}} = 1.5$ GeV and only three templates for the Γ_t are available that correspond to values $\Gamma_t = 1.0, 2.0$ and 3.0 GeV. Then, in an ideal scenario, the fit should converge to a point where only templates corresponding to $\Gamma_t = 1.0$ and 2.0 GeV have a non-zero contribution and each template contributes with the weight equal to 0.5. The validation of the procedure for the distributions used in the measurement is summarised in Section 10.5.

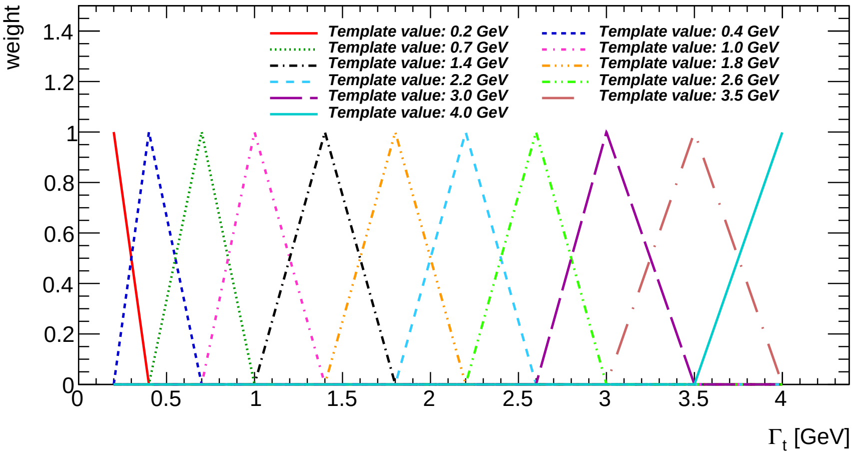

Figure 10.5.: Weights used in the fit with the Γ_t templates using the profile likelihood technique. Lines with different colours represent the weights for a given template.

10.4. Choice of observables

The 8 TeV analysis showed that the choice of observables used in the fit affects the total uncertainty of the measurement. The 13 TeV measurement utilises different observables in the individual analysis regions. If the observables from a single channel are uncorrelated, the definition of the likelihood from Equation (10.10) can be easily extended by multiplying the likelihoods for the considered distributions for each observable. The observables are split into observables that are sensitive to the decay width of the top quark, and observables that are insensitive to the decay width but are sensitive to the dominant systematic uncertainties affecting the measurement. The observables sensitive to the decay width act as *signal regions* in the “standard” profile likelihood measurements and observables insensitive to the decay width act as *control regions*. The *control regions* are designed to control and, potentially, constrain the dominant systematic uncertainties.

The $m_{\ell b}$ distribution has been proven to be the optimal variable for the measurement of the top-quark decay width in the 8 TeV analysis and it is also used for the 13 TeV measurement in both analysis channels. To minimise the NLO effect in the decay vertex, the $m_{\ell b}$ distributions are restricted to $m_{\ell b} < 150$ GeV.

10.4.1. Lepton+jets channel

The choice of the $m_{\ell b}$ distribution in the lepton+jets channel allows distributions from the hadronic hemisphere of the $t\bar{t}$ decay to be used, as these distributions originate from a different top quark than the $m_{\ell b}$ and are expected to be uncorrelated. A natural choice for a variable that is insensitive to the decay width of the top quark but is sensitive to the dominant systematic uncertainties, especially JES and JER, is the reconstructed mass of the W boson from the hadronically decaying W, m_W. Additionally, the ratio of the reconstructed invariant top-quark mass and the reconstructed invariant mass of the W boson, $R_{3/2}$, can be used in the measurement of the decay width due to its large sensitivity to the decay width and small sensitivity to scales and their uncertainties. The ambiguity in the jet-to-parton assignment is resolved following techniques summarised in Section 8.1. The $m_{\ell b}$ and $R_{3/2}$ distributions for various top-quark decay widths, obtained from the reweighting technique described in Section 10.1.1, are displayed in Figure 10.6. Two different choices of variables in the lepton+jets channel are compared:

1. $m_{\ell b}$ distribution from combined electron+jets and muon+jets events as a variable sensitive to the top-quark decay width, and m_W from the combined electron+jets and muon+jets events as a control variable.

2. $m_{\ell b}$ distribution from combined electron+jets and muon+jets events, and $R_{3/2}$ from muon +jets events as variables sensitive to the top-quark decay width. The m_W distribution from electron+jets events is used as a control variable. Distributions of $R_{3/2}$ and m_W are expected to be correlated and thus they need to come from an orthogonal selection, which is ensured by the split by charged lepton flavours.

Variables originating from the decays of the semileptonically and fully hadronically decaying top quark are expected to be uncorrelated but due to the reconstruction technique described in Section 8.1, a correlation can appear. The correlations are ≤ 0.01 and the variables are thus treated as uncorrelated further in the analysis. The corresponding figures are presented in Appendix E.

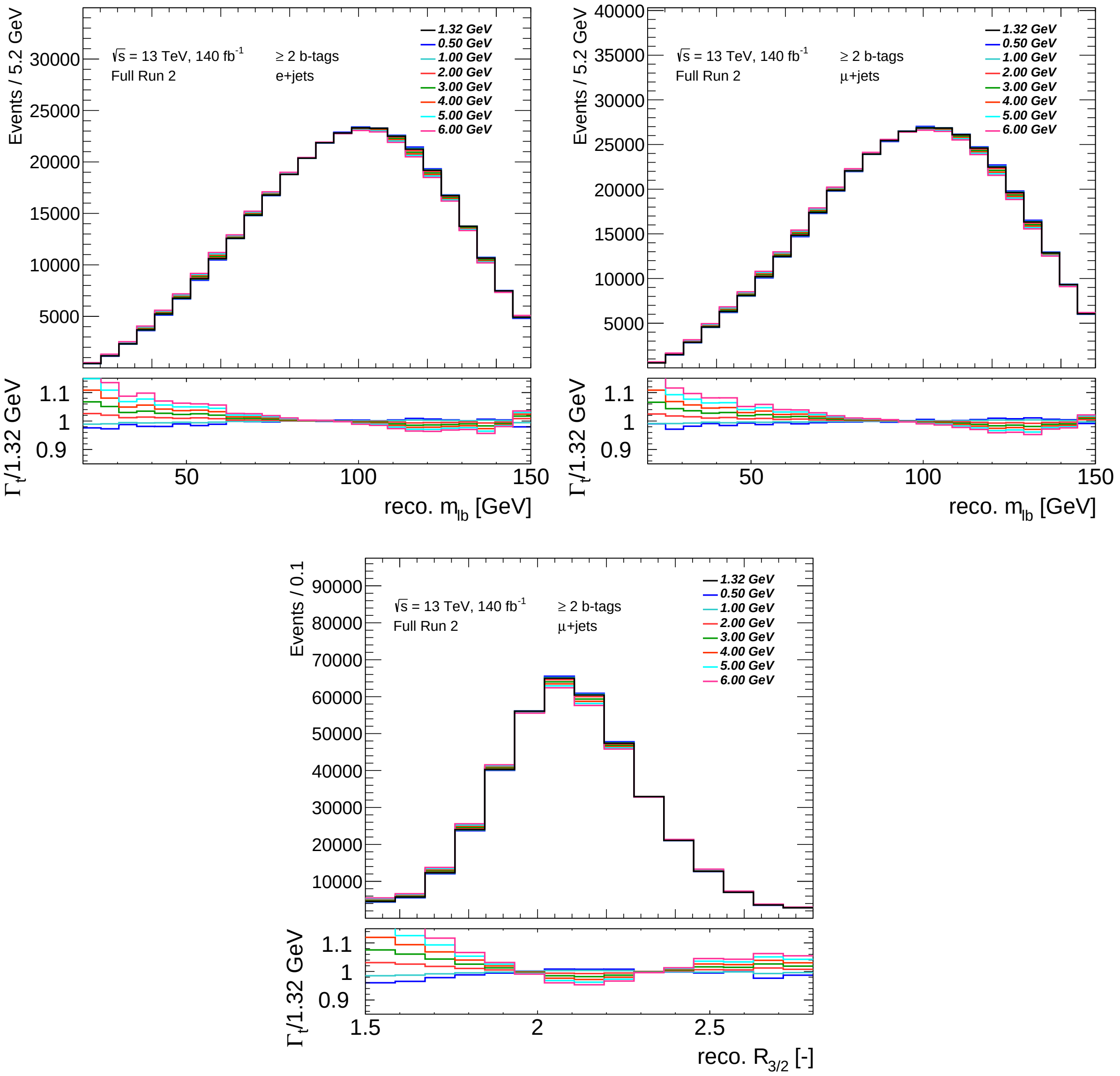

Figure 10.6.: Template distributions for various values of Γ_t for the $m_{\ell b}$ distribution in the electron+jets channel (top-left), muon+jets channel (top-right) and for the $R_{3/2}$ distribution in muon+jets channel (bottom). The additional requirement on the BDT score > 0.7 is applied. The bottom part of each plot shows the ratio of events for alternative top-quark decay widths with respect to the SM expected value $\Gamma_t = 1.32$ GeV. The first bins contain underflow events. The last bin contains overflow events in the case of $R_{3/2}$ distribution.

10.4.2. Dilepton channel

The choice of the variables in the dilepton channel is limited considering that any techniques that reconstruct the full kinematics of the decaying top quarks suffer from large systematic uncertainties, mainly from the uncertainty of $E_{\mathrm{T}}^{\mathrm{miss}}$ energy scale and resolution. Despite the limited possibilities, the $m_{\ell b}$ observables can be easily reconstructed without the need to reconstruct the kinematics of the neutrinos. Thus, $m_{\ell b}$ is chosen as the observable sensitive to the decay width of the top quark. For the same reasons as in the lepton+jets channel, only values of $m_{\ell b} < 150$ GeV are considered in the fit. Due to two top quarks decaying leptonically present in the dilepton channel, two $m_{\ell b}$ variables can be reconstructed in the dilepton channel per event. Both of these variables are considered, and the corresponding histograms are filled twice per event, the ambiguity of the pairing of the charged leptons and the b-jets is resolved with the technique described in Section 8.2. The distribution of the $m_{\ell b}$ variable in the dilepton channel for various values of the Γ_t is displayed in Figure 10.7.

The variable insensitive to the top-quark decay width and sensitive to the dominant systematic uncertainties is m_{bb}, the invariant mass of the two b-jet system. m_{bb} does not originate from a decay of an unstable particle and is not expected to have a distinct peak in the distribution. Nevertheless, m_{bb} is the variable that is sensitive to the JES and JER and especially to the JES uncertainties related to the b-jets, which may differ from those for the light-flavour jets. The combination of the lepton+jets channel and the dilepton channel thus provides strong control of the jet related uncertainties via m_W and m_{bb} observables. Since $m_{\ell b}$ and m_{bb} observables from the dilepton channel are expected to be correlated, an orthogonal event selection is used for the variables. The $m_{\ell b}$ distribution is built from events containing exactly one electron and one muon, the $e\mu$ channel, while the m_{bb} distribution is built from combined events with the same flavour of the leptons, ee and $\mu\mu$, which ensures the statistical independence of the distributions. The $m_{\ell b}$ distribution exploits $e\mu$ events as these events have a higher expected number of events, due to the branching ratio of the process and looser selection criteria but also due to the smaller expected background.

10.4.3. Lepton+jets optimisation

To identify the optimal selection on the BDT score (see Section 8.1), different selection values of the BDT output have been tested in the early stages of the analysis to identify the selection that leads to the lowest total expected uncertainty on Γ_t in the lepton+jets channel. Selection with a BDT output $> 0.3, > 0.5, > 0.7$ and > 0.9 are compared in a fit with the dominant systematic uncertainties, that were available during the time of the test, to the distributions representing $\Gamma_t = 1.32$ GeV and $m_t = 172.5$ GeV. Table 10.5 shows the total expected uncertainties for various BDT selection requirements for the configuration with the $R_{3/2}$ variable. Although some of the systematic uncertainties were not available during the test, it can be seen that the BDT selection criterion does not affect the expected uncertainty significantly between BDT requirements of 0.3–0.7. The requirement of BDT score > 0.7 has lead to the lowest expected total uncertainty on the decay width, and is used further in the analysis.

As described in Section 10.4.1 two sets of observables are tested in the lepton+jets channel, with and one set without the $R_{3/2}$ observable. The expected uncertainties for both choices are compared in the fit to expected distributions for $\Gamma_t = 1.32$ GeV and $m_t = 172.5$ GeV. The fit includes all considered systematic uncertainties for the analysis. Table 10.6 shows the expected uncertainties for both configurations. Since the setup that includes the $R_{3/2}$ observable yields only marginally better expected uncertainty, other criteria have to be considered. One of the

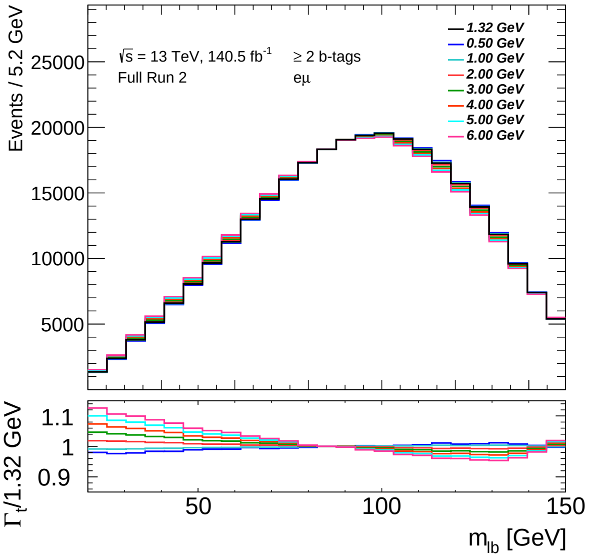

Figure 10.7.: Template distributions for various values of Γ_t for the $m_{\ell b}$ distribution in the $e\mu$ channel. The bottom part of the plot shows the ratio of events for alternative top-quark decay widths with respect to the SM expected value $\Gamma_t = 1.32$ GeV. The first bin contains underflow events.

BDT score	**Total exp. uncertainty**
> 0.3	± 0.367 GeV
> 0.5	± 0.355 GeV
> 0.7	± 0.349 GeV
> 0.9	± 0.490 GeV

Table 10.5.: Total expected uncertainty estimated in the early stages of the analysis in the lepton+jets channel for various requirements on the BDT score. The fit setup with the $R_{3/2}$ variable is used. Some of the systematic uncertainties were not available for the comparison.

main disadvantages of using the setup with $R_{3/2}$ is the stability of the fit. Including the $R_{3/2}$ observable in the fit increases the number of bins significantly, thus making the fit less stable. This results in frequent non-convergence with even minor changes in the fit, e.g. decorrelating some of the NP between the distributions. Therefore a setup that only includes distributions of $m_{\ell b}$ and m_W from the combined electron+jet and the muon+jets channel is used further in the analysis.

Fit setup	**Total exp. uncertainty**
With $R_{3/2}$	$+0.64$ GeV -0.49 GeV
Without $R_{3/2}$	$+0.68$ GeV -0.53 GeV

Table 10.6.: Expected total uncertainties on Γ_t for two sets of observables. The first set contains $m_{\ell b}$, $R_{3/2}$ and m_W, the second set contains $m_{\ell b}$ and m_W. The uncertainties are obtained from the fit to the expected distribution representing $\Gamma_t = 1.32$ GeV and $m_t = 172.5$ GeV. The BDT score is required to be > 0.7.

10.5. Fit validation

Several procedures have been employed to validate the fitting procedure. The tests for the linearity of the response to the decay width variations rely on the fits of the width templates, as described in Section 10.3, to a combination of background templates and a $t\bar{t}$ signal template with a fixed Γ_t, the so called *Asimov fits*[8]. The tests are carried out to check the mean value of the fitted Γ_t. The fitted value should correspond to the value of Γ_t used to build the given Asimov dataset. Deviations from this value would correspond to a bias in the procedure. Furthermore, the post-fit mean values of the NP probability density functions, so called *pulls*[9], should be centred at zero as all the Asimov templates are built from the nominal distributions. Pulls not-centred at zero would point to a non-linearity of the response to the decay width, as some of the width effects would be compensated by the pulls of systematic uncertainties. The post-fit standard deviations of the NP probability density functions represent the posterior uncertainty of the given NP. Table 10.7 shows the fitted value of Γ_t with the corresponding uncertainties in two fit scenarios: a) when no systematic uncertainties are considered (fit with statistics only) and b) fit with all considered systematic uncertainties as summarised in Chapter 9. Results of the Asimov fit for both $t\bar{t}$ decay channels are shown. Good agreement between the fitted values and the input values is obtained, with the non-closure ≤ 0.02 GeV. It can also be seen that the expected total uncertainty depends on the mean value of the fit.

The pull distributions for the Asimov fits with input $\Gamma_t = 1.32$ GeV are displayed in Figure 10.8 for the lepton+jets channel and in Figure 10.9 for the dilepton channel. No pulls are observed in the Asimov fits, while some of the NPs are constrained in the fit. These include mainly uncertainties for the $t\bar{t}$ modelling and, to some extent, also for the JES and JER uncertainties. The constraints partially arise from the fact that some of the uncertainties are

---

[8] Asimov dataset is named after a short story *Franchise*, by Issac Asimov (Isaac Asimov, Franchise, in Isaac Asimov: The Complete Stories, Vol. 1, Broadway Books, 1990), where elections are held by selection of a single person to represent the entire population.

[9] Sometimes the word *pull* is used to represent both the shift of the mean value and the standard deviation.

conservative, especially $t\bar{t}$ modelling uncertainties, while the JES and JER uncertainties are constrained because the dedicated calibrations do not use the full Run 2 dataset of 140 fb^{-1}, and for JER the calibrations are done only with the dedicated 2017 LHC conditions and they do not reflect LHC conditions of the whole Run 2.

Correlations of the NP, obtained from the minimisation technique described in Section 10.3.2, are displayed in Appendix G. Figure 10.10 shows the likelihood scan of Γ_t and the NP ranking plot for the lepton+jets channel, and similarly for the dilepton channel in Figure 10.11. The nuisance parameter ranking plot is obtained from running the Asimov fit to systematically shifted distributions for both up and down variation with the pre- and post-fit constraints, the difference between the fitted values and the nominal values are shown, which gives a hint on the impact of the individual uncertainty sources on the measurement. It can be seen that the lepton+jets channel is dominated by the uncertainties in the normalisation of the multijet background as well as $t\bar{t}$ modelling uncertainties. Although, the multijet process has only small contribution it has a distinct effect on the Γ_t as the multijet process populates mostly regions with low value of $m_{\ell b}$. But the regions with low value of $m_{\ell b}$ are also very sensitive to the decay width as is displayed in Figures 10.6 and 10.7. The dilepton channel is dominated by the $t\bar{t}$ modelling uncertainties. The likelihood scan is obtained by setting the POI, Γ_t, to a fixed value and then running the minimisation procedure to obtain the best likelihood value, these values are displayed on the vertical axis[10].

To further validate the fitting procedure the pseudo-experiment approach is used to cross-check the expected statistical uncertainties obtained from the fit. Pseudo-data are generated 3000 times and then fitted with the procedure outlined in Section 10.3.3 while excluding systematic uncertainties. The mean values of the individual fits are then filled into a histogram. The resulting histograms are then fitted with a Gaussian function. The mean value and standard deviation of the Gaussian fits are compared to the input decay widths and expected statistical uncertainties obtained from the fit. Possible deviations of the mean values from the input widths would imply a bias in the technique. Deviations of the width of the Gaussian from the expected statistical uncertainties would suggest an incorrect estimation of the uncertainties. The mean values of the fits agree with the input width within uncertainties, for the input $\Gamma_t > 0.5$ GeV. Deviations from the Gaussian shape are observed for $\Gamma_t < 0.5$ GeV which is reflected by the mean values and standard deviations. The deviations originate from the sharp edge at $\Gamma_t = 0.2$ GeV which is the smallest considered width template. For $\Gamma_t > 0.5$ GeV the widths of the Gaussian curves correspond to the expected statistical uncertainties obtained from the fit as summarised in Table 10.7. This provides a strong proof that the chosen fitting strategy is valid. The individual distributions are presented in Appendix F.

---

[10] The values are shifted by the likelihood value for the most probable value of Γ_t.

		Lepton+jets		**Dilepton**	
Input Γ_t [GeV]	**Fit setting**	**Mean value** [GeV]	**Uncert.** [GeV]	**Mean value** [GeV]	**Uncert.** [GeV]
0.5	Stat	0.51	$^{+0.14}_{-0.13}$	0.51	$^{+0.17}_{-0.16}$
0.7	Stat	0.70	$^{+0.15}_{-0.14}$	0.70	$^{+0.19}_{-0.17}$
1.0	Stat	1.00	$^{+0.16}_{-0.15}$	1.00	$^{+0.20}_{-0.19}$
1.32	Stat	1.32	$^{+0.16}_{-0.16}$	1.32	$^{+0.21}_{-0.20}$
1.5	Stat	1.50	$^{+0.16}_{-0.16}$	1.50	$^{+0.21}_{-0.21}$
2.0	Stat	2.00	$^{+0.16}_{-0.16}$	2.00	$^{+0.22}_{-0.22}$
2.5	Stat	2.50	$^{+0.16}_{-0.16}$	2.50	$^{+0.22}_{-0.22}$
0.5	Stat+Syst	0.52	$^{+0.38}_{-0.22}$	0.51	$^{+0.39}_{-0.28}$
0.7	Stat+Syst	0.70	$^{+0.49}_{-0.31}$	0.70	$^{+0.44}_{-0.35}$
1.0	Stat+Syst	1.00	$^{+0.60}_{-0.42}$	1.00	$^{+0.47}_{-0.42}$
1.32	Stat+Syst	1.32	$^{+0.68}_{-0.53}$	1.32	$^{+0.48}_{-0.46}$
1.5	Stat+Syst	1.50	$^{+0.71}_{-0.57}$	1.50	$^{+0.49}_{-0.47}$
2.0	Stat+Syst	2.00	$^{+0.78}_{-0.66}$	2.00	$^{+0.51}_{-0.48}$
2.5	Stat+Syst	2.50	$^{+0.83}_{-0.73}$	2.50	$^{+0.53}_{-0.50}$

Table 10.7.: Summary of the tests of the fitting procedure with the statistics only fit and a fit with the full systematics model for the fixed template for various top-quark decay widths. Mean value and the expected uncertainty for each fit are shown for the lepton+jets channel and for the dilepton channel. Good agreement between the input width and the fitted width is observed.

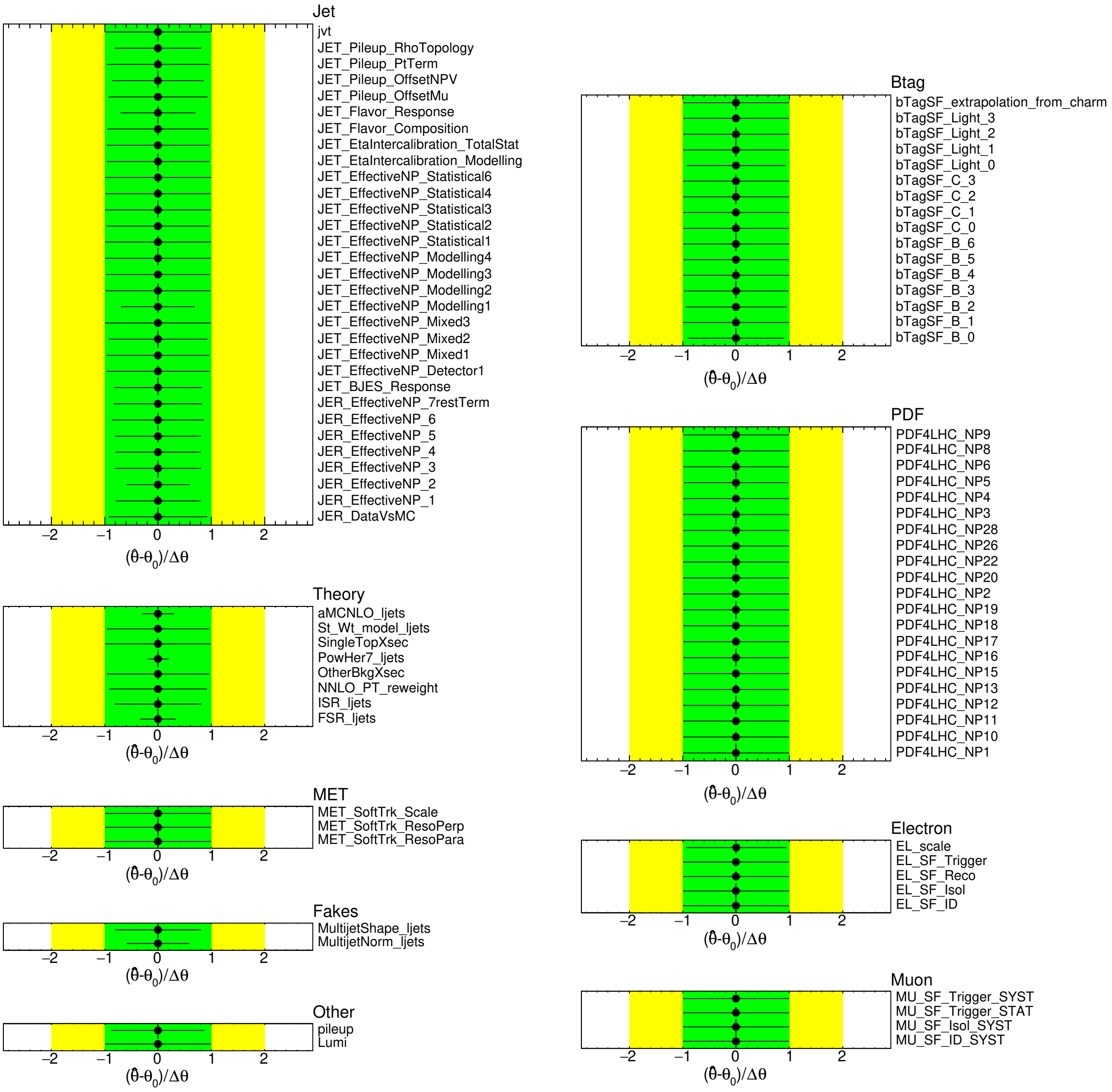

Figure 10.8.: The pull distributions for the NPs used in the fit for the lepton+jets channel. The black dots represent the post-fit mean value of the NP, the lines represent the post-fit NP uncertainties. The green and the yellow bands represent the pre-fit one and two standard deviations, respectively.

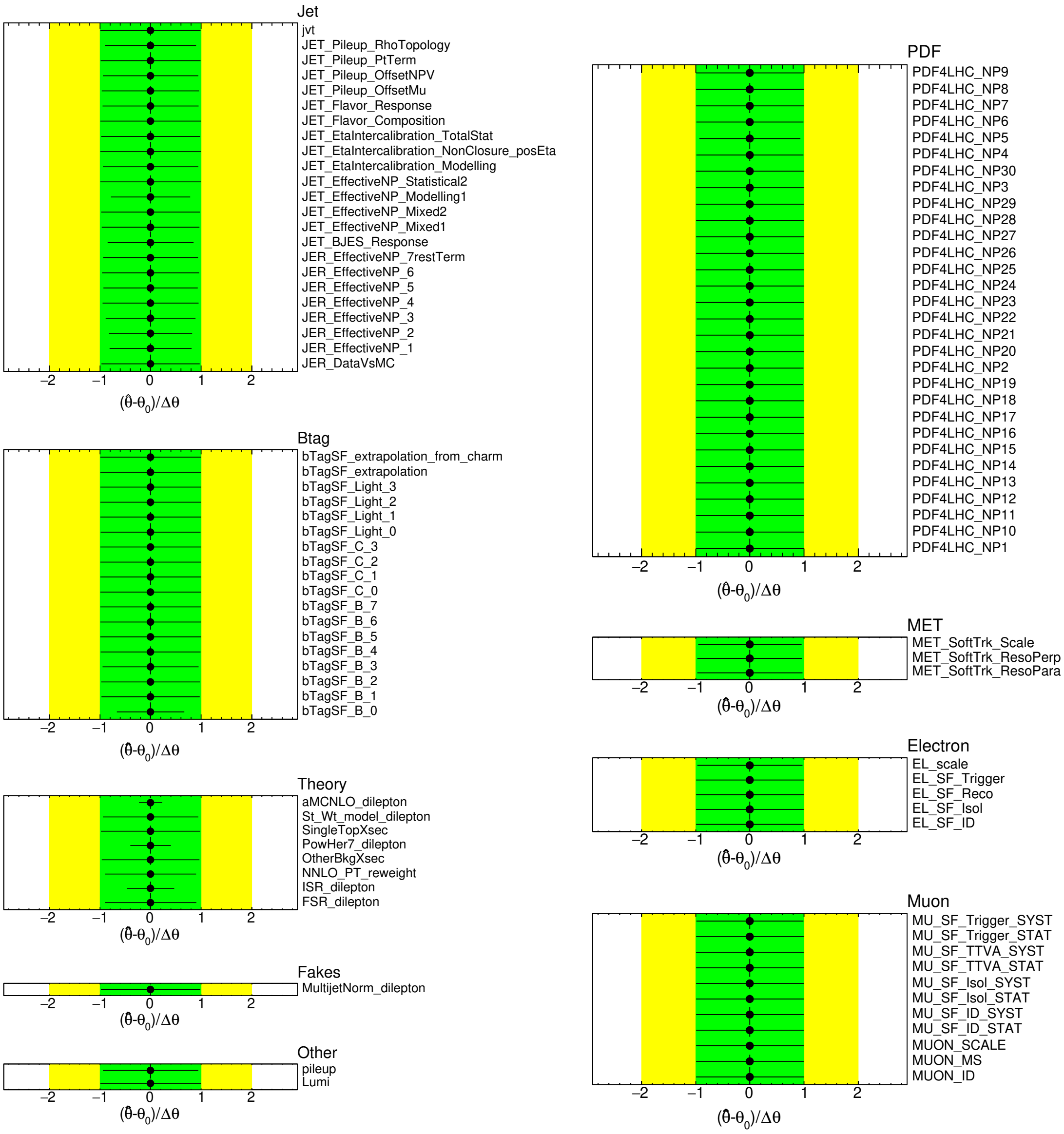

Figure 10.9.: The pull distributions for the NPs used in the fit for the dilepton channel. The black dots represent the post-fit mean value of the NP, the lines represent the post-fit NP uncertainties. The green and the yellow bands represent the pre-fit one and two standard deviations, respectively.

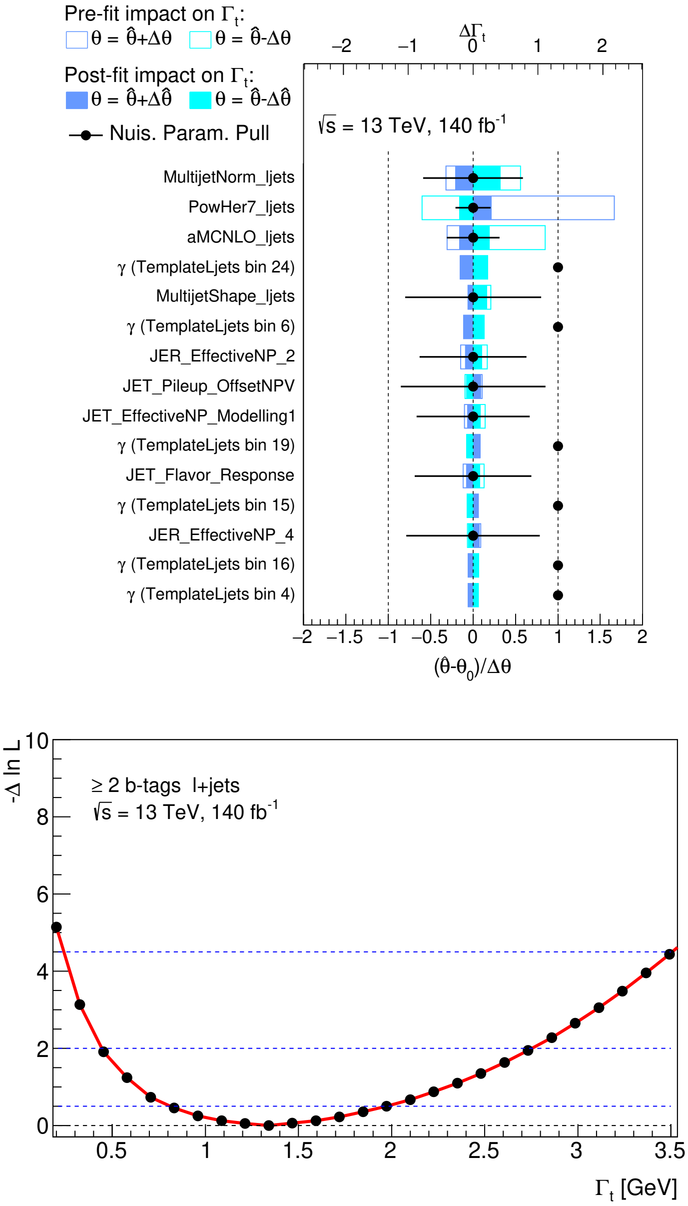

Figure 10.10.: The ranking plot (top) and the likelihood scan (bottom) for the top-quark decay width in the lepton+jets channel. Only the 15 highest ranking NPs are shown. The boxes represent the effect on Γ_t with the full boxes representing the post-fit values and empty boxes representing the pre-fit values. The points with the error bars represent the pulls of the NPs. For the NPs related to the MC statistical uncertainties, γ, the nominal value is represented by 1, while for other NPs it is represented by 0. The input top-quark decay width is $\Gamma_t = 1.32$ GeV.

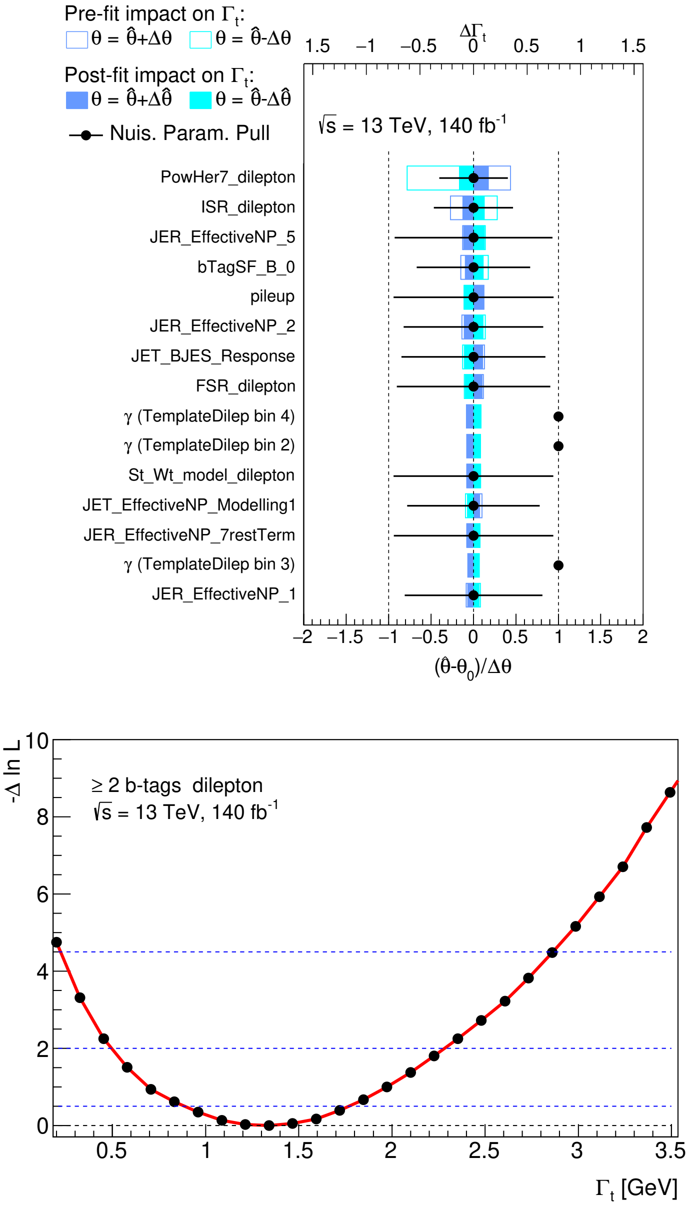

Figure 10.11.: The ranking plot (top) and the likelihood scan (bottom) for the top-quark decay width in the dilepton channel. Only the 15 highest ranking NPs are shown. The boxes represent the effect on Γ_t with the full boxes representing the post-fit values and empty boxes representing the pre-fit values. The points with the error bars represent the pulls of the NPs. For the NPs related to the MC statistical uncertainties, γ, the nominal value is represented by 1, while for other NPs it is represented by 0. The input top-quark decay width is $\Gamma_t = 1.32$ GeV.

CHAPTER 11

Results

This chapter summarises the results obtained from the fit to data. Section 11.1 focuses on the results obtained from the 8 TeV measurement using the concatenated distributions of the $m_{\ell b}$ and $\Delta R_{\text{min}}(j_b, j_l)$ observables in eight orthogonal regions. The 8 TeV result has been published in Reference [245]. The results of the 13 TeV measurement are presented in Section 11.2 and Section 11.3 for the lepton+jets and the dilepton channels, respectively. Finally, Section 11.4 summarises the results of the combined lepton+jets and dilepton channel profile likelihood template fit to the data at $\sqrt{s} = 13$ TeV.

11.1. 8 TeV results

Concatenated distributions of $m_{\ell b}$ and $\Delta R_{\text{min}}(j_b, j_l)$, defined in Section 10.2, are split into eight orthogonal regions and are simultaneously fitted to the data following the binned likelihood template fit described in Section 10.2.3. Figure 11.2 shows the post-fit comparison of the concatenated distributions. For reasons of visibility, the jet $|\eta|$ regions are split into two figures.

Figure 11.1 displays the likelihood curve of the fit of the 55 width templates as discussed in Section 10.2.3. A quadratic fit to the likelihood points, which follows the parabolic shape, is shown. The likelihood values, given as twice the negative logarithm of the likelihood, $-2\mathfrak{L}$, are shifted so that the minimum of the curve corresponds to $-2\Delta\mathfrak{L} = 0$. The statistical uncertainty, which contains the contributions from the finite number of the data events and normalisation of the backgrounds, is inferred from the likelihood curve as the width of the curve at $-2\Delta\mathfrak{L} = 1$ around the minimum.

The measured decay width reads

$$\Gamma_t = 1.76 \pm 0.33(\text{stat.})^{+0.79}_{-0.68}(\text{syst.})\text{ GeV} = 1.76^{+0.86}_{-0.76}\text{ GeV}, \tag{11.1}$$

assuming the top-quark mass $m_t = 172.5$ GeV. The result is in good agreement with the SM prediction of $\Gamma_t = 1.322$ GeV corresponding to NNLO corrections [132].

The pre-fit and post-fit yields for signal and backgrounds are summarised in Table 11.1. Both absolute and relative differences are shown, the relative difference is also displayed in terms of standard deviations, σ, summarised in Table 10.1. The measured $t\bar{t}$ cross-section of 258.3 pb agrees well with the predicted cross-section of the $t\bar{t}$ process, $\sigma_{t\bar{t}} = 253^{+15}_{-16}$ pb [67, 69–71].

Process	**Pre-fit yields**	**Post-fit yields**	**Rel. difference**	**Rel. difference [σ]**
$t\bar{t}$	153138± 9847	156363± 750	+ 2.1 %	+0.33
SingleTop	6731± 1144	5704± 925	−15.3 %	−0.90
$W + bb/cc$	8381± 922	7063± 507	−15.7 %	−1.43
$W + c$	3363± 908	1650± 550	−50.9 %	−1.89
$W +$ light	1629± 65	1603± 81	− 1.6 %	−0.40
Z+jets	2521± 1210	2772± 710	+10.0 %	+0.21
Diboson	522± 251	322± 241	−38.3 %	−0.80
Multijet	5810± 1739	6074± 377	+ 4.5 %	+0.15
Total	182083±10160	181551±1640	− 0.3 %	−0.05

Table 11.1.: Pre-fit and post-fit yields for the $t\bar{t}$ signal and individual backgrounds. The numbers represent the total yields summed over all eight analysis channels. Relative differences in percentages and in standard deviations, σ, are shown.

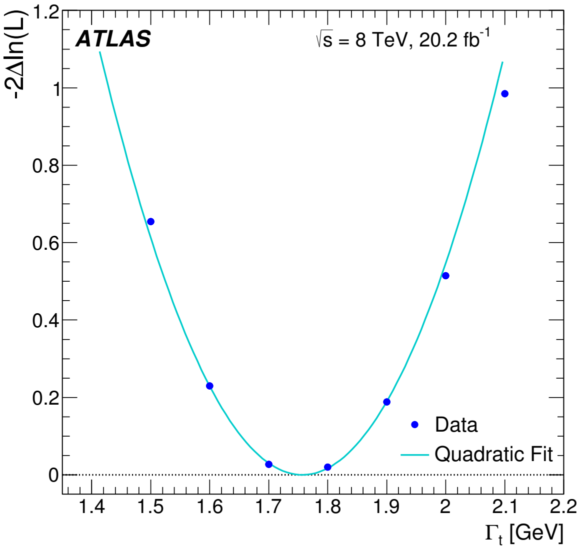

Figure 11.1.: Likelihood curve obtained from the binned likelihood fit to the data. The quadratic fit to the likelihood points illustrates the parabolic behaviour of the fit [245].

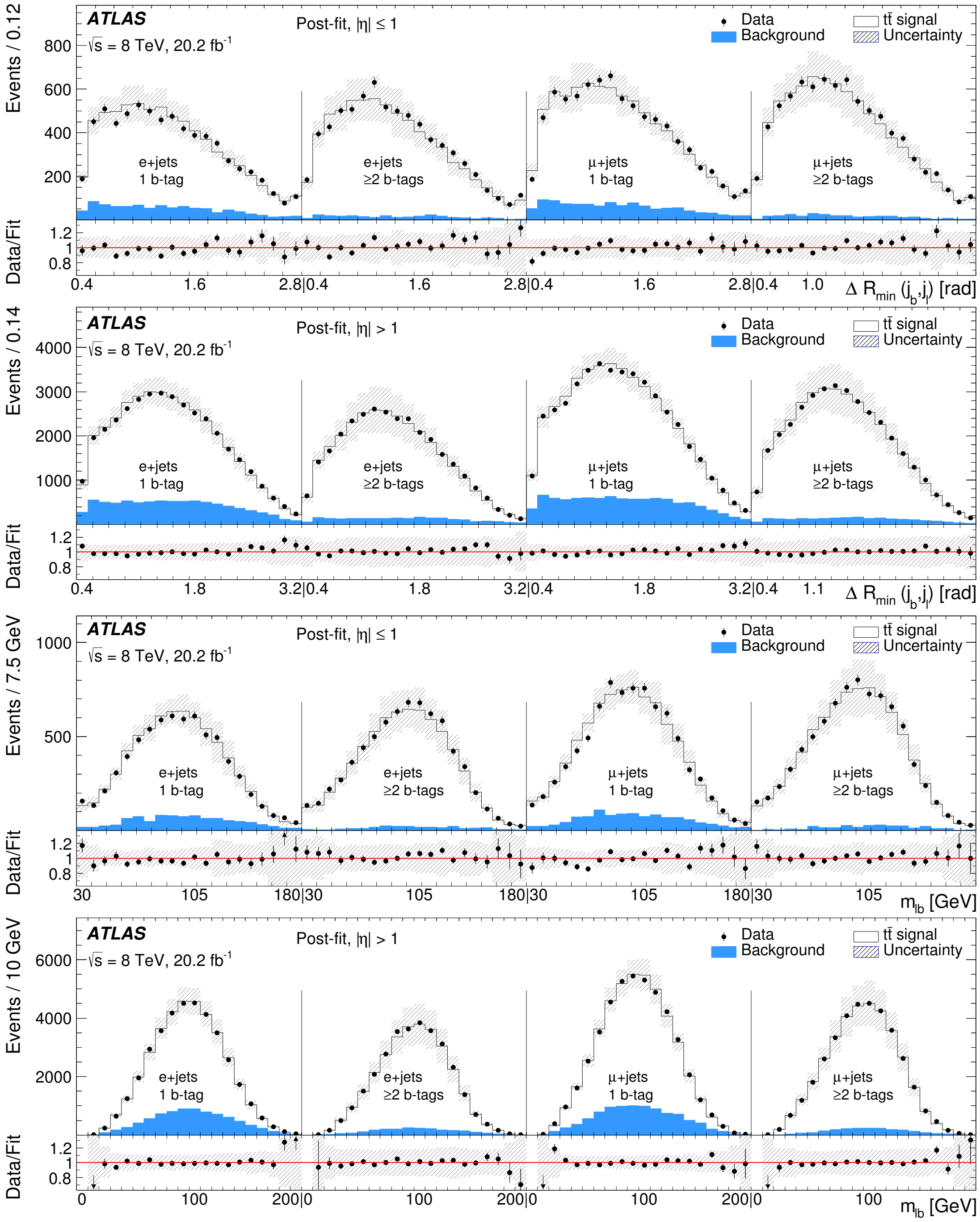

Figure 11.2.: Post-fit distributions based on the best fit template for $\Delta R_{\text{min}}(j_b, j_l)$ (top) and $m_{\ell b}$ (bottom). The background contributions are combined into a single contribution. The vertical lines show boundaries between individual flavour, b-tag and jet $|\eta|$ regions. The hatched bands represent the total uncertainty. The systematic uncertainties are calculated bin-by-bin from the systematic variations by adding differences in quadrature. Then, statistical and systematic uncertainties are added in quadrature to obtain the quoted total uncertainty. The lower panel shows the ratio of observed data and the post-fit sum of the $t\bar{t}$ signal and background [245].

11.2. 13 TeV lepton+jets result

A profile likelihood fit is employed to extract the top-quark decay width from the observed data collected by the ATLAS detector in the years 2015–2018 for events that pass the lepton+jets selection described in Section 7.3. Templates corresponding to various input decay widths are constructed for the $m_{\ell b}$ observable from the combined distributions from the electron+jets and the muon+jets channels. Additionally, a control region comprised of the distribution of the reconstructed W boson mass in the combined electron+jets and muon+jets channel is used to control and constrain the dominant systematic uncertainties considered in the analysis. The measured top-quark decay width in the lepton+jets channel is

$$\Gamma_t = 1.30^{+0.50}_{-0.59}\ \text{GeV}, \tag{11.2}$$

assuming $m_t = 172.5$ GeV.

Figure 11.3 shows pulls and constraints of the NPs of all systematic uncertainties considered in the measurement. The likelihood scan of the POI, the decay width, and the systematic uncertainty ranking is shown in Figure 11.4. Some differences in the ranking are observed compared to the Asimov fits in Section 10.5, in particular the multijet background shape contribution is not present in the 15 highest ranking sources. This can be explained by the lower fitted value of the multijet normalisation which results in the lower impact of multijet uncertainties. It can be seen that the likelihood curve is not perfectly smooth, especially around the edges of the nominal values for the width templates. Nevertheless, a clear minimum is observed and the uncertainties represent the Γ_t values where the likelihood value changes by 0.5. The ranking of sources of systematic uncertainties shows the non-symmetric behaviour of the effects of the individual systematic uncertainties. This behaviour is also reflected in the non symmetric likelihood curve around the observed minimum. Figure 11.5 illustrates the pre- and post-fit distributions for observables m_W and $m_{\ell b}$. A significant reduction of the uncertainty band is observed, this is the prime reason for the choice of the profile likelihood technique. Correlations between the NPs are summarised in Appendix G.

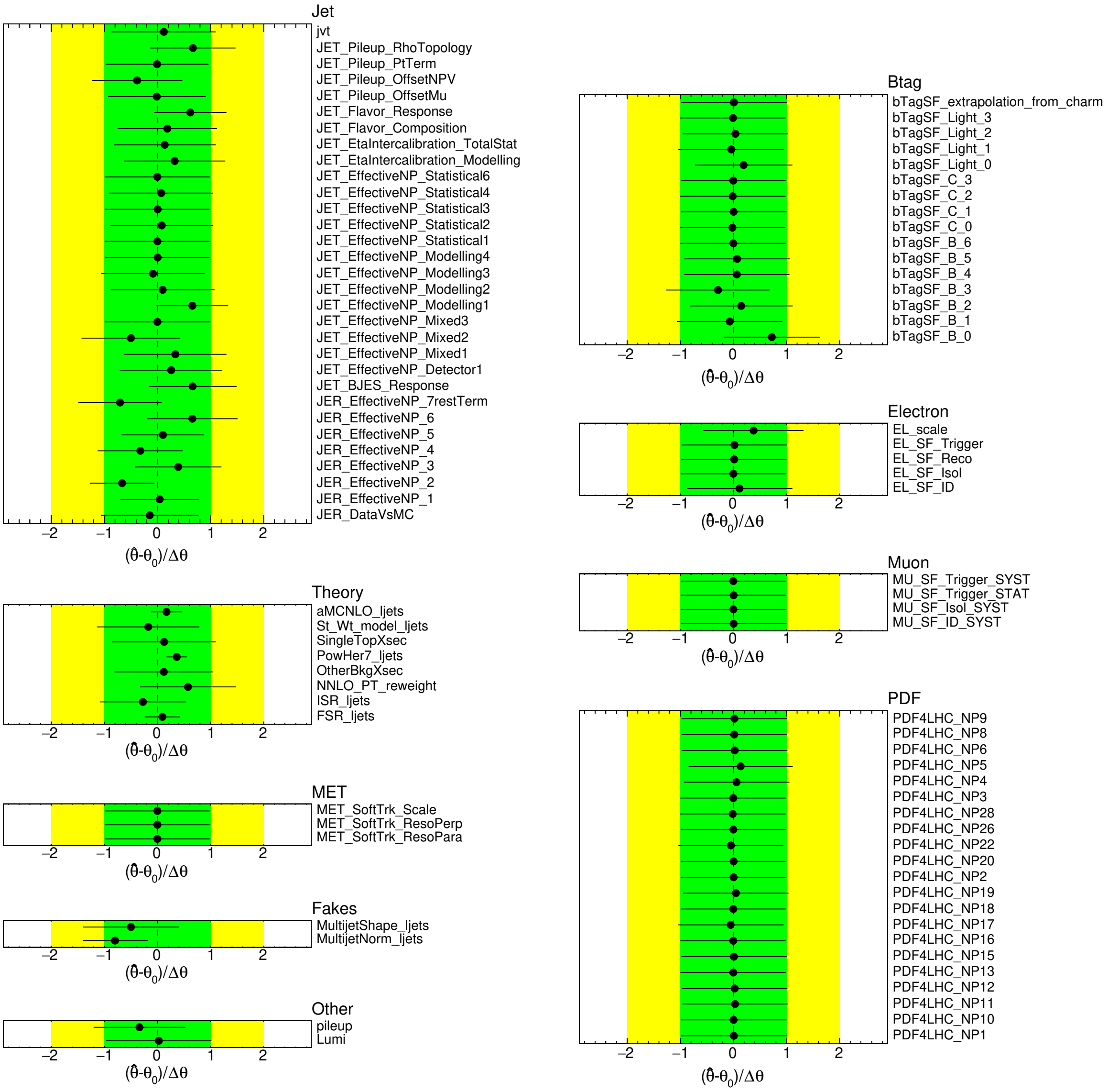

Figure 11.3.: The pull distributions for the NPs used in the fit to the observed data for the lepton+jets channel. The black dots represent the post-fit mean value of the NP, the lines represent the post-fit NP uncertainties. The green and the yellow bands represent the pre-fit one and two standard deviations, respectively.

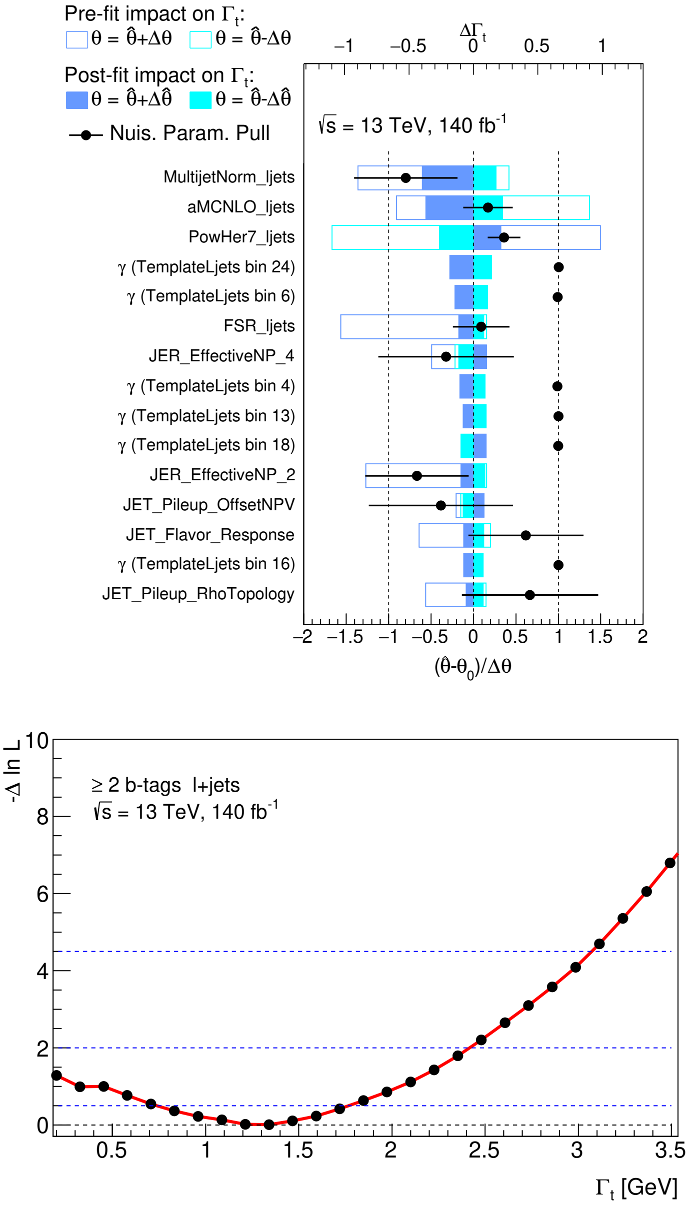

Figure 11.4.: The ranking of the systematic uncertainties (top) and the likelihood scan for Γ_t (bottom) in the lepton+jets. Only the 15 highest ranking NPs are shown. The boxes represent the effect on Γ_t with the full boxes representing the post-fit value and empty boxes representing the pre-fit values. The points with the error bars represent the pulls of each NP. For the NPs related to the MC statistical uncertainties, γ, the nominal value is represented by 1, while for other NPs it is represented by 0.

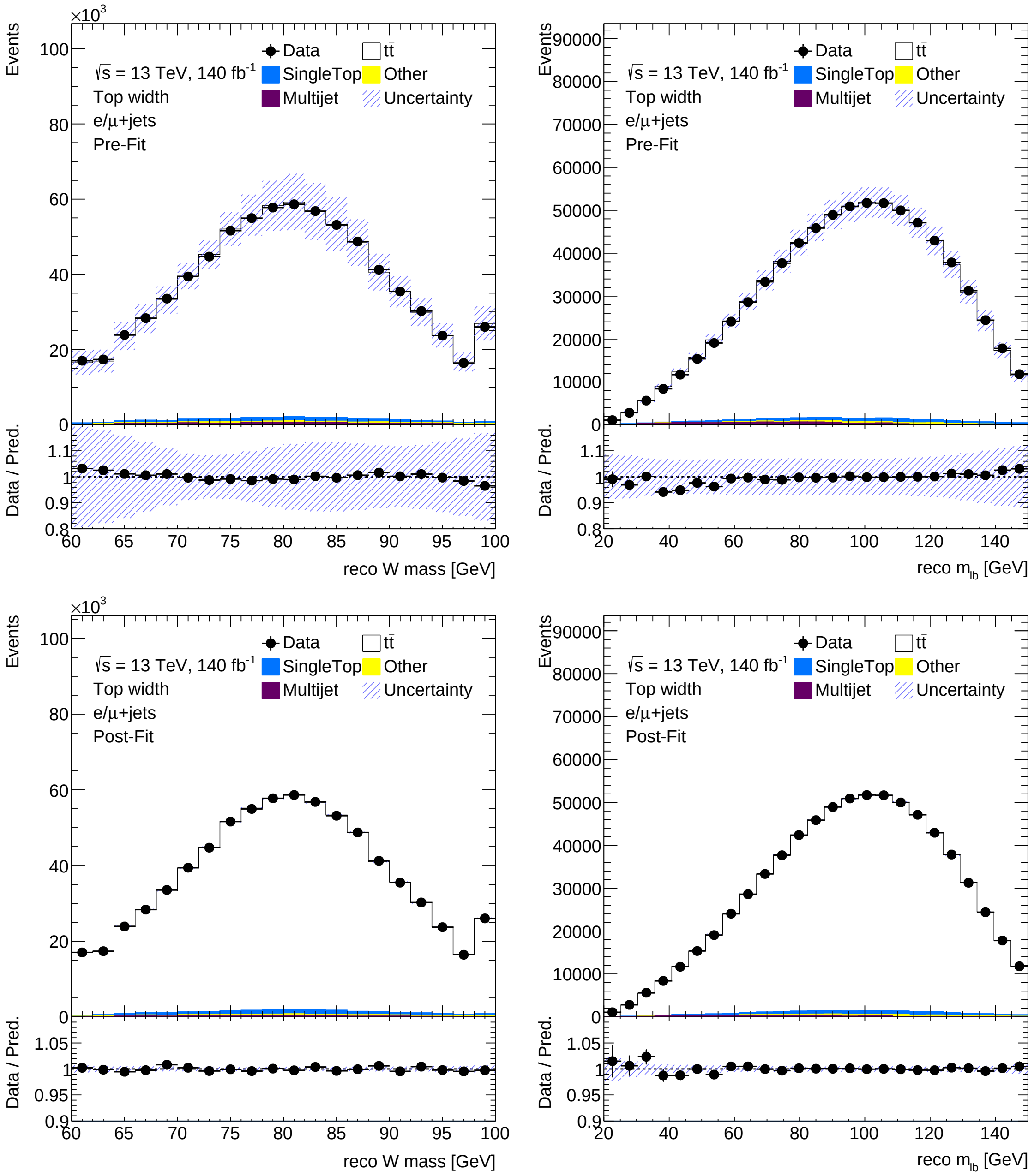

Figure 11.5.: Pre-fit (top) and post-fit (bottom) distributions for the m_W mass distribution (left) and the $m_{\ell b}$ distribution (right) for the combined electron+jets and muon+jets events. The bottom panel shows the ratio of the data over prediction. The shaded bands represent the total uncertainty. Significant improvement in the agreement between data and prediction is observed as well as decreased total uncertainties after the fit. The SM prediction of $\Gamma_t = 1.32$ GeV is assumed in the pre-fit plots. The vertical axis in the bottom panel of the post-fit distributions has a reduced range compared to the pre-fit distribution.

11.3. 13 TeV dilepton result

Data collected by the ATLAS detector in the years 2015–2018 passing the dilepton selection summarised in Section 7.4 are fitted using the profile likelihood technique. The $m_{\ell b}$ distribution of $e\mu$ is used as an observable sensitive to the top-quark decay width, while the m_{bb} distribution for combined ee and $\mu\mu$ events is used as control region in the fit. The top-quark decay width in the dilepton channel is found to be

$$\Gamma_t = 1.89^{+0.49}_{-0.47}\ \text{GeV}, \tag{11.3}$$

assuming $m_t = 172.5$ GeV.

Pulls and constraints of the NPs for systematic sources considered in the analysis are illustrated in Figures 11.6 and 11.7. The likelihood scan of Γ_t and the ranking of the systematic uncertainties is shown in Figure 11.8. Figure 11.9 illustrates the pre- and post-fit distributions of $m_{\ell b}$ and m_{bb}. Similarly to the lepton+jets channel, a significant improvement in the uncertainty band is observed. Correlations between the NPs are summarised in Appendix G.

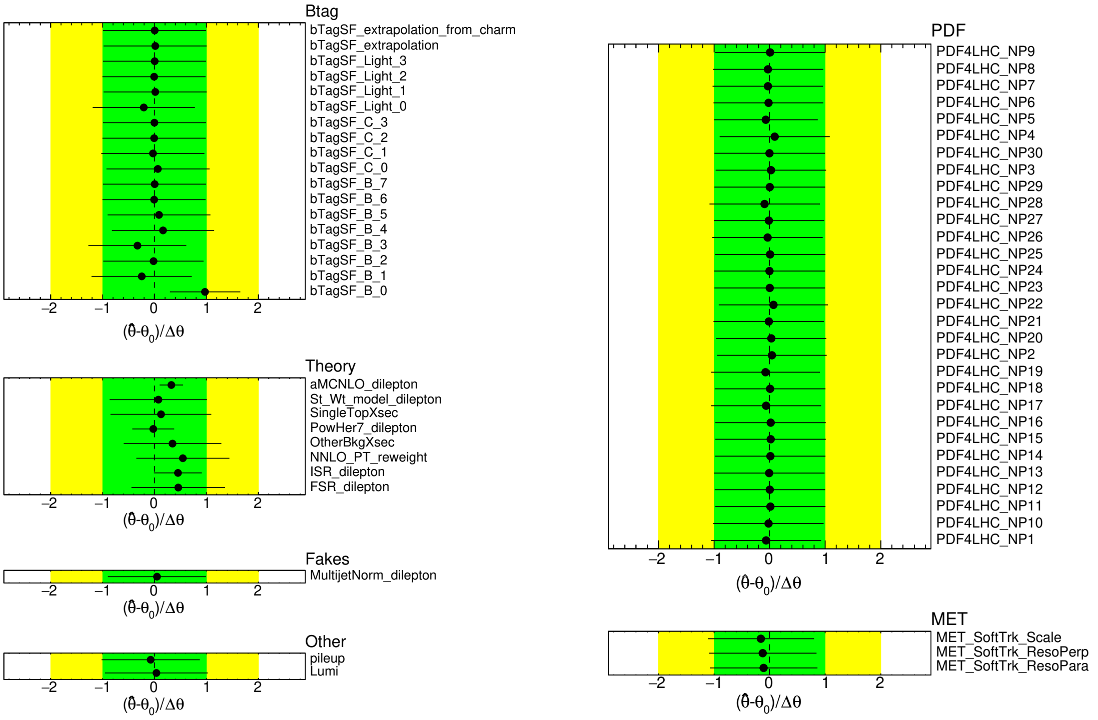

Figure 11.6.: The pull distributions for the NPs used in the fit to the observed data for the dilepton channel. The black dots represent the post-fit mean value of the NP, the lines represent the post-fit NP uncertainties. The green and the yellow bands represent the pre-fit one and two standard deviations, respectively.

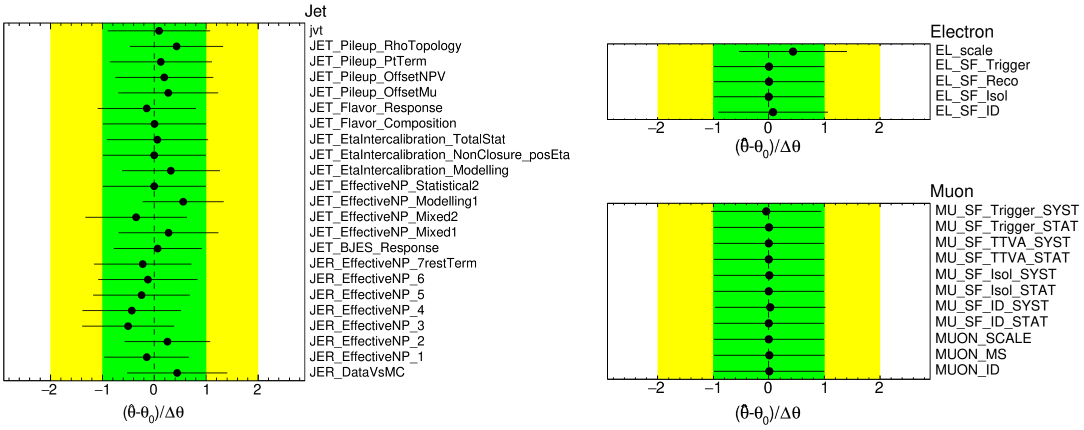

Figure 11.7.: The pull distributions for the NPs used in the fit to the observed data for the dilepton channel. The black dots represent the post-fit mean value of the NP, the lines represent the post-fit NP uncertainties. The green and the yellow bands represent the pre-fit one and two standard deviations, respectively.

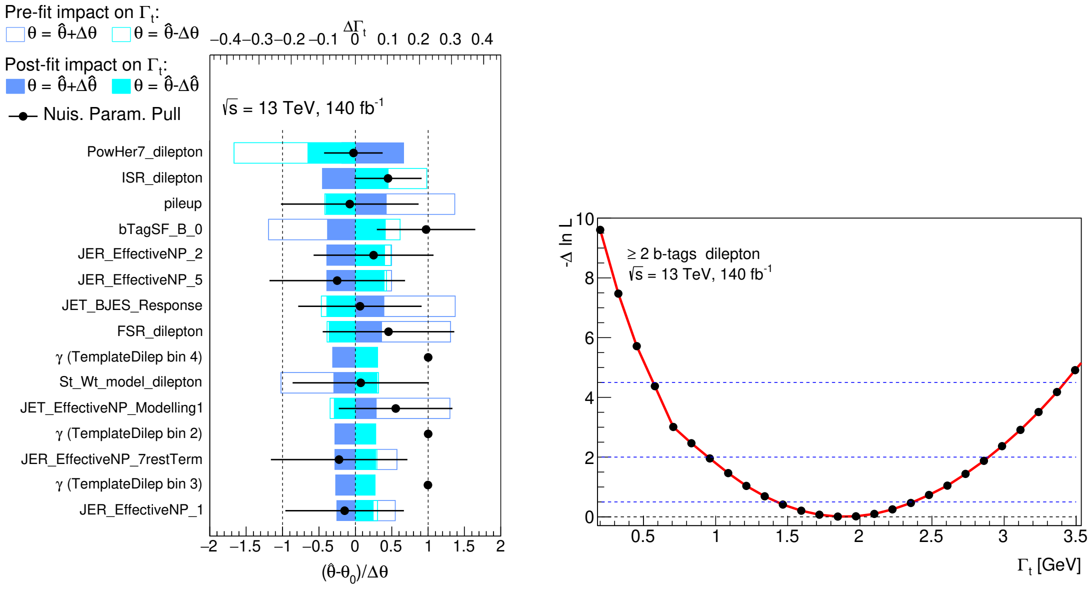

Figure 11.8.: The ranking of the systematic uncertainties (left) and the likelihood scan for Γ_t (right) in the dilepton channel. Only the 15 highest ranking NPs are shown. The boxes represent the effect on Γ_t with the full boxes representing the post-fit value and empty boxes representing the pre-fit values. The points with the error bars represent the pulls of each NP. For the NPs related to the MC statistical uncertainties, γ, the nominal value is represented by 1, while for other NPs it is represented by 0.

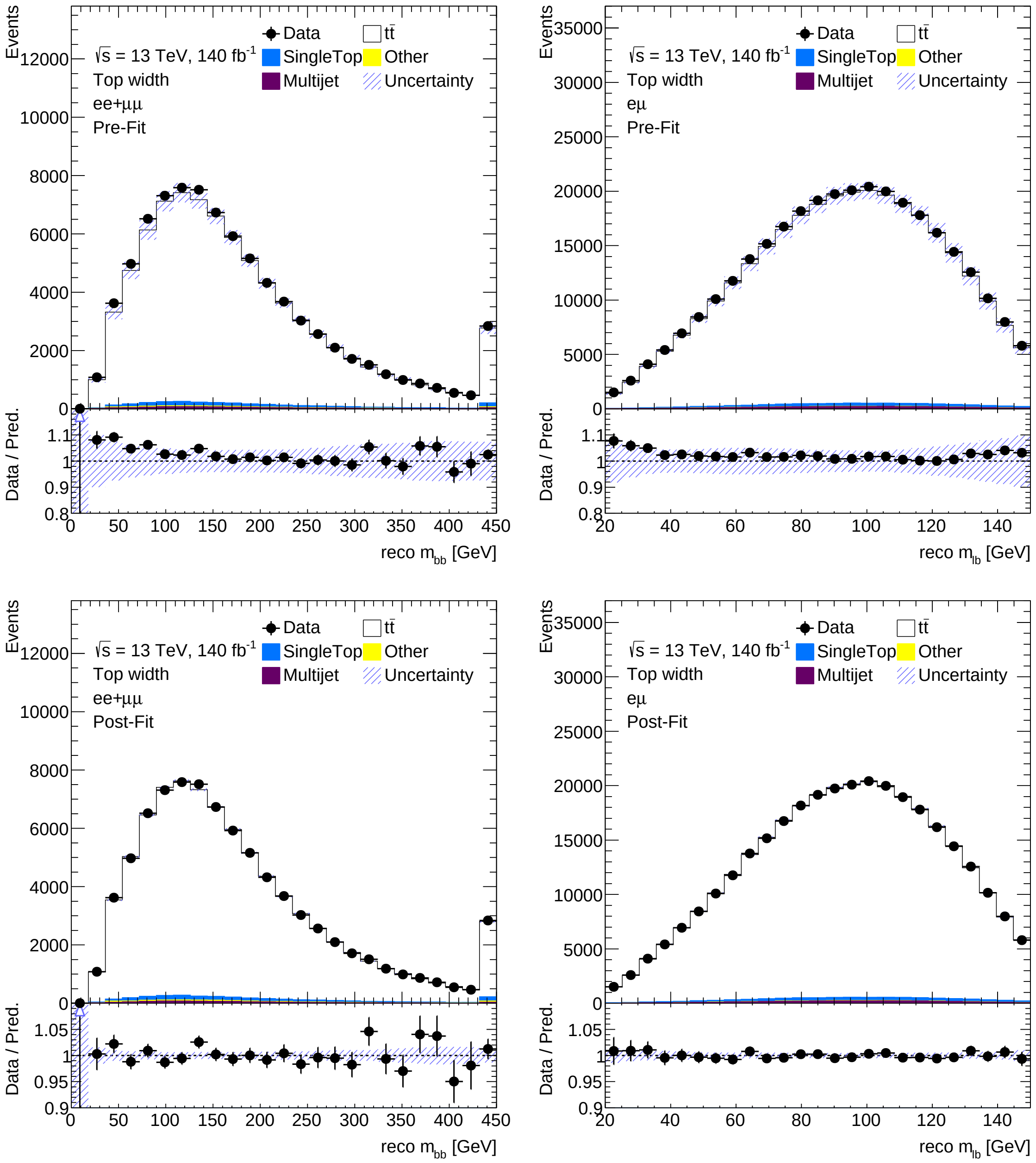

Figure 11.9.: Pre-fit (top) and post-fit (bottom) distributions for the m_{bb} mass distribution for combined ee and $\mu\mu$ events (left) and the $m_{\ell b}$ distribution in the $e\mu$ channel (right). The bottom panel shows the ratio of the data over prediction. The shaded bands represent the total uncertainty. Significant improvement in the agreement between data and prediction is observed as well as decreased total uncertainties after the fit. The SM prediction of $\Gamma_t = 1.32$ GeV is assumed in the pre-fit plots. The vertical axis in the bottom panel of the post-fit distributions has a reduced range compared to the pre-fit distribution.

11.4. 13 TeV combination

Due to the orthogonal selection that is applied to the lepton+jets and the dilepton channels, the simulated MC and the observed data distributions are statistically independent. Thus the combination can be simply performed by multiplying the individual likelihoods, as defined in Section 10.3, for the two channels. Systematic uncertainties, however, are treated as fully correlated between the channels for all sources of uncertainties with the exception of the $t\bar{t}$ modelling uncertainties, that are uncorrelated between the regions. The motivation to decorrelate the $t\bar{t}$ modelling uncertainties come from the fact that these uncertainties are significantly constrained and constraints from one region would propagate to the other region. This is potentially dangerous as the two regions can be sensitive to different modelling effects thus the correlation could lead to unjustified constraints. The normalisation of $t\bar{t}$ signal, which is a free floating parameter in both channels is also fully correlated in the combined fit. Finally, top-quark decay width values of templates have been chosen to be the same for both channels to simplify the combination. The combined fit yields

$$\Gamma_t = 1.46^{+0.30}_{-0.27}\ \text{GeV}, \tag{11.4}$$

assuming $m_t = 172.5$ GeV.

Pulls and constraints of individual fits as well as the combined fit results are summarised in Figure 11.10. Figure 11.11 shows the likelihood scan for the top-quark decay width for the combined fit of the lepton+jets and the dilepton channel. Small instabilities, represented by non-smoothness of the curve, especially around the values of Γ_t that correspond to the edges of width templates are observed, originating from the interpolation technique used in the fit. Nevertheless, a clear minimum is observed and thus the obtained value can be trusted.

The best fit value for the $t\bar{t}$ signal strength and its uncertainty is presented in Table 11.2. The uncertainty on the normalisation does not represent the true uncertainty, as estimated in a real cross-section measurement, as some of the normalisation effects were neglected in the effect of the $t\bar{t}$ modelling uncertainties. A correlation matrix of NPs is presented in Appendix G. The post-fit distributions of the observables used in the fit are displayed in Figure 11.13.

Due to non-negligible pulls and constraints for $t\bar{t}$ modelling uncertainties, a test of the consistency of the obtained results has been employed. In this test, the $t\bar{t}$ modelling uncertainties were treated as uncorrelated not only between the individual channels but also between the variables in each channels. This results in smaller constraints of the NPs as each of the $t\bar{t}$ modelling uncertainties affects only one distribution, but can result in larger pulls. The result of this modified fit yields

$$\Gamma_t = 1.32^{+0.30}_{-0.40}\ \text{GeV}, \tag{11.5}$$

The high asymmetry of the uncertainty reflects the fact that the fit with uncorrelated $t\bar{t}$ modelling uncertainties is generally less stable compared to the configuration where the $t\bar{t}$ modelling uncertainties are treated as correlated between variables in one region. Nevertheless, the obtained value is consistent with the previously quoted result. The pulls of the $t\bar{t}$ modelling NPs are displayed in Figure 11.12. A clear reduction of the constraints of the NPs is observed compared to Figure 11.10. However, for some NPs the mean post-fit value deviates more from zero compared the previously presented pull distributions.

To further validate the results, distributions that are not used in the fit are investigated. Figures 11.14 and 11.15 show the data and prediction comparison for the pre-fit distributions where all systematic uncertainties are neither pulled nor constrained. The post-fit distributions show data and prediction that is corrected by the pulls, constraints and correlations of the NPs obtained from the fit to the combined lepton+jets and the dilepton channel. A significant improvement in the agreement is observed which indicates that the pulls of the NPs are not related to specific distributions used in the fit but represent general features of the prediction.

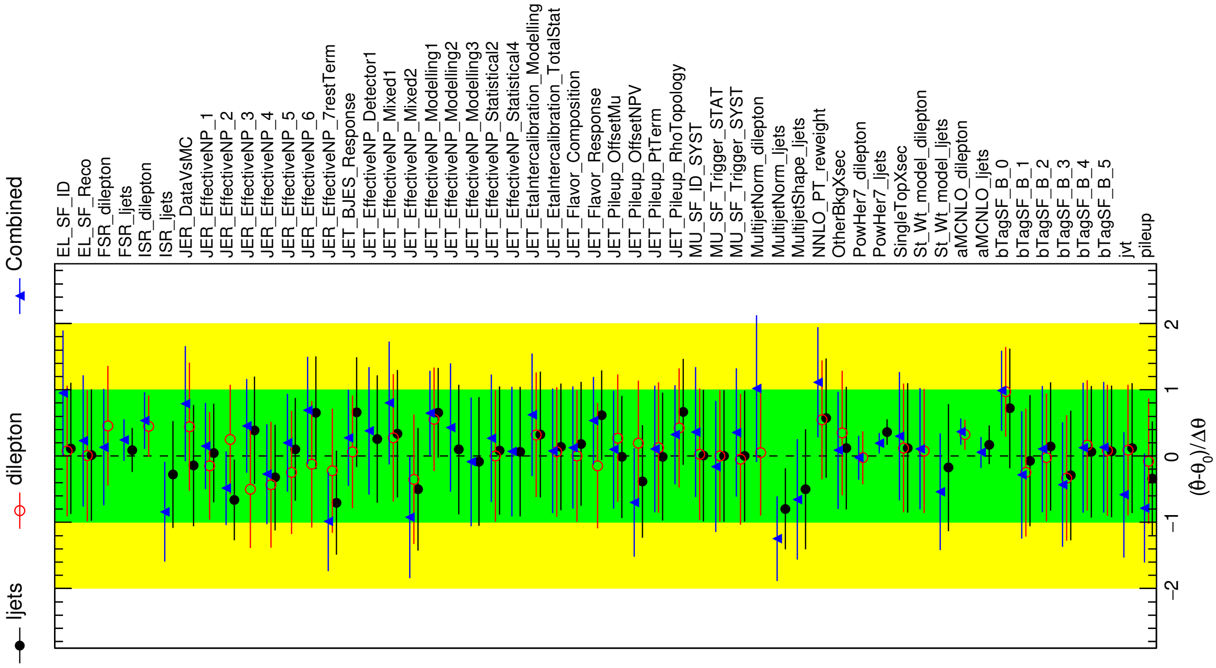

Figure 11.10.: Pulls and constraints for NPs considered in the combined fit of lepton+jets and dilepton channel. The black dots represent the post-fit mean value of the NP, the lines represent the post-fit NP uncertainties. The green and the yellow bands represent the pre-fit one and two standard deviations, respectively. Pulls for fit of individual channels are compared: lepton+jets in full black dots, dilepton in empty red dots and the combination with blue triangles. Only NPs with significant pulls and/or constraints are shown.

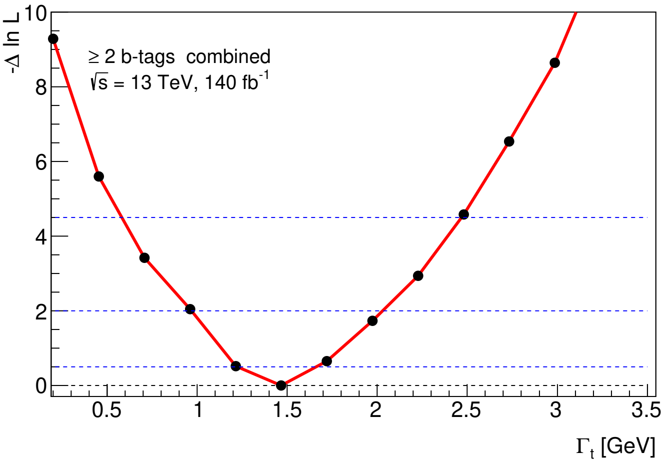

Figure 11.11.: The likelihood scan of the Γ_t parameter in the combined fit of the lepton+jets and the dilepton channel.

Channel	**Signal strength**
Lepton+jets	0.94 ± 0.04
Dilepton	0.98 ± 0.03
Combined	0.97 ± 0.03

Table 11.2.: Best fit values and their uncertainties for the signal strength of the $t\bar{t}$ process. Best fit values for individual channels are compared. Uncertainties include statistical and all considered systematic uncertainties, however the $t\bar{t}$ modelling uncertainties affect only the shapes of the distributions, thus the uncertainty underestimates the "true" uncertainty of the $t\bar{t}$ normalisation.

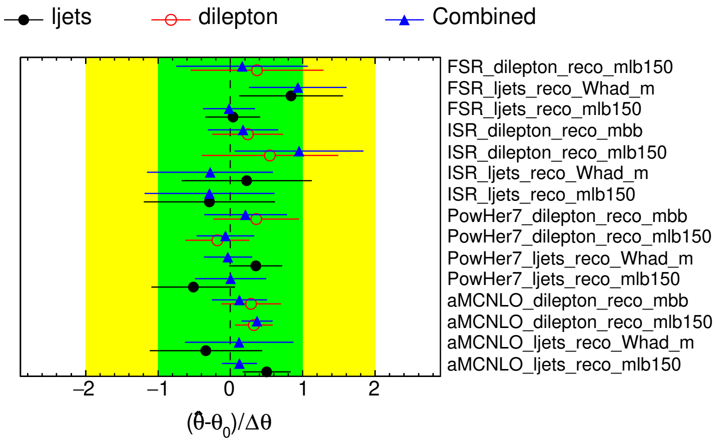

Figure 11.12.: Pulls and constraints for the $t\bar{t}$ modelling NPs considered in the combined fit of lepton+jets and dilepton channel when treating them uncorrelated between all fitted observables. Pulls for fit of individual channels are compared: lepton+jets in full black dots, dilepton in empty red dots and combination with blue triangles. The black dots represent the post-fit mean value of the NP, the lines represent the post-fit NP uncertainties. The green and the yellow bands represent the pre-fit one and two standard deviations, respectively.

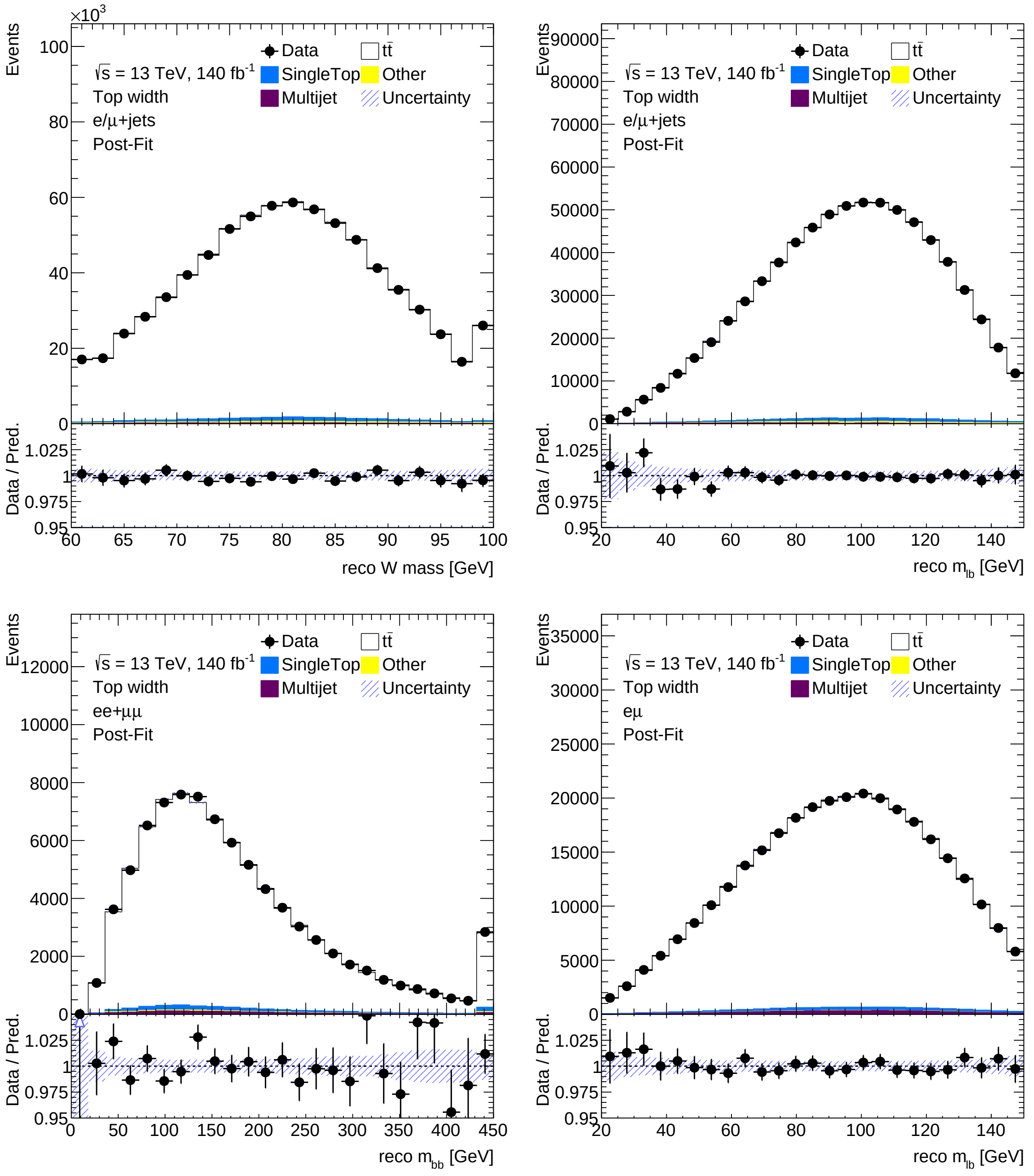

Figure 11.13.: Post-fit distributions for the m_W mass distribution (top-left) and the $m_{\ell b}$ distribution (top-right) for the lepton+jets channel and for the m_{bb} distribution (bottom-left) and the $m_{\ell b}$ distribution (bottom-right) in the dilepton channel. The post-fit pulls and constraints are propagated from the combined fit of the lepton+jets and the dilepton channel. The bottom panel shows the ratio of the data over prediction. The shaded bands represent the total uncertainty.

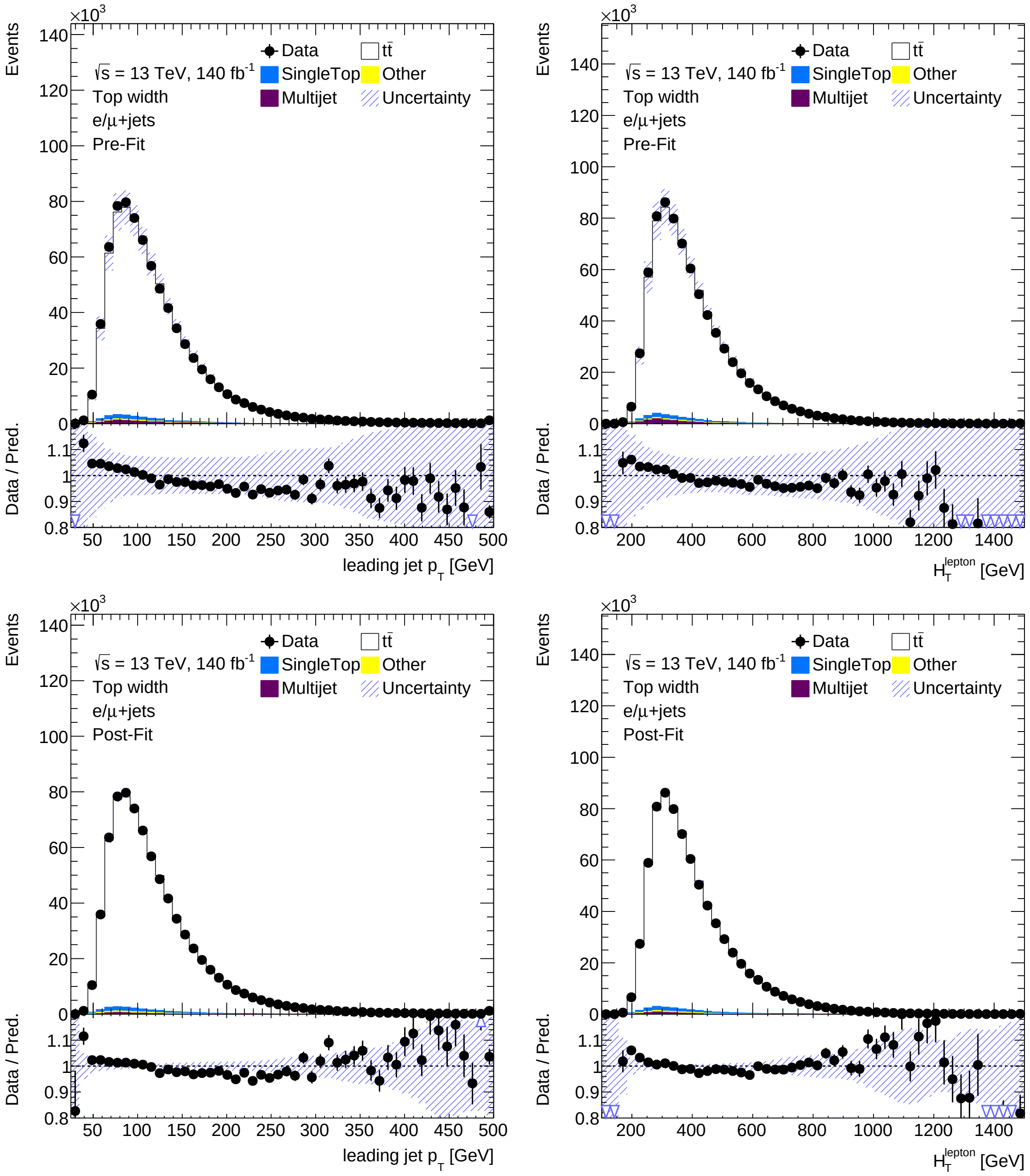

Figure 11.14.: Pre-fit (top) and post-fit (bottom) distributions of the leading jet p_{T} (left) and the scalar sum of all jets and the charged lepton (right) in the lepton+jets channel. The post-fit pulls and constraints are propagated from the combined fit of the lepton+jets and the dilepton channel. A significant improvement in the agreement of the data and prediction is observed in the post-fit distributions. The bottom panel shows the ratio of the data over prediction. The shaded bands represent the total uncertainty.

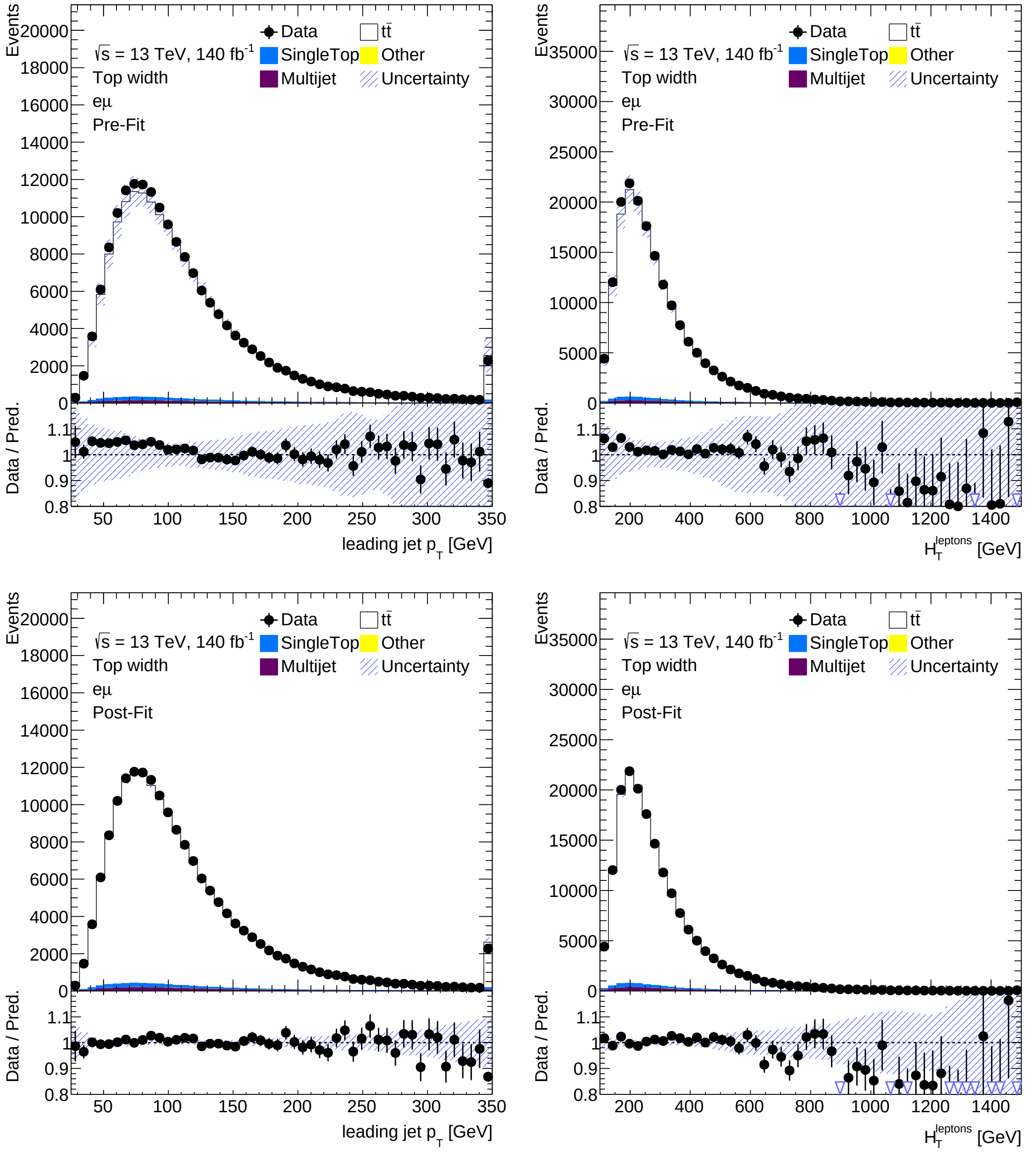

Figure 11.15.: Pre-fit (top) and post-fit (bottom) distributions of the leading jet p_T (left) and the scalar sum of all jets and the charged leptons (right) in the $e\mu$ channel. The post-fit pulls and constraints are propagated from the combined fit of the lepton+jets and the dilepton channel. A significant improvement in the agreement of the data and prediction is observed in the post-fit distributions. The bottom panel shows the ratio of the data over prediction. The shaded bands represent the total uncertainty.

11.4.1. Top-quark mass dependence

In the SM, the top-quark decay width depends on the top-quark mass as has been presented in Section 3.3. All results presented in the previous section relied on the assumption of the top-quark mass being equal to $m_t = 172.5$ GeV. To estimate the impact of the top-quark mass on the measured Γ_t, dedicated Powheg interfaced with Pythia 8 $t\bar{t}$ MC samples have been generated with the identical setting as the nominal $t\bar{t}$ sample used with the exception of the top-quark mass and, naturally, the decay width. Table 11.3 shows the available $t\bar{t}$ MC samples.

In the 8 TeV measurement the mass dependence has been estimated only approximately as MC samples with variations of 1.5 and 2.5 GeV away from the nominal prediction of $m_t = 172.5$ GeV have been available. This far exceeds the current uncertainty on the top-quark mass, thus an interpolation between the alternative samples has been employed to estimate the effect of the top-quark mass on the measured Γ_t. Variations of m_t representing shifts of the top mass by ± 0.5 GeV obtained from the interpolation technique yield the effect of up to 0.2 GeV on the measured decay width.

For the 13 TeV measurement, the effect of the top-quark mass is estimated by distributions generated with an alternative m_t as a NP that enters the fit, but is not allowed to change. To estimate the effect of the top-quark mass, this NP is fixed to $-1\ \sigma$ (representing $m_t = 172$ GeV) and $+1\ \sigma$ (representing $m_t = 173$ GeV)[1]. Currently the MC samples with alternative m_t are available only in the mc16a and mc16d campaigns representing luminosity and LHC conditions of years 2015, 2016 and 2017. The missing samples make the estimate of the effect of m_t on the decay width less reliable. Thus comparing the available distributions with the distributions representing the full Run 2 luminosity and LHC conditions is not possible. Nevertheless, an approximation of the effect is estimated by comparing only the shapes of the distributions (normalising the distributions with the alternative m_t to the expected yields from full Run 2 expectation with $m_t = 172.5$ GeV). Table 11.4 shows the obtained values for Γ_t and its uncertainties from the combined fit of the lepton+jets and the dilepton channels for configurations where the NP representing the difference in m_t is fixed to values corresponding to $m_t = 172$ and 173 GeV. The shifts in the mean value for the alternative m_t samples with respect to the nominal setting with $m_t = 172.5$ GeV are of the order of the measured uncertainty for the nominal configuration. However, a clear trend in the evolution of the mean fitted values for Γ_t as a function of the input top-quark mass is seen.

m_t [GeV]	Γ_t [GeV] (Theory)
172	1.306
172.5	1.320
173	1.333

Table 11.3.: Available $t\bar{t}$ Powheg interfaced with Pythia 8 samples with alternative m_t. For each value of the top-quark mass, the corresponding SM expectation for the top-quark decay width is used in the MC samples as represented by the right column. The nominal sample uses $m_t = 172.5$ GeV and $\Gamma_t = 1.32$ GeV.

---

[1] Fixing the NP value to zero leads to the nominal fit assuming $m_t = 172.5$ GeV.

m_t [GeV]	Γ_t [GeV]	Uncertainty [GeV]
172	1.60	$+0.33$ -0.30
172.5	1.46	$+0.30$ -0.27
173	1.14	$+0.30$ -0.37

Table 11.4.: Fitted values for Γ_t and its uncertainties for different assumptions of the underlying mass of the top quark. The shape effects are considered for the alternative top-quark mass variations.

CHAPTER 12

Conclusions and outlook

This thesis presented two direct measurements of the top-quark decay width with ATLAS data at centre-of-mass energies of $\sqrt{s} = 8$ and 13 TeV. The 8 TeV measurement was briefly summarised and was used as a stepping stone for the more sophisticated 13 TeV measurement. The decay width of the top quark is an important property of the top quark since it is closely related to its decays. Many properties of the top quark have been measured with high precision, however its decay width has been precisely determined only with model-dependent measurements. Direct measurements have a weaker dependence on the assumed physics models thus they provide larger sensitivity to potential BSM scenarios.

This chapter provides a summary of the obtained results in Section 12.1. Prospects for the future measurement of Γ_t are provided in Section 12.2.

12.1. Summary

The first measurement described in the thesis was performed using 8 TeV data collected with the ATLAS detector in proton-proton collisions, corresponding to an integrated luminosity of 20.2 fb^{-1}. The measurement was performed in the lepton+jets decay channel of the $t\bar{t}$ pairs. The measurement exploits a binned likelihood fit of the template distributions, corresponding to various top-quark decay widths, to the observed data. The templates are split into eight orthogonal regions according to the lepton flavour, number of b-tagged jets and jet $|\eta|$. Two observables are used in a simultaneous fit of the eight regions: $m_{\ell b}$, the invariant mass of the charged lepton and the corresponding b-jet from the semileptonic top quark decay and $\Delta R_{\min}(j_b, j_l)$, the angular distance between the b-jet, j_b, associated with the hadronic top quark and the closest light jet, j_l, from the hadronically decaying W boson. The obtained Γ_t value from the fit to data yields

$$\Gamma_t = 1.76 \pm 0.33(\text{stat.})^{+0.79}_{-0.68}(\text{syst.})\text{ GeV} = 1.76^{+0.86}_{-0.76}\text{ GeV}, \qquad (12.1)$$

assuming $m_t = 172.5$ GeV. This is in good agreement with the SM predictions [132]. The measurement is currently the best published direct measurement of the top-quark decay width, and the only published direct measurement from the LHC. The measurement has been published in European Physics Journal C [245].

The second measurement, which was the main topic of the thesis, was performed using the $\sqrt{s}$ = 13 TeV dataset collected with the ATLAS detector in proton-proton collisions, corresponding to an integrated luminosity of 140 fb^{-1}. The measurement exploits lepton+jets as well as dilepton channels of the $t\bar{t}$ pair decays. A dedicated multivariate technique, BDT, is employed in the lepton+jets channel to resolve the ambiguity of the jet-to-parton assignment. A profile likelihood method with templates for various widths, generated by reweighting, has been developed and used for the measurement. Each decay channel utilises observables that are sensitive to the decay width of the top quark as well as distributions that are sensitive to the dominant systematic uncertainties and are insensitive to the decay width. This allows the dominant sources of systematic uncertainties to be controlled and constrained. Variables used in the fit to the data are: $m_{\ell b}$ as a variable sensitive to the decay width, as well as distributions of m_W (lepton+jets channel) and m_{bb} (dilepton channel) to control the systematic uncertainties. The fit to data yields

$$\Gamma_t = 1.46^{+0.30}_{-0.27}\ \text{GeV}, \tag{12.2}$$

assuming m_t = 172.5 GeV, which is in a good agreement with the SM expectation of Γ_t = 1.32 GeV.

12.2. Outlook

Since the measurement is dominated by systematic uncertainties, the measurement is planned to be updated with the final recommendations for physics object corrections and uncertainties, which is expected to be provided by the beginning of the year 2020. Particularly uncertainties in the jet energy scale and jet energy resolution are expected to decrease with the final object calibrations which could lead to a further decrease of the total uncertainty. Additionally, MC samples with an alternative configuration representing colour reconnection modelling uncertainties will be generated that will allow this uncertainty to be included in the fitting model. It should be noted that the technique developed for this measurement—profile likelihood fit with templates—is now being used by several analyses in the ATLAS Collaboration.

As mentioned in the previous section, several improvements are expected for the 13 TeV measurement for the definition and calibration of the physics objects used in the analysis. The most important change could originate from a different definition of jets, so called *Particle flow* (PFlow) jets [252]. PFlow jets integrate both tracking information and calorimeter information about jets. The charged component of the jets is measured with the tracking detector while the neutral component is measured from the calorimeters. Due to the evolution of the uncertainties as a function of energy (momentum) in calorimeters (tracking), the total jet energy scale and resolution uncertainties follow different formulae compared to the jets that use solely calorimeters for energy measurements. Thus, PFlow jets have smaller energy scale and resolution uncertainties for jets with p_{T} below about 200 GeV [252]. Improvement in the jet energy scale and resolution uncertainties could impact the measurement of the decay width.

Despite the improvements in the object uncertainties, analyses exploiting binned likelihood fits for the top-quark decay width are not expected to reach a precision below 200 MeV. New ideas are required to reach a few-% precision in the decay width. One of the new approaches to the decay width measurement could exploit single top events with high luminosity future colliders [253]. Comparing s- and t-channel scattering of $Wb(+j)$ processes is sensitive to Γ_t and is expected to reach a precision of $O(100)$ MeV with an integrated luminosity of 3000 fb^{-1} at the high-luminosity upgrade of the LHC [254].

Bibliography

[1] J. J. Thomson, *Cathode rays*, Philosophical Magazine (1897).

[2] H. Geiger and R. Ernest, *Scattering of α particles by matter*, Proceedings of the Royal Society of London **83** (1910).

[3] J. C. Street and E. C. Stevenson, *New Evidence for the Existence of a Particle of Mass Intermediate Between the Proton and Electron*, Phys. Rev. **52** (1937) 1003–1004.

[4] CMS Collaboration, *Observation of a new boson at a mass of 125 GeV with the CMS experiment at the LHC*, Phys. Lett. B **716** (2012) 30–61.

[5] ATLAS Collaboration, *Observation of a new particle in the search for the Standard Model Higgs boson with the ATLAS detector at the LHC*, Phys. Lett. B **716** (2012) 1–29.

[6] DØ Collaboration, *Observation of the top quark*, Phys. Rev. Lett. **74** (1995) 2632–2637.

[7] CDF Collaboration, *Observation of top quark production in $\bar{p}p$ collisions*, Phys. Rev. Lett. **74** (1995) 2626–2631.

[8] C. N. Yang and R. L. Mills, *Conservation of Isotopic Spin and Isotopic Gauge Invariance*, Phys. Rev. **96** (1954) 191–195.

[9] G. 't Hooft, *Renormalizable Lagrangians for Massive Yang-Mills Fields*, Nucl. Phys. B **35** (1971) 167–188.

[10] G. 't Hooft and M. J. G. Veltman, *Regularization and Renormalization of Gauge Fields*, Nucl. Phys. B **44** (1972) 189–213.

[11] F. Halzen and A. D. Martin, *Quarks And Leptons: An Introductory Course In Modern Particle Physics*. Wiley, 1984.

[12] D. J. Gross and F. Wilczek, *Ultraviolet Behavior of Non-Abelian Gauge Theories*, Phys. Rev. Lett. **30** (1973) 1343–1346.

[13] K. G. Wilson, *Confinement of quarks*, Phys. Rev. D **10** (1974) 2445–2459.

[14] S. L. Glashow, *Partial Symmetries of Weak Interactions*, Nucl. Phys. **22** (1961) 579–588.

[15] S. Weinberg, *A Model of Leptons*, Phys. Rev. Lett. **19** (1967) 1264–1266.

[16] X. Qian and P. Vogel, *Neutrino Mass Hierarchy*, Prog. Part. Nucl. Phys. **83** (2015) 1–30.

[17] M. Kobayashi and T. Maskawa, *CP Violation in the Renormalizable Theory of Weak Interaction*, Prog. Theor. Phys. **49** (1973) 652–657.

[18] N. Cabibbo, *Unitary Symmetry and Leptonic Decays*, Phys. Rev. Lett. **10** (1963) 531–533.

[19] M. Gell-Mann, *Symmetries of Baryons and Mesons*, Phys. Rev. **125** (1962) 1067–1084.

[20] M. Gell-Mann, *The interpretation of the new particles as displaced charge multiplets*, Nuovo Cim. **4** (1956) 848–866.

[21] T. Nakano and K. Nishijima, *Charge Independence for V-particles**, Progress of Theoretical Physics **10** (1953) 581–582.

[22] L. D. Faddeev and V. N. Popov, *Feynman Diagrams for the Yang-Mills Field*, Phys. Lett. B **25** (1967) 29–30.

[23] W. Heisenberg, *Über den Bau der Atomkerne. I*, Zeitschrift für Physik **77** (1932) 1–11.

[24] R. Bjorklund, et al., *High Energy Photons from Proton-Nucleon Collisions*, Phys. Rev. **77** (1950) 213–218.

[25] M. Gell-Mann, *THE EIGHTFOLD WAY: A THEORY OF STRONG INTERACTION SYMMETRY*, California Inst. of Tech., Pasadena. Synchrotron Lab. (1961).

[26] V. E. Barnes, et al., *Observation of a Hyperon with Strangeness Minus Three*, Phys. Rev. Lett. **12** (1964) 204–206.

[27] M. Gell-Mann, *A Schematic Model of Baryons and Mesons*, Phys. Lett. **8** (1964) 214–215.

[28] G. Zweig, *An SU(3) model for strong interaction symmetry and its breaking. Version 2*. Developments in the Quark Theory of Hadrons, 1964.

[29] R. P. Feynman, *The behavior of hadron collisions at extreme energies*, Conf. Proc. C **690905** (1969) 237–258.

[30] J. D. Bjorken, *Asymptotic Sum Rules at Infinite Momentum*, Phys. Rev. **179** (1969) 1547–1553.

[31] Y. L. Dokshitzer, *Calculation of the Structure Functions for Deep Inelastic Scattering and e+ e- Annihilation by Perturbation Theory in Quantum Chromodynamics.*, Sov. Phys. JETP **46** (1977) 641–653, [Zh. Eksp. Teor. Fiz.73,1216(1977)].

[32] V. N. Gribov and L. N. Lipatov, *Deep inelastic e p scattering in perturbation theory*, Sov. J. Nucl. Phys. **15** (1972) 438–450, [Yad. Fiz.15,781(1972)].

[33] G. Altarelli and G. Parisi, *Asymptotic Freedom in Parton Language*, Nucl. Phys. B **126** (1977) 298–318.

[34] H.-L. Lai, et al., *New parton distributions for collider physics*, Phys. Rev. D **82** (2010) 074024.

[35] R. D. Ball, et al., *A first unbiased global NLO determination of parton distributions and their uncertainties*, Nucl. Phys. B **838** (2010) 136–206.

[36] A. D. Martin, et al., *Parton distributions for the LHC*, Eur. Phys. J. C **63** (2009) 189–285.

[37] E. Fermi, *Versuch einer Theorie der β-Strahlen. I*, Zeitschrift für Physik **88** (1934) 161–177.

[38] T. D. Lee and C. N. Yang, *Question of Parity Conservation in Weak Interactions*, Phys. Rev. **104** (1956) 254–258.

[39] C. S. Wu, et al., *Experimental Test of Parity Conservation in Beta Decay*, Phys. Rev. **105** (1957) 1413–1415.

[40] R. P. Feynman and M. Gell-Mann, *Theory of the Fermi Interaction*, Phys. Rev. **109** (1958) 193–198.

[41] H. Georgi and S. L. Glashow, *Unified Weak and Electromagnetic Interactions without Neutral Currents*, Phys. Rev. Lett. **28** (1972) 1494–1497.

[42] UA1 Collaboration, *Experimental Observation of Isolated Large Transverse Energy Electrons with Associated Missing Energy at $\sqrt{s} = 540$ GeV*, Phys. Lett. B **122** (1983) 103–116.

[43] UA2 Collaboration, *Observation of Single Isolated Electrons of High Transverse Momentum in Events with Missing Transverse Energy at the CERN anti-p p Collider*, Phys. Lett. B **122** (1983) 476–485.

[44] UA1 Collaboration, *Experimental Observation of Lepton Pairs of Invariant Mass Around 95 GeV/c^2 at the CERN SPS Collider*, Phys. Lett. B **126** (1983) 398–410.

[45] UA2 Collaboration, *Evidence for $Z^0 \to e^+e^-$ at the CERN anti-p p Collider*, Phys. Lett. B **129** (1983) 130–140.

[46] F. Englert and R. Brout, *Broken Symmetry and the Mass of Gauge Vector Mesons*, Phys. Rev. Lett. **13** (1964) 321–323.

[47] P. W. Higgs, *Broken symmetries, massless particles and gauge fields*, Phys. Lett. **12** (1964) 132–133.

[48] P. W. Higgs, *Broken Symmetries and the Masses of Gauge Bosons*, Phys. Rev. Lett. **13** (1964) 508–509.

[49] G. S. Guralnik, C. R. Hagen, and T. W. B. Kibble, *Global Conservation Laws and Massless Particles*, Phys. Rev. Lett. **13** (1964) 585–587.

[50] D. Clowe, et al., *A direct empirical proof of the existence of dark matter*, Astrophys. J. **648** (2006) L109–L113.

[51] A. D. Sakharov, *Violation of CP Invariance, C asymmetry, and baryon asymmetry of the universe*, Pisma Zh. Eksp. Teor. Fiz. **5** (1967) 32–35, [Usp. Fiz. Nauk161,no.5,61(1991)].

[52] Supernova Search Team Collaboration, A. G. Riess et al., *Observational evidence from supernovae for an accelerating universe and a cosmological constant*, Astron. J. **116** (1998) 1009–1038.

[53] A. G. Riess, et al., *Observational Evidence from Supernovae for an Accelerating Universe and a Cosmological Constant*, The Astronomical Journal **116** (1998) 1009.

[54] P. Ramond, *Dual Theory for Free Fermions*, Phys. Rev. D **3** (1971) 2415–2418.

[55] Yu. A. Golfand and E. P. Likhtman, *Extension of the Algebra of Poincare Group Generators and Violation of p Invariance*, JETP Lett. **13** (1971) 323–326, [Pisma Zh. Eksp. Teor. Fiz.13,452(1971)].

[56] J. Wess and B. Zumino, *A Lagrangian Model Invariant Under Supergauge Transformations*, Phys. Lett. B **49** (1974) 52.

[57] J. Wess and B. Zumino, *Supergauge Transformations in Four-Dimensions*, Nucl. Phys. B **70** (1974) 39–50.

[58] S. L. Glashow, J. Iliopoulos, and L. Maiani, *Weak Interactions with Lepton-Hadron Symmetry*, Phys. Rev. D **2** (1970) 1285–1292.

[59] *ATLAS Standard Model summary plots*, `https://atlas.web.cern.ch/Atlas/GROUPS/PHYSICS/CombinedSummaryPlots/SM/`. Accessed: 2018-11-20.

[60] J. H. Christenson, et al., *Evidence for the* 2π *Decay of the* K_2^0 *Meson*, Phys. Rev. Lett. **13** (1964) 138–140.

[61] M. L. Perl et al., *Evidence for Anomalous Lepton Production in* e^+e^- *Annihilation*, Phys. Rev. Lett. **35** (1975) 1489–1492.

[62] S. W. Herb et al., *Observation of a Dimuon Resonance at 9.5 GeV in 400 GeV Proton-Nucleus Collisions*, Phys. Rev. Lett. **39** (1977) 252–255.

[63] *Review of Particle Physics*, Phys. Rev. D **98** (2018) 030001.

[64] I. I. Y. Bigi, et al., *Production and Decay Properties of Ultraheavy Quarks*, Phys. Lett. B **181** (1986) 157–163.

[65] J. C. Collins, D. E. Soper, and G. F. Sterman, *Factorization of Hard Processes in QCD*, Adv. Ser. Direct. High Energy Phys. **5** (1989) 1–91.

[66] W. Bernreuther, M. Fücker, and Z.-G. Si, *Weak interaction corrections to hadronic top quark pair production: Contributions from quark-gluon and b anti-b induced reactions*, Phys. Rev. D **78** (2008) 017503.

[67] M. Cacciari, et al., *Top-pair production at hadron colliders with next-to-next-to-leading logarithmic soft-gluon resummation*, Phys. Lett. B **710** (2012) 612–622.

[68] P. Bernreuther, M. Czakon, and A. Mitov, *Percent Level Precision Physics at the Tevatron: First Genuine NNLO QCD Corrections to* $q\bar{q} \rightarrow t\bar{t} + X$, Phys. Rev. Lett. **109** (2012) 132001.

[69] M. Czakon and A. Mitov, *NNLO corrections to top-pair production at hadron colliders: the all-fermionic scattering channels*, JHEP **12** (2012) 054.

[70] M. Czakon and A. Mitov, *NNLO corrections to top pair production at hadron colliders: the quark-gluon reaction*, JHEP **01** (2013) 080.

[71] M. Czakon, P. Fiedler, and A. Mitov, *Total Top-Quark Pair-Production Cross Section at Hadron Colliders Through* $O(\alpha_S^4)$, Phys. Rev. Lett. **110** (2013) 252004.

[72] M. Czakon and A. Mitov, *Top++: A Program for the Calculation of the Top-Pair Cross-Section at Hadron Colliders*, Comput. Phys. Commun. **185** (2014) 2930.

[73] ATLAS Collaboration, *Measurement of the* $t\bar{t}$ *production cross-section using* $e\mu$ *events with b-tagged jets in pp collisions at* $\sqrt{s} = 7$ *and 8 TeV with the ATLAS detector*, Eur. Phys. J. C **74** (2014) 3109.

[74] *Measurements of the* $t\bar{t}$ *production cross-section in the dilepton and lepton-plus-jets channels and of the ratio of the* $t\bar{t}$ *and Z boson cross-sections in pp collisions at* $\sqrt{s} = 13$ *TeV with the ATLAS detector*, Tech. Rep. ATLAS-CONF-2015-049, CERN, Geneva, Sep, 2015. `https://cds.cern.ch/record/2052605`.

[75] ATLAS Collaboration, *Measurement of the* $t\bar{t}$ *production cross-section using* $e\mu$ *events with b-tagged jets in pp collisions at* $\sqrt{s} = 13$ *TeV with the ATLAS detector*, Phys. Lett. B **761** (2016) 136–157, [Erratum: Phys. Lett.B772,879(2017)].

[76] CMS Collaboration, *Measurement of the inclusive* $\mathrm{t\bar{t}}$ *cross section in pp collisions at* $\sqrt{s} = 5.02$ *TeV using final states with at least one charged lepton*, JHEP **03** (2018) 115.

[77] CMS Collaboration, *Measurement of the* $t\bar{t}$ *production cross section in the* $e\mu$ *channel in proton-proton collisions at* $\sqrt{s} = 7$ *and 8 TeV*, JHEP **08** (2016) 029.

[78] CMS Collaboration, *Measurement of the* $t\bar{t}$ *production cross section using events in the* $e\mu$ *final state in pp collisions at* $\sqrt{s} = 13$ *TeV*, Eur. Phys. J. C **77** (2017) 172.

[79] CDF and DØ Collaborations, *Combination of measurements of the top-quark pair production cross section from the Tevatron Collider*, Phys. Rev. D **89** (2014) 072001.

[80] ATLAS and CMS Collaborations, *Combination of ATLAS and CMS top quark pair cross section measurements in the* $e\mu$ *final state using proton-proton collisions at 8 TeV*, Tech. Rep. CMS-PAS-TOP-14-016, CERN, Geneva, 2014. `http://cds.cern.ch/record/1950834`.

[81] *ATLAS Top Quark summary plots*, `https://twiki.cern.ch/twiki/bin/view/AtlasPublic/TopPublicResults`. Accessed: 2018-11-23.

[82] N. Kidonakis, *NNLL resummation for s-channel single top quark production*, Phys. Rev. D **81** (2010) 054028.

[83] N. Kidonakis, *Next-to-next-to-leading-order collinear and soft gluon corrections for t-channel single top quark production*, Phys. Rev. D **83** (2011) 091503.

[84] N. Kidonakis, *Two-loop soft anomalous dimensions for single top quark associated production with a W- or H-*, Phys. Rev. D **82** (2010) 054018.

[85] P. Kant, et al., *HatHor for single top-quark production: Updated predictions and uncertainty estimates for single top-quark production in hadronic collisions*, Comput. Phys. Commun. **191** (2015) 74–89.

[86] M. Aliev, et al., *HATHOR: HAdronic Top and Heavy quarks crOss section calculatoR*, Comput. Phys. Commun. **182** (2011) 1034–1046.

[87] ATLAS Collaboration, *Comprehensive measurements of t-channel single top-quark production cross sections at $\sqrt{s} = 7$ TeV with the ATLAS detector*, Phys. Rev. D **90** (2014) 112006.

[88] ATLAS Collaboration, *Fiducial, total and differential cross-section measurements of t-channel single top-quark production in pp collisions at 8 TeV using data collected by the ATLAS detector*, Eur. Phys. J. C **77** (2017) 531.

[89] ATLAS Collaboration, *Measurement of the inclusive cross-sections of single top-quark and top-antiquark t-channel production in pp collisions at $\sqrt{s} = 13$ TeV with the ATLAS detector*, JHEP **2017** (2017) 86.

[90] ATLAS Collaboration, *Measurement of the inclusive cross-sections of single top-quark and top-antiquark t-channel production in pp collisions at $\sqrt{s} = 13$ TeV with the ATLAS detector*, JHEP **04** (2017) 086.

[91] CMS Collaboration, *Measurement of the t-channel single-top-quark production cross section and of the $\mid V_{tb} \mid$ CKM matrix element in pp collisions at $\sqrt{s} = 8$ TeV*, JHEP **06** (2014) 090.

[92] CMS Collaboration, *Measurement of the single-top-quark t-channel cross section in pp collisions at $\sqrt{s} = 7$ TeV*, JHEP **12** (2012) 035.

[93] CMS Collaboration, *Cross section measurement of t-channel single top quark production in pp collisions at $\sqrt{s} = 13$ TeV*, Phys. Lett. B **772** (2017) 752–776.

[94] ATLAS Collaboration, *Measurement of the production cross-section of a single top quark in association with a W boson at 8 TeV with the ATLAS experiment*, JHEP **01** (2016) 064.

[95] ATLAS Collaboration, *Measurement of the cross-section for producing a W boson in association with a single top quark in pp collisions at $\sqrt{s} = 13$ TeV with ATLAS*, JHEP **01** (2018) 063.

[96] ATLAS Collaboration, *Evidence for the associated production of a W boson and a top quark in ATLAS at $\sqrt{s} = 7$ TeV*, Phys. Lett. B **716** (2012) 142–159.

[97] CMS Collaboration, *Evidence for Associated Production of a Single Top Quark and W Boson in pp Collisions at $\sqrt{s} = 7$ TeV*, Phys. Rev. Lett. **110** (2013) 022003.

[98] CMS Collaboration, *Observation of the Associated Production of a Single Top Quark and a W Boson in pp Collisions at $\sqrt{s}$ =8 TeV*, Phys. Rev. Lett. **112** (2014) 231802.

[99] CMS Collaboration, *Measurement of the production cross section for single top quarks in association with W bosons in proton-proton collisions at $\sqrt{s} =$ 13 TeV*, JHEP **10** (2018) 117.

[100] ATLAS and CMS Collaborations, *Combination of cross-section measurements for associated production of a single top-quark and a W boson at $\sqrt{s} =$ 8 TeV with the ATLAS and CMS experiments*, Tech. Rep. ATLAS-CONF-2016-023, CERN, Geneva, May, 2016. `http://cds.cern.ch/record/2153385`.

[101] ATLAS Collaboration, *Evidence for single top-quark production in the s-channel in proton-proton collisions at $\sqrt{s} =$ 8 TeV with the ATLAS detector using the Matrix Element Method*, Phys. Lett. B **756** (2016) 228–246.

[102] CMS Collaboration, *Search for s-channel single top quark production in pp collisions at $\sqrt{s} =$ 7 and 8 TeV*, JHEP **09** (2016) 027.

[103] ATLAS Collaboration, *Search for s-channel single top-quark production in pp collisions at $\sqrt{s} =$ 7 TeV*, Tech. Rep. ATLAS-CONF-2011-118, CERN, Geneva, Aug, 2011. `http://cds.cern.ch/record/1376410`.

[104] *ATLAS Top Quark summary plots*, `https://twiki.cern.ch/twiki/bin/view/AtlasPublic/TopPublicResults`. Accessed: 2018-11-20.

[105] The Gfitter Group, *The global electroweak fit at NNLO and prospects for the LHC and ILC*, Eur. Phys. J. C **74** (2014) 3046.

[106] J. Haller, et al., *Update of the global electroweak fit and constraints on two-Higgs-doublet models*, Eur. Phys. J. C **78** (2018) 675.

[107] G. Isidori, G. Ridolfi, and A. Strumia, *On the metastability of the standard model vacuum*, Nucl. Phys. B **609** (2001) 387–409.

[108] *First combination of Tevatron and LHC measurements of the top-quark mass*, Tech. Rep. ATLAS-CONF-2014-008, ATLAS-CONF-2014-008, CDF-NOTE-11071, CMS-PAS-TOP-13-014, D0-NOTE-6416, CERN, Geneva, Mar, 2014. `http://cds.cern.ch/record/1669819`.

[109] ATLAS Collaboration, *Measurement of the top quark mass in the $t\bar{t} \to$ lepton+jets and $t\bar{t} \to$ dilepton channels using $\sqrt{s} =$ 7 TeV ATLAS data*, Eur. Phys. J. C **75** (2015) 330.

[110] ATLAS Collaboration, *Measurement of the top quark mass in the $t\bar{t} \to$ lepton+jets channel from $\sqrt{s} =$ 8 TeV ATLAS data and combination with previous results*, Submitted to: Eur. Phys. J. (2018).

[111] ATLAS Collaboration, *Top-quark mass measurement in the all-hadronic $t\bar{t}$ decay channel at $\sqrt{s} =$ 8 TeV with the ATLAS detector*, JHEP **2017** (2017) 118.

[112] ATLAS Collaboration, *Measurement of the top-quark mass in the fully hadronic decay channel from ATLAS data at $\sqrt{s} =$ 7 TeV*, Eur. Phys. J. C **75** (2015) 158.

[113] *Measurement of the top quark mass in topologies enhanced with single top-quarks produced in the t-channel in $\sqrt{s}$ = 8 TeV ATLAS data*, Tech. Rep. ATLAS-CONF-2014-055, CERN, Geneva, Sep, 2014. `https://cds.cern.ch/record/1951323`.

[114] ATLAS Collaboration, *Measurement of the top quark mass in the $t\bar{t} \rightarrow$ dilepton channel from $\sqrt{s}$ = 8 TeV ATLAS data*, Phys. Lett. B **761** (2016) 350 – 371.

[115] CMS Collaboration, *Measurement of the top-quark mass in $t\bar{t}$events with lepton+jets final states in pp collisions at $\sqrt{s}$ = 7 TeV*, JHEP **2012** (2012) 105.

[116] CMS Collaboration, *Measurement of the top-quark mass in $t\bar{t}$events with dilepton final states in pp collisions at $\sqrt{s}$ = 7 TeV*, Eur. Phys. J. C **72** (2012) 2202.

[117] CMS Collaboration, *Measurement of the top-quark mass in all-jets $t\bar{t}$ events in pp collisions at $\sqrt{s}$ =7 TeV*, Eur. Phys. J. C **74** (2014) 2758.

[118] CMS Collaboration, *Measurement of the top quark mass using proton-proton data at $\sqrt{s}$ = 7 and 8 TeV*, Phys. Rev. D **93** (2016) 072004.

[119] CMS Collaboration, *Measurement of the top quark mass using single top quark events in proton-proton collisions at $\sqrt{s}$ = 8 TeV*, Eur. Phys. J. C **77** (2017) 354.

[120] CMS Collaboration, *Measurement of the top quark mass with lepton+jets final states using* p p *collisions at $\sqrt{s}$ = 13 TeV*, Eur. Phys. J. C **78** (2018) 891.

[121] CMS Collaboration, *Measurement of the top quark mass in the all-jets final state at $\sqrt{s}$ = 13 TeV*, Tech. Rep. CMS-PAS-TOP-17-008, CERN, Geneva, 2018. `https://cds.cern.ch/record/2628540`.

[122] A. H. Hoang, *The Top Mass: Interpretation and Theoretical Uncertainties*, in *Proceedings, 7th International Workshop on Top Quark Physics (TOP2014): Cannes, France, September 28-October 3, 2014*. 2014.

[123] P. Marquard, et al., *Quark Mass Relations to Four-Loop Order in Perturbative QCD*, Phys. Rev. Lett. **114** (2015) 142002.

[124] M. Beneke, et al., *On the ultimate uncertainty of the top quark pole mass*, Phys. Lett. B **775** (2017) 63–70.

[125] ATLAS Collaboration, *Determination of the top-quark pole mass using $t\bar{t}$ + 1-jet events collected with the ATLAS experiment in 7 TeV pp collisions*, JHEP **10** (2015) 121.

[126] ATLAS Collaboration, *Measurement of the $t\bar{t}$ production cross-section using $e\mu$ events with b-tagged jets in pp collisions at $\sqrt{s}$ = 7 and 8 TeV with the ATLAS detector*, Eur. Phys. J. C **74** (2014) 3109, [Addendum: Eur. Phys. J.C76,no.11,642(2016)].

[127] ATLAS Collaboration, *Measurement of lepton differential distributions and the top quark mass in $t\bar{t}$ production in pp collisions at $\sqrt{s}$ = 8 TeV with the ATLAS detector*, Eur. Phys. J. C **77** (2017) 804.

[128] G. Breit and E. Wigner, *Capture of Slow Neutrons*, Phys. Rev. **49** (1936) 519–531.

[129] M. Jezabek and J. H. Kühn, *QCD Corrections to Semileptonic Decays of Heavy Quarks*, Nucl. Phys. B **314** (1989) 1–6.

[130] A. Czarnecki and K. Melnikov, *Two loop QCD corrections to top quark width*, Nucl. Phys. B **544** (1999) 520–531.

[131] K. G. Chetyrkin, et al., *Second Order QCD Corrections to* $\Gamma(t \to Wb)$, Phys. Rev. D **60** (1999) 114015. 21 p.

[132] J. Gao, C. S. Li, and H. X. Zhu, *Top Quark Decay at Next-to-Next-to Leading Order in QCD*, Phys. Rev. Lett. **110** (2013) 042001.

[133] A. Dabelstein, et al., *Strong supersymmetric quantum effects on the top quark width*, Nucl. Phys. B **454** (1995) 75–85.

[134] J. I. Guasch, *Supersymmetric radiative corrections to top quark and Higgs boson physics*. PhD thesis, Barcelona, Autonoma U., 1999. `arXiv:hep-ph/9906517`.

[135] ATLAS Collaboration, *Search for a scalar partner of the top quark in the jets plus missing transverse momentum final state at* $\sqrt{s}$*=13 TeV with the ATLAS detector*, JHEP **12** (2017) 085.

[136] ATLAS Collaboration, *Search for top-squark pair production in final states with one lepton, jets, and missing transverse momentum using 36 fb*^{1} *of* $\sqrt{s}$ *=13 TeV pp collision data with the ATLAS detector*, JHEP **06** (2018) 108.

[137] ATLAS Collaboration, *Search for dark matter and other new phenomena in events with an energetic jet and large missing transverse momentum using the ATLAS detector*, JHEP **01** (2018) 126.

[138] ATLAS Collaboration, *Search for supersymmetry in final states with charm jets and missing transverse momentum in 13 TeV pp collisions with the ATLAS detector*, JHEP **09** (2018) 050.

[139] J. Guasch, et al., *Top quark production and decay in the MSSM*, `arXiv:hep-ph/0003109`.

[140] J. E. Kim, *Light Pseudoscalars, Particle Physics and Cosmology*, Phys. Rept. **150** (1987) 1–177.

[141] J. M. Cline and P.-A. Lemieux, *Electroweak phase transition in two Higgs doublet models*, Phys. Rev. D **55** (1997) 3873–3881.

[142] M. Laine and K. Rummukainen, *Two Higgs doublet dynamics at the electroweak phase transition: A Nonperturbative study*, Nucl. Phys. B **597** (2001) 23–69.

[143] L. Fromme, S. J. Huber, and M. Seniuch, *Baryogenesis in the two-Higgs doublet model*, JHEP **11** (2006) 038.

[144] F. Larios, R. Martínez, and M. A. Perez, *New physics effects in the flavor-changing neutral couplings of the top quark*, Int. J. Mod. Phys. A **21** (2006) 3473–3494.

[145] A. J. Buras, *Flavor changing neutral current processes*, Proceedings, 28th International Conference, ICHEP 96, Warsaw, Poland (1996) 243–270.

[146] J. Alwall, et al., *Is $V_{tb} \simeq 1$?*, Eur. Phys. J. C **49** (2007) 791–801.

[147] Y. Chao, et al., *Threshold Effects in the Decay of Heavy b' and t' Quarks*, Tech. Rep. arXiv:1101.0592, Jan, 2011. `http://cds.cern.ch/record/1318995`.

[148] B. Holdom, et al., *Four Statements about the Fourth Generation*, PMC Phys. A **3** (2009) 4.

[149] M. Carena, et al., *Electroweak baryogenesis and new TeV fermions*, Nucl. Phys. B **716** (2005) 319–351.

[150] DØ Collaboration, *Determination of the width of the top quark*, Phys. Rev. Lett. **106** (2011) 022001.

[151] DØ Collaboration, *An Improved determination of the width of the top quark*, Phys. Rev. D **85** (2012) 091104.

[152] CMS Collaboration, *Measurement of the ratio $\mathcal{B}(t \to Wb)/\mathcal{B}(t \to Wq)$ in pp collisions at $\sqrt{s}$ = 8 TeV*, Phys. Lett. B **736** (2014) 33–57.

[153] CDF Collaboration, *Direct Bound on the Total Decay Width of the Top Quark in $p\bar{p}$ Collisions at $\sqrt{s}$ = 1.96 TeV*, Phys. Rev. Lett. **102** (2009) 042001.

[154] CDF Collaboration, *Direct Measurement of the Total Decay Width of the Top Quark*, Phys. Rev. Lett. **111** (2013) 202001.

[155] CMS Collaboration,, *Bounding the top quark width using final states with two charged leptons and two jets at $\sqrt{s}$ = 13 TeV*, Tech. Rep. CMS-PAS-TOP-16-019, CERN, Geneva, 2016. `http://cds.cern.ch/record/2218019`.

[156] L. Evans and P. Bryant, *LHC Machine*, JINST **3** (2008) S08001.

[157] *ATLAS luminosity public plots*, `https://twiki.cern.ch/twiki/bin/view/AtlasPublic/LuminosityPublicResultsRun2`. Accessed: 2018-12-10.

[158] ATLAS Collaboration, *The ATLAS Experiment at the CERN Large Hadron Collider*, JINST **3** (2008) S08003.

[159] CMS Collaboration, *The CMS Experiment at the CERN LHC*, JINST **3** (2008) S08004.

[160] LHCb Collaboration, *The LHCb Detector at the LHC*, JINST **3** (2008) S08005.

[161] ALICE Collaboration, *The ALICE experiment at the CERN LHC*, JINST **3** (2008) S08002.

[162] MoEDAL Collaboration, *Technical Design Report of the MoEDAL Experiment*, Tech. Rep. CERN-LHCC-2009-006. MoEDAL-TDR-001, Jun, 2009. `https://cds.cern.ch/record/1181486`.

[163] TOTEM Collaboration, *TOTEM: Technical design report. Total cross section, elastic scattering and diffraction dissociation at the Large Hadron Collider at CERN*, `https://cds.cern.ch/record/644582`.

[164] LHCf Collaboration, *The LHCf detector at the CERN Large Hadron Collider*, JINST **3** (2008) S08006.

[165] M. Capeans, et al., *ATLAS Insertable B-Layer Technical Design Report*, Tech. Rep. CERN-LHCC-2010-013. ATLAS-TDR-19, Sep, 2010. `https://cds.cern.ch/record/1291633`.

[166] V. L. Ginzburg and I. M. Frank, *Radiation of a uniformly moving electron due to its transition from one medium into another*, J. Phys.(USSR) **9** (1945) 353–362, [Zh. Eksp. Teor. Fiz.16,15(1946)].

[167] B. Dolgoshein, *Transition radiation detectors*, Nucl. Instrum. Meth. A **326** (1993) 434–469.

[168] A. Ruiz-Martínez and ATLAS Collaboration, *The Run-2 ATLAS Trigger System*, Tech. Rep. ATL-DAQ-PROC-2016-003, CERN, Geneva, Feb, 2016. `https://cds.cern.ch/record/2133909`.

[169] ATLAS Collaboration, *Luminosity determination in pp collisions at* $\sqrt{s} = 8$ *TeV using the ATLAS detector at the LHC*, Eur. Phys. J. C **76** (2016) 653.

[170] P. Jenni and M. Nessi, *ATLAS Forward Detectors for Luminosity Measurement and Monitoring*, Tech. Rep. CERN-LHCC-2004-010. LHCC-I-014, CERN, Geneva, Mar, 2004. `https://cds.cern.ch/record/721908`. revised version number 1 submitted on 2004-03-22 14:56:11.

[171] P. Jenni, M. Nessi, and M. Nordberg, *Zero Degree Calorimeters for ATLAS*, Tech. Rep. CERN-LHCC-2007-001. LHCC-I-016, CERN, Geneva, Jan, 2007. `http://cds.cern.ch/record/1009649`.

[172] P. Jenni, et al., *ATLAS Forward Detectors for Measurement of Elastic Scattering and Luminosity*. Technical Design Report ATLAS. CERN, Geneva, 2008. `https://cds.cern.ch/record/1095847`.

[173] S. van der Meer, *Calibration of the effective beam height in the ISR*, Tech. Rep. CERN-ISR-PO-68-31. ISR-PO-68-31, CERN, Geneva, 1968. `https://cds.cern.ch/record/296752`.

[174] H. Burkhardt and P. Grafström, *Absolute Luminosity from Machine Parameters*, Tech. Rep. LHC-PROJECT-Report-1019. CERN-LHC-PROJECT-Report-1019, 2007. `https://cds.cern.ch/record/1056691`.

[175] AFP Collaboration, S. Grinstein, *The ATLAS Forward Proton Detector (AFP)*, Nucl. Part. Phys. Proc. **273-275** (2016) 1180–1184. 5 p.

[176] ATLAS Collaboration, *The ATLAS Simulation Infrastructure*, Eur. Phys. J. C **70** (2010) 823–874.

[177] W. Lampl, et al., *Calorimeter Clustering Algorithms: Description and Performance*, Tech. Rep. ATL-LARG-PUB-2008-002. ATL-COM-LARG-2008-003, CERN, Geneva, Apr, 2008. `https://cds.cern.ch/record/1099735`.

[178] ATLAS Collaboration, *Electron efficiency measurements with the ATLAS detector using the 2015 LHC proton-proton collision data*, Tech. Rep. ATLAS-CONF-2016-024, CERN, Geneva, Jun, 2016. `https://cds.cern.ch/record/2157687`.

[179] ATLAS Collaboration, *Electron and photon energy calibration with the ATLAS detector using data collected in 2015 at* $\sqrt{s}$ *= 13 TeV*, Tech. Rep. ATL-PHYS-PUB-2016-015, CERN, Geneva, Aug, 2016. `https://cds.cern.ch/record/2203514`.

[180] ATLAS Collaboration, *Muon reconstruction performance of the ATLAS detector in proton-proton collision data at* $\sqrt{s}$ *=13 TeV*, Eur. Phys. J. C **76** (2016) 292.

[181] M. Cacciari, G. P. Salam, and G. Soyez, *The anti-*k_t *jet clustering algorithm*, JHEP **04** (2008) 063.

[182] M. Cacciari and G. P. Salam, *Dispelling the* N^3 *myth for the* k_t *jet-finder*, Phys. Lett. B **641** (2006) 57–61.

[183] M. Cacciari, G. P. Salam, and G. Soyez, *FastJet user manual*, Eur. Phys. J. C **72** (2012) 1896.

[184] S. Catani, et al., *New clustering algorithm for multi - jet cross-sections in e+ e- annihilation*, Phys. Lett. B **269** (1991) 432–438.

[185] Y. L. Dokshitzer, et al., *Better jet clustering algorithms*, JHEP **08** (1997) 001.

[186] G. P. Salam, *Towards Jetography*, Eur. Phys. J. C **67** (2010) 637–686.

[187] ATLAS Collaboration, *Jet energy scale measurements and their systematic uncertainties in proton-proton collisions at* $\sqrt{s}$ *= 13 TeV with the ATLAS detector*, Phys. Rev. D **96** (2017) 072002.

[188] ATLAS Collaboration, *Tagging and suppression of pileup jets with the ATLAS detector*, Tech. Rep. ATLAS-CONF-2014-018, CERN, Geneva, May, 2014. `https://cds.cern.ch/record/1700870`.

[189] ATLAS Collaboration, *Pile-up subtraction and suppression for jets in ATLAS*, Tech. Rep. ATLAS-CONF-2013-083, CERN, Geneva, Aug, 2013. `http://cds.cern.ch/record/1570994`.

[190] ATLAS Collaboration, *Performance of missing transverse momentum reconstruction with the ATLAS detector using proton-proton collisions at* $\sqrt{s}$ *= 13 TeV*, Eur. Phys. J. C **78** (2018) 903.

[191] ATLAS Collaboration, *Measurements of b-jet tagging efficiency with the ATLAS detector using* $t\bar{t}$ *events at* $\sqrt{s}$ *= 13 TeV*, JHEP **08** (2018) 089.

[192] R. E. Kálmán, *A New Approach to Linear Filtering and Prediction Problems*, Journal of Basic Engineering **82** (1960) 35.

[193] ATLAS Collaboration, *Performance of b-Jet Identification in the ATLAS Experiment*, JINST **11** (2016) P04008.

[194] ATLAS Collaboration, *Measurement of b-tagging Efficiency of c-jets in $t\bar{t}$ Events Using a Likelihood Approach with the ATLAS Detector*, Tech. Rep. ATLAS-CONF-2018-001, CERN, Geneva, Mar, 2018. `http://cds.cern.ch/record/2306649`.

[195] ATLAS Collaboration, *Calibration of light-flavour jet b-tagging rates on ATLAS proton-proton collision data at $\sqrt{s} = 13$ TeV*, Tech. Rep. ATLAS-CONF-2018-006, CERN, Geneva, Apr, 2018. `http://cds.cern.ch/record/2314418`.

[196] W. Lukas, *Fast Simulation for ATLAS: Atlfast-II and ISF*, Tech. Rep. ATL-SOFT-PROC-2012-065, CERN, Geneva, Jun, 2012. `https://cds.cern.ch/record/1458503`.

[197] E. Richter-Was, D. Froidevaux, and L. Poggioli, *ATLFAST 2.0 a fast simulation package for ATLAS*, Tech. Rep. ATL-PHYS-98-131, CERN, Geneva, Nov, 1998. `https://cds.cern.ch/record/683751`.

[198] T. Sjöstrand, S. Mrenna, and P. Z. Skands, *PYTHIA 6.4 Physics and Manual*, JHEP **05** (2006) 026.

[199] T. Sjöstrand, S. Mrenna, and P. Z. Skands, *A Brief Introduction to PYTHIA 8.1*, Comput. Phys. Commun. **178** (2008) 852–867.

[200] T. Sjöstrand, et al., *An Introduction to PYTHIA 8.2*, Comput. Phys. Commun. **191** (2015) 159–177.

[201] P. Nason, *A New method for combining NLO QCD with shower Monte Carlo algorithms*, JHEP **11** (2004) 040.

[202] S. Frixione, P. Nason, and C. Oleari, *Matching NLO QCD computations with Parton Shower simulations: the POWHEG method*, JHEP **11** (2007) 070.

[203] S. Alioli, et al., *A general framework for implementing NLO calculations in shower Monte Carlo programs: the POWHEG BOX*, JHEP **06** (2010) 043.

[204] D. J. Lange, *The EvtGen particle decay simulation package*, Nucl. Instrum. Meth. A **462** (2001) 152–155.

[205] R. D. Ball et al., *Parton distributions with LHC data*, Nucl. Phys. B **867** (2013) 244–289.

[206] A. Buckley, *ATLAS Pythia 8 tunes to 7 TeV data*, Tech. Rep. ATL-PHYS-PROC-2014-273, CERN, Geneva, Dec, 2014. `https://cds.cern.ch/record/1974411`.

[207] J. Bellm et al., *Herwig 7.0/Herwig++ 3.0 release note*, Eur. Phys. J. C **76** (2016) 196.

[208] M. Bahr et al., *Herwig++ Physics and Manual*, Eur. Phys. J. C **58** (2008) 639–707.

[209] L. A. Harland-Lang, et al., *Parton distributions in the LHC era: MMHT 2014 PDFs*, Eur. Phys. J. C **75** (2015) 204.

[210] J. Alwall, et al., *The automated computation of tree-level and next-to-leading order differential cross sections, and their matching to parton shower simulations*, JHEP **07** (2014) 079.

[211] T. Ježo, et al., *An NLO+PS generator for $t\bar{t}$ and Wt production and decay including non-resonant and interference effects*, Eur. Phys. J. C **76** (2016) 691.

[212] T. Ježo and P. Nason, *On the Treatment of Resonances in Next-to-Leading Order Calculations Matched to a Parton Shower*, JHEP **12** (2015) 065.

[213] E. Re, *Single-top Wt-channel production matched with parton showers using the POWHEG method*, Eur. Phys. J. C **71** (2011) 1547.

[214] T. Gleisberg, et al., *Event generation with SHERPA 1.1*, JHEP **02** (2009) 007.

[215] J. Butterworth, et al., *Single Boson and Diboson Production Cross Sections in pp Collisions at $\sqrt{s} = 7$ TeV*, Tech. Rep. ATL-COM-PHYS-2010-695, CERN, Geneva, Aug, 2010. `https://cds.cern.ch/record/1287902`.

[216] ATLAS Collaboration, *Measurement of W and Z Boson Production Cross Sections in pp Collisions at $\sqrt{s} = 13$ TeV in the ATLAS Detector*, Tech. Rep. ATLAS-CONF-2015-039, CERN, Geneva, Aug, 2015. `https://cds.cern.ch/record/2045487`.

[217] J. M. Campbell and R. K. Ellis, *An Update on vector boson pair production at hadron colliders*, Phys. Rev. D **60** (1999) 113006.

[218] LHC Higgs Cross Section Working Group Collaboration, D. de Florian et al., *Handbook of LHC Higgs Cross Sections: 4. Deciphering the Nature of the Higgs Sector*, `arXiv:1610.07922`.

[219] DØ Collaboration, *Measurement of the $t\bar{t}$ production cross section in $p\bar{p}$ collisions at $\sqrt{s} = 1.96$ TeV using kinematic characteristics of lepton + jets events*, Phys. Rev. D **76** (2007) 092007.

[220] R. Brun and F. Rademakers, *ROOT: An object oriented data analysis framework*, Nucl. Instrum. Meth. A **389** (1997) 81–86.

[221] A. Höcker, et al., *TMVA - Toolkit for Multivariate Data Analysis with ROOT: Users guide.*, Tech. Rep. physics/0703039, CERN, Geneva, Mar, 2007. `https://cds.cern.ch/record/1019880`.

[222] J. Erdmann, et al., *A likelihood-based reconstruction algorithm for top-quark pairs and the KLFitter framework*, Nucl. Instrum. Meth. A **748** (2014) 18–25.

[223] A. C. Caldwell, D. Kollár, and K. Kröninger, *BAT - The Bayesian Analysis Toolkit*, JPCS **219** (2010) 032013.

[224] ATLAS Collaboration, *Measurement of the W boson polarisation in $t\bar{t}$ events from pp collisions at $\sqrt{s} = 8$ TeV in the lepton+jets channel with ATLAS*, Eur. Phys. J. C **77** (2017) 264.

[225] D. Azevedo, et al., *CP tests of Higgs couplings in $t\bar{t}h$ semileptonic events at the LHC*, Phys. Rev. D **98** (2018) 033004.

[226] ATLAS Collaboration, *Measurements of charge and CP asymmetries in b-hadron decays using top-quark events collected by the ATLAS detector in pp collisions at $\sqrt{s} = 8$ TeV*, JHEP **02** (2017) 071.

[227] DØ Collaboration, *Measurement of the top quark mass using dilepton events*, Phys. Rev. Lett. **80** (1998) 2063–2068.

[228] *Quark versus Gluon Jet Tagging Using Charged Particle Multiplicity with the ATLAS Detector*, Tech. Rep. ATL-PHYS-PUB-2017-009, CERN, Geneva, May, 2017. `http://cds.cern.ch/record/2263679`.

[229] J. Gallicchio and M. D. Schwartz, *Quark and Gluon Jet Substructure*, JHEP **04** (2013) 090.

[230] ATLAS Collaboration, *Jet energy measurement with the ATLAS detector in proton-proton collisions at $\sqrt{s} = 7$ TeV*, Eur. Phys. J. C **73** (2013) 2304.

[231] ATLAS Collaboration, *Performance of Missing Transverse Momentum Reconstruction in ATLAS studied in Proton-Proton Collisions recorded in 2012 at 8 TeV*, Tech. Rep. ATLAS-CONF-2013-082, CERN, Geneva, Aug, 2013. `https://cds.cern.ch/record/1570993`.

[232] Z. Marshall, *Simulation of Pile-up in the ATLAS Experiment*, Tech. Rep. ATL-SOFT-PROC-2013-030, CERN, Geneva, Oct, 2013. `https://cds.cern.ch/record/1616394`.

[233] B. Andersson, et al., *Parton Fragmentation and String Dynamics*, Phys. Rept. **97** (1983) 31–145.

[234] B. R. Webber, *A QCD Model for Jet Fragmentation Including Soft Gluon Interference*, Nucl. Phys. B **238** (1984) 492–528.

[235] *ATLAS Run 1 Pythia8 tunes*, Tech. Rep. ATL-PHYS-PUB-2014-021, CERN, Geneva, Nov, 2014. `https://cds.cern.ch/record/1966419`.

[236] P. Z. Skands, *Tuning Monte Carlo Generators: The Perugia Tunes*, Phys. Rev. D **82** (2010) 074018.

[237] *Simulation of top quark production for the ATLAS experiment at $\sqrt{s} = 13$ TeV*, Tech. Rep. ATL-PHYS-PUB-2016-004, CERN, Geneva, Jan, 2016. `https://cds.cern.ch/record/2120417`.

[238] J. Butterworth et al., *PDF4LHC recommendations for LHC Run II*, J. Phys. G **43** (2016) 023001.

[239] S. Dulat, et al., *New parton distribution functions from a global analysis of quantum chromodynamics*, Phys. Rev. D **93** (2016) 033006.

[240] J. H. Friedman, *Data Analysis Techniques for High-Energy Particle Physics*, p. , 271. 1974. `http://www-public.slac.stanford.edu/sciDoc/docMeta.aspx?slacPubNumber=slac-r-176.html`.

[241] P. Stolte, *Direct Top Quark Decay Width Measurement in the $t\bar{t}$ Lepton+Jets Channel at 8 TeV with the ATLAS Experiment.* II.Physik-UniGö-Diss-2017/03, Georg-August-Universität Göttingen, 2017.

[242] P. Stolte, T. Dado et al. (ATLAS Collaboration), *Direct Top-Quark Decay Width Measurement in the* $t\bar{t}$ *Lepton+Jets Channel at* $\sqrt{s} = 8$ *TeV with the ATLAS Experiment*, Tech. Rep. ATL-COM-PHYS-2017-377, CERN, Geneva, Apr, 2017. `https://cds.cern.ch/record/2259348`.

[243] ATLAS Collaboration, *Measurement of the charge asymmetry in top-quark pair production in the lepton-plus-jets final state in pp collision data at* $\sqrt{s} = 8$ *TeV with the ATLAS detector*, Eur. Phys. J. C **76** (2016) 87, [Erratum: Eur. Phys. J.C77,564(2017)].

[244] W. Verkerke and D. P. Kirkby, *The RooFit toolkit for data modeling*, eConf **C0303241** (2003) MOLT007.

[245] ATLAS Collaboration, *Direct top-quark decay width measurement in the* $t\bar{t}$ *lepton+jets channel at* $\sqrt{s}$ *=8 TeV with the ATLAS experiment*, Eur. Phys. J. C **78** (2018) 129.

[246] ROOT Collaboration, K. Cranmer, et al., *HistFactory: A tool for creating statistical models for use with RooFit and RooStats*, Tech. Rep. CERN-OPEN-2012-016, New York U., New York, Jan, 2012. `https://cds.cern.ch/record/1456844`.

[247] R. Barlow and C. Beeston, *Fitting using finite Monte Carlo samples*, Comput. Phys. Commun. **77** (1993) 219–228. 16 p.

[248] F. James and M. Roos, *MINUIT: a system for function minimization and analysis of the parameter errors and corrections*, Comput. Phys. Commun. **10** (1975) 343–367. 38 p.

[249] W. C. Davidon, *Variable Metric Method for Minimization*, SIAM J. Optim. **1** (1990) 1–17. 17 p.

[250] M. J. D. Powell, *Variable Metric Methods for Constrained Optimization*. Springer Berlin Heidelberg, Berlin, Heidelberg, 1983. `https://doi.org/10.1007/978-3-642-68874-4_12`.

[251] R. Fletcher, *A new approach to variable metric algorithms*, Comput. J. **13** (1970) 317–322.

[252] ATLAS Collaboration, *Jet reconstruction and performance using particle flow with the ATLAS Detector*, Eur. Phys. J. C **77** (2017) 466.

[253] P. P. Giardino and C. Zhang, *Probing the top-quark width using the charge identification of b jets*, Phys. Rev. D **96** (2017) 011901.

[254] G. Apollinari, et al., *High Luminosity Large Hadron Collider HL-LHC*, CERN Yellow Report (2015) 1–19.

Appendices

APPENDIX A

Additional control histograms

A.1. Lepton+jets control histograms without BDT selection

This section shows additional control histograms for basic kinematic variables for both lepton+jets channels when no requirements on the BDT output is imposed.

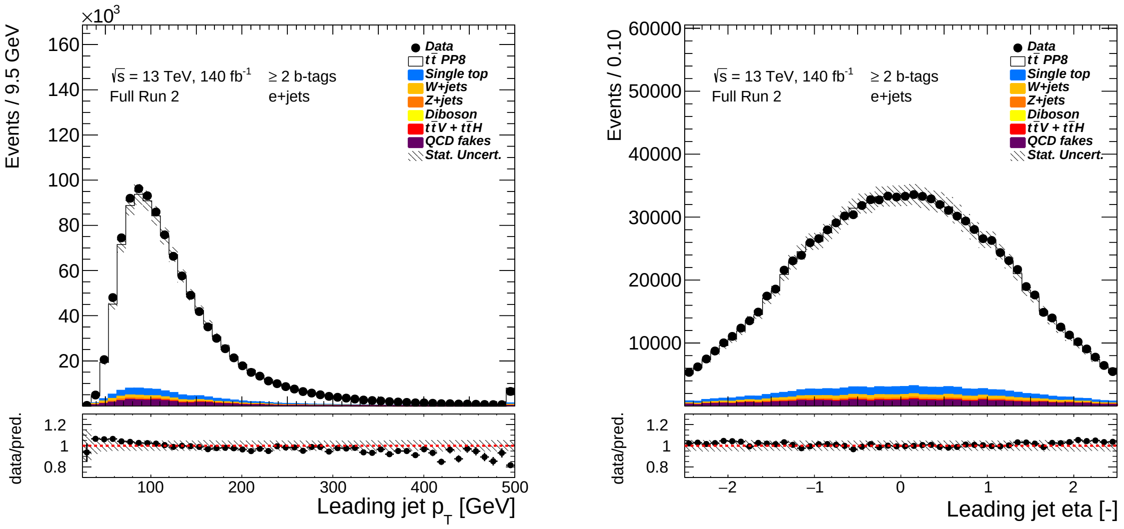

(a) Leading (highest p_T) jet p_T.

(b) Leading (highest p_T) jet η.

Figure A.1.: Data/MC comparison for basic kinematic properties in the electron+jets decay channel. The hashed bands show the uncertainty originating from finite statistics in the MC samples as well as normalisation uncertainty on each signal/background source. The first and last bin contain underflow and overflow events, respectively.

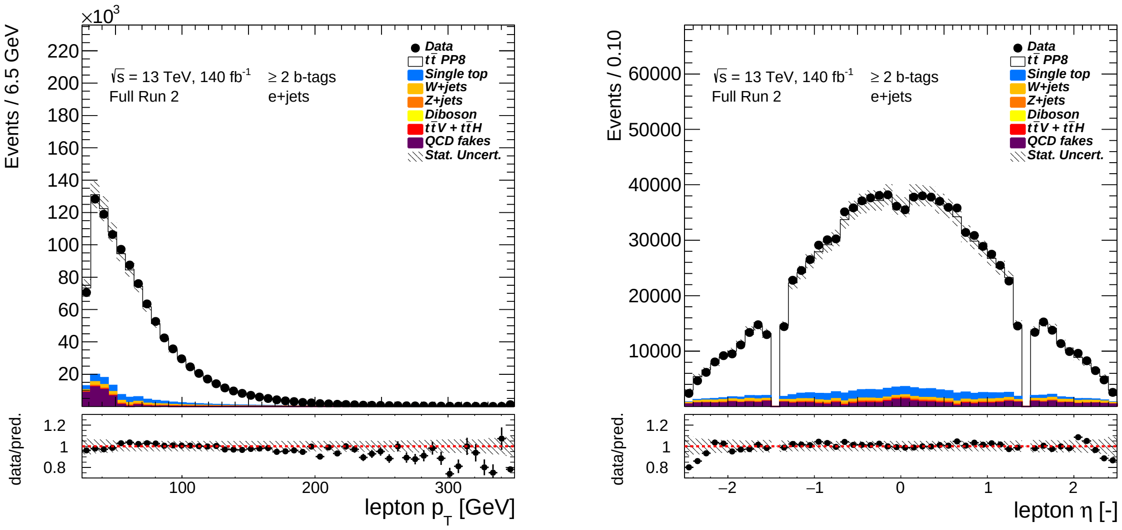

(a) Electron p_{T}.

(b) Electron η.

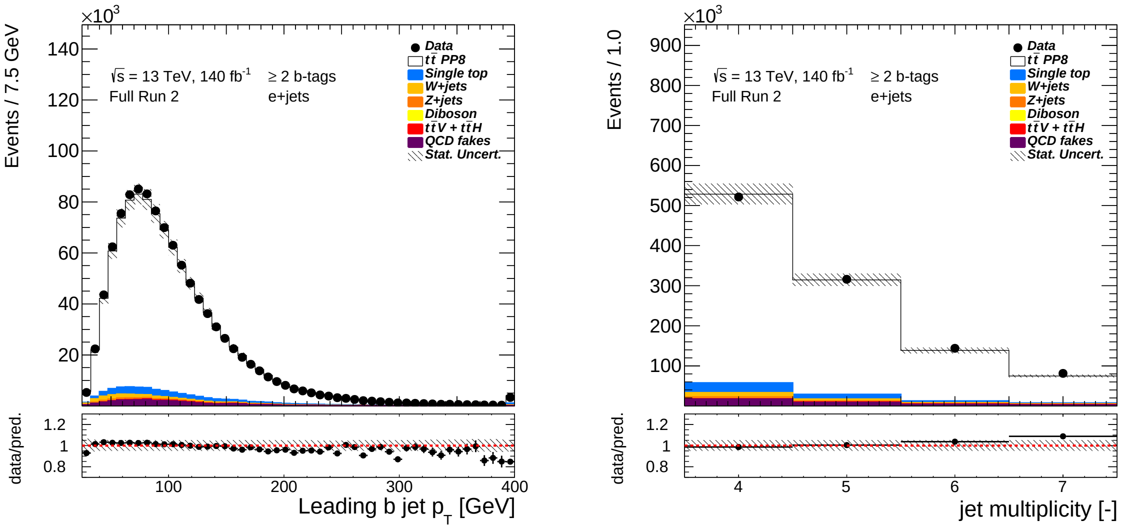

(c) Leading b-tagged jet p_{T}.

(d) Number of jets.

Figure A.2.: Data/MC comparison for basic kinematic properties in the electron+jets decay channel. The hashed bands show the uncertainty originating from finite statistics in the MC samples as well as normalisation uncertainty on each signal/background source. The first and last bin contain underflow and overflow events, respectively.

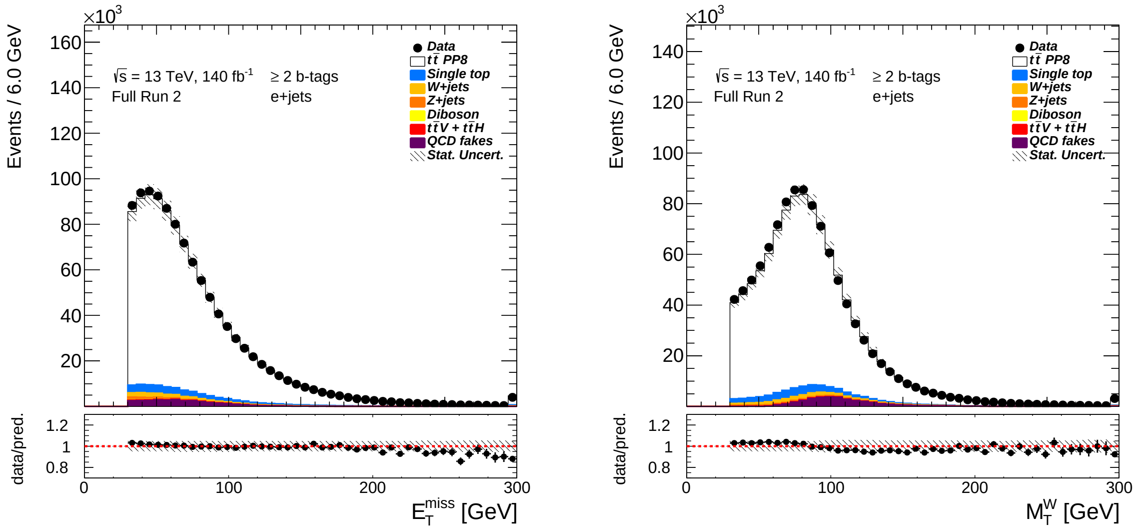

(a) Missing transverse momentum.

(b) Transverse mass of the W boson.

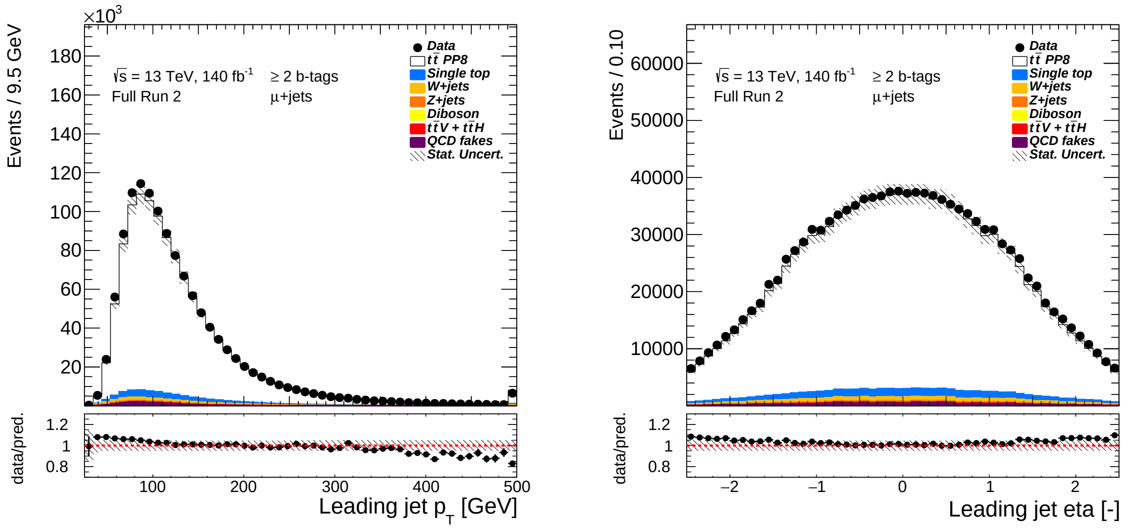

(c) Leading (highest p_T) jet p_T.

(d) Leading (highest p_T) jet η.

Figure A.3.: Data/MC comparison for basic kinematic properties in the electron+jets and muon+jets decay channel. The hashed bands show the uncertainty originating from finite statistics in the MC samples as well as normalisation uncertainty on each signal/background source. The first and last bin contain underflow and overflow events, respectively.

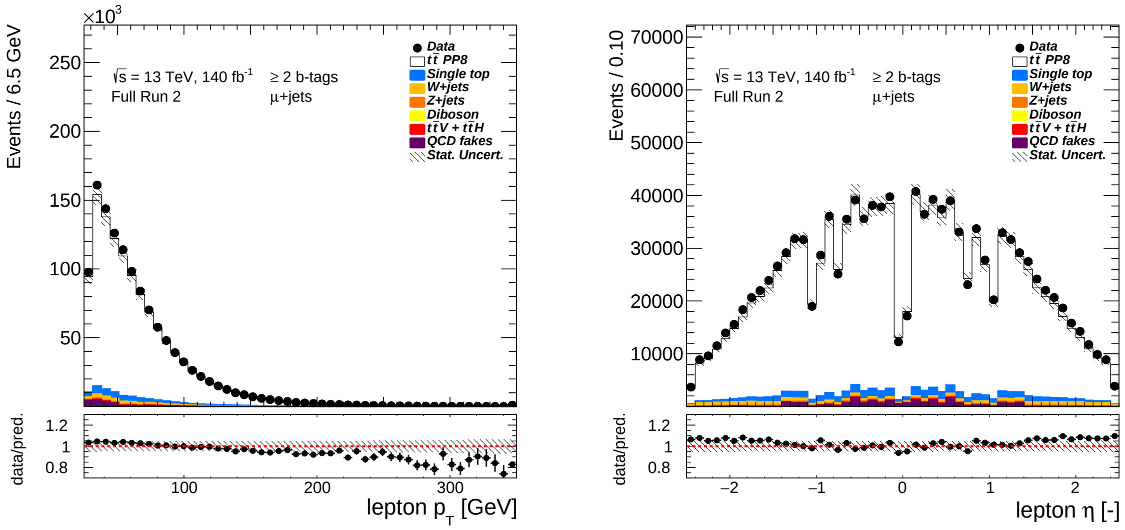

(a) Muon p_T.

(b) Muon η.

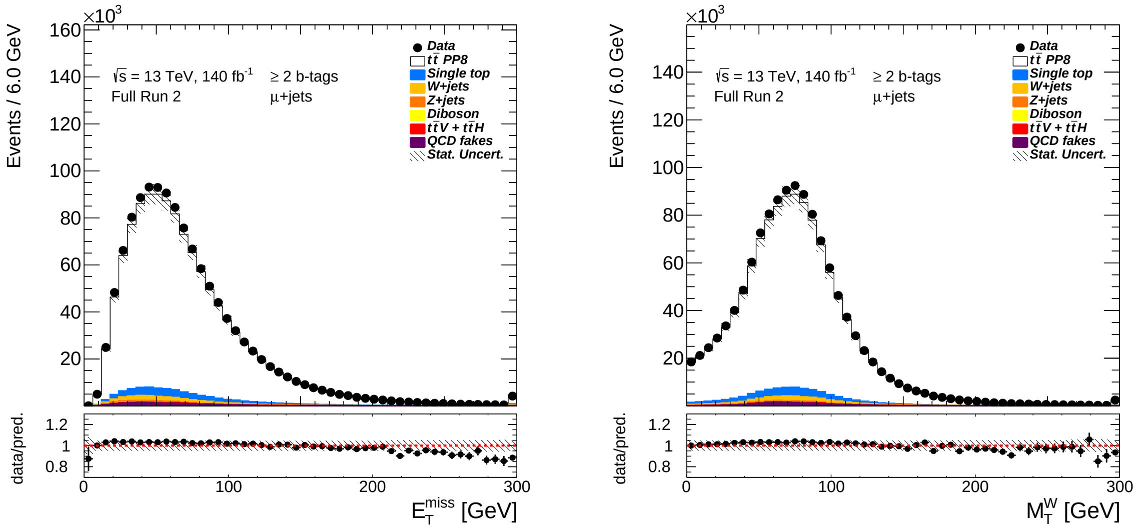

(c) Missing transverse momentum.

(d) Transverse mass of the W boson.

Figure A.4.: Data/MC comparison for basic kinematic properties in the muon+jets decay channel. The hashed bands show the uncertainty originating from finite statistics in the MC samples as well as normalisation uncertainty on each signal/background source. The first and last bin contain underflow and overflow events, respectively.

A.2. Lepton+jets control histograms for variables that require event reconstruction

This section illustrates data to prediction comparison for distributions in the lepton+jets channel where event reconstruction is needed. No requirement on the BDT score is imposed.

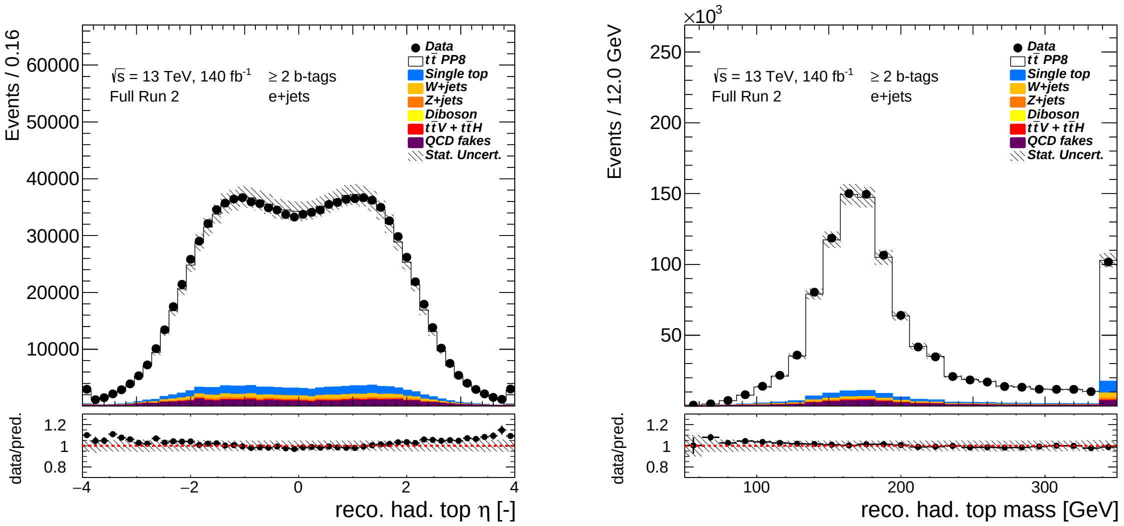

(a) Reconstructed hadronic top-quark η. (b) Reconstructed hadronic top-quark mass.

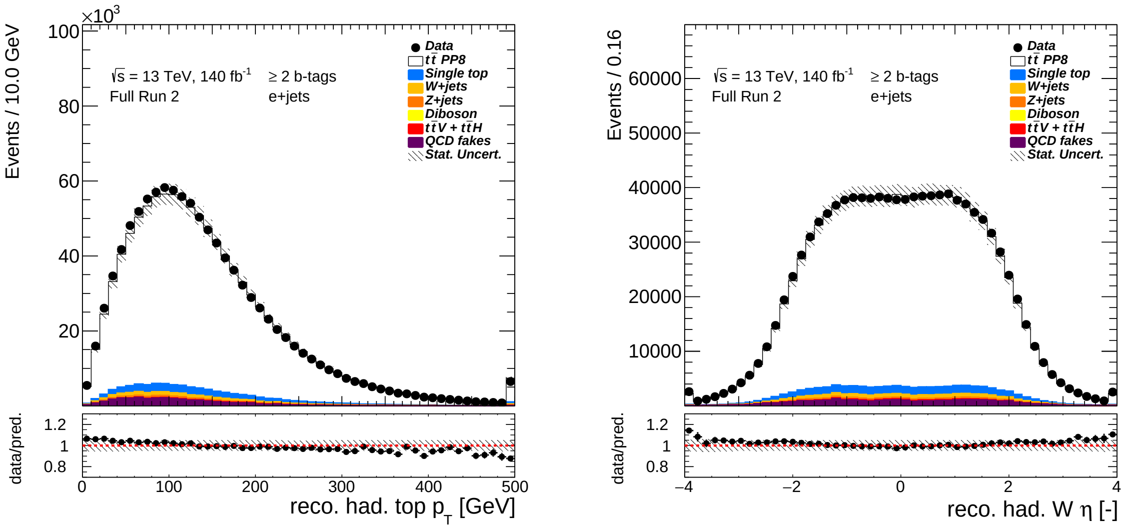

(c) Reconstructed hadronic top-quark p_{T}. (d) Reconstructed hadronic W boson η.

Figure A.5.: Control histograms for the reconstructed hadronically decaying top quark (top) and hadronically decaying W boson (bottom) in the analysis for electron+jets events. No selection on the BDT score is applied. Shaded areas show MC statistical uncertainty and normalisation uncertainty. The first and last bin contain underflow and overflow events, respectively.

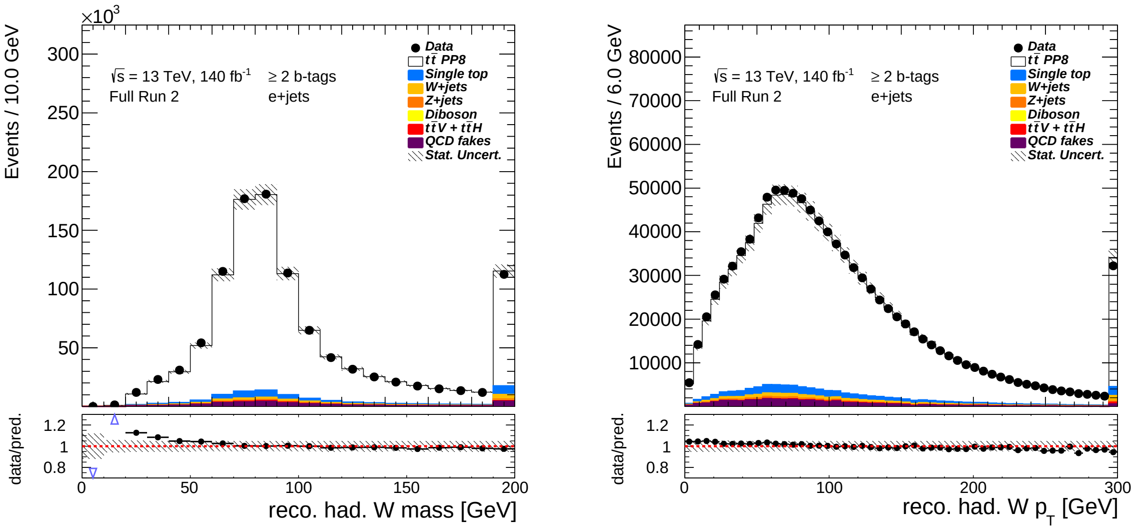

(a) Reconstructed hadronic W boson mass.

(b) Reconstructed hadronic W boson p_{T}.

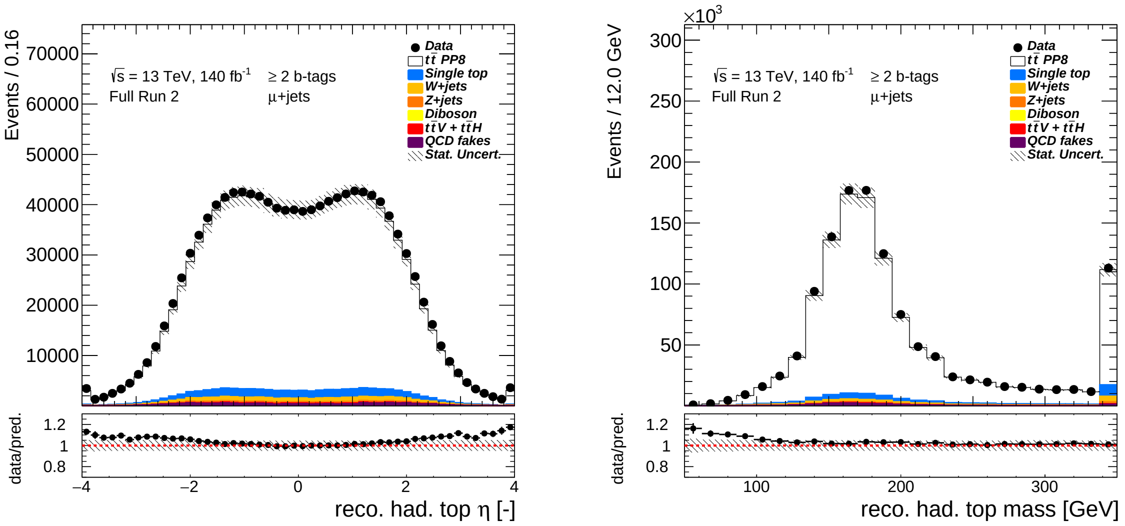

(c) Reconstructed hadronic top-quark η.

(d) Reconstructed hadronic top-quark mass.

Figure A.6.: Control histograms for the reconstructed hadronically decaying top quark (top) and hadronically decaying W boson (bottom) in the analysis for electron+jets and muon+jets events. No selection on the BDT score is applied. Shaded areas show MC statistical uncertainty and normalisation uncertainty. The first and last bin contain underflow and overflow events, respectively.

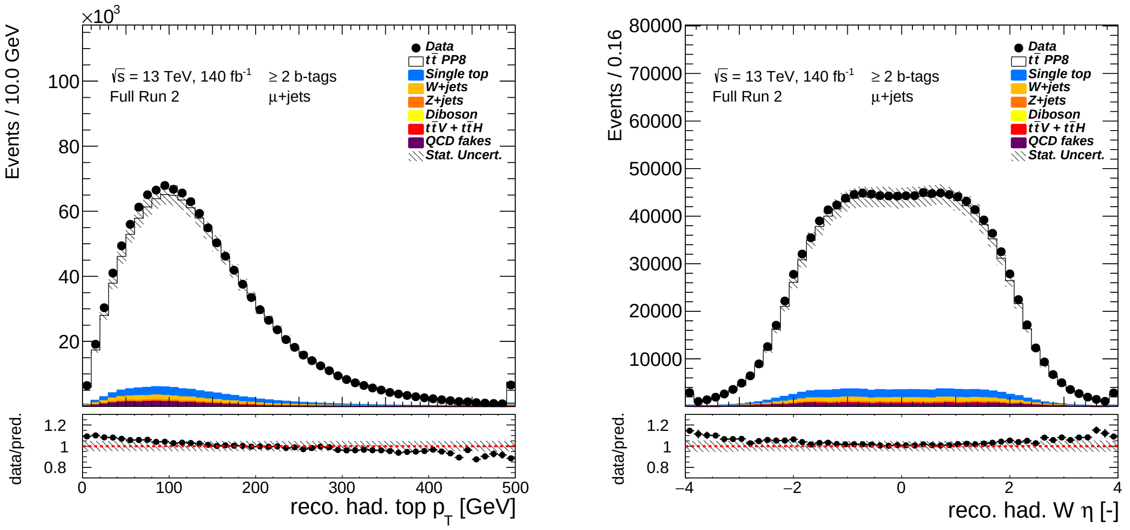

(a) Reconstructed hadronic top-quark p_{T}.

(b) Reconstructed hadronic W boson η.

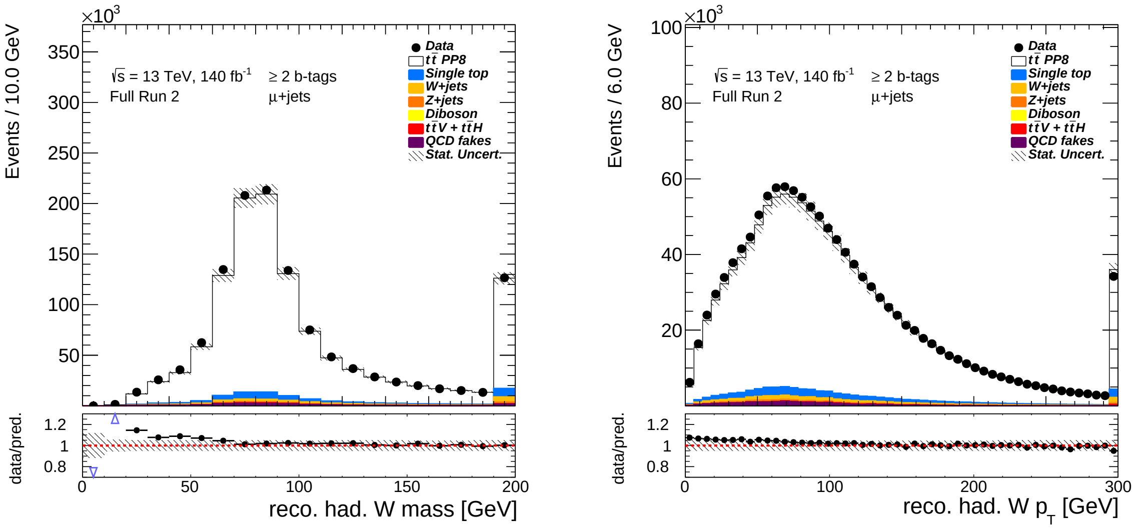

(c) Reconstructed hadronic W boson mass.

(d) Reconstructed hadronic W boson p_{T}.

Figure A.7.: Control histograms for the reconstructed hadronically decaying top quark (top) and hadronically decaying W boson (bottom) in the analysis for muon+jets events. No selection on the BDT score is applied. Shaded areas show MC statistical uncertainty and normalisation uncertainty. The first and last bin contain underflow and overflow events, respectively.

A.3. Dilepton ee and $\mu\mu$ control histograms

This section shows control histograms for basic kinematic distributions in the dilepton ee and $\mu\mu$ channels.

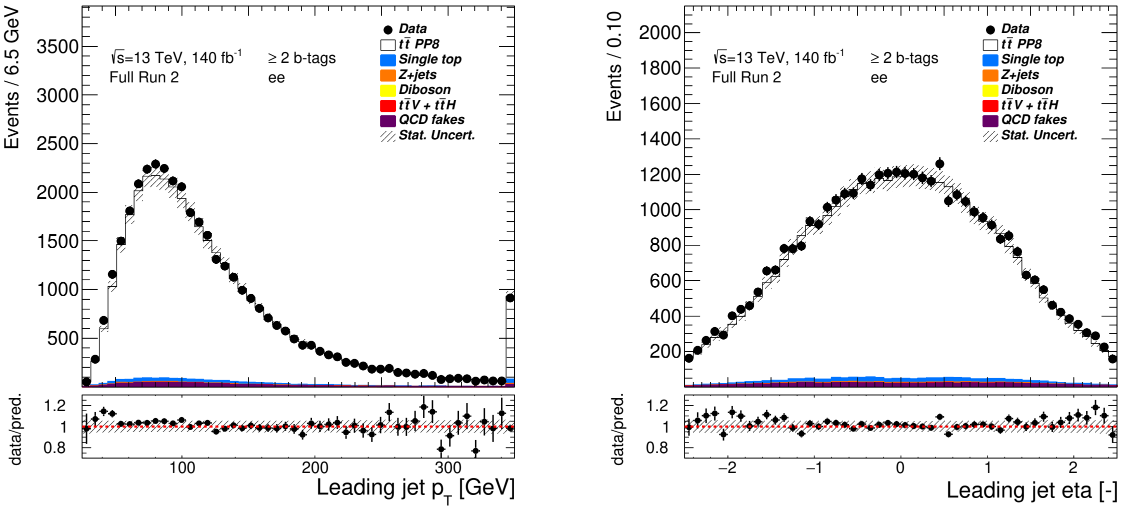

(a) Leading (highest p_{T}) jet p_{T}.

(b) Leading (highest p_{T}) jet η.

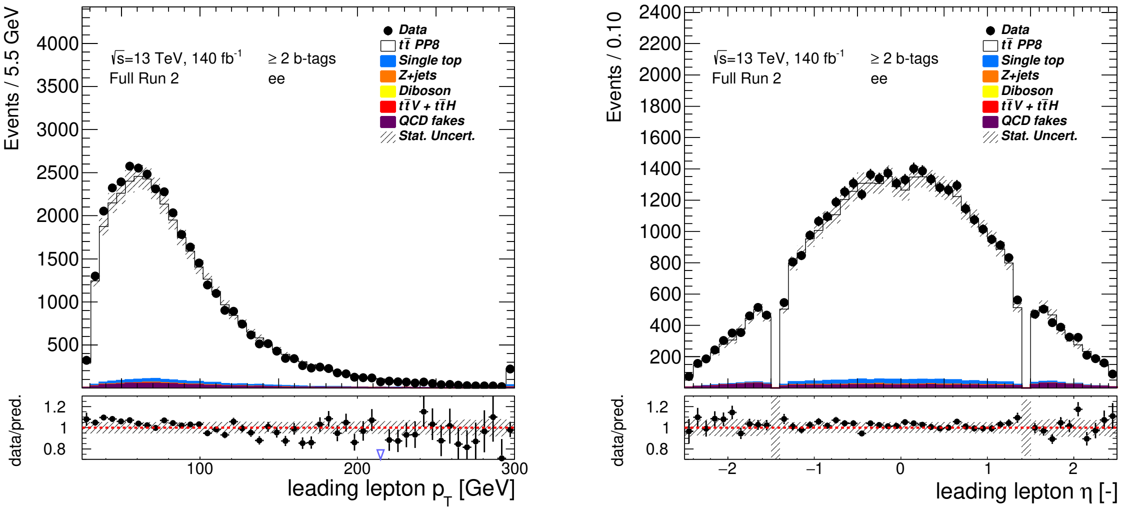

(c) Leading electron p_{T}.

(d) Leading electron η.

Figure A.8.: Data/MC comparison for basic kinematic properties in the dilepton decay channel with electron-electron events. MC statistical uncertainty together with the normalisation uncertainty is shown by the hashed fields. The first and the last bins correspond to the underflow and the overflow events respectively.

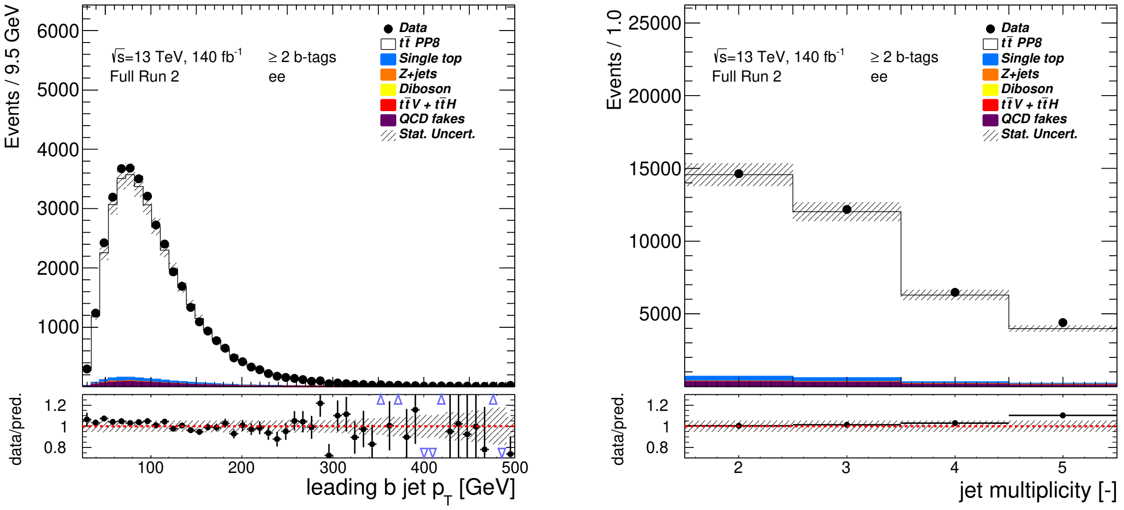

(a) Leading b-tagged jet p_{T}.

(b) Number of jets.

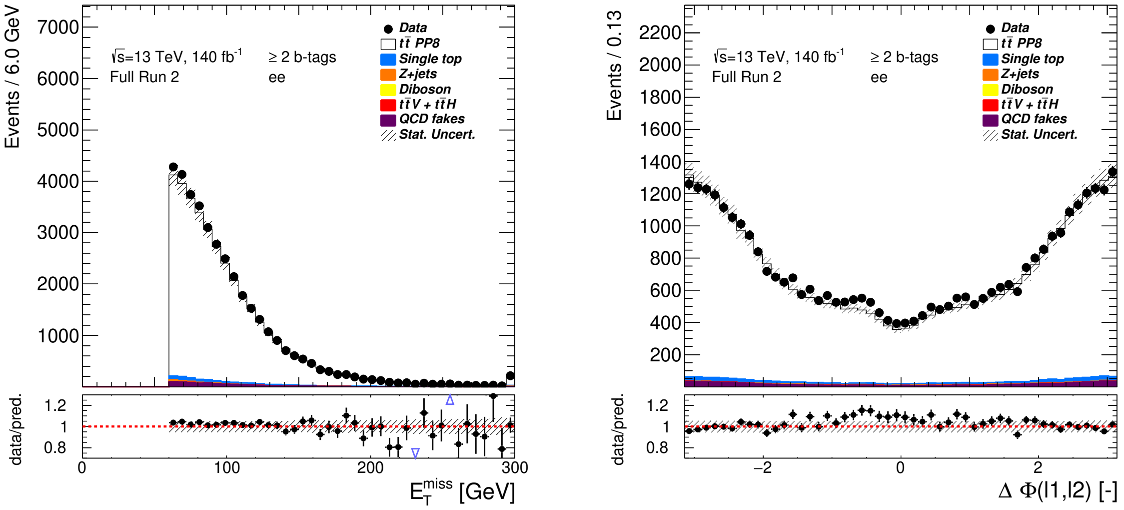

(c) Missing transverse momentum.

(d) $\Delta\phi$ between the two electrons.

Figure A.9.: Data/MC comparison for basic kinematic properties in the dilepton decay channel with electron-electron events. MC statistical uncertainty together with the normalisation uncertainty is shown by the hashed fields. The first and the last bins correspond to the underflow and the overflow events respectively.

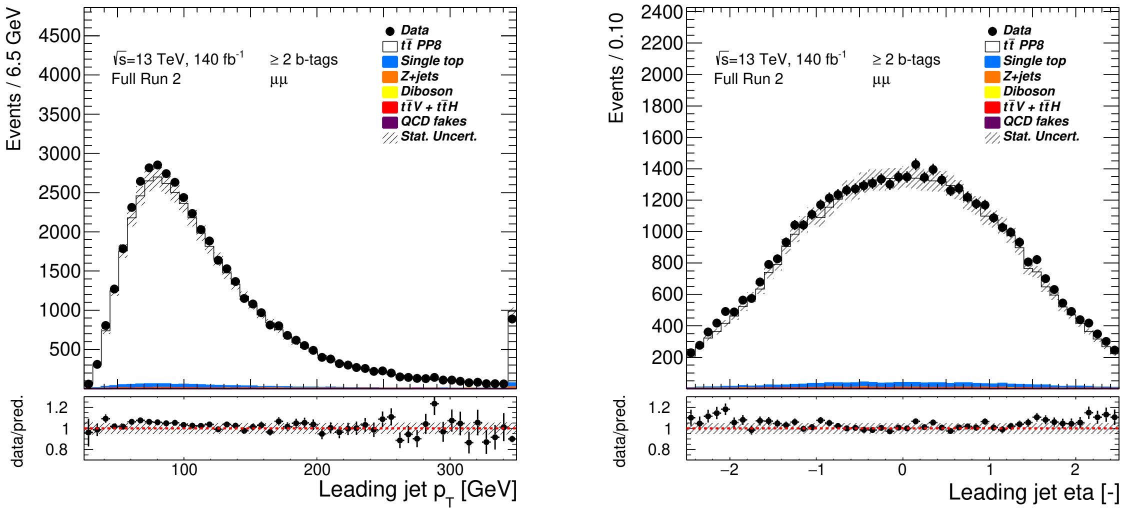

(a) Leading (highest p_{T}) jet p_{T}.

(b) Leading (highest p_{T}) jet η.

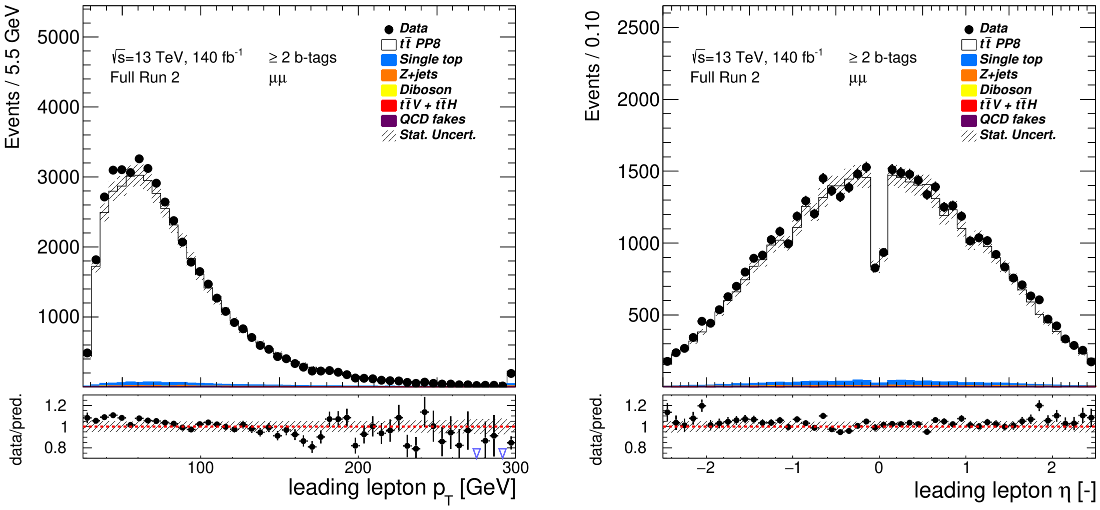

(c) Leading muon p_{T}.

(d) Leading muon η.

Figure A.10.: Data/MC comparison for basic kinematic properties in the dilepton decay channel with muon-muon events. MC statistical uncertainty together with the normalisation uncertainty is shown by the hashed fields. The first and the last bins correspond to the underflow and the overflow events respectively.

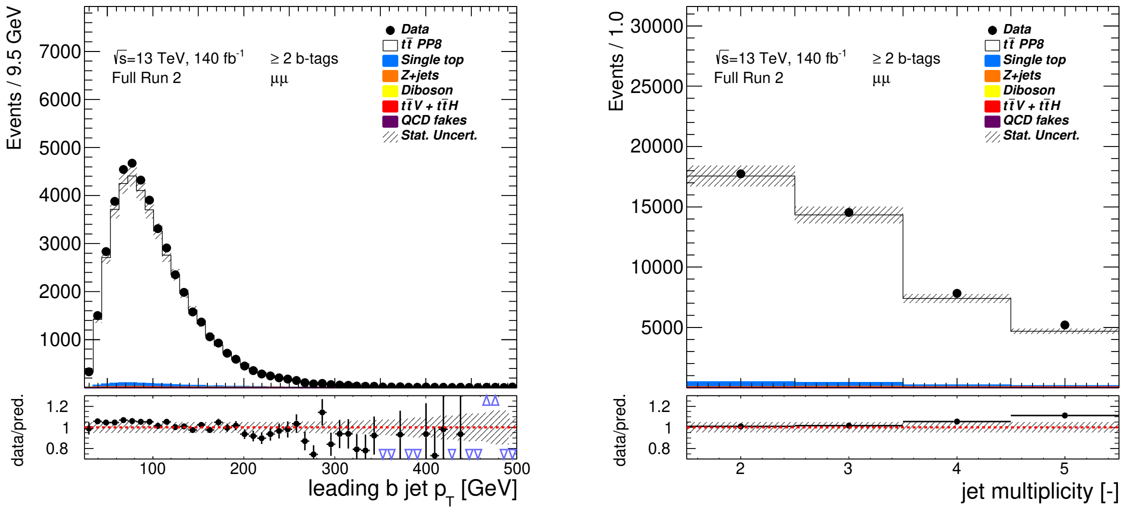

(a) Leading *b*-tagged jet p_{T}.

(b) Number of jets.

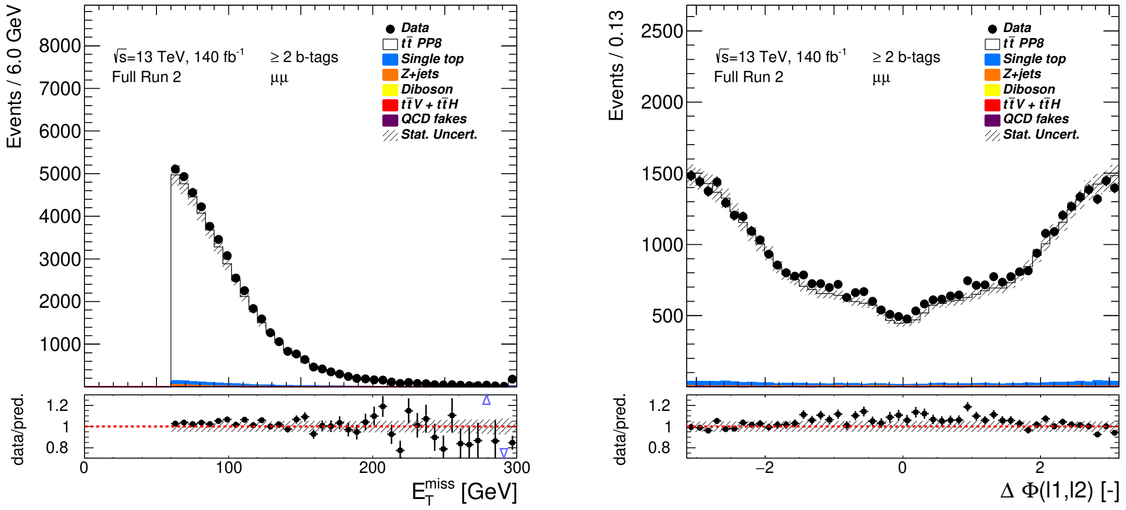

(c) Missing transverse momentum.

(d) $\Delta\phi$ between the two muons.

Figure A.11.: Data/MC comparison for basic kinematic properties in the dilepton decay channel with muon-muon events. MC statistical uncertainty together with the normalisation uncertainty is shown by the hashed fields. The first and the last bins correspond to the underflow and the overflow events respectively.

APPENDIX B

KLFitter transfer functions

Transfer functions (TFs) are essential to the KLFitter algorithm as they enter its likelihood, as described in Section 8.1.1. The KLFitter TFs represent a conditional probability to measure a certain response on the reconstruction level for physics objects with a certain energy (momentum in the case of muons) and object $|\eta|$. The KLFitter TFs constitute a continuous parametrisation of the probability. Historically, double Gaussian functions are used to parametrise the observed reconstructed energy as a function of the true (from the MC truth record) energy of jets, and electrons. For muons, the double Gaussian parametrises the response in muon momentum instead of muon energy. The double Gaussian provides a heuristic, approximate description of the detector response. The double Gaussian formula reads

$$W(\Delta E) = \frac{1}{\sqrt{2\pi}(p_2 + p_3 p_5)} \left(e^{-(\Delta E - p_1)^2/2p_2^2} + p_3 e^{-(\Delta E - p_4)^2/2p_5^2} \right), \tag{B.1}$$

where ΔE is the relative energy difference between the true energy and the reconstructed energy $\Delta E = (E_{\text{truth}} - E_{\text{reco}})/E_{\text{truth}}$. For muons, the transverse momentum, p_{T}, is used. The parameters p_i depend on energy (momentum in case if muons) of the objects, the object $|\eta|$, and the object type. The following parametrisations for electrons and jets are used

$$\begin{aligned} &p_1 = a_1 + b_1 E_{\text{truth}}, \qquad p_2 = a_2/\sqrt{E_{\text{truth}}} + b_2, \\ &p_3 = a_3 + b_3 E_{\text{truth}}, \qquad p_4 = a_4/\sqrt{E_{\text{truth}}} + b_4, \qquad p_5 = a_5 + b_5 E_{\text{truth}}. \end{aligned} \tag{B.2}$$

Where the parameter dependence on the truth object energy is motivated by the calorimeter resolution that is dominated by the $\sim 1/\sqrt{E_{\text{truth}}}$ term. For muons the parametrisation reads

$$p_i = a_i + b_i p_{\text{T,truth}} \qquad \text{for} \quad i = 1, 2, 3, 4, 5. \tag{B.3}$$

The motivation for the parametrisation lies in the tracking based momentum measurements for muons, that follow $\sigma_{p_{\text{T}}}/p_{\text{T}} \sim p_{\text{T}}$. The values of a_i and b_i are estimated separately for b-jets, light-flavour-jets, electrons and muons. Furthermore, the calculation is performed independently in $|\eta|$ regions - $|\eta| = [0, 0.8, 1.37, 1.52, 4.5]$ for b-jets and light-flavour-jets, $|\eta| = [0, 0.8, 1.37, 1.52]$ for electrons and $|\eta| = [0, 1.11, 1.25, 2.5]$ for muons. The parameters a_i and b_i are determined from a global fit to each particle type in each η region.

The TFs for $E_{\mathrm{T}}^{\mathrm{miss}}$ provide a mapping between the x and y components of the missing transverse momentum. The corresponding TFs are parametrised as $E_{x,y}^{\mathrm{miss}} - p_{x,y}^{\nu}$, where $p_{x,y}^{\nu}$ are the x and y components of the true neutrino momentum. The missing momentum response is parametrised as a function of H_{T}, the scalar sum of the energies of all reconstructed jets. A sigmoid function parametrisation is used

$$\sigma(H_{\mathrm{T}}) = p_0 + \frac{p_1}{1 + e^{-p_2(H_{\mathrm{T}} - p_3)}}. \tag{B.4}$$

The TFs have been estimated from 8 TeV $t\bar{t}$ samples generated with the MC@NLO [210] event generator, and the obtained parametrisations are used in the 8 TeV measurement. Only objects that are matched to their parton counterparts, are considered for the measurement of the TFs. Objects are considered matched if $\Delta R < 0.3$ between the reconstructed objects and the corresponding partons, in the case of jets. $\Delta R < 0.1$ is required for electrons and muons.

The TFs, in theory, do not depend on the centre-of-mass energy as they only measure the detector response, which is determined by the detector geometry and the detector material. However, the detector material changes through time, usually matching the changes in centre-of-mass energy, thus it is desirable to calculate the TFs for a new $\sqrt{s}$. This has been done using the 13 TeV $t\bar{t}$ MC samples generated with POWHEG interfaced with PYTHIA 6 [199, 201, 202], using the parametrisation mentioned above. Some technical disadvantages have been discovered during the validation of the 13 TeV version of the TFs. The double Gaussians have five parameters which make it difficult to fit the distribution even in a single object $|\eta|$ and p_{T} region, and the global fit is even more difficult. Furthermore, the complexity of the fit results in multiple set of parameters, p_i, that represent very similar distributions. This makes the fit technically difficult and requires fine-tuning of the initial fit parameters.

Because of the difficulties, an alternative approach has been tested which uses *Crystal Ball functions*[1] parametrisation for jets (both b-jets and light-flavour-jets). The Crystal Ball function, $CB(x)$, is defined as

---

[1] Named after the *Crystal Ball* experiment.

$$
\begin{aligned}
CB(x) &= N \begin{cases} \exp\left(-\frac{(x-\mu)^2}{2\sigma^2}\right) & \text{for} \qquad \frac{x-\mu}{\sigma} > -\alpha, \\ A\left(B - \frac{x-\mu}{\sigma}\right)^{-n} & \text{for} \qquad \frac{x-\mu}{\sigma} \leq -\alpha, \end{cases} \\
A &= \left(\frac{n}{|\alpha|}\right)^n \exp\left(-\frac{|\alpha|^2}{2}\right), \\
B &= \frac{n}{|\alpha|} - |\alpha|, \\
N &= \frac{1}{\sigma(C+D)}, \\
C &= \frac{n}{|\alpha|}\frac{1}{n-1}\exp\left(-\frac{|\alpha|^2}{2}\right), \\
D &= \sqrt{\frac{\pi}{2}}\left[1 + \text{erf}\left(\frac{|\alpha|}{\sqrt{2}}\right)\right], \qquad \text{(B.5)}
\end{aligned}
$$

where erf is the error function. The definition of $CB(x)$ does not seem to be less complex than the double Gaussian formula, however, it has only four independent parameters instead of five for the double Gaussian. Moreover, the Crystal Ball function naturally has a distinct tail, a feature that is observed in b-jets distributions for the energy response, originating from the presence of semileptonic decays if the heavy mesons resulting in a neutrino in the final state that is not measured in the detector. The parameters of the $CB(x)$ are chosen to follow

$$
\begin{aligned}
\alpha &= a_1 + b_1 E_{\text{truth}}, \\
n &= a_2 + b_2 E_{\text{truth}}, \\
\sigma &= a_3 + b_3/\sqrt{E_{\text{truth}}}, \\
\mu &= a_4 + b_4/\sqrt{E_{\text{truth}}}, \qquad \text{(B.6)}
\end{aligned}
$$

following the same logic as for the case of the double Gaussian parametrisation reflecting the expected response of the calorimeters. The parametrisation for electrons, muons and $E_{\text{T}}^{\text{miss}}$ uses simple Gaussian functions

$$
\frac{1}{\sqrt{2\pi}\sigma} e^{-\frac{(x-\mu)^2}{2\sigma^2}}, \qquad \text{(B.7)}
$$

where

$$
\begin{aligned}
\mu &= a_1 + b_1/\sqrt{E_{\text{truth}}}, \\
\sigma &= a_2 + b_2/\sqrt{E_{\text{truth}}}, \qquad \text{(B.8)}
\end{aligned}
$$

for electrons. For muons the parametrisation reads

$$
\begin{aligned}
\mu &= a_1 + b_1 p_{\text{T},truth}, \\
\sigma &= a_2 + b_2 p_{\text{T},truth}. \qquad \text{(B.9)}
\end{aligned}
$$

The parametrisation for the $E_{\mathrm{T}}^{\mathrm{miss}}$ reads

$$\sigma = a_1 + b_1 H_{\mathrm{T}}, \tag{B.10}$$

where the TFs for $E_{\mathrm{T}}^{\mathrm{miss}}$ are parametrised in $E_{x,y}^{\mathrm{miss}} - p_{x,y}^{\nu}$. The strategy for the global parametrisation follows the steps outlined above for the double Gaussian parametrisation where the individual fits depend on the object type and the object $|\eta|$. The new parametrisations provide a simplified version of the TFs compared to the usage of double Gaussians, while still preserving the important features of the TFs. As an illustration of the fits, Figure B.1 shows the detector response for jets fitted with the Crystal Ball function.

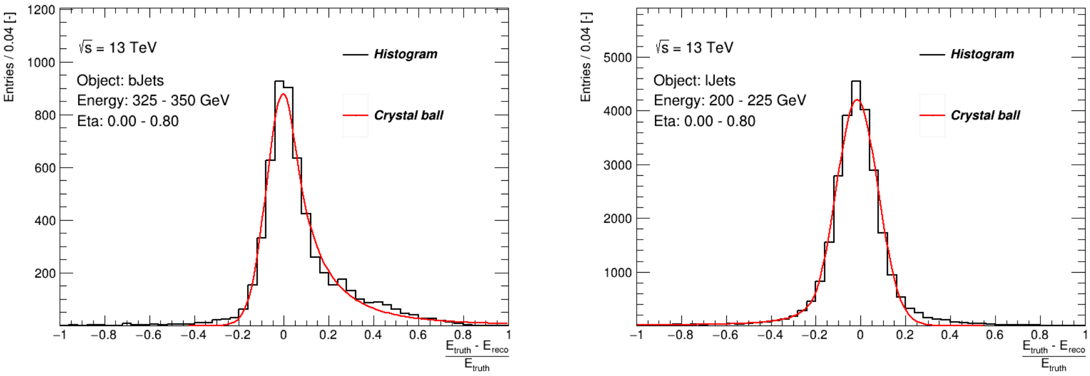

Figure B.1.: An example of the fit with the Crystal Ball function to the detector response for b-jets with $|\eta| < 0.8$ and $325 < p_{\mathrm{T}} < 350$ GeV (left), and light-flavour jets with $|\eta| < 0.8$ and $200 < p_{\mathrm{T}} < 225$ GeV (right).

APPENDIX C

BDT input variables

This appendix shows input variables used in the BDT training of the jet-to-parton assignment in the lepton+jets channel. Figures C.1–C.2 and C.3–C.4 demonstrate that the input variables used for the BDT training agree between the prediction and the observed data and thus are safe to use further in the training process. Figures C.5–C.8 illustrate the separation power for the input variables of the reconstruction BDT between permutations where all four partons from the $t\bar{t}$ decay are correctly assigned to their corresponding jets (signal) and permutations where at least one of the partons is not assigned correctly (background). Correlations between the input variables are shown in Figure C.9.

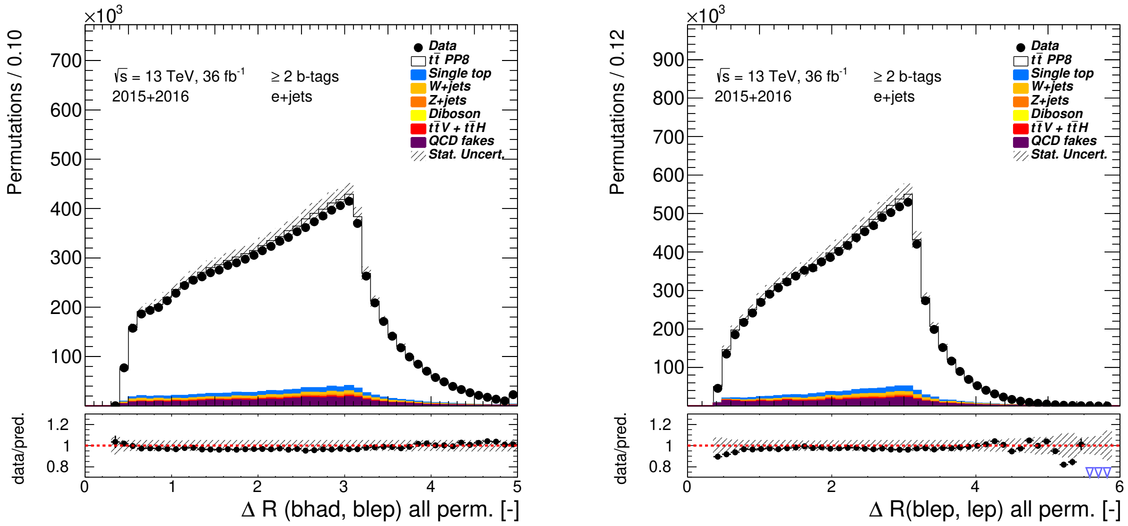

(a) ΔR between the two b-jets.

(b) ΔR between the b-jet and the electron.

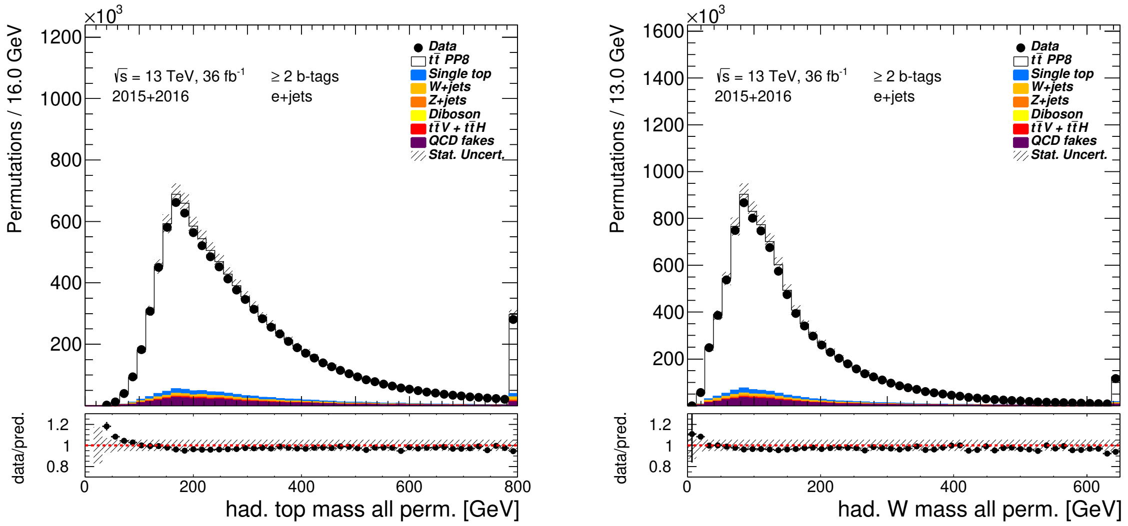

(c) Reconstructed hadronic top-quark mass.

(d) Reconstructed hadronic W boson mass.

Figure C.1.: Control plots displaying the data/prediction comparison for the input variables of the reconstruction BDT in the electron+jets decay channel. Histograms are filled multiple times per event, once for each considered permutations of reconstructed jets to the corresponding partons. Only data recorded in 2015 and 2016 are compared with their corresponding prediction. The hashed bands show the uncertainty originating from finite number of events in the MC samples as well as normalisation uncertainty on each signal/background source. The first and last bin contain underflow and overflow events, respectively.

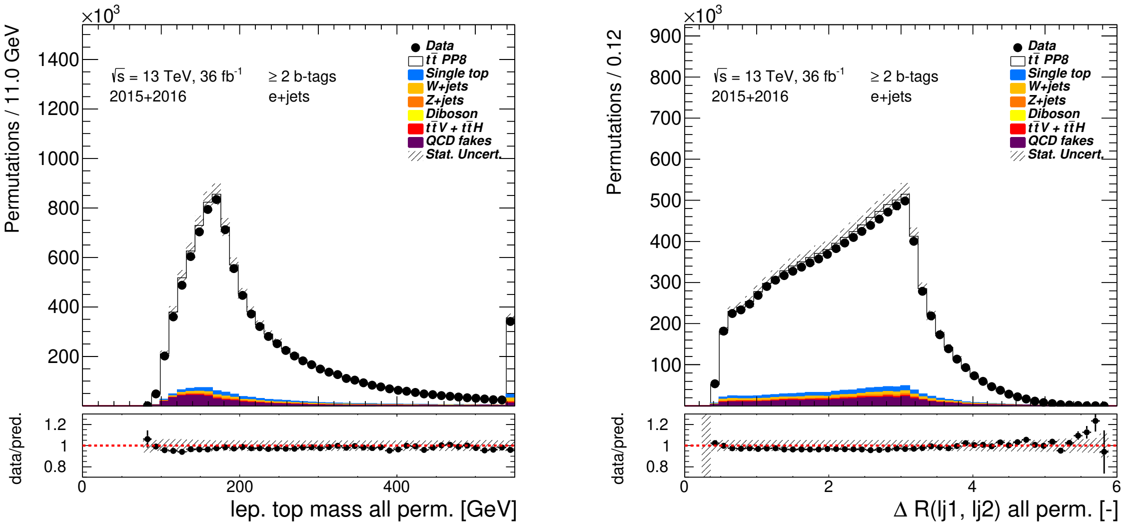

(a) Reconstructed leptonic top-quark mass.

(b) ΔR between the two light-flavour jets.

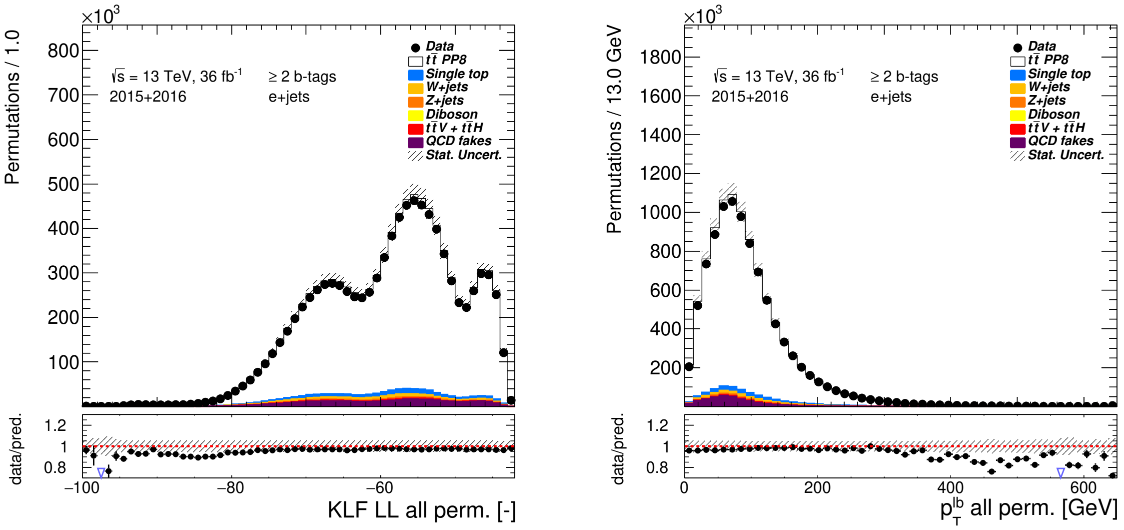

(c) KLFitter logarithm of the likelihood.

(d) p_{T} of the electron and the b-jet pair.

Figure C.2.: Control plots displaying the data/prediction comparison for the input variables of the reconstruction BDT in the electron+jets. Histograms are filled multiple times per event, once for each considered permutations of reconstructed jets to the corresponding partons. Only data recorded in 2015 and 2016 are compared with their corresponding prediction. The hashed bands show the uncertainty originating from finite number of events in the MC samples as well as normalisation uncertainty on each signal/background source. The first and last bin contain underflow and overflow events, respectively.

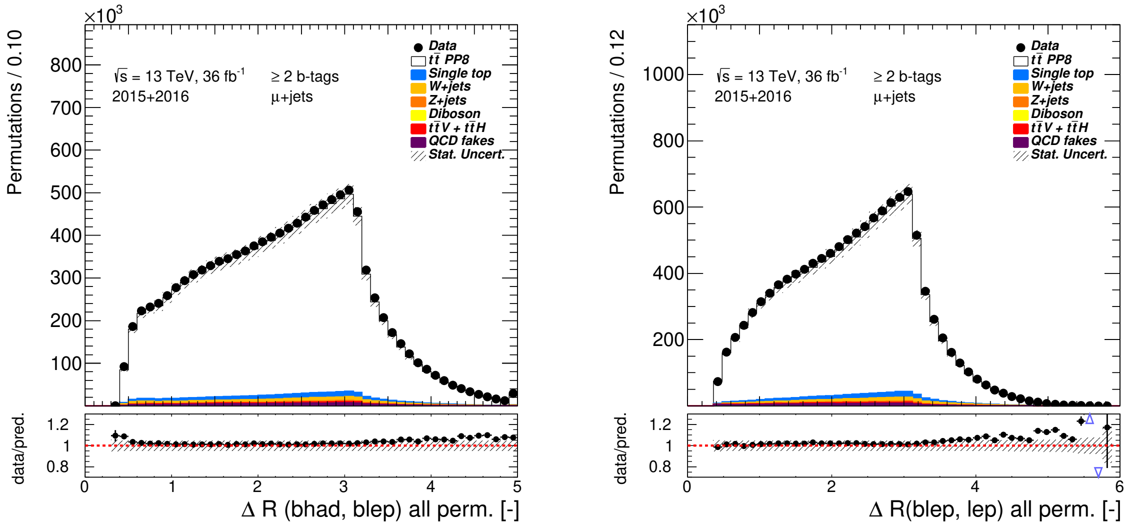

(a) ΔR between the two b-jets.

(b) ΔR between the b-jet and the muon.

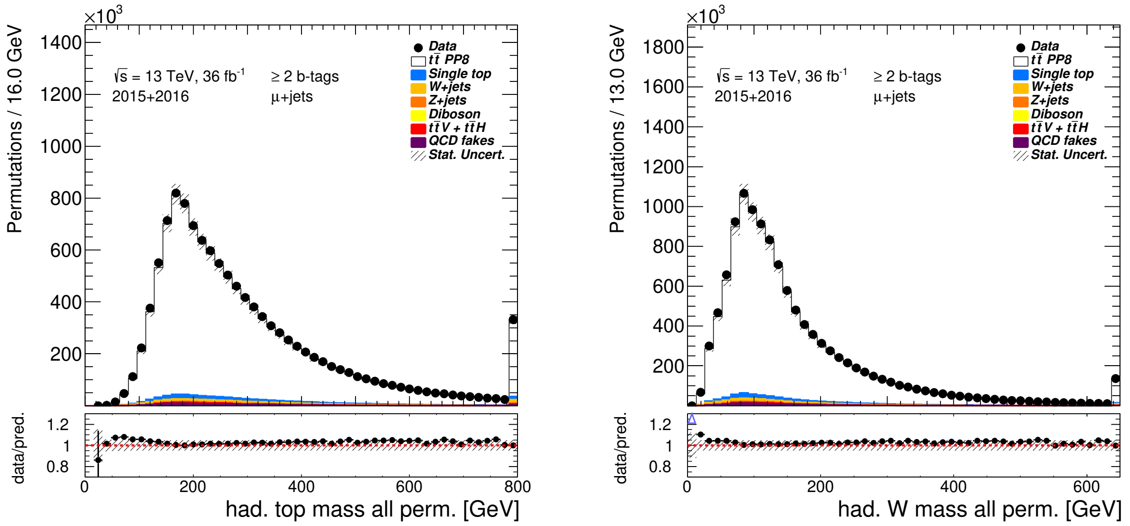

(c) Reconstructed hadronic top-quark mass.

(d) Reconstructed hadronic W boson mass.

Figure C.3.: Control plots displaying the data/prediction comparison for the input variables of the reconstruction BDT in the muon+jets decay channel. Histograms are filled multiple times per event, once for each considered permutations of reconstructed jets to the corresponding partons. Only data recorded in 2015 and 2016 are compared with their corresponding prediction. The hashed bands show the uncertainty originating from finite number of events in the MC samples as well as normalisation uncertainty on each signal/background source. The first and last bin contain underflow and overflow events, respectively.

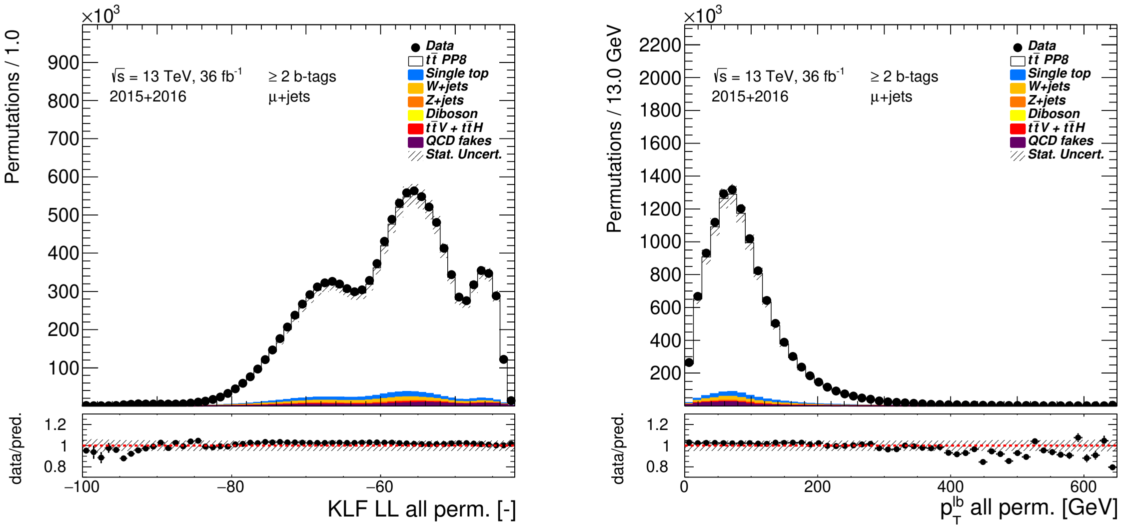

(a) KLFitter logarithm of the likelihood.

(b) p_{T} of the muon and the b-jet pair.

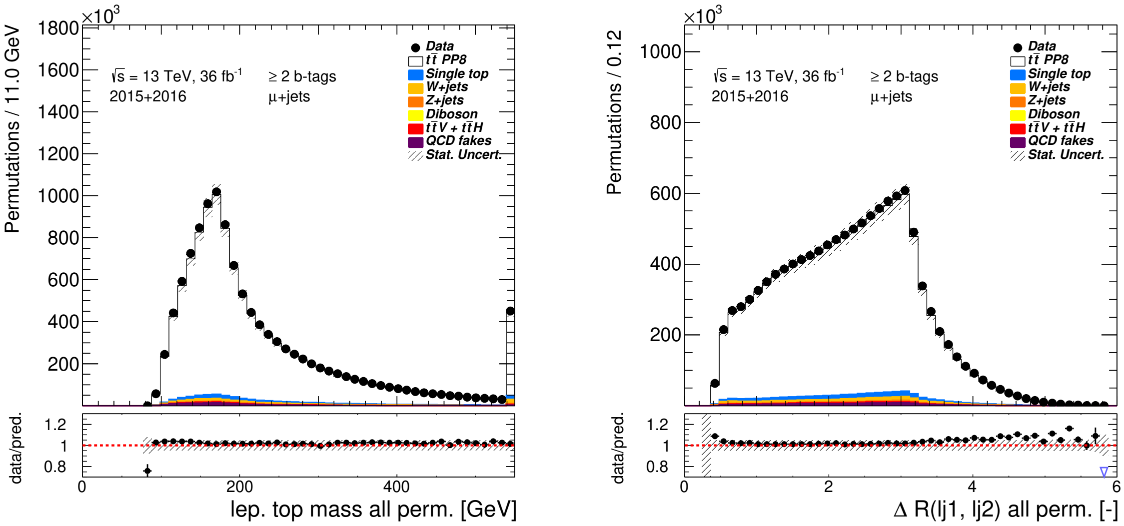

(c) Reconstructed leptonic top-quark mass.

(d) ΔR between the two light-flavour jets.

Figure C.4.: Control plots displaying the data/prediction comparison for the input variables of the reconstruction BDT in the muon+jets decay channel. Histograms are filled multiple times per event, once for each considered permutations of reconstructed jets to the corresponding partons. Only data recorded in 2015 and 2016 are compared with their corresponding prediction. The hashed bands show the uncertainty originating from finite number of events in the MC samples as well as normalisation uncertainty on each signal/background source. The first and last bin contain underflow and overflow events, respectively.

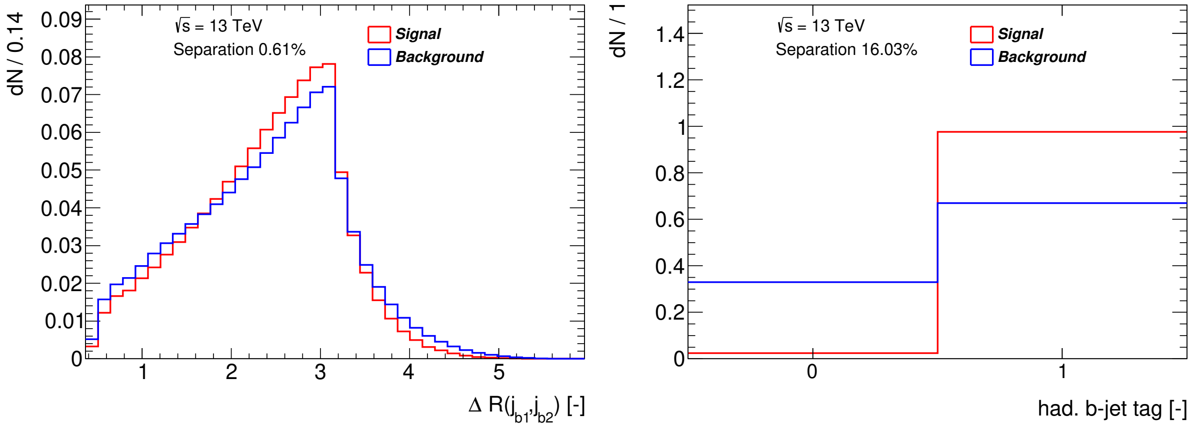

(a) ΔR between the two b-jets.

(b) b-tag of the assumed b-jet from the hadronic top quark decay.

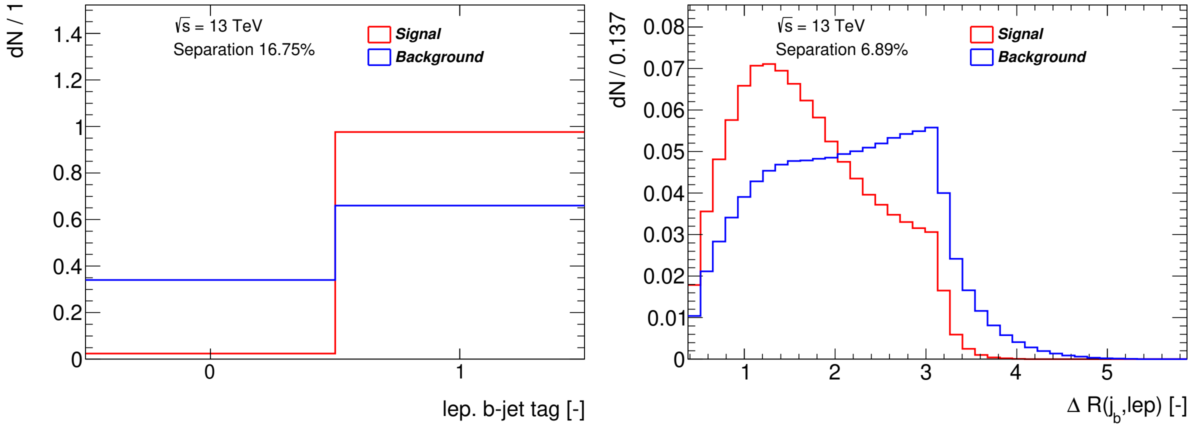

(c) b-tag of the assumed b-jet from the semileptonic top quark decay.

(d) ΔR between the b-jet and the muon.

Figure C.5.: Separation power of the input variables for the reconstruction BDT. Signal (red) represents permutations where all four partons from the $t\bar{t}$ decay are correctly assigned to their corresponding jets, while background (blue) denotes permutations where at least on of the partons is not assigned correctly. Signal and background contributions are normalised to unity. Electron+jets and muon+jets events are combined.

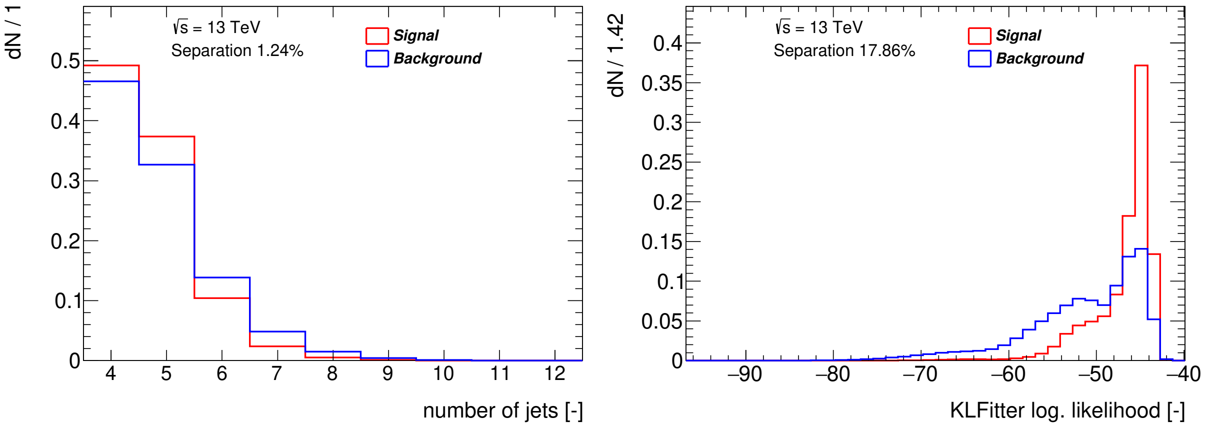

(a) Number of jets.

(b) KLFitter logarithm of the likelihood.

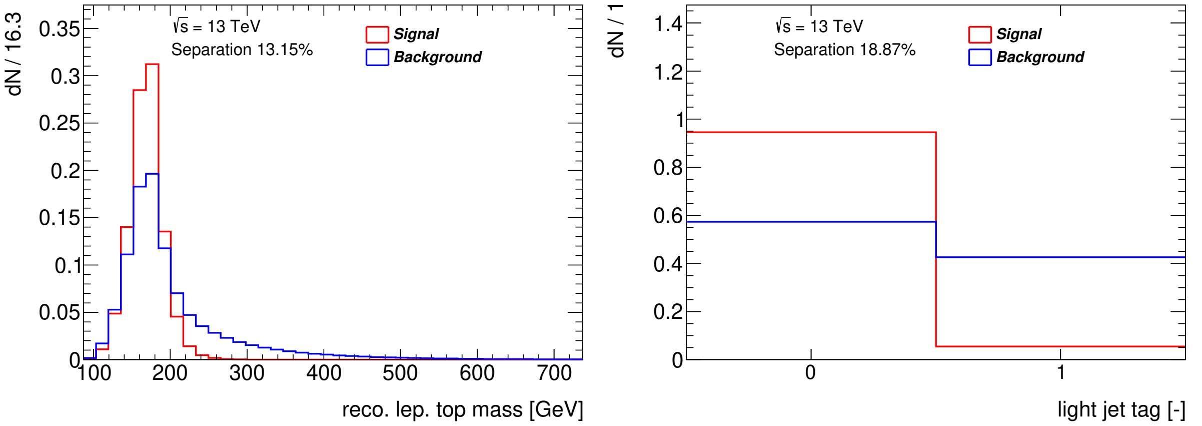

(c) Reconstructed leptonic top-quark mass.

(d) b-tag of the assumed light-jet from the W boson decay.

Figure C.6.: Separation power of the input variables for the reconstruction BDT. Signal (red) represents permutations where all four partons from the $t\bar{t}$ decay are correctly assigned to their corresponding jets, while background (blue) denotes permutations where at least on of the partons is not assigned correctly. Signal and background contributions are normalised to unity. Electron+jets and muon+jets events are combined.

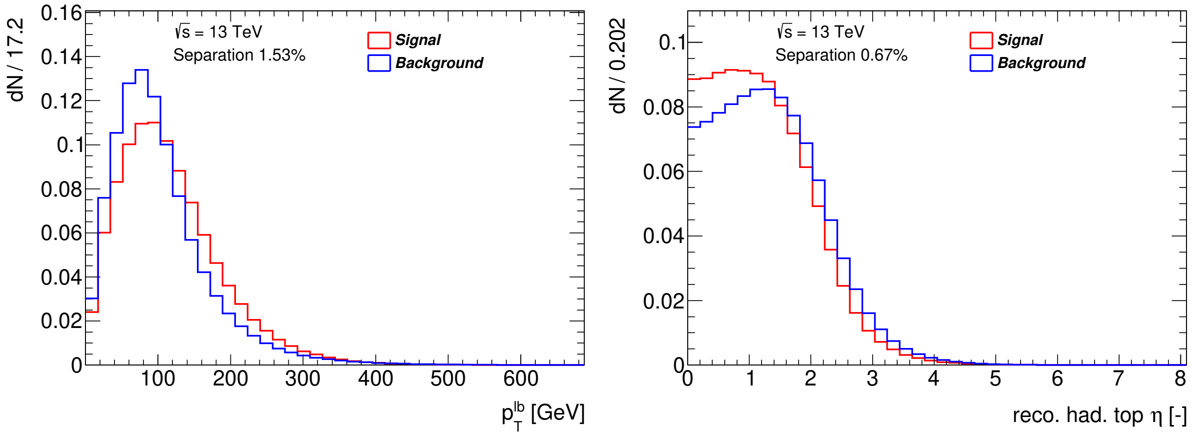

(a) p_{T} of the muon and the b-jet system.

(b) Reconstructed hadronic top-quark η.

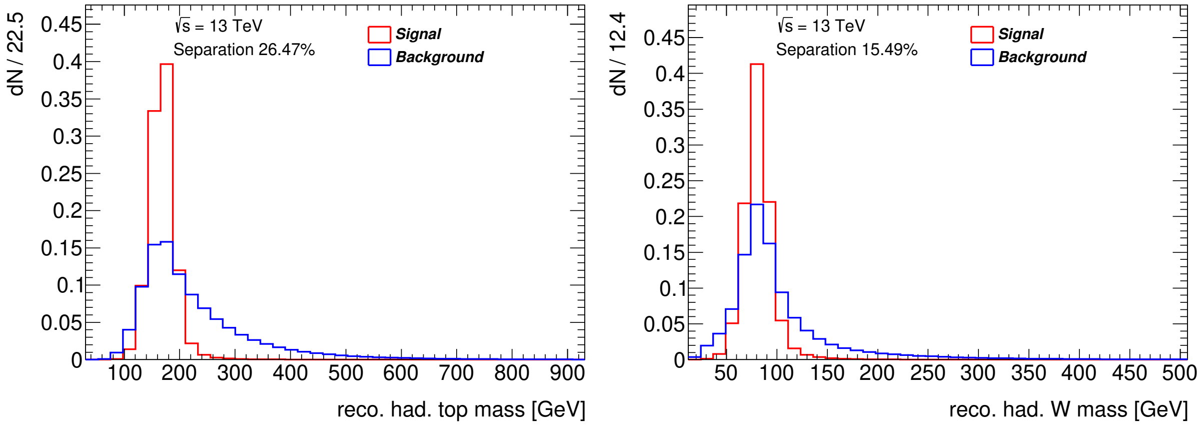

(c) Reconstructed hadronic top-quark mass.

(d) Reconstructed hadronic W boson mass.

Figure C.7.: Separation power of the input variables for the reconstruction BDT. Signal (red) represents permutations where all four partons from the $t\bar{t}$ decay are correctly assigned to their corresponding jets, while background (blue) denotes permutations where at least on of the partons is not assigned correctly. Signal and background contributions are normalised to unity. Electron+jets and muon+jets events are combined.

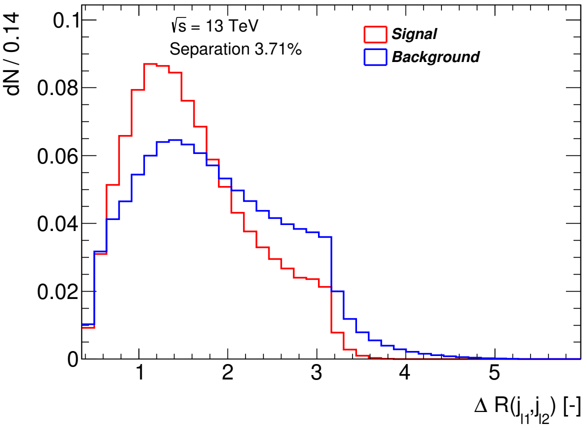

(a) ΔR between the two light-flavour jets.

Figure C.8.: Separation power of the input variables for the reconstruction BDT. Signal (red) represents permutations where all four partons from the $t\bar{t}$ decay are correctly assigned to their corresponding jets, while background (blue) denotes permutations where at least on of the partons is not assigned correctly. Signal and background contributions are normalised to unity. Electron+jets and muon+jets events are combined.

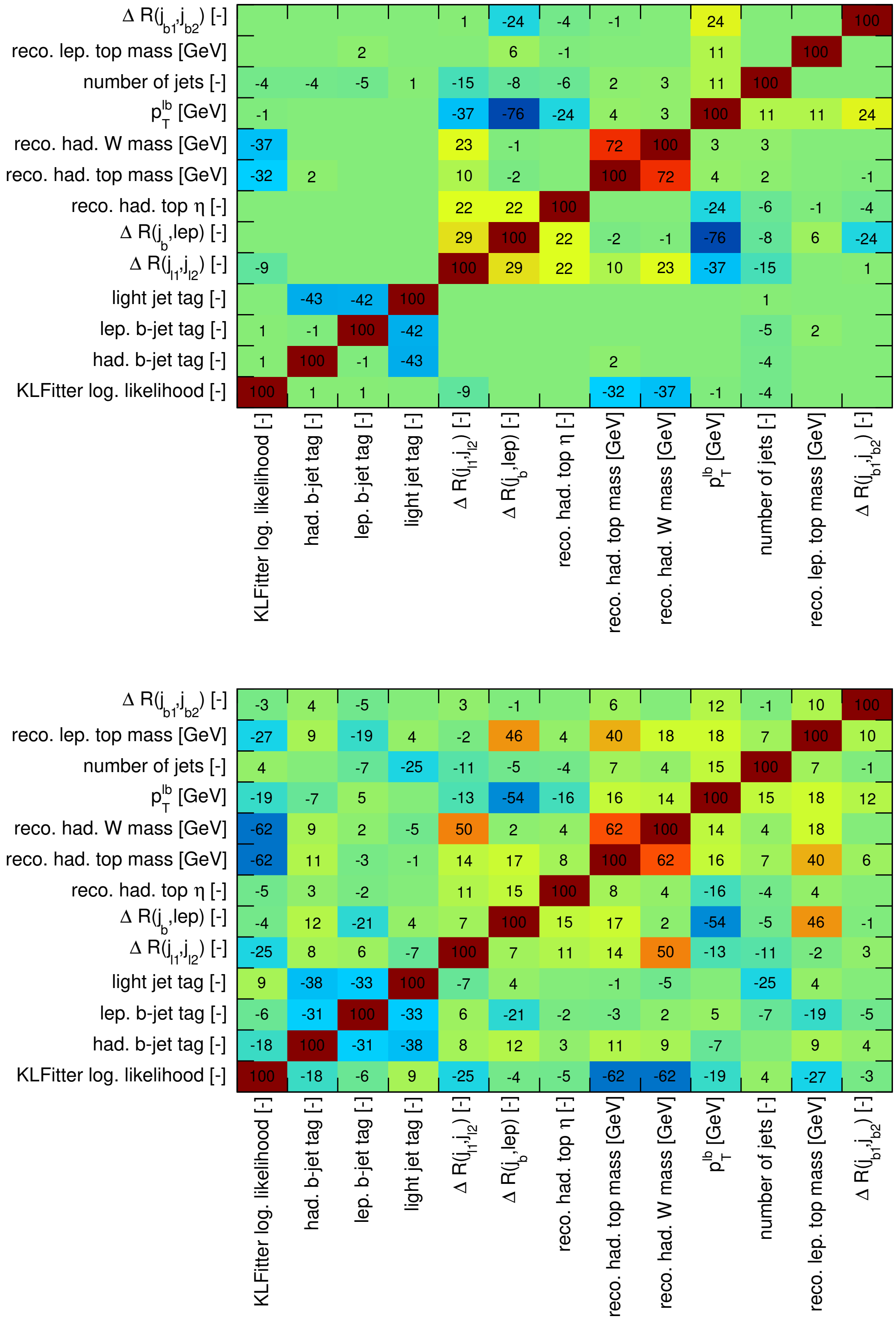

	KLFitter log. likelihood [-]	had. b-jet tag [-]	lep. b-jet tag [-]	light jet tag [-]	$\Delta R(j_{l1},j_{l2})$ [-]	$\Delta R(j_b,\mathrm{lep})$ [-]	reco. had. top η [-]	reco. had. top mass [GeV]	reco. had. W mass [GeV]	p_T^{lb} [GeV]	number of jets [-]	reco. lep. top mass [GeV]	$\Delta R(j_{b1},j_{b2})$ [-]
$\Delta R(j_{b1},j_{b2})$ [-]					1	-24	-4	-1		24			100
reco. lep. top mass [GeV]			2			6	-1			11		100	
number of jets [-]	-4	-4	-5	1	-15	-8	-6	2	3	11	100		
p_T^{lb} [GeV]	-1				-37	-76	-24	4	3	100	11	11	24
reco. had. W mass [GeV]	-37				23	-1		72	100	3	3		
reco. had. top mass [GeV]	-32	2			10	-2		100	72	4	2		-1
reco. had. top η [-]					22	22	100			-24	-6	-1	-4
$\Delta R(j_b,\mathrm{lep})$ [-]					29	100	22	-2	-1	-76	-8	6	-24
$\Delta R(j_{l1},j_{l2})$ [-]	-9				100	29	22	10	23	-37	-15		1
light jet tag [-]		-43	-42	100							1		
lep. b-jet tag [-]	1	-1	100	-42							-5	2	
had. b-jet tag [-]	1	100	-1	-43				2			-4		
KLFitter log. likelihood [-]	100	1	1		-9			-32	-37	-1	-4		

	KLFitter log. likelihood [-]	had. b-jet tag [-]	lep. b-jet tag [-]	light jet tag [-]	$\Delta R(j_{l1},j_{l2})$ [-]	$\Delta R(j_b,\mathrm{lep})$ [-]	reco. had. top η [-]	reco. had. top mass [GeV]	reco. had. W mass [GeV]	p_T^{lb} [GeV]	number of jets [-]	reco. lep. top mass [GeV]	$\Delta R(j_{b1},j_{b2})$ [-]
$\Delta R(j_{b1},j_{b2})$ [-]	-3	4	-5		3	-1		6		12	-1	10	100
reco. lep. top mass [GeV]	-27	9	-19	4	-2	46	4	40	18	18	7	100	10
number of jets [-]	4		-7	-25	-11	-5	-4	7	4	15	100	7	-1
p_T^{lb} [GeV]	-19	-7	5		-13	-54	-16	16	14	100	15	18	12
reco. had. W mass [GeV]	-62	9	2	-5	50	2	4	62	100	14	4	18	
reco. had. top mass [GeV]	-62	11	-3	-1	14	17	8	100	62	16	7	40	6
reco. had. top η [-]	-5	3	-2		11	15	100	8	4	-16	-4	4	
$\Delta R(j_b,\mathrm{lep})$ [-]	-4	12	-21	4	7	100	15	17	2	-54	-5	46	-1
$\Delta R(j_{l1},j_{l2})$ [-]	-25	8	6	-7	100	7	11	14	50	-13	-11	-2	3
light jet tag [-]	9	-38	-33	100	-7	4		-1	-5		-25	4	
lep. b-jet tag [-]	-6	-31	100	-33	6	-21	-2	-3	2	5	-7	-19	-5
had. b-jet tag [-]	-18	100	-31	-38	8	12	3	11	9	-7		9	4
KLFitter log. likelihood [-]	100	-18	-6	9	-25	-4	-5	-62	-62	-19	4	-27	-3

Figure C.9.: Correlation of the BDT input variables for the signal permutations (top) and combinatorial background (bottom). Values in each bin represent the correlation between variables in percentages. Electron+jets and muon+jets events are plotted together.

APPENDIX D

Decomposition of systematic uncertainties for the 8 TeV analysis

This appendix summarises the effects of individual sources of the considered systematic uncertainties on the measurement of the top-quark decay width at $\sqrt{s} = 8$ TeV. The presented values correspond to the final setup used in the fit to the data using $m_{\ell b}$ and $\Delta R_{\mathrm{min}}(j_b, j_l)$ observables in the eight orthogonal channels as described in Section 10.2.3. The systematic uncertainties are displayed in Table D.1.

Source	**Uncertainty [GeV]**	
Detector model		
Electron	+ 0.14	− 0.07
Muon	+ 0.11	− 0.06
Jet energy scale	+ 0.42	− 0.30
Jet energy resolution	+ 0.27	− 0.27
Jet vertex fraction	+ 0.13	− 0.03
Jet reconstruction efficiency	+ 0.03	− 0.03
$E_{\mathrm{T}}^{\mathrm{miss}}$	+ 0.01	− 0.01
Flavour-tagging	+ 0.32	− 0.24
Signal model		
ME generator	+ 0.41	− 0.41
Colour reconnection	+ 0.19	− 0.19
Underlying event	+ 0.11	− 0.11
Radiation	+ 0.07	− 0.07
PDF	+ 0.06	− 0.06
PS/fragmentation	+ 0.05	− 0.05
Background model		
Multijet	+ 0.04	− 0.00
W+jets	+ 0.02	− 0.02
Single top	$<$ 0.01	$<$ 0.01
Template statistical uncertainty	+ 0.07	− 0.07
Luminosity	+ 0.03	− 0.00
Total systematic uncertainty	+ 0.79	− 0.68

Table D.1.: Summary of all systematic uncertainties for the individual sources of uncertainties in the measurement of the top-quark decay width. The total systematic uncertainty is shown in the last row.

APPENDIX E

Correlation of observables in lepton+jets channel

This appendix shows correlations between the distributions considered in the fit in the lepton+jets channel at 13 TeV. Figures E.1 and E.2 show the correlations between $m_{\ell b}$ and $R_{3/2}$, and $m_{\ell b}$ and m_W, respectively.

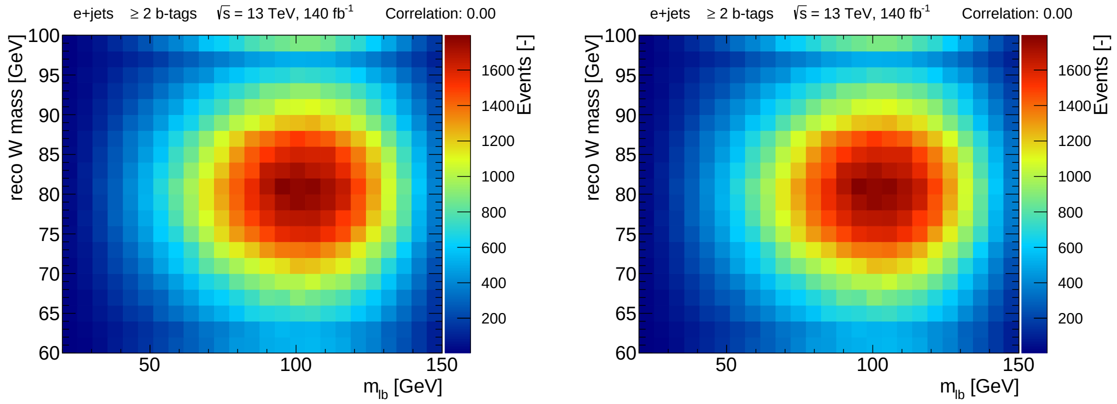

Figure E.1.: Correlation between the variables tested for the top-quark decay width measurement in the electron+jets (left) and muon+jets (right) channel for the reconstructed mass of the W boson and $m_{\ell b}$. The additional requirement on the BDT score > 0.7 is applied. The measured correlation allows to treat the observables as uncorrelated.

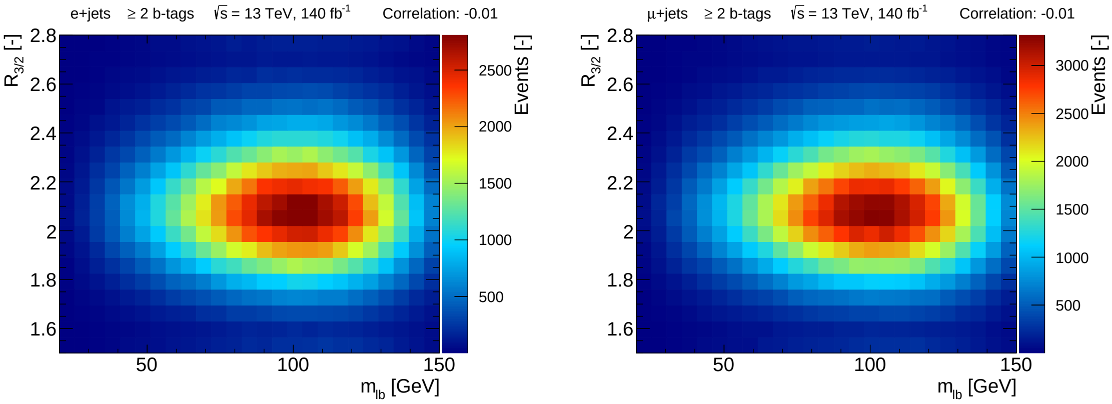

Figure E.2.: Correlation between the variables tested for the top-quark decay width measurement in the electron+jets (left) and muon+jets (right) channel for the reconstructed mass of the $R_{3/2}$ boson and $m_{\ell b}$. The additional requirement on the BDT score > 0.7 is applied. The measured correlation allows to treat the observables as uncorrelated.

APPENDIX F

Results of pseudoexperiments

The result of the pseudo-experiments for various input decay widths are summarised in Figures F.1–F.2 and Figure F.3 for the lepton+jets channel and the dilepton channel, respectively.

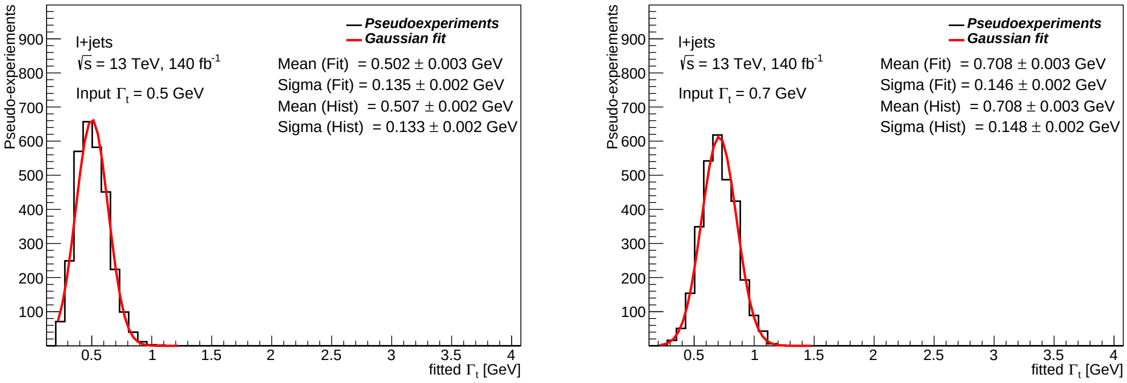

Figure F.1.: Fitted values for 3000 pseudo-experiments in the lepton+jets channel using statistical only fits. Various input widths for the pseudo-data are used: $\Gamma_t = 0.5, 0.7, 1.0, 1.5$ GeV. Good agreement between the input and the mean fitted value is observed. A deviation from Gaussian shape is observed for input width of 0.5 GeV due to the edge at 0.2 GeV.

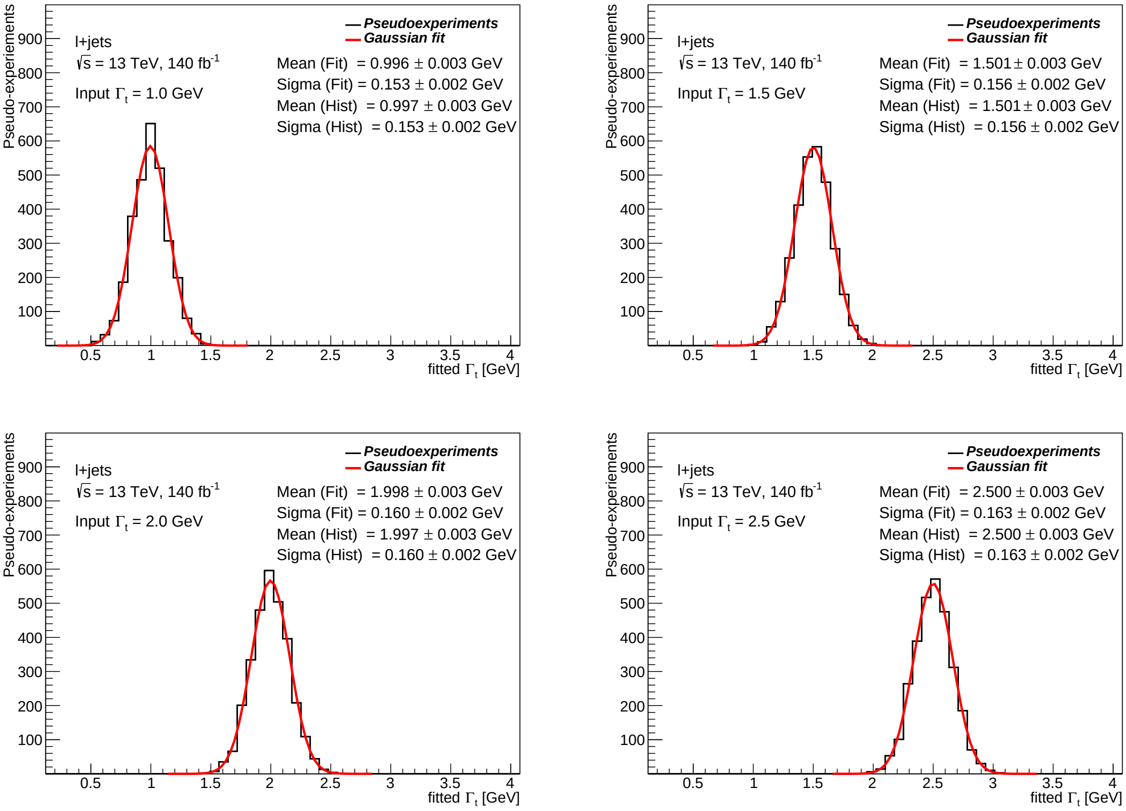

Figure F.2.: Fitted values for 3000 pseudo-experiments in the lepton+jets channel using statistical only fits. Various input widths for the pseudo-data are used: $\Gamma_t = 0.5, 0.7, 1.0, 1.5$ GeV. Good agreement between the input and the mean fitted value is observed.

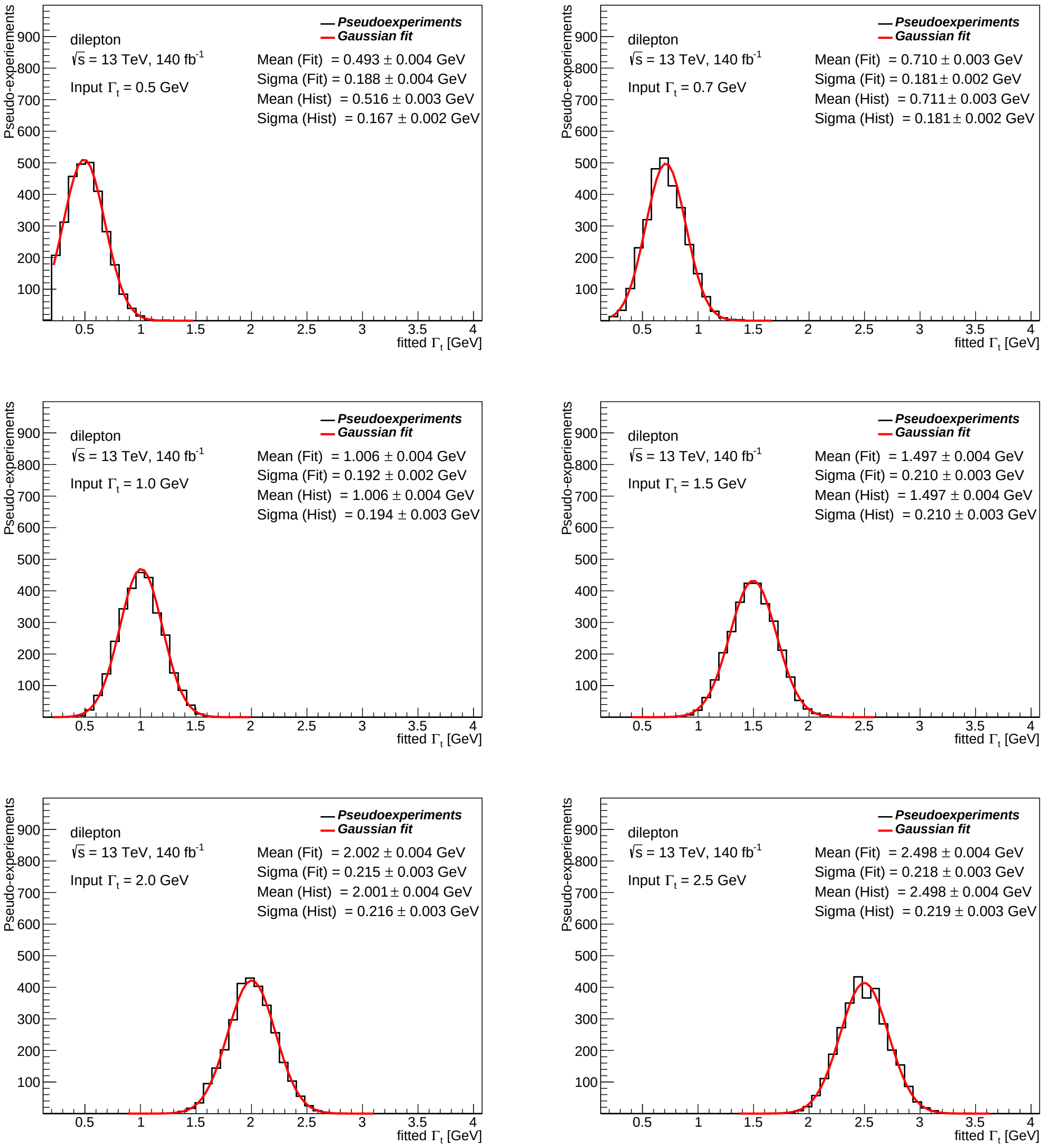

Figure F.3.: Fitted values for 3000 pseudo-experiments in the dilepton channel using statistical only fits. Various input widths for the pseudo-data are used: $\Gamma_t = 0.5, 0.7, 1.0, 1.5$ GeV. Good agreement between the input and the mean fitted value is observed. A deviation from Gaussian shape is observed for input width of 0.5 GeV due to the edge at 0.2 GeV.

APPENDIX G

Nuisance parameters correlation matrices

This appendix shows correlation matrices of the nuisance parameters for the systematic sources considered in the profile likelihood template fit. Correlations are obtained from a minimisation technique described in Section 10.3.2. Correlations of the NPs from Asimov fits are shown in Figure G.1 for the lepton+jets channel and in Figure G.2 for the dilepton channel. Correlations of the NPs from fit to the observed data are shown in Figure G.3 for the lepton+jets channel and in Figure G.4 for the dilepton channel. Finally, the correlations of the NP from the fit to data in the combined lepton+jets and the dilepton channel are presented in FIgure G.5.

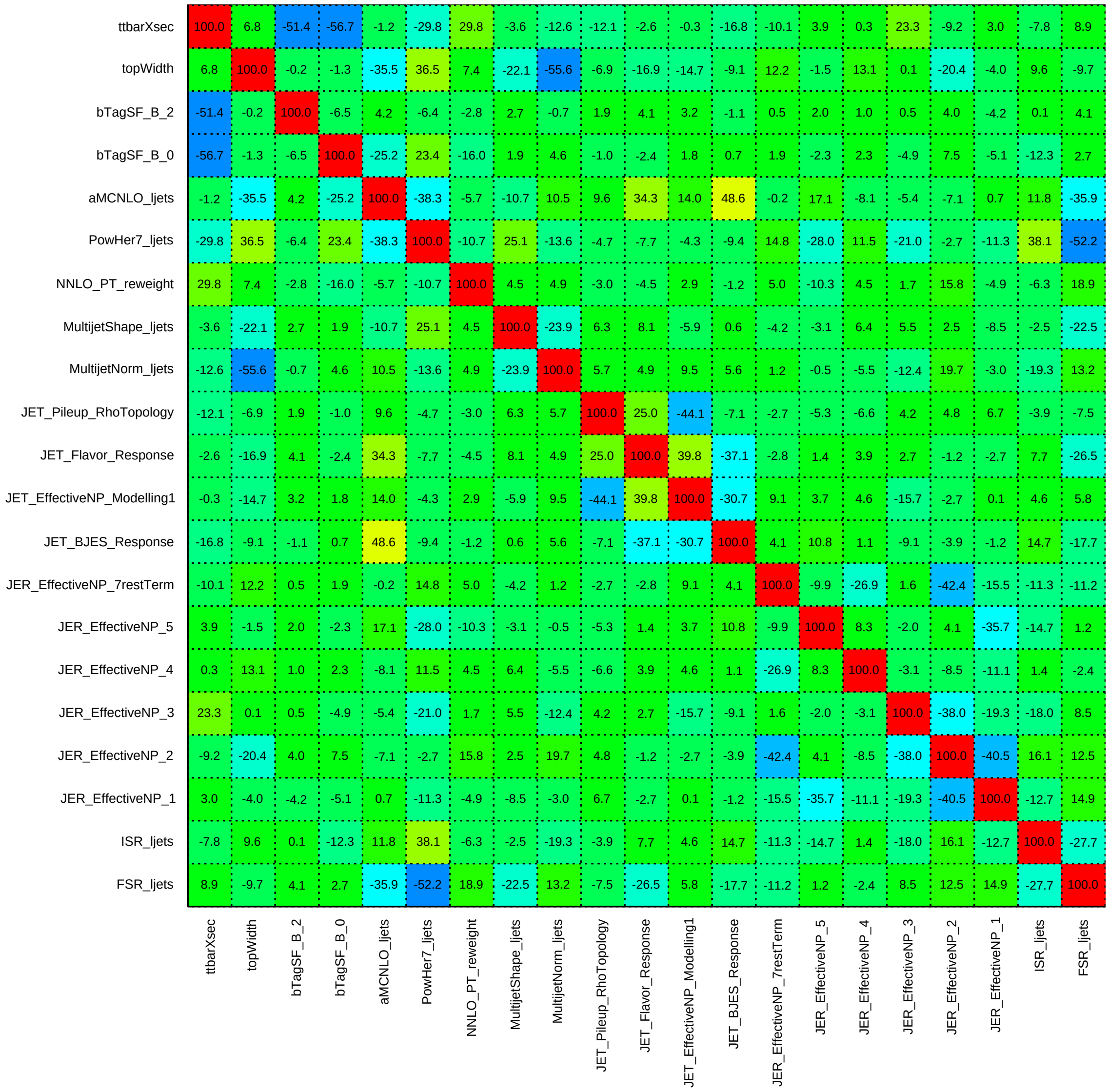

	ttbarXsec	topWidth	bTagSF_B_2	bTagSF_B_0	aMCNLO_ljets	PowHer7_ljets	NNLO_PT_reweight	MultijetShape_ljets	MultijetNorm_ljets	JET_Pileup_RhoTopology	JET_Flavor_Response	JET_EffectiveNP_Modelling1	JET_BJES_Response	JER_EffectiveNP_7restTerm	JER_EffectiveNP_5	JER_EffectiveNP_4	JER_EffectiveNP_3	JER_EffectiveNP_2	JER_EffectiveNP_1	ISR_ljets	FSR_ljets
ttbarXsec	100.0	6.8	-51.4	-56.7	-1.2	-29.8	29.8	-3.6	-12.6	-12.1	-2.6	-0.3	-16.8	-10.1	3.9	0.3	23.3	-9.2	3.0	-7.8	8.9
topWidth	6.8	100.0	-0.2	-1.3	-35.5	36.5	7.4	-22.1	-55.6	-6.9	-16.9	-14.7	-9.1	12.2	-1.5	13.1	0.1	-20.4	-4.0	9.6	-9.7
bTagSF_B_2	-51.4	-0.2	100.0	-6.5	4.2	-6.4	-2.8	2.7	-0.7	1.9	4.1	3.2	-1.1	0.5	2.0	1.0	0.5	4.0	-4.2	0.1	4.1
bTagSF_B_0	-56.7	-1.3	-6.5	100.0	-25.2	23.4	-16.0	1.9	4.6	-1.0	-2.4	1.8	0.7	1.9	-2.3	2.3	-4.9	7.5	-5.1	-12.3	2.7
aMCNLO_ljets	-1.2	-35.5	4.2	-25.2	100.0	-38.3	-5.7	-10.7	10.5	9.6	34.3	14.0	48.6	-0.2	17.1	-8.1	-5.4	-7.1	0.7	11.8	-35.9
PowHer7_ljets	-29.8	36.5	-6.4	23.4	-38.3	100.0	-10.7	25.1	-13.6	-4.7	-7.7	-4.3	-9.4	14.8	-28.0	11.5	-21.0	-2.7	-11.3	38.1	-52.2
NNLO_PT_reweight	29.8	7.4	-2.8	-16.0	-5.7	-10.7	100.0	4.5	4.9	-3.0	-4.5	2.9	-1.2	5.0	-10.3	4.5	1.7	15.8	-4.9	-6.3	18.9
MultijetShape_ljets	-3.6	-22.1	2.7	1.9	-10.7	25.1	4.5	100.0	-23.9	6.3	8.1	-5.9	0.6	-4.2	-3.1	6.4	5.5	2.5	-8.5	-2.5	-22.5
MultijetNorm_ljets	-12.6	-55.6	-0.7	4.6	10.5	-13.6	4.9	-23.9	100.0	5.7	4.9	9.5	5.6	1.2	-0.5	-5.5	-12.4	19.7	-3.0	-19.3	13.2
JET_Pileup_RhoTopology	-12.1	-6.9	1.9	-1.0	9.6	-4.7	-3.0	6.3	5.7	100.0	25.0	-44.1	-7.1	-2.7	-5.3	-6.6	4.2	4.8	6.7	-3.9	-7.5
JET_Flavor_Response	-2.6	-16.9	4.1	-2.4	34.3	-7.7	-4.5	8.1	4.9	25.0	100.0	39.8	-37.1	-2.8	1.4	3.9	2.7	-1.2	-2.7	7.7	-26.5
JET_EffectiveNP_Modelling1	-0.3	-14.7	3.2	1.8	14.0	-4.3	2.9	-5.9	9.5	-44.1	39.8	100.0	-30.7	9.1	3.7	4.6	-15.7	-2.7	0.1	4.6	5.8
JET_BJES_Response	-16.8	-9.1	-1.1	0.7	48.6	-9.4	-1.2	0.6	5.6	-7.1	-37.1	-30.7	100.0	4.1	10.8	1.1	-9.1	-3.9	-1.2	14.7	-17.7
JER_EffectiveNP_7restTerm	-10.1	12.2	0.5	1.9	-0.2	14.8	5.0	-4.2	1.2	-2.7	-2.8	9.1	4.1	100.0	-9.9	-26.9	1.6	-42.4	-15.5	-11.3	-11.2
JER_EffectiveNP_5	3.9	-1.5	2.0	-2.3	17.1	-28.0	-10.3	-3.1	-0.5	-5.3	1.4	3.7	10.8	-9.9	100.0	8.3	-2.0	4.1	-35.7	-14.7	1.2
JER_EffectiveNP_4	0.3	13.1	1.0	2.3	-8.1	11.5	4.5	6.4	-5.5	-6.6	3.9	4.6	1.1	-26.9	8.3	100.0	-3.1	-8.5	-11.1	1.4	-2.4
JER_EffectiveNP_3	23.3	0.1	0.5	-4.9	-5.4	-21.0	1.7	5.5	-12.4	4.2	2.7	-15.7	-9.1	1.6	-2.0	-3.1	100.0	-38.0	-19.3	-18.0	8.5
JER_EffectiveNP_2	-9.2	-20.4	4.0	7.5	-7.1	-2.7	15.8	2.5	19.7	4.8	-1.2	-2.7	-3.9	-42.4	4.1	-8.5	-38.0	100.0	-40.5	16.1	12.5
JER_EffectiveNP_1	3.0	-4.0	-4.2	-5.1	0.7	-11.3	-4.9	-8.5	-3.0	6.7	-2.7	0.1	-1.2	-15.5	-35.7	-11.1	-19.3	-40.5	100.0	-12.7	14.9
ISR_ljets	-7.8	9.6	0.1	-12.3	11.8	38.1	-6.3	-2.5	-19.3	-3.9	7.7	4.6	14.7	-11.3	-14.7	1.4	-18.0	16.1	-12.7	100.0	-27.7
FSR_ljets	8.9	-9.7	4.1	2.7	-35.9	-52.2	18.9	-22.5	13.2	-7.5	-26.5	5.8	-17.7	-11.2	1.2	-2.4	8.5	12.5	14.9	-27.7	100.0

Figure G.1.: Correlations for the nuisance parameters considered in the Asimov fit in the lepton+jets channel. Only correlations larger than 25 % are displayed.

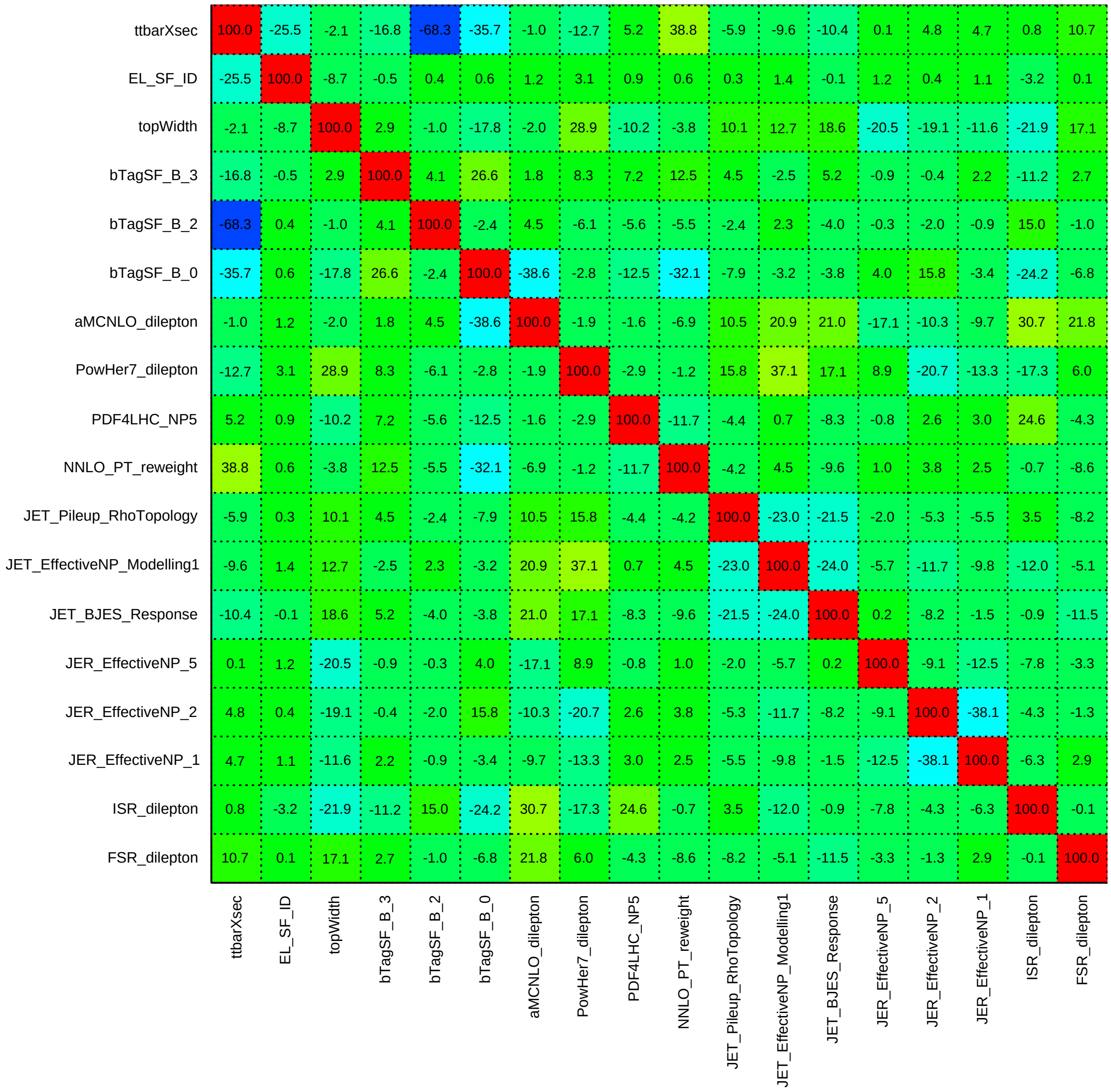

	ttbarXsec	EL_SF_ID	topWidth	bTagSF_B_3	bTagSF_B_2	bTagSF_B_0	aMCNLO_dilepton	PowHer7_dilepton	PDF4LHC_NP5	NNLO_PT_reweight	JET_Pileup_RhoTopology	JET_EffectiveNP_Modelling1	JET_BJES_Response	JER_EffectiveNP_5	JER_EffectiveNP_2	JER_EffectiveNP_1	ISR_dilepton	FSR_dilepton
ttbarXsec	100.0	-25.5	-2.1	-16.8	-68.3	-35.7	-1.0	-12.7	5.2	38.8	-5.9	-9.6	-10.4	0.1	4.8	4.7	0.8	10.7
EL_SF_ID	-25.5	100.0	-8.7	-0.5	0.4	0.6	1.2	3.1	0.9	0.6	0.3	1.4	-0.1	1.2	0.4	1.1	-3.2	0.1
topWidth	-2.1	-8.7	100.0	2.9	-1.0	-17.8	-2.0	28.9	-10.2	-3.8	10.1	12.7	18.6	-20.5	-19.1	-11.6	-21.9	17.1
bTagSF_B_3	-16.8	-0.5	2.9	100.0	4.1	26.6	1.8	8.3	7.2	12.5	4.5	-2.5	5.2	-0.9	-0.4	2.2	-11.2	2.7
bTagSF_B_2	-68.3	0.4	-1.0	4.1	100.0	-2.4	4.5	-6.1	-5.6	-5.5	-2.4	2.3	-4.0	-0.3	-2.0	-0.9	15.0	-1.0
bTagSF_B_0	-35.7	0.6	-17.8	26.6	-2.4	100.0	-38.6	-2.8	-12.5	-32.1	-7.9	-3.2	-3.8	4.0	15.8	-3.4	-24.2	-6.8
aMCNLO_dilepton	-1.0	1.2	-2.0	1.8	4.5	-38.6	100.0	-1.9	-1.6	-6.9	10.5	20.9	21.0	-17.1	-10.3	-9.7	30.7	21.8
PowHer7_dilepton	-12.7	3.1	28.9	8.3	-6.1	-2.8	-1.9	100.0	-2.9	-1.2	15.8	37.1	17.1	8.9	-20.7	-13.3	-17.3	6.0
PDF4LHC_NP5	5.2	0.9	-10.2	7.2	-5.6	-12.5	-1.6	-2.9	100.0	-11.7	-4.4	0.7	-8.3	-0.8	2.6	3.0	24.6	-4.3
NNLO_PT_reweight	38.8	0.6	-3.8	12.5	-5.5	-32.1	-6.9	-1.2	-11.7	100.0	-4.2	4.5	-9.6	1.0	3.8	2.5	-0.7	-8.6
JET_Pileup_RhoTopology	-5.9	0.3	10.1	4.5	-2.4	-7.9	10.5	15.8	-4.4	-4.2	100.0	-23.0	-21.5	-2.0	-5.3	-5.5	3.5	-8.2
JET_EffectiveNP_Modelling1	-9.6	1.4	12.7	-2.5	2.3	-3.2	20.9	37.1	0.7	4.5	-23.0	100.0	-24.0	-5.7	-11.7	-9.8	-12.0	-5.1
JET_BJES_Response	-10.4	-0.1	18.6	5.2	-4.0	-3.8	21.0	17.1	-8.3	-9.6	-21.5	-24.0	100.0	0.2	-8.2	-1.5	-0.9	-11.5
JER_EffectiveNP_5	0.1	1.2	-20.5	-0.9	-0.3	4.0	-17.1	8.9	-0.8	1.0	-2.0	-5.7	0.2	100.0	-9.1	-12.5	-7.8	-3.3
JER_EffectiveNP_2	4.8	0.4	-19.1	-0.4	-2.0	15.8	-10.3	-20.7	2.6	3.8	-5.3	-11.7	-8.2	-9.1	100.0	-38.1	-4.3	-1.3
JER_EffectiveNP_1	4.7	1.1	-11.6	2.2	-0.9	-3.4	-9.7	-13.3	3.0	2.5	-5.5	-9.8	-1.5	-12.5	-38.1	100.0	-6.3	2.9
ISR_dilepton	0.8	-3.2	-21.9	-11.2	15.0	-24.2	30.7	-17.3	24.6	-0.7	3.5	-12.0	-0.9	-7.8	-4.3	-6.3	100.0	-0.1
FSR_dilepton	10.7	0.1	17.1	2.7	-1.0	-6.8	21.8	6.0	-4.3	-8.6	-8.2	-5.1	-11.5	-3.3	-1.3	2.9	-0.1	100.0

Figure G.2.: Correlations for the nuisance parameters considered in the Asimov fit in the dilepton channel. Only correlations larger than 20 % are displayed.

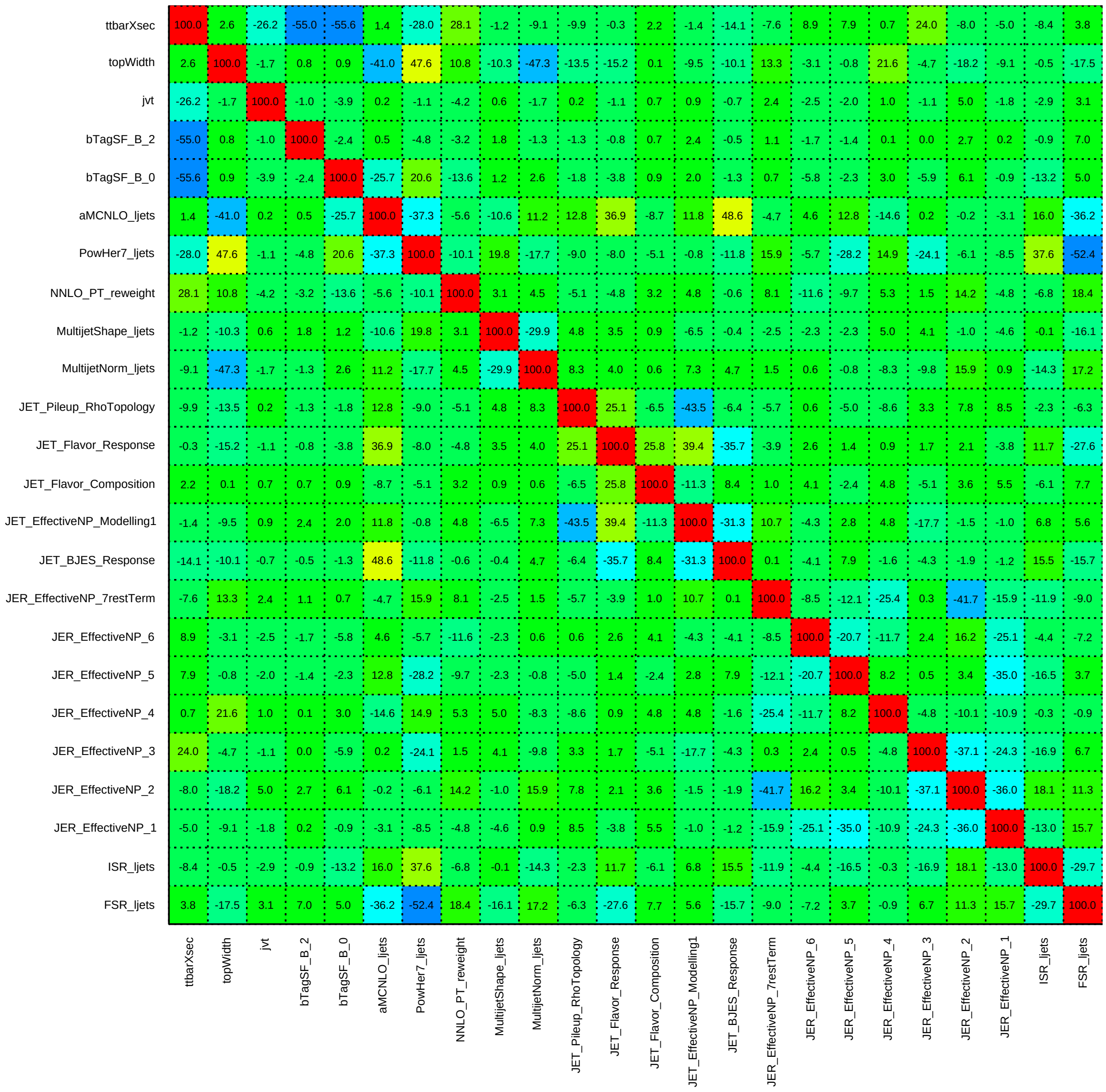

	ttbarXsec	topWidth	jvt	bTagSF_B_2	bTagSF_B_0	aMCNLO_ljets	PowHer7_ljets	NNLO_PT_reweight	MultijetShape_ljets	MultijetNorm_ljets	JET_Pileup_RhoTopology	JET_Flavor_Response	JET_Flavor_Composition	JET_EffectiveNP_Modelling1	JET_BJES_Response	JER_EffectiveNP_7restTerm	JER_EffectiveNP_6	JER_EffectiveNP_5	JER_EffectiveNP_4	JER_EffectiveNP_3	JER_EffectiveNP_2	JER_EffectiveNP_1	ISR_ljets	FSR_ljets
ttbarXsec	100.0	2.6	-26.2	-55.0	-55.6	1.4	-28.0	28.1	-1.2	-9.1	-9.9	-0.3	2.2	-1.4	-14.1	-7.6	8.9	7.9	0.7	24.0	-8.0	-5.0	-8.4	3.8
topWidth	2.6	100.0	-1.7	0.8	0.9	-41.0	47.6	10.8	-10.3	-47.3	-13.5	-15.2	0.1	-9.5	-10.1	13.3	-3.1	-0.8	21.6	-4.7	-18.2	-9.1	-0.5	-17.5
jvt	-26.2	-1.7	100.0	-1.0	-3.9	0.2	-1.1	-4.2	0.6	-1.7	0.2	-1.1	0.7	0.9	-0.7	2.4	-2.5	-2.0	1.0	-1.1	5.0	-1.8	-2.9	3.1
bTagSF_B_2	-55.0	0.8	-1.0	100.0	-2.4	0.5	-4.8	-3.2	1.8	-1.3	-1.3	-0.8	0.7	2.4	-0.5	1.1	-1.7	-1.4	0.1	0.0	2.7	0.2	-0.9	7.0
bTagSF_B_0	-55.6	0.9	-3.9	-2.4	100.0	-25.7	20.6	-13.6	1.2	2.6	-1.8	-3.8	0.9	2.0	-1.3	0.7	-5.8	-2.3	3.0	-5.9	6.1	-0.9	-13.2	5.0
aMCNLO_ljets	1.4	-41.0	0.2	0.5	-25.7	100.0	-37.3	-5.6	-10.6	11.2	12.8	36.9	-8.7	11.8	48.6	-4.7	4.6	12.8	-14.6	0.2	-0.2	-3.1	16.0	-36.2
PowHer7_ljets	-28.0	47.6	-1.1	-4.8	20.6	-37.3	100.0	-10.1	19.8	-17.7	-9.0	-8.0	-5.1	-0.8	-11.8	15.9	-5.7	-28.2	14.9	-24.1	-6.1	-8.5	37.6	-52.4
NNLO_PT_reweight	28.1	10.8	-4.2	-3.2	-13.6	-5.6	-10.1	100.0	3.1	4.5	-5.1	-4.8	3.2	4.8	-0.6	8.1	-11.6	-9.7	5.3	1.5	14.2	-4.8	-6.8	18.4
MultijetShape_ljets	-1.2	-10.3	0.6	1.8	1.2	-10.6	19.8	3.1	100.0	-29.9	4.8	3.5	0.9	-6.5	-0.4	-2.5	-2.3	-2.3	5.0	4.1	-1.0	-4.6	-0.1	-16.1
MultijetNorm_ljets	-9.1	-47.3	-1.7	-1.3	2.6	11.2	-17.7	4.5	-29.9	100.0	8.3	4.0	0.6	7.3	4.7	1.5	0.6	-0.8	-8.3	-9.8	15.9	0.9	-14.3	17.2
JET_Pileup_RhoTopology	-9.9	-13.5	0.2	-1.3	-1.8	12.8	-9.0	-5.1	4.8	8.3	100.0	25.1	-6.5	-43.5	-6.4	-5.7	0.6	-5.0	-8.6	3.3	7.8	8.5	-2.3	-6.3
JET_Flavor_Response	-0.3	-15.2	-1.1	-0.8	-3.8	36.9	-8.0	-4.8	3.5	4.0	25.1	100.0	25.8	39.4	-35.7	-3.9	2.6	1.4	0.9	1.7	2.1	-3.8	11.7	-27.6
JET_Flavor_Composition	2.2	0.1	0.7	0.7	0.9	-8.7	-5.1	3.2	0.9	0.6	-6.5	25.8	100.0	-11.3	8.4	1.0	4.1	-2.4	4.8	-5.1	3.6	5.5	-6.1	7.7
JET_EffectiveNP_Modelling1	-1.4	-9.5	0.9	2.4	2.0	11.8	-0.8	4.8	-6.5	7.3	-43.5	39.4	-11.3	100.0	-31.3	10.7	-4.3	2.8	4.8	-17.7	-1.5	-1.0	6.8	5.6
JET_BJES_Response	-14.1	-10.1	-0.7	-0.5	-1.3	48.6	-11.8	-0.6	-0.4	4.7	-6.4	-35.7	8.4	-31.3	100.0	0.1	-4.1	7.9	-1.6	-4.3	-1.9	-1.2	15.5	-15.7
JER_EffectiveNP_7restTerm	-7.6	13.3	2.4	1.1	0.7	-4.7	15.9	8.1	-2.5	1.5	-5.7	-3.9	1.0	10.7	0.1	100.0	-8.5	-12.1	-25.4	0.3	-41.7	-15.9	-11.9	-9.0
JER_EffectiveNP_6	8.9	-3.1	-2.5	-1.7	-5.8	4.6	-5.7	-11.6	-2.3	0.6	0.6	2.6	4.1	-4.3	-4.1	-8.5	100.0	-20.7	-11.7	2.4	16.2	-25.1	-4.4	-7.2
JER_EffectiveNP_5	7.9	-0.8	-2.0	-1.4	-2.3	12.8	-28.2	-9.7	-2.3	-0.8	-5.0	1.4	-2.4	2.8	7.9	-12.1	-20.7	100.0	8.2	0.5	3.4	-35.0	-16.5	3.7
JER_EffectiveNP_4	0.7	21.6	1.0	0.1	3.0	-14.6	14.9	5.3	5.0	-8.3	-8.6	0.9	4.8	4.8	-1.6	-25.4	-11.7	8.2	100.0	-4.8	-10.1	-10.9	-0.3	-0.9
JER_EffectiveNP_3	24.0	-4.7	-1.1	0.0	-5.9	0.2	-24.1	1.5	4.1	-9.8	3.3	1.7	-5.1	-17.7	-4.3	0.3	2.4	0.5	-4.8	100.0	-37.1	-24.3	-16.9	6.7
JER_EffectiveNP_2	-8.0	-18.2	5.0	2.7	6.1	-0.2	-6.1	14.2	-1.0	15.9	7.8	2.1	3.6	-1.5	-1.9	-41.7	16.2	3.4	-10.1	-37.1	100.0	-36.0	18.1	11.3
JER_EffectiveNP_1	-5.0	-9.1	-1.8	0.2	-0.9	-3.1	-8.5	-4.8	-4.6	0.9	8.5	-3.8	5.5	-1.0	-1.2	-15.9	-25.1	-35.0	-10.9	-24.3	-36.0	100.0	-13.0	15.7
ISR_ljets	-8.4	-0.5	-2.9	-0.9	-13.2	16.0	37.6	-6.8	-0.1	-14.3	-2.3	11.7	-6.1	6.8	15.5	-11.9	-4.4	-16.5	-0.3	-16.9	18.1	-13.0	100.0	-29.7
FSR_ljets	3.8	-17.5	3.1	7.0	5.0	-36.2	-52.4	18.4	-16.1	17.2	-6.3	-27.6	7.7	5.6	-15.7	-9.0	-7.2	3.7	-0.9	6.7	11.3	15.7	-29.7	100.0

Figure G.3.: Correlations for the nuisance parameters considered in the fit to the observed data in the lepton+jets channel. Only correlations larger than 25 % are displayed.

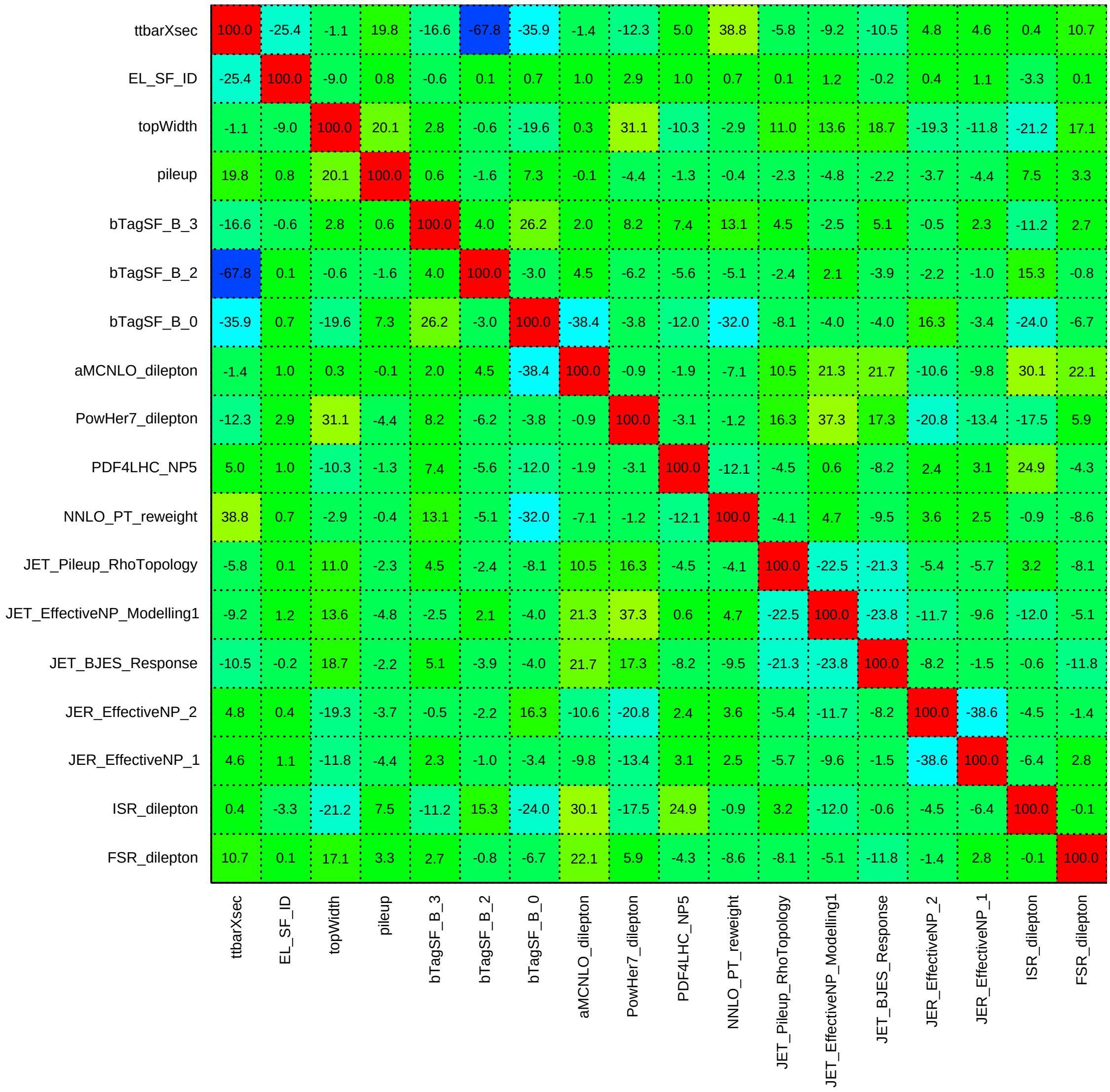

	ttbarXsec	EL_SF_ID	topWidth	pileup	bTagSF_B_3	bTagSF_B_2	bTagSF_B_0	aMCNLO_dilepton	PowHer7_dilepton	PDF4LHC_NP5	NNLO_PT_reweight	JET_Pileup_RhoTopology	JET_EffectiveNP_Modelling1	JET_BJES_Response	JER_EffectiveNP_2	JER_EffectiveNP_1	ISR_dilepton	FSR_dilepton
ttbarXsec	100.0	-25.4	-1.1	19.8	-16.6	-67.8	-35.9	-1.4	-12.3	5.0	38.8	-5.8	-9.2	-10.5	4.8	4.6	0.4	10.7
EL_SF_ID	-25.4	100.0	-9.0	0.8	-0.6	0.1	0.7	1.0	2.9	1.0	0.7	0.1	1.2	-0.2	0.4	1.1	-3.3	0.1
topWidth	-1.1	-9.0	100.0	20.1	2.8	-0.6	-19.6	0.3	31.1	-10.3	-2.9	11.0	13.6	18.7	-19.3	-11.8	-21.2	17.1
pileup	19.8	0.8	20.1	100.0	0.6	-1.6	7.3	-0.1	-4.4	-1.3	-0.4	-2.3	-4.8	-2.2	-3.7	-4.4	7.5	3.3
bTagSF_B_3	-16.6	-0.6	2.8	0.6	100.0	4.0	26.2	2.0	8.2	7.4	13.1	4.5	-2.5	5.1	-0.5	2.3	-11.2	2.7
bTagSF_B_2	-67.8	0.1	-0.6	-1.6	4.0	100.0	-3.0	4.5	-6.2	-5.6	-5.1	-2.4	2.1	-3.9	-2.2	-1.0	15.3	-0.8
bTagSF_B_0	-35.9	0.7	-19.6	7.3	26.2	-3.0	100.0	-38.4	-3.8	-12.0	-32.0	-8.1	-4.0	-4.0	16.3	-3.4	-24.0	-6.7
aMCNLO_dilepton	-1.4	1.0	0.3	-0.1	2.0	4.5	-38.4	100.0	-0.9	-1.9	-7.1	10.5	21.3	21.7	-10.6	-9.8	30.1	22.1
PowHer7_dilepton	-12.3	2.9	31.1	-4.4	8.2	-6.2	-3.8	-0.9	100.0	-3.1	-1.2	16.3	37.3	17.3	-20.8	-13.4	-17.5	5.9
PDF4LHC_NP5	5.0	1.0	-10.3	-1.3	7.4	-5.6	-12.0	-1.9	-3.1	100.0	-12.1	-4.5	0.6	-8.2	2.4	3.1	24.9	-4.3
NNLO_PT_reweight	38.8	0.7	-2.9	-0.4	13.1	-5.1	-32.0	-7.1	-1.2	-12.1	100.0	-4.1	4.7	-9.5	3.6	2.5	-0.9	-8.6
JET_Pileup_RhoTopology	-5.8	0.1	11.0	-2.3	4.5	-2.4	-8.1	10.5	16.3	-4.5	-4.1	100.0	-22.5	-21.3	-5.4	-5.7	3.2	-8.1
JET_EffectiveNP_Modelling1	-9.2	1.2	13.6	-4.8	-2.5	2.1	-4.0	21.3	37.3	0.6	4.7	-22.5	100.0	-23.8	-11.7	-9.6	-12.0	-5.1
JET_BJES_Response	-10.5	-0.2	18.7	-2.2	5.1	-3.9	-4.0	21.7	17.3	-8.2	-9.5	-21.3	-23.8	100.0	-8.2	-1.5	-0.6	-11.8
JER_EffectiveNP_2	4.8	0.4	-19.3	-3.7	-0.5	-2.2	16.3	-10.6	-20.8	2.4	3.6	-5.4	-11.7	-8.2	100.0	-38.6	-4.5	-1.4
JER_EffectiveNP_1	4.6	1.1	-11.8	-4.4	2.3	-1.0	-3.4	-9.8	-13.4	3.1	2.5	-5.7	-9.6	-1.5	-38.6	100.0	-6.4	2.8
ISR_dilepton	0.4	-3.3	-21.2	7.5	-11.2	15.3	-24.0	30.1	-17.5	24.9	-0.9	3.2	-12.0	-0.6	-4.5	-6.4	100.0	-0.1
FSR_dilepton	10.7	0.1	17.1	3.3	2.7	-0.8	-6.7	22.1	5.9	-4.3	-8.6	-8.1	-5.1	-11.8	-1.4	2.8	-0.1	100.0

Figure G.4.: Correlations for the nuisance parameters considered in the fit to the observed data in the dilepton channel. Only correlations larger than 20 % are displayed.

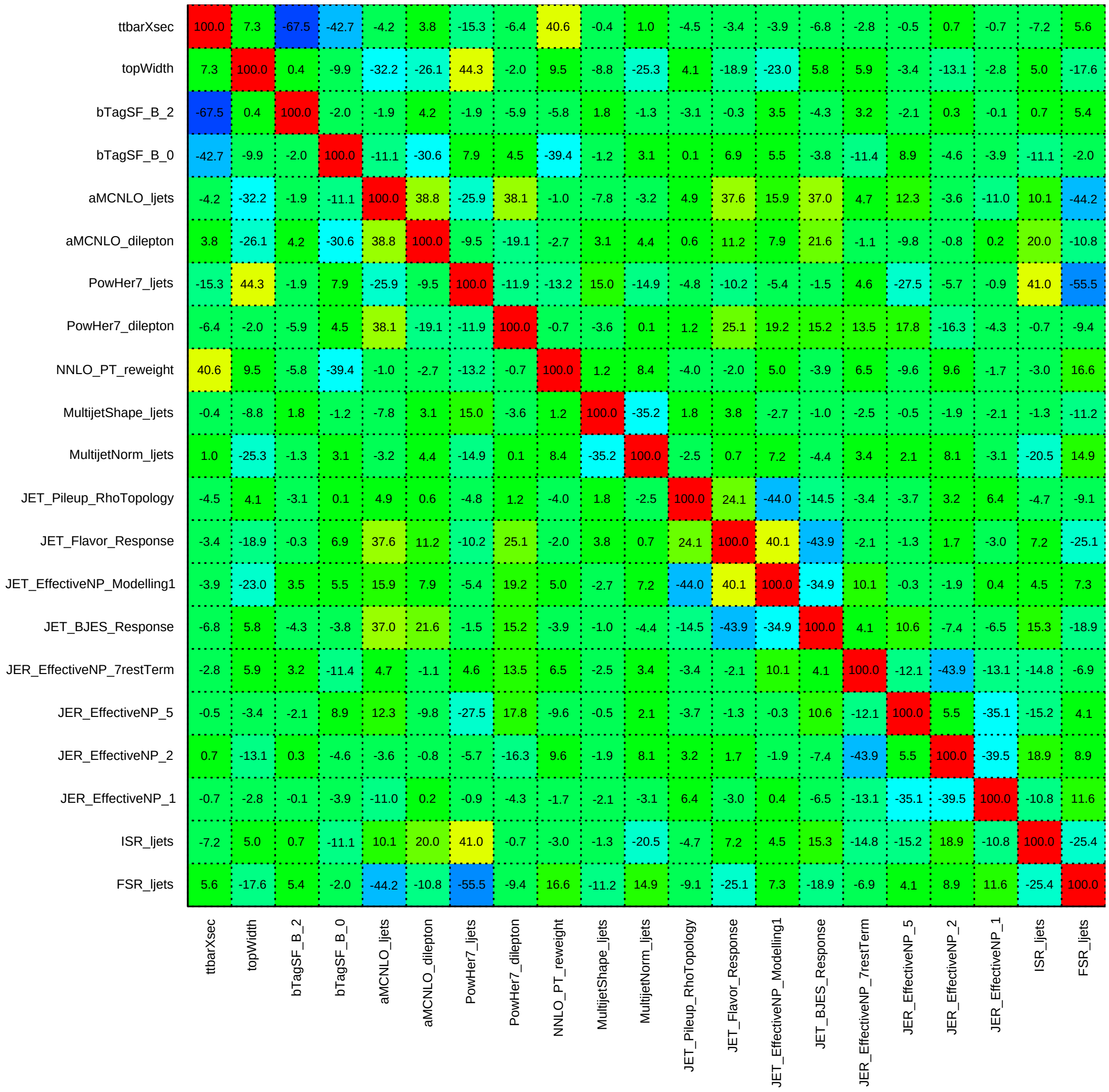

	ttbarXsec	topWidth	bTagSF_B_2	bTagSF_B_0	aMCNLO_ljets	aMCNLO_dilepton	PowHer7_ljets	PowHer7_dilepton	NNLO_PT_reweight	MultijetShape_ljets	MultijetNorm_ljets	JET_Pileup_RhoTopology	JET_Flavor_Response	JET_EffectiveNP_Modelling1	JET_BJES_Response	JER_EffectiveNP_7restTerm	JER_EffectiveNP_5	JER_EffectiveNP_2	JER_EffectiveNP_1	ISR_ljets	FSR_ljets
ttbarXsec	100.0	7.3	-67.5	-42.7	-4.2	3.8	-15.3	-6.4	40.6	-0.4	1.0	-4.5	-3.4	-3.9	-6.8	-2.8	-0.5	0.7	-0.7	-7.2	5.6
topWidth	7.3	100.0	0.4	-9.9	-32.2	-26.1	44.3	-2.0	9.5	-8.8	-25.3	4.1	-18.9	-23.0	5.8	5.9	-3.4	-13.1	-2.8	5.0	-17.6
bTagSF_B_2	-67.5	0.4	100.0	-2.0	-1.9	4.2	-1.9	-5.9	-5.8	1.8	-1.3	-3.1	-0.3	3.5	-4.3	3.2	-2.1	0.3	-0.1	0.7	5.4
bTagSF_B_0	-42.7	-9.9	-2.0	100.0	-11.1	-30.6	7.9	4.5	-39.4	-1.2	3.1	0.1	6.9	5.5	-3.8	-11.4	8.9	-4.6	-3.9	-11.1	-2.0
aMCNLO_ljets	-4.2	-32.2	-1.9	-11.1	100.0	38.8	-25.9	38.1	-1.0	-7.8	-3.2	4.9	37.6	15.9	37.0	4.7	12.3	-3.6	-11.0	10.1	-44.2
aMCNLO_dilepton	3.8	-26.1	4.2	-30.6	38.8	100.0	-9.5	-19.1	-2.7	3.1	4.4	0.6	11.2	7.9	21.6	-1.1	-9.8	-0.8	0.2	20.0	-10.8
PowHer7_ljets	-15.3	44.3	-1.9	7.9	-25.9	-9.5	100.0	-11.9	-13.2	15.0	-14.9	-4.8	-10.2	-5.4	-1.5	4.6	-27.5	-5.7	-0.9	41.0	-55.5
PowHer7_dilepton	-6.4	-2.0	-5.9	4.5	38.1	-19.1	-11.9	100.0	-0.7	-3.6	0.1	1.2	25.1	19.2	15.2	13.5	17.8	-16.3	-4.3	-0.7	-9.4
NNLO_PT_reweight	40.6	9.5	-5.8	-39.4	-1.0	-2.7	-13.2	-0.7	100.0	1.2	8.4	-4.0	-2.0	5.0	-3.9	6.5	-9.6	9.6	-1.7	-3.0	16.6
MultijetShape_ljets	-0.4	-8.8	1.8	-1.2	-7.8	3.1	15.0	-3.6	1.2	100.0	-35.2	1.8	3.8	-2.7	-1.0	-2.5	-0.5	-1.9	-2.1	-1.3	-11.2
MultijetNorm_ljets	1.0	-25.3	-1.3	3.1	-3.2	4.4	-14.9	0.1	8.4	-35.2	100.0	-2.5	0.7	7.2	-4.4	3.4	2.1	8.1	-3.1	-20.5	14.9
JET_Pileup_RhoTopology	-4.5	4.1	-3.1	0.1	4.9	0.6	-4.8	1.2	-4.0	1.8	-2.5	100.0	24.1	-44.0	-14.5	-3.4	-3.7	3.2	6.4	-4.7	-9.1
JET_Flavor_Response	-3.4	-18.9	-0.3	6.9	37.6	11.2	-10.2	25.1	-2.0	3.8	0.7	24.1	100.0	40.1	-43.9	-2.1	-1.3	1.7	-3.0	7.2	-25.1
JET_EffectiveNP_Modelling1	-3.9	-23.0	3.5	5.5	15.9	7.9	-5.4	19.2	5.0	-2.7	7.2	-44.0	40.1	100.0	-34.9	10.1	-0.3	-1.9	0.4	4.5	7.3
JET_BJES_Response	-6.8	5.8	-4.3	-3.8	37.0	21.6	-1.5	15.2	-3.9	-1.0	-4.4	-14.5	-43.9	-34.9	100.0	4.1	10.6	-7.4	-6.5	15.3	-18.9
JER_EffectiveNP_7restTerm	-2.8	5.9	3.2	-11.4	4.7	-1.1	4.6	13.5	6.5	-2.5	3.4	-3.4	-2.1	10.1	4.1	100.0	-12.1	-43.9	-13.1	-14.8	-6.9
JER_EffectiveNP_5	-0.5	-3.4	-2.1	8.9	12.3	-9.8	-27.5	17.8	-9.6	-0.5	2.1	-3.7	-1.3	-0.3	10.6	-12.1	100.0	5.5	-35.1	-15.2	4.1
JER_EffectiveNP_2	0.7	-13.1	0.3	-4.6	-3.6	-0.8	-5.7	-16.3	9.6	-1.9	8.1	3.2	1.7	-1.9	-7.4	-43.9	5.5	100.0	-39.5	18.9	8.9
JER_EffectiveNP_1	-0.7	-2.8	-0.1	-3.9	-11.0	0.2	-0.9	-4.3	-1.7	-2.1	-3.1	6.4	-3.0	0.4	-6.5	-13.1	-35.1	-39.5	100.0	-10.8	11.6
ISR_ljets	-7.2	5.0	0.7	-11.1	10.1	20.0	41.0	-0.7	-3.0	-1.3	-20.5	-4.7	7.2	4.5	15.3	-14.8	-15.2	18.9	-10.8	100.0	-25.4
FSR_ljets	5.6	-17.6	5.4	-2.0	-44.2	-10.8	-55.5	-9.4	16.6	-11.2	14.9	-9.1	-25.1	7.3	-18.9	-6.9	4.1	8.9	11.6	-25.4	100.0

Figure G.5.: Correlations for the nuisance parameters considered in the fit to the observed data in the combined lepton+jets and the dilepton channel. Only correlations larger than 35 % are displayed.